Applications of Photoredox Chemistry for the Generation of Valuable Products

Tong Zhang

Hoofdpromotor: Prof. dr. Shoubhik Das

Lokale promotor: Prof. dr. Bert U. W. Maes

Proefschrift voorgelegd tot het behalen van de graad van Doctor in de Wetenschappen: Chemie

Departement Chemie, Faculteit Wetenschappen —— Antwerpen, België, 2023

Universiteit Antwerpen

Applications of Photoredox Chemistry for the Generation of Valuable Products

Proefschrift voorgelegd tot het behalen van de graad van
Doctor in de Wetenschappen: Chemie
aan de Universiteit Antwerpen
te verdedigen door

Tong Zhang
Uit Jiangsu, P. R. China

Hoofdpromotor:
Prof. dr. Shoubhik Das
Lokale promotor:
Prof. dr. Bert U. W. Maes

Departement Chemie
Faculteit Wetenschappen
Antwerpen, België, 2023

Dutch translation of the title:

Toepassingen van Photoredox-chemie voor het genereren van waardevolle producten

Preface and Scientific goal

Due to the climate change, pollutions, energy shortage and other interrelated global crises, there is always an increasing demand for the development of environmentally friendly processes in the chemical industries. In the last two decades, the field of photochemistry has emerged as a potent methodology across diverse domains, enabling the synthesis of numerous intricate compounds through environmentally sustainable means.

This thesis aims to demonstrate the advantages of photochemistry as a potent methodology for synthesizing valuable products across diverse domains. **Chapter 1** introduced the fundamental principles and concepts underlying photochemistry, elucidating them through existing methodologies or systems. To show the efficiency, safety and circularity of photochemistry, four distinct methodologies (**Chapter 2-5**) were developed and employed, utilizing photoredox and photochemical reactions to produce valuable products across various domains, demonstrating the practical application of photochemistry in synthesis. All these methodologies rely on the photochemistry, aiming to engineer or create environmentally sustainable and milder reaction systems to attain specific desired products.

The thesis is divided into five chapters:

- **Chapter 1**: An overview and introductory exposition of the fundamental principles and concepts pertaining to photochemistry are provided.
- **Chapter 2**: We have enhanced the generation of hydrogen peroxide by introducing an aryl amino group in polymeric carbon nitrides *via* visible light-mediated photocatalysis. In addition to increasing the efficiency of photocatalytic system, the description of the whole

reactive scenario for the polymeric carbon nitrides has been depicted by combining diverse characteristic methods and theoretical calculations. Futhermore, the possible active catalytic sites are identified with the aid of ^{15}N and ^{19}F solid state NMR without using any expensive labeling reagent.

- **Chapter 3**: We have developed a unique methodology for the generation of α-amino radicals under the irradiation of visible light under a metal-free condition. This strategy is induced by π–π stacking and ion-pairing interactions and facilitated the synthesis of functionalized amines through three-component coupling reactions.
- **Chapter 4**: We have designed an efficient method for the red light-mediated sulfonyltrifluoromethylation of olefins which provide remarkable regioselectivity. This reaction system has been thoughtfully designed, and excellent substrate compatibility and functional group tolerance exhibits the industrial potential, thus validating the significance of this strategy.
- **Chapter 5**: We have developed a metal-free photocatalytic system for the transformation of biomass into formic acid. Compared to previous strategies, our method can work efficiently at room temperature and atmospheric pressure. Notably, real biomass and even daily-life-based-materials such as waste papers and oak cork stoppers of wine bottles are also smoothly converted to formic acid.

Schematic main content of Thesis:

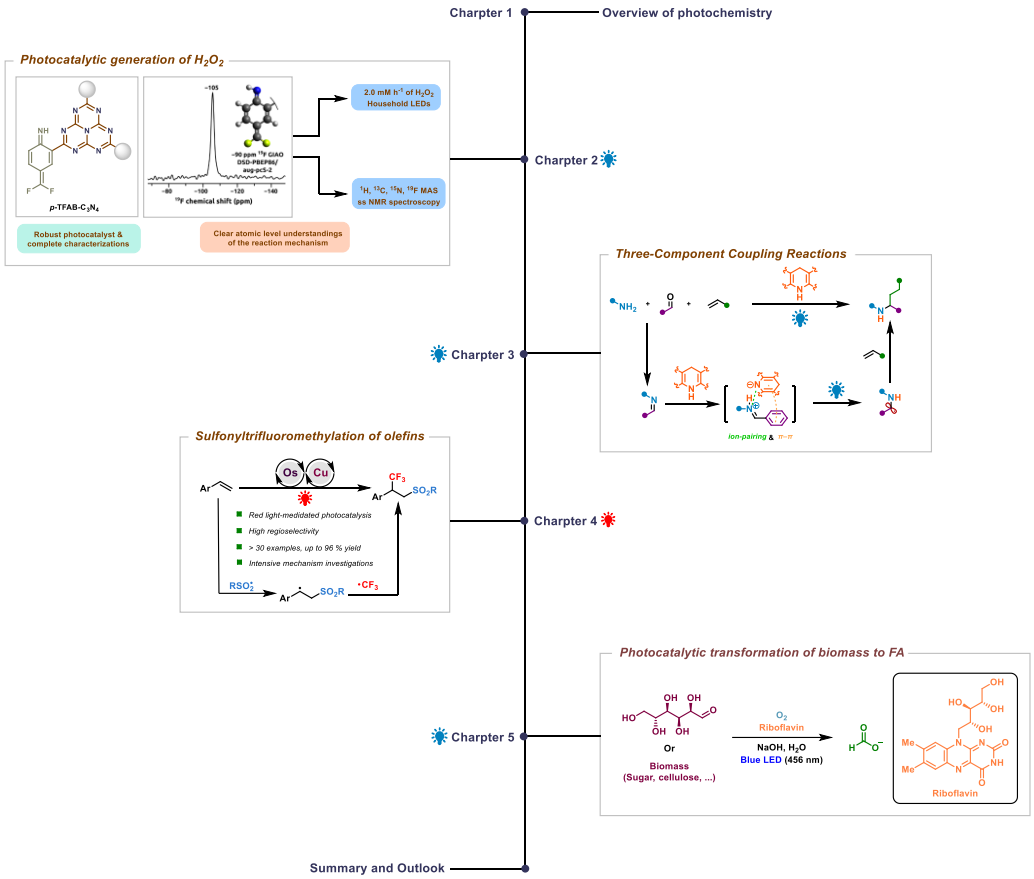

Content

Acknowledgement

I would like to express my heartfelt gratitude to all those who have supported and guided me throughout my doctoral journey.

First and foremost, I would like to express my genuine thanks and deep appreciation to my supervisor, Prof. Shoubhik Das. I am incredibly grateful for the opportunity to undertake my doctoral studies under his expert guidance. We crossed paths in Göttingen during my master's studies. Since then your unwavering support, guidance, and expertise have been the cornerstone of my research journey. Your mentorship has not only enriched my academic pursuits but has also profoundly influenced my personal and professional growth. I am grateful for the countless hours you spent reviewing my work, providing valuable feedback, and patiently answering my questions. The full independence in science you have granted me has provided me with the opportunity to explore and study topics that truly pique my interest. I have experienced a wonderful and enjoyable time in my doctoral journey.

I am also grateful to all the jury members of my thesis: Prof. Bert U. W. Maes, Prof. Filip Lemière, Prof. Ana Cunha, Prof. Pascal Van Der Voort, Prof. Dirk De Vos and Prof. Pieter Billen for their willingness to evaluate my doctoral thesis work and for their invaluable suggestions.

In this remarkable journey, numerous enthusiastic and talented friends and scientists have provided me with invaluable advice, assistance, companionship and friendship. I would like to thank Dr. Yu Zhang, Dr. Daniel Riemer and Dr. Waldemar Schilling, our previous group members, for their fully support and guidance at the beginning of my PhD carrier. I would like to thank Dr. Aswin Gopakumar, Dr. Rakesh Maiti, Dr. Suman Pradhan, Dr. Topi Ghosh, Miss. Yuman Qin, Miss. Lulu Chen, Mr. Robin

Cauwenbergh, Mr. Peng Ren, Mr. Jaro Vanderghinste and Mr. Jian Zhu for being the fantastic and friendly labmates. I really enjoyed and will miss the brainstorming discussions in chemistry as well as the dinners and beer breaks with all of you. I wish to extend my special gratitude to Dr. Yufeng Liang, Dr. Yang Liu and Dr. Xingfeng Bai, three mentors within the lab. They not only provided me with insightful explanations in the field of science but also offered invaluable guidance regarding conduct and the right attitude towards scientific pursuits. I also would like to thank our whole ORSY, particularly, Mr. Philippe Franck, Dr. H.Y. Vincent Ching, Mr. Rui An, for all their supports and assistances.

I am grateful to Prof. Sabine Van Doorslaer and Dr. H.Y. Vincent Ching for EPR measurements and analyses. I am grateful to Mr. Philippe Franck, Prof. Filip Lemière and Mr. Glenn Van Haesendonck for HPLC and HRMS measurements. I express my profound appreciation to the University of Antwerp for providing the necessary resources and financial assistance (DocPro doctoral scholarship). I would like to thank the Research Foundation–Flanders for their financial support (Fonds voor Wetenschappelijk Onderzoek (FWO) fellowship).

Outside of chemistry, I would like to thank my friends in Germany, Mr. Yue Wang, Mr. Jin Ye, Mr. Zeyu Feng and Mr. Wei Li, for their encouragement. The distance did not change anything. I also would like to thank Dr. Hui Shi, Dr. Yun Ling, Mr. Zehua Tao, Mr. Shangkun Li, Mr. Qihang Yao and Mr. Qiang Lu, for being close friends. I enjoyed and will miss every trip, every meal and every moment with all of you.

I would like to thank my buddies/ besties in China, Dr. Liya Ma, Mr. Hui Xian, Miss. Zhe Zhang, Miss. Hongjin Wu, Mr. Shuyang Zhao, Mr. Aojun Zhang, Miss. Yiming Ma, Mr. Xiang Li, Miss. Shuyu Zhang, Mr. Chunyang Zhai, Miss. Jiali Liu and Miss. Tianyu Sun for their company and encouragement.

At last, my deepest thanks and gratitude to my parents, Mr. Lianshun Zhang and Miss. Fengqin Sun, for their undying love and support. A Chinese proverb: “As long as parents are alive, one should not travel far.” Despite studying in Europe for nearly eight years, they have no complaints about me. I could not finish my PhD journey smoothly without their sacrifices, especially during challenging times caused by the Covid. They cleared the path of obstacles, enabling me to reach for the star in the sky. My love and gratitude to them would be never enough.

List of Abbreviations

2-MeTHF	2-methyl tetrahydrofuran
4CzIPN	1,2,3,5-tetrakis(carbazol-9-yl)-4,6-dicyanobenzene
Ac	acetyl
AcOH	acetic acid
AIBN	2,2′-azobis(isobutyronitrile)
API	active pharmaceutical ingredient
aq.	aqueous
Ar	aryl
Ar	argon
atm.	atmosphere
ATR	attenuated total reflection
ATRA	atom-transfer radical addition
BDE	bond dissociation energy
BHT	butylated hydroxytoluene; 2,6-di-*tert*-butyl-4-methylphenol
BINAP	2,2′-bis(diphenylphosphino)-1,1′-binaphthyl
BINOL	1,1′-bi-2-naphthol
Bn	benzyl
Boc	*tert*-butyloxycarbonyl; di-*tert*-butyl dicarbonate
bpm	2,2'-bipyrimidine

bpy	2,2′-bipyridine
bpz	2,2'-bipyrazine
br. s	broad singlet
Bu	butyl
^{n}Bu	*n*-butyl
Bz	benzoyl
c	molar concentration
cat	catalyst
CB	conduction band
Cbz	carboxylbenzyl
CFL	compact fluorescent light
cm	centimeter
COD	1,5-cyclooctadiene
conPET	consecutive photoinduced electron transfer
CT	charge-transfer
CV	cyclic voltammetry
cw EPR	continuous wave electron paramagnetic resonance
Cy	cyclohexyl
d	doublet
dap	2,9-bis(*para*-anisyl)-1,10-phenanthroline
DABCO	1,4-diazabicyclo[2.2.2]octane
DBU	1,8-diazabicyclo[5.4.0]undec-7-ene
DCE	1,2-dichloroethane

DCM	dichloromethane
dd	doublet of a doublet
ddd	doublet of a doublet of doublet
ddt	doublet of a doublet of triplet
de	diastereomeric excess
dF(CF$_3$)ppy	2-(2,4-difluorophenyl)-5-trifluoromethylpyridine
DFT	density functional theory
DIPEA	*N*,*N*-diisopropylethylamine
DMA	*N*,*N*-dimethylacetamide
DMC	dimethyl carbonate
DMAP	4-dimethylaminopyridine
DMF	*N*,*N*-dimethylformamide
dmp	2,9-dimethyl-1,10-phenanthroline
DMPO	5,5-dimethyl-1-pyrroline *N*-oxide
DMPU	*N*,*N*-dimethylpropyleneurea
DMSO	dimethyl sulfoxide
DNA	deoxyribonucleic acid
DPEphos	bis[(2-diphenylphosphino)phenyl]ether
dpp	2,9-diphenyl-1,10-phenanthroline
dr	diastereomeric ratio
dt	doublet of a triplet
dtbbpy	4,4′-di-*tert*-butyl-2,2′-dipyridine
E	energy

Et	ethyl
EDA	electron donor-acceptor
EDG	electron donating group
e.g.	exempli gratia (for example)
ee	enantiomeric excess
EnT	energy transfer
EPR	electron paramagnetic resonance
equiv.	equivalent
er	enantiomeric ratio
Et	ethyl
et al.	et alia (and others)
ESI	electron spray ionization (mass spectrometry)
E/Z	entgegen/zusammen
eV	electronvolt
EWG	electron withdrawing group
Exp.	experimental spectrum
f	frequency
fac	facial
FTIR	Fourier transform infrared spectroscopy
g	gram(s)
GCMS	gas chromatography mass spectrometry
HAT	hydrogen atom transfer
HFIP	1,1,1,3,3,3-hexafluoro-2-propanol

HOMO	highest occupied molecular orbital
HPLC	high-performance liquid chromatography
HRMS	high resolution mass spectrometry
HSQC	heteronuclear single-quantum correlation
Hz	Hertz
i.e.	it est (that is)
^{i}Pr	isopropyl
IR	infrared
ISC	intersystem crossing
L	ligand
LA	Lewis acid
LDA	lithium diisopropylamide
LED	light emitting diode
LMCT	ligand to metal charge transfer
LUMO	lowest unoccupied molecular orbital
m	multiplet
M	metal; molar
***m*-**	meta-
***m*-CPBA**	meta-chloro perbenzoic acid
Me	methyl
MeCN	acetonitrile
Mes	mesityl

Mes-Acr^{+}-Me ClO_4^-	9-mesityl-10-methylacridinium perchlorate, CAS 674783-97-2
mg	milligram(s)
MHz	mega hertz
min	minute
mL	milliliter(s)
MLCT	metal-to-ligand charge transfer
mmol	millimole
mol%	mole percent
mp	melting point
MS	molecular sieves
MTBE	methyl *tert*-butyl ether
m/z	mass to charge ratio
NCS	*N*-chlorosuccinimide
NHPI	*N*-hydroxyphthalimide
NIR	near-infrared
NIS	*N*-iodosuccinimide
nm	nanometer
NMP	*N*-methyl-2-pyrrolidone
NMR	nuclear magnetic resonance
NOESY	nuclear Overhauser effect spectroscopy
^{n}Pr	*n*-propyl
ns	nanosecond(s)

Nu	nucleophile
***o*-**	ortho-
OAc	acetate
***p*-**	para-
PC	photocatalyst
***PC**	electronically excited photocatalyst
$PC^{\bullet+}$	oxidized photocatalyst
$PC^{\bullet-}$	reduced photocatalyst
PCET	proton-coupled electron transfer
PET	photoinduced electron transfer
PG	protecting group
Ph	phenyl
phen	1,10-phenanthroline
ppm	parts per million
ppy	2-phenylpyridine
Pr	propyl
***p*-TSA**	para-toluenesulfonic acid
q	quartet
Q-TOF MS	quadrupole-time of flight mass spectrometer
R	rectus, Latin for right
R_f	retention factor
r.t.	room temperature
s	singlet

S	sinister, Latin for left
SCE	saturated calomel electrode
sept	septet
SET	single electron transfer
sp	synperiplanar
t	triplet
T_1	triplet excited-state
TBADT	tetrabutylammonium decatungstate
^{t}Bu	*tert*-butyl
TDDFT	time-dependent density functional theory
TEMP	2,2,6,6-tetramethylpiperidine
TEMPO	2,2,6,6-tetramethylpiperidin-1-oxyl
tert	tertiary
Tf	trifyl (trifluoromethane sulfonyl)
TFA	trifluoroacetic acid
TFE	2,2,2-trifluoroethanol
TfOH	triflic acid
THF	tetrahydrofuran
TLC	thin layer chromatography
TM	transition-metal
TMS	trimethylsilyl
UV	ultraviolet
V	volt

VB	valence band
vs.	versus (against)
v/v	volume per volume
W	Watt
X	arbitrary halogen
Xantphos	3,5-bis(diphenylphosphino)-9,9-dimethylxanthene
XPhos	2-dicyclohexylphosphino-2′,4′,6′-triisopropylbiphenyl

List of Symbols

Å	Ångström
δ	chemical shift in parts per million
Δ	heat
E_T	triplet-energy
$E_{0,0}$	excited-state energy
E_{ox}	ground-state oxidation potential
$^*E_{ox}$	excited-state oxidation potential
E_{red}	ground-state reduction potential
$^*E_{red}$	excited-state reduction potential
g_{iso}	isotropic g-value
h	Planck's constant (= 1.58×10^{-37} kcal·s)
h^+	electron hole
J	coupling constant
l	path length
λ (=*lambda*)	wavelength
λ_{max}	maximum absorption wavelength
λ_{em}	emission wavelength
λ_{ex}	exitation wavelength
ν (=nu)	frequency
Q or Φ	quantum yield
S_0	singlet ground state

S_1	singlet excited state
τ	excited state lifetime
E^0	standard potential
$E_{0,0}$	excited state energy of an electronically excited fluorophore in its lowest energy vibrational state
$E_{1/2}$	half-wave potential
E_{ox}	oxidation potential
$E_{p/2}$	half-peak potential
E_{red}	reduction potential
F	Faraday constant (23.061 kcal·mol^{-1} or 96485 C·mol^{-1})
λ	wavelength
R	ideal gas constant (8.31447 J·mol^{-1}·K^{-1})
τ	lifetime
ν	scan rate

Chapter 1

Overview and basic concepts of photochemistry

ABSTRACT: In this chapter, an overview and basic concept of homogeneous and heterogeneous photoredox/photochemical reactions are succinctly introduced. Within each section of different concepts, selective applications related to the corresponding synthesis or methodologies are described and explained.

Homogeneous photocatalysis

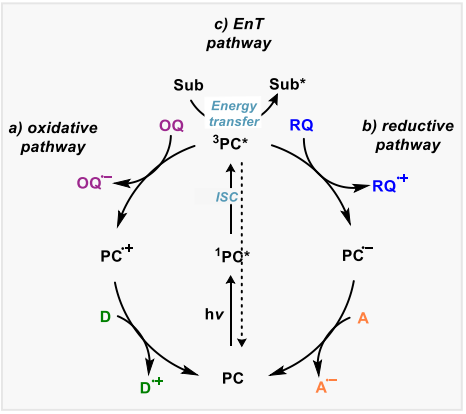

Heterogeneous photocatalysis

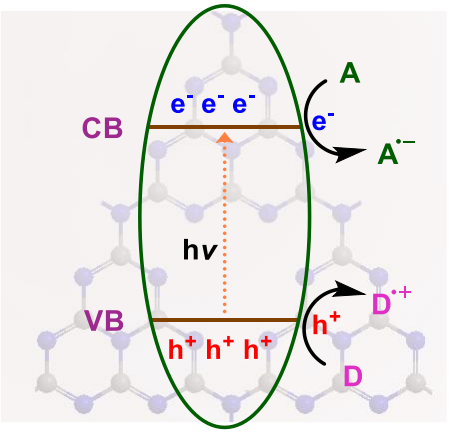

Noncovalent interactions-driven photochemistry

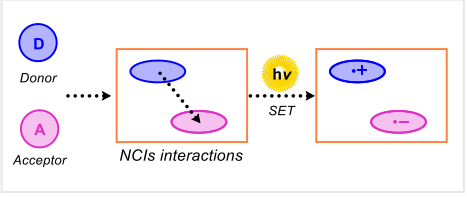

Red light-mediated photochemistry

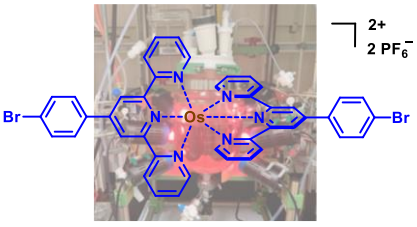

1.1 Introduction

In ancient civilizations, a collective awareness existed to reduce the effects of solar irradiation when foods such as oils, coffee, spices, and wines were stored, although a comprehensive understanding of these processes was still distant by then.[1] Encouraged by these early observations, scientists and scholars have investigated the phenomenon of light-triggered chemical reactions with notable milestones and discoveries.[2] In 1777, Carl Wilhelm Scheele, a Swedish chemist, has discovered that silver chloride became dark upon the irradiation of light.[3] Later in the mid of 19th centuries, Robert Bunsen and Henry Roscoe put efforts on the photochemical reactions of gaseous substances, which laid the foundation of understanding the importance of light intensity and wavelength in these reactions.[4] In the 20th century, propelled by the contemporary theoretical frameworks and the deployment of analytical techniques, the comprehension of photochemical processes were progressively attained.[5] For instance, Giacomo Luigi Ciamician, an Italian chemist, envisioned the potential of harnessing photochemical apparatuses capable of converting solar energy into fuels for the sustenance of human civilization.[6,7] Nowadays, photochemistry has emerged as a potent methodology across diverse domains including both academia and industries.[8]

Among different strategies in photochemistry, visible light-mediated photoreactions experienced a pronounced renaissance due to their environmental friendliness and low energy requirement in comparison to the energy-intensive ultraviolet (UV) light.[9] Additionally, compared to the UV light-mediated reactions and thermal reactions, less heat is generated in visible light-mediated photoreactions, resulting in less undesired products which can be induced by thermal effect.[10] Furthermore, in contrast to the UV light, compounds containing fragile chemical bonds could be less sensitive toward visible light due to their lower energy and in this way, prevent the photodecomposition.[11] Due to

all these advantages, visible light-mediated photochemistry has rapidly grown and diverse methodologies have been established in synthetic organic chemistry.[12] Thus, in this chapter, basic principles of visible light-mediated photochemistry and its selective applications in synthetic organic chemistry will be introduced.

1.2 Homogeneous photocatalysis

1.2.1 Catalytic pathways of homogeneous photocatalysis

Homogeneous catalysis is defined when the substrate and the catalyst coexist in one phase in a catalytic system. Nowadays, readily available transition metal complexes such as ruthenium (Ru)- and iridium (Ir)-based photocatalysts along with metal-free organic dyes have been extensively utilized in various areas (**Figure 1.1**).[13, 14]

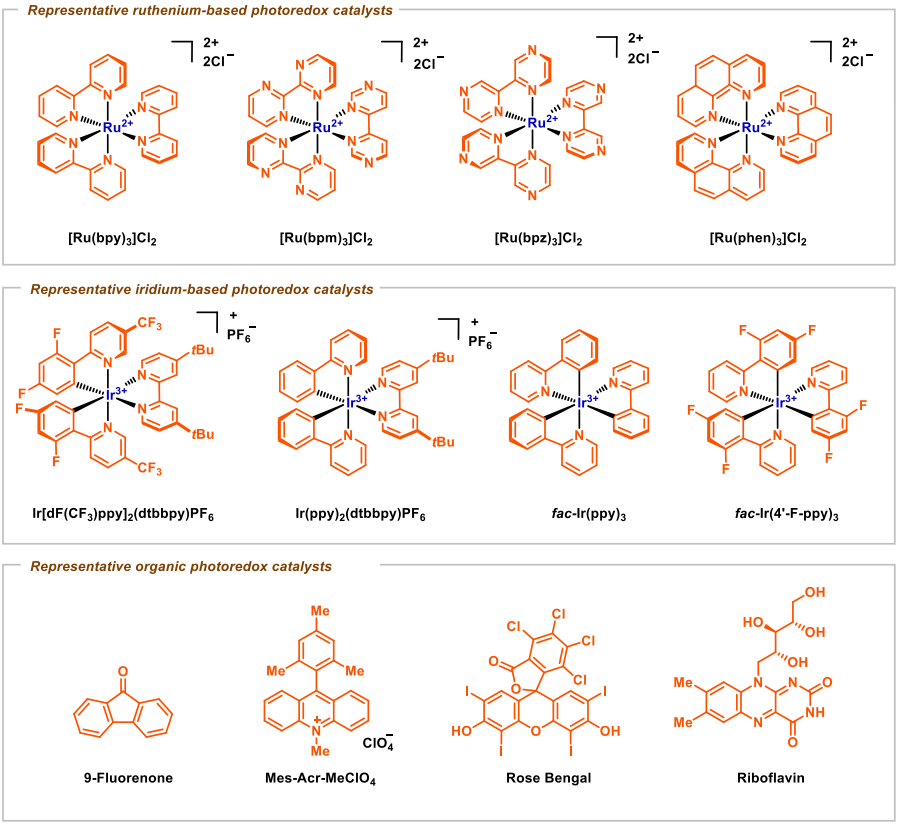

Figure 1.1. Representative common homogeneous photocatalysts.

These photocatalysts are able to absorb the light within the visible segment of the electromagnetic spectrum, resulting in the formation of stable and long-lived photoexcited states.[15, 16] On a molecular level, an electron migrates from the HOMO level to the LUMO level of the photocatalyst after the absorption of light, resulting in the formation of singlet excited state of the photocatalyst. Subsequently, the photocatalyst undergoes intersystem crossing to its triplet excited state, which has longer lifetime.[17] Compared to the photocatalyst at the ground state, the triplet excited state of the photocatalyst serves as either a stronger oxidant or a stronger reductant in photoredox process since an electron is at the higher energy level (lowest unoccupied molecular orbital (LUMO) level of its ground state) and a vacant orbital at lower energy level (highest occupied molecular orbital (HOMO) level of its ground state) is also available to accept an electron. As elucidated in **Figure 1.2**, the triplet excited state of photocatalyst can be quenched through a) oxidative pathway or b) reductive pathway. Besides the photoredox process, photocatalysts could also activate the substrates *via* energy transfer (EnT) process.[18] After excitation of the photocatalyst by the light, the photocatalyst as an excited donor transfers the excited-state energy to a ground-state acceptor (the substrate) which cannot be directly activated by the light (**Figure 1.2c**).[19] Another type of EnT, namely Dexter EnT, holds predominant significance and will be explained in detail.[20] Similar process to reach the triplet state of the photocatalyst, the EnT can be described as a contemporaneous mechanism involving the exchange of two electrons: the donor facilitates the electron transfer to the LUMO of the acceptor, concomitantly acquiring an electron from the HOMO of the acceptor. Consequently, the excited-state energy is transferred, resulting in forming the excited triplet state of the acceptor and simultaneously regenerating the ground state of the donor (**Figure 1.2d**).[21]

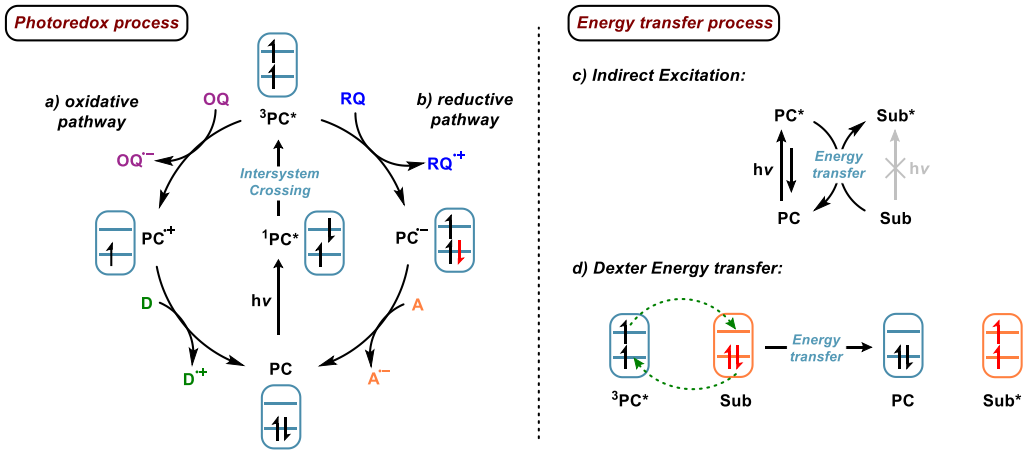

Figure 1.2. Schematic overview of the catalytic pathways of photocatalysis. **Left**: Photoredox process includes a) oxidative and b) reductive pathways. PC: photocatalyst, ^{1}PC*: singlet excited state of photocatalyst, ^{3}PC*: triplet excited state of photocatalyst, OQ: oxidative quencher, RQ: reductive quencher, D: electron donor, A: electron acceptor, hν: light irradiation. **Right**: Energy transfer process includes c) indirect excitation and d) dexter energy transfer. Sub: substrate, Sub*: light-excited/activated substrate.

To provide a more comprehensive understanding about the homogeneous photocatalysis, selective examples in synthetic organic chemistry will be introduced in the following sections.

1.2.2 Selective examples *via* oxidative pathway

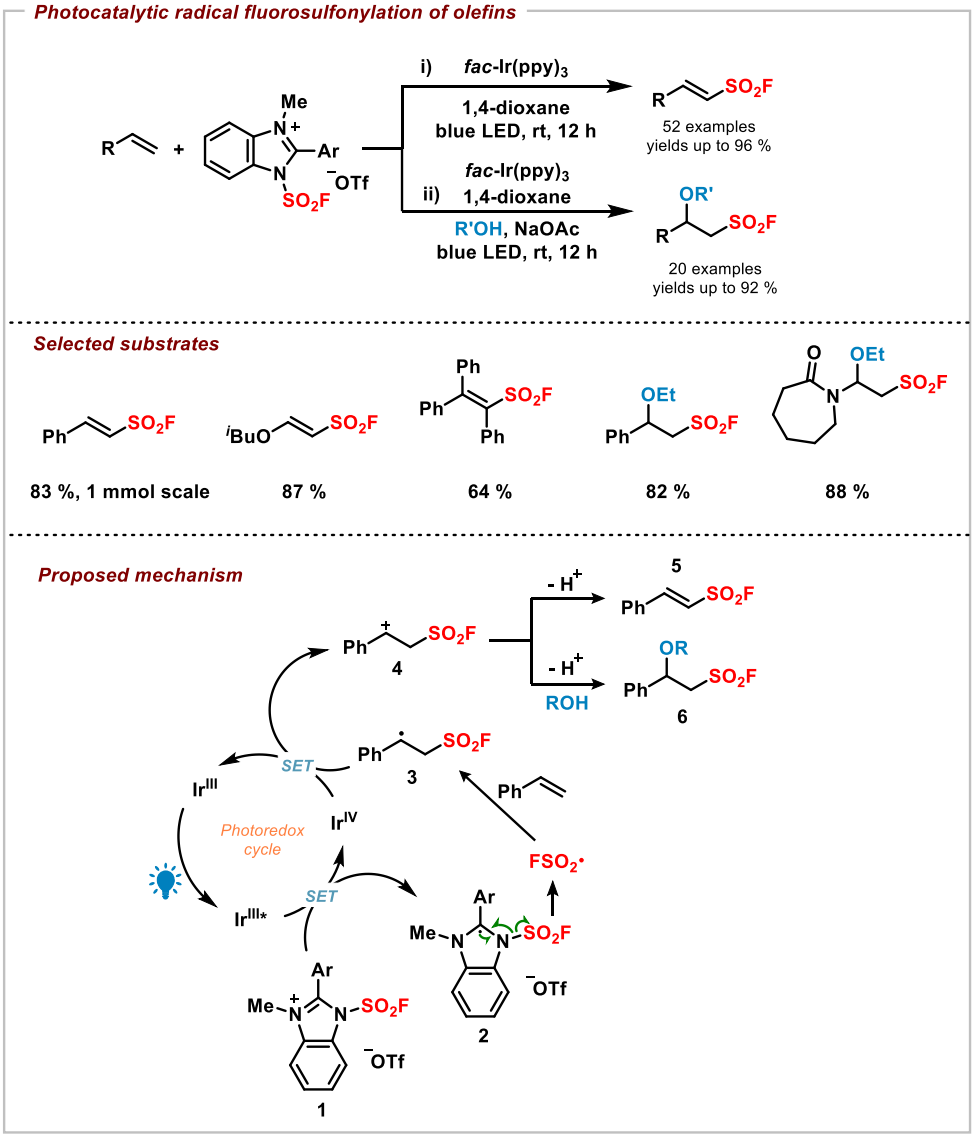

Figure 1.3. Reaction conditions: i) 0.1 or 0.2 mmol olefin, 2-3 equiv. FABI, 1mol % *fac*-Ir(ppy)$_3$ in 1,4-dioxane (0.025 M) at room temperature for 12 h under the irradiation of 6W blue LEDs.; ii) 0.1 mmol olefin, 3 equiv. FABI, 10 equiv. EtOH, 1mol % *fac*-Ir(ppy)$_3$, 1 equiv. NaOAc in 1,4-dioxane (0.1 M) at room temperature for 12 h under the irradiation of 6W blue LEDs.[22]

In 2022, Liao group reported a novel class of solid-state and redox-active fluorosulfonyl radical reagents which denoted as 1-fluorosulfonyl

2-aryl benzoimidazolium triflate (FABI) salts. Indeed, a facile radical fluorosulfonylation of olefin was achieved under photoredox conditions with these reagents (**Figure 1.3**).[22] In their proposed mechanism, FABI (**1**) was used as an oxidative quencher to accept an electron from the excited iridium photocatalyst ($\mathbf{Ir^{III*}}$) *via* single electron transfer (SET), followed by a homolytic cleavage of the N–S bond to deliver fluorosulfonyl radical ($FSO_2\bullet$). Subsequently, $FSO_2\bullet$ was added to styrene to form the carbon-centered radical intermediate (**3**) and followed by this, **3** was further oxidized by $\mathbf{Ir^{IV}}$ to afford the cationic species (**4**) and regenerated the iridium catalyst. At the end, **4** was either deprotonated or trapped by alcohols (ROH) to form the final product (**5**) or (**6)**, respectively. It is worth noting that the oxidative pathway was verified by the fluorescence quenching experiments. It demonstrated that as the concentration of FABI salt was increased, there was a notable reduction in fluorescence intensity.

1.2.3 Selective examples *via* reductive pathway

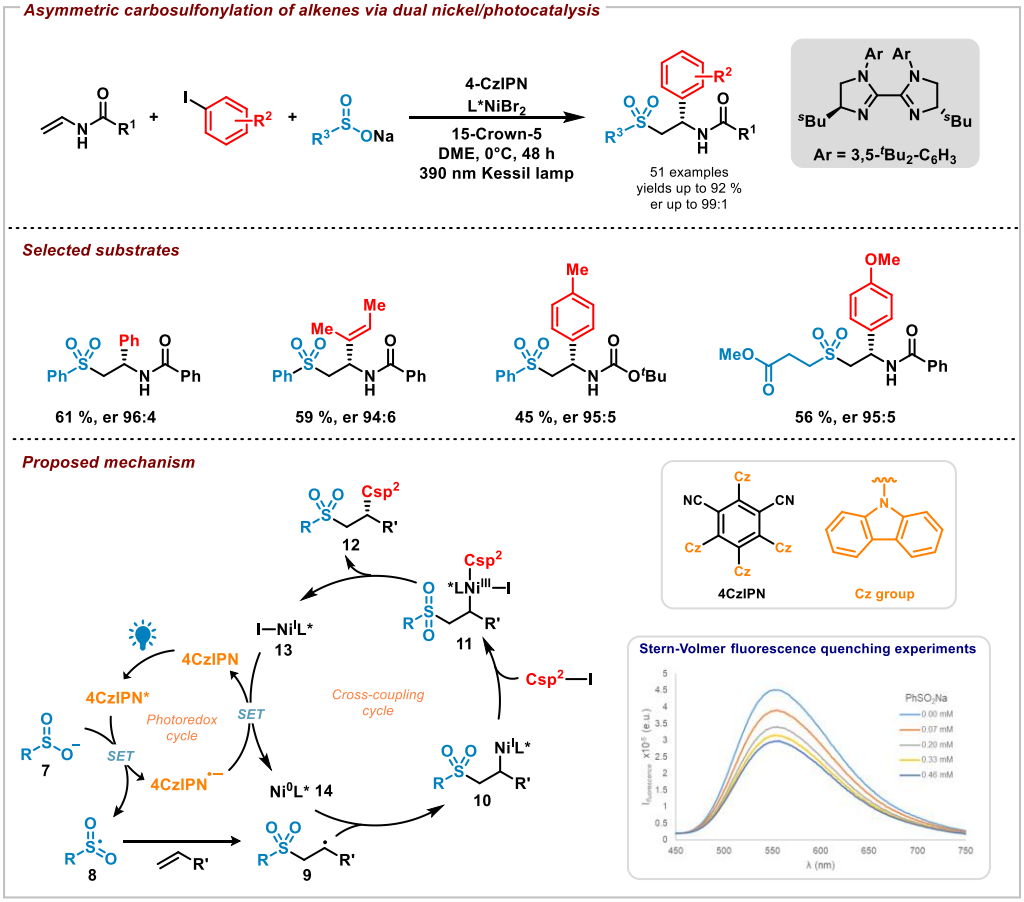

Figure 1.4. Reaction conditions: 0.1 mmol of aryl iodide, 0.2 mmol of alkene (), 0.2 mmol of sulfinate, 10 mol% of L*NiBr$_2$, 1 mol% of 4-CzIPN, 0.9 mmol of 15-crown-5 in DME (0.025 M) under the irradiation of Kessil LED (390 nm 45 W) at 0 °C for 48 h.

Recently, Nevado et *al.* has developed a dual nickel/photoredox catalytic reaction system for the synthesis of asymmetric carbosulfonylated products from alkenes (**Figure 1.4**).[23] In this three-component enantioselective carbonsulfonylation reaction, a sulfinate (**7**) was employed as an electron donor which was oxidized by the excited state of 1,2,3,5-tetrakis(carbazol-9-yl)-4,6-dicyanobenzene (4CzIPN*) to provide a sulfonyl radical (**8**). The radical (**8**) was added to an olefin to generate an alkyl radical (**9**) which was captured by the Ni^0 species (**14**)

to deliver a Ni^{I} species (**10**). Subsequently, Ni^{III} species (**11**) was formed by reacting with aryl iodide *via* oxidative addition reaction. At last, facile reductive elimination underwent to provide the enantioselective product (**12**) and the Ni^{I}–I species (**13**). The sodium sulfinates salts were also verified as reductive quenchers by the Stern-Volmer fluorescence quenching experiments.

1.2.4 Selective examples *via* energy transfer pathway

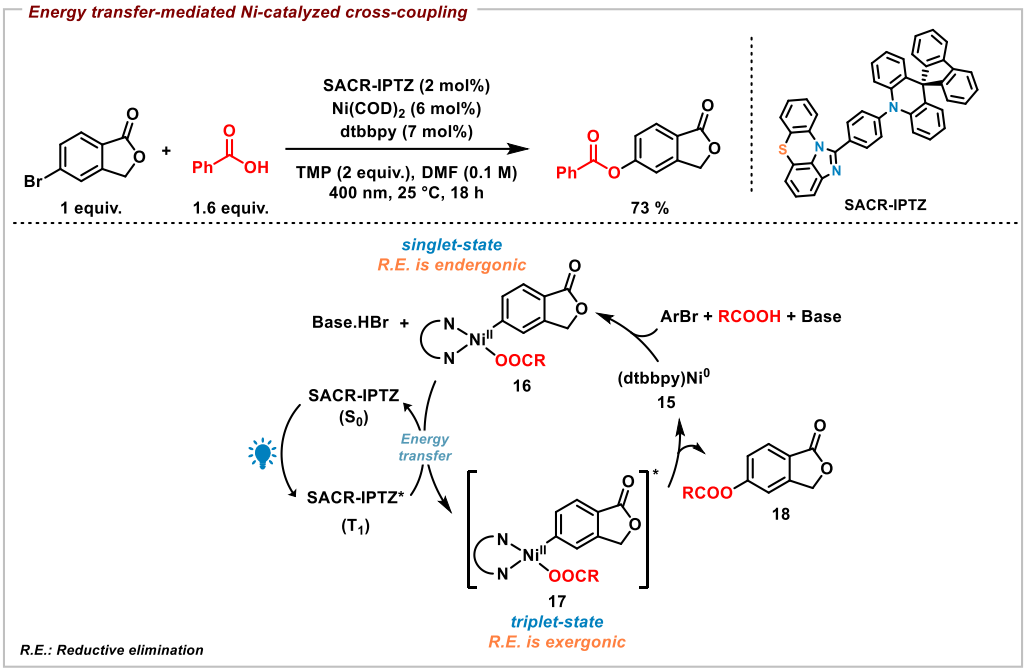

Figure 1.5. Ni-catalyzed esterifications by energy transfer.

Thermally activated delayed fluorescence (TADF) constitutes a mechanism that the electrons from the triplet states are efficiently harvested and harnessed to facilitate the induction of fluorescence. Photosensitizers characterized by the manifestation of TADF are emerged as a powerful tool in EnT photocatalysis. In 2023, group of Hudson has synthesized a series of imidazophenothiazine-based compounds as EnT photocatalysts which had the triplet energies up to

63.9 kcal mol^{-1}.[24] The designed catalysts demonstrated high efficacy to facilitate [2+2] cycloaddition reactions, disulfide-ene reactions, and Ni-catalyzed cross-coupling reactions between aryl halides and acids to achieve the corresponding esters. In the aforementioned esterification reaction, the base-mediated oxidative addition of an aryl halide with the (dtbbpy)Ni^0 species (**15**) proceeded to form the aryl–Ni^{II} species (**16**). Subsequent activation of **16** to its triplet state (**17**) occurred through an energy transfer mechanism which was facilitated by the triplet state of the imidazophenothiazine-based photocatalyst (SACR-IPTZ*). Facile reductive elimination of **17** allowed to provide the product (**18**) and (dtbbpy)Ni^0 species. It should be noted that the triplet energy (E_T) of aryl–Ni^{II} species (**16**, E_T = 20–24 kcal mol^{-1}) was lower than the E_T of SACR-IPTZ (E_T = 58–64 kcal mol^{-1}), which was pivotal to enable the activation process.

1.3 Heterogeneous photocatalysis

In contrast to the homogeneous catalysis, the catalyst exists within a distinct phase relative to the reactants in heterogeneous photocatalytic systems.[25, 26] At present, heterogeneous photocatalysis as a sustainable tool has garnered significant interest in organic synthesis since it is of great interest from the industrial point of view owing to its inherent advantages of facile catalyst separation from the reaction mixture and further reuse in the reaction.[27]

In the realm of the heterogeneous photocatalysts, metal oxides such as titanium dioxide (TiO_2) are popular and standard semiconductors which are used in photocatalysis for water splitting or other environmental applications.[28-30] These metal oxides possess a large band gap and make diverse reactions that are thermodynamically possible. However, it is a dilemma that strong light irradiation like UV light is required for the activation of these photocatalysts due to their large band gap. The adverse impact of UV light in photocatalysis has been described

in the previous introduction. Simultaneously, the expanded redox range of catalysts attributed to their wide band gap could give rise to the selectivity issue as the potential for unforeseen reactions is concurrently heightened.[31] Therefore, it becomes appealing to employ heterogeneous photocatalysts which can be activated by the visible light.

To overcome this obstacle, loading noble metal particles e.g. gold and silver on metal oxides is an efficient way to enhance the photocatalytic reactivity under the irradiation of visible light.[32] The metal oxides loaded with the noble metal nanoparticles which are regulated with comparatively small size and narrow size distribution, are capable of enhancing the absorption of visible light *via* surface plasmon resonance (SPR), which is a phenomenon observed when incident light at a specific angle excite electrons within a thin metal surface, subsequently causing their propagation in parallel along the surface.[33] Thus the number of photoexcited electron-hole pairs generated in the photocatalysts is increased. Simultaneously, the photogenerated electrons can be trapped by metal nanoparticles, resulting in an efficient separation of photogenerated charge carriers (**Figure 1.6**).[34] Both can lead to improved photocatalytic reactivity and efficiency compared to the original metal oxide semiconductors.

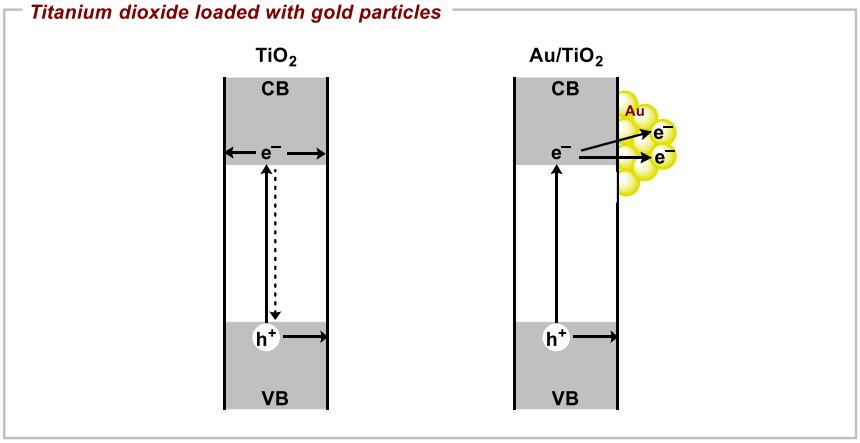

Figure 1.6. Efficient separation of photogenerated charge carriers in TiO_2, facilitated by the loading of gold particles.

Besides aforementioned photocatalysts, metal-free semiconductors such as covalent organic framework (COF) and polymeric carbon nitrides (PCN) have also received significant attention and are applied in areas such as water splitting, organic synthesis and for the degradation of pollutants (**Figure 1.7**).[35-41] In the context of organic synthesis and heterogeneous photocatalysis, PCN has already been developed and become one of the most popular candidates since the groups of Antonietti and Wang discovered its photocatalytic reactivity for the evolution of hydrogen and oxygen.[42]

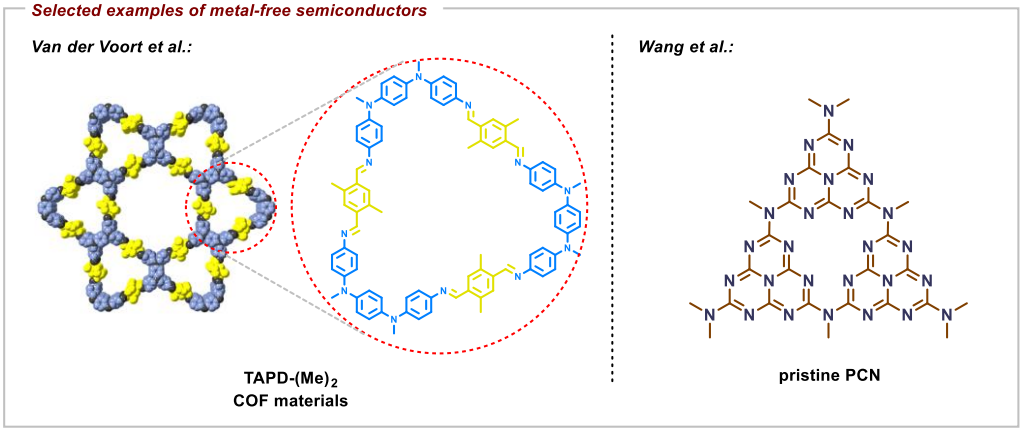

Figure 1.7. Examples of selected metal-free semiconductors.

1.3.1 General mechanism of heterogeneous photocatalysis with PCN

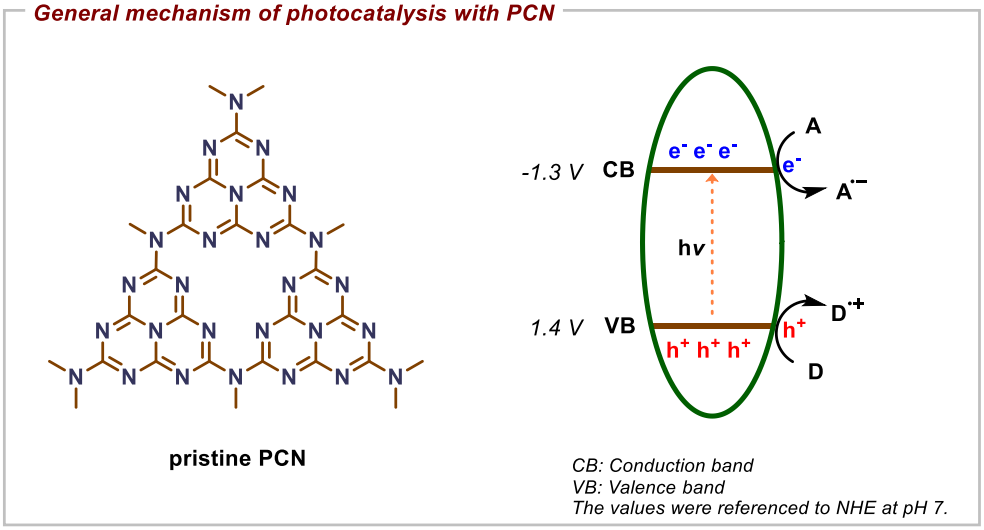

Figure 1.8. Schematic representation of the general mechanism of the photocatalysis with PCN.

The pristine PCN possess a band gap of ca. 2.7 eV (CB = -1.3 V vs. NHE at pH 7, VB = 1.4 V vs. NHE at pH 7). Therefore, PCN can be activated by the absorption of visible light, resulting in the excitation of the electrons in the valence band. The excited electrons are migrated to the conduction band, leading to the formation of positive holes in the valence band. The photogenerated electron-hole pairs are separated and further are migrated to the surface of the catalyst which react with the chemical donors (D) and acceptors (A) (**Figure 1.8**).[43] To enhance the photocatalytic reactivity, the redox potentials of donors and acceptors should be within the potential range of CB and VB. Moreover, the redox processes must exhibit pronounced efficiency to forestall the recombination of photoinduced electrons and holes.[44] Based on these requisite conditions, suitable sacrificial agents or modification of PCN are required.

Compared to the modification of PCN, using suitable sacrificial agents is a straightforward strategy to manage the reactions. Amines or alcohols are frequently used as sacrificial electron donors as they are comparatively easier to be oxidized.[45] Similarly, molecular oxygen is preferably used as an electron acceptor since its single-electron reduction potential is around -0.16 V vs. NHE at pH 7. In addition, superoxide radical anion ($O_2^{\bullet-}$) generated as the crucial intermediate can be further transformed into hydrogen peroxide (H_2O_2) which is a valuable green oxidant and a pulp bleaching reagent.[46, 47]

Nonetheless, within the realm of organic synthesis, the manipulation of PCN stands as a promising avenue for expediting reaction kinetics and expanding the scope of applicable substrates: i) the potentials of CB or VB can be adjusted by the formation of PCN by using different precursors. ii) It is also conceivable that these precursors possess the capability to bind with diverse functional groups or reactive scaffolds, leading to the corresponding derivatives of PCN. iii) Similar to metal oxides, PCN exhibit the capability to undergo metal loading, thereby enhancing both catalytic reactivity and stability. iv) Furthermore, the introduction of defects or atomic vacancies has been validated as a prospective approach for the optimization of electronic structure, concurrently serving as catalytically active site for reactive molecular species.[48] In the following sections, selective examples of visible light-mediated photocatalysis by using modified PCN is introduced.

1.3.2 Modification of PCN based on various precursors

The PCNs are synthesized by a thermal polymerization by using various precursors. The frequent used precursors include urea, thiourea, dicyandiamide (DCDA) and melamine (**Figure 1.9**).

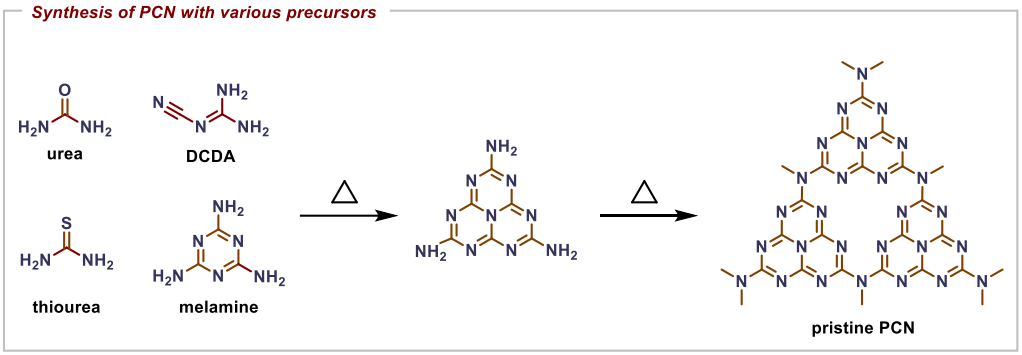

Figure 1.9. Synthetic route of PCN starting from different precursors.

In 2012, Groups of Antonietti and Wang have reported a facile modification of PCN with simple co-monomers to optimize the visible light-mediated hydrogen evolution reaction (**Figure 1.10**).[49] Various aromatic co-monomers such as organic compounds bearing amino cyano moieties were introduced in the copolymeric process, leading to the PCN with functional groups grafted on the surface. In principle, those functional groups were capable of tuning the electronic structures, electronic conductivities or morphologies of PCN which played the crucial roles for hydrogen evolution under the irradiation of visible light. This bottom-up fabrication of PCN was also able to be guided by the theoretical calculations, facilitating comprehension and the scalable manipulation of carbon nitride substructures.

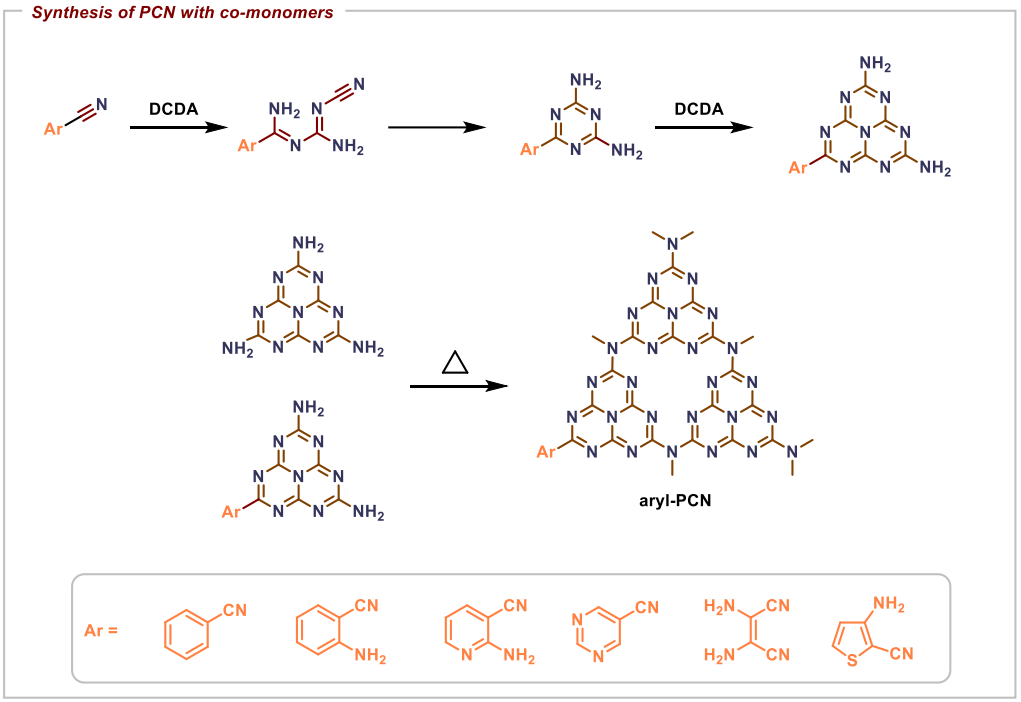

Figure 1.10. Schematic synthetic route of PCN with co-monomers.

1.3.3 Modifications of PCN with reactive scaffolds

As mentioned in **1.3.1**, the pristine PCN possesses a suitable band gap for the visible light-mediated generation of H_2O_2. In order to achieve high efficiency, alcohols rather than water were used as electron donors as the potential of VB of PCN is insufficient for the water oxidation due to limited thermodynamic driving force. To use green and earth-abundant water in place of alcohols, enhancing the catalytic efficacy of PCN to facilitate the process of water oxidation emerges as an imperative requisite. In 2014, Hirai group incorporated an aromatic diimides, pyromellitic diimide (PDI), into PCN by a thermal condensation reaction to promote the water oxidation (**Figure 1.11**).[50] PDI as a n-type organic semiconductor with high electron affinity was introduced in PCN so that it could positively shift the potentials of CB and VB which should allow water oxidation reaction. By incorporating different amount of PDI units, the potential of VB reached up to 1.89 V vs. Ag/AgCl at pH 6.6, while the

potential of CB was still sufficient for the reduction of oxygen. As expected, the photocatalytic production of H_2O_2 with PCN/PDI$_{51}$ occurred smoothly under the irradiation of visible light with a comparative amount of H_2O_2 (ca. 50.6 μmol). It was observed that the system demonstrated efficacy even when it was exposed to the solar light.

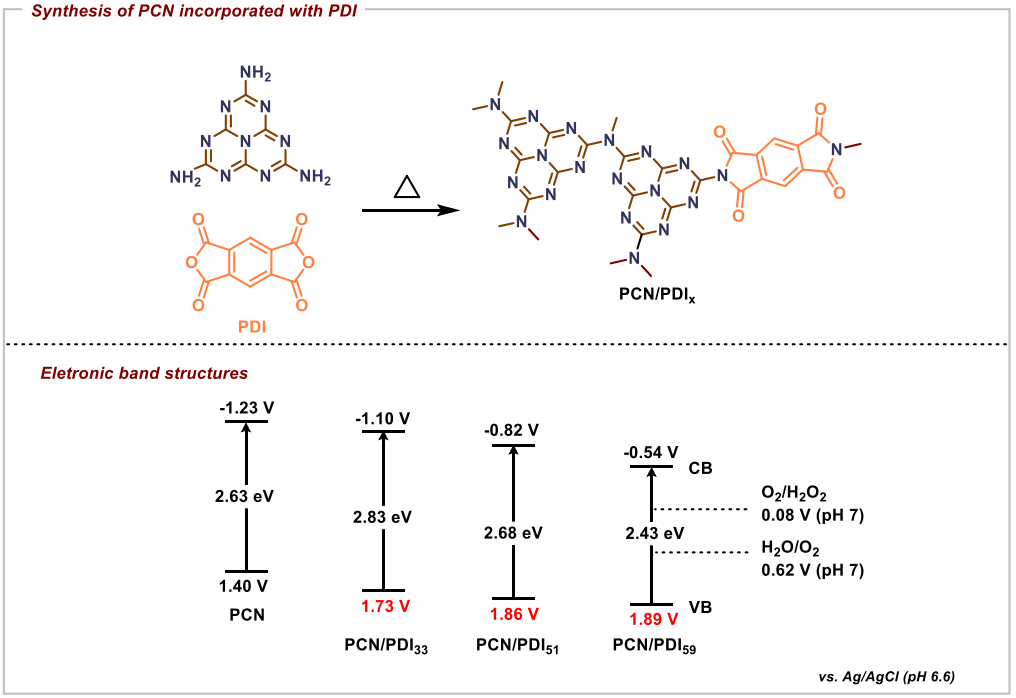

Figure 1.11. Top: Schematic synthetic route for the PCN incorporated with PDI. **Bottom:** Electronic band structures of the pristine PCN and PCN/PDIx.

1.3.4 Modifications of PCN by different metal loading

Similar to other semiconductors, many examples have shown that the loading of metals on PCN is considered as one of the effective strategies to improve the photocatalysis. Within the metal loading approach, dispersing metal atoms such as iron, nickel and platinum on PCN, is known as single-metal-atom catalysts (SACs) and currently, have been extensively investigated.[51,52] Compared to metal clusters or nanoparticles, SACs could provide more active sites of the transition metal to enhance the reactivity and selectivity in catalysis. Recently, our group has

fabricated a series of SACs comprised of atomically dispersed manganese situated on aryl amino-grafted PCN (Mn-SACs) for the photocatalytic generation of H_2O_2 from seawater (**Figure 1.12**).[47] The unsaturated Mn-Nx sites on aryl amino-grafted PCN facilitated the O_2 absorption and activation, preventing the recombination of photogenerated electron–hole pairs. Simultaneously, the aryl amino functional group shortened the band gap and enhanced the light absorption. The dispersed Mn-atoms and grafted aryl amino moieties synergistically promoted the catalytic reactivity for the production of H_2O_2 from seawater without the presence of any organic electron donor.

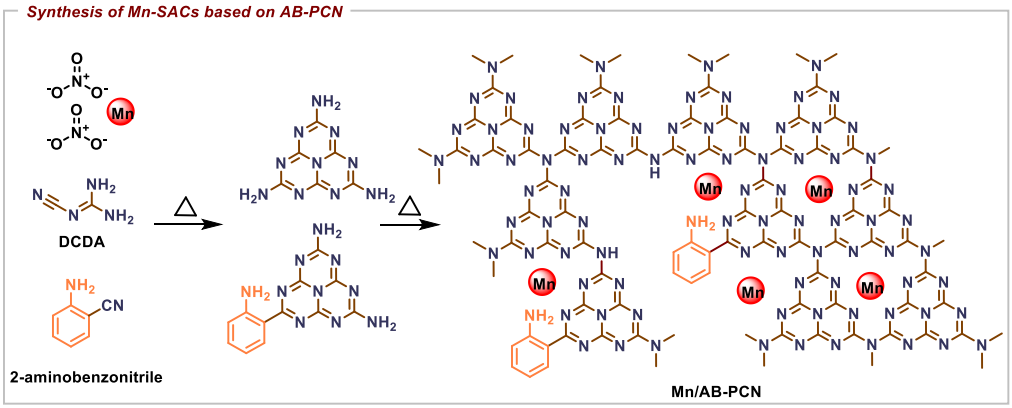

Figure 1.12. Schematic synthetic route of Mn-SACs (Mn/AB-PCN was shown as an example).

1.3.5 Modifications of PCN by introducing defect

Formerly, defects within materials were regarded as sites that were conducive to charge recombination. However, in recent times, defects have been verified to facilitate the photocatalysis when meticulously regulated.[53] Introducing defects in semiconductors could adjust the electronic band structures for the absorption of light as midgap states are formed between CB and VB. Simultaneously, the defects possess the potential to function as catalytically active sites for the organic molecules. Furthermore, defects can serve as trapping sites which can impede the recombination of the photogenerated electron-hole pairs.

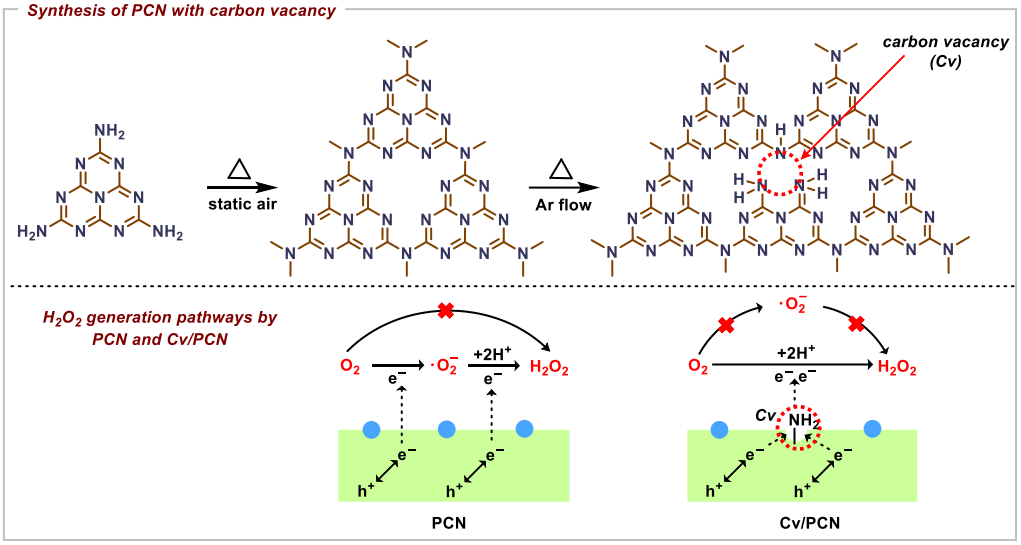

Figure 1.13. Top: Schematic synthetic route for Cv/PCN. **Bottom:** Different H_2O_2 production pathways by PCN and Cv/PCN.

In 2016, Wang group reported that the PCN was modulated by carbon vacancies for the photocatalytic production of H_2O_2 under the irradiation of visible light (**Figure 1.13**).[54] In fact, in contrast to the pristine PCN, the PCN containing carbon vacancies (Cv/PCN) exhibited a notable enhancement in photocatalytic reactivity, achieving a 14-fold increase in the absence of any organic scavenging agents. It should be noted that the mechanism of H_2O_2 generation in the context of the Cv/PCN system had transitioned from a sequential single-electron reduction process to a singular two-electron reduction process (**Figure 1.13 Bottom**). In pristine PCN, oxygen was reduced firstly to superoxide radical anion *via* SET, followed by additional single-electron-reduction. Compared to pristine PCN, the Cv/PCN could facilitate the reduction of oxygen directly *via* two-electron transfer and form the H_2O_2 with two protons.

1.4 Noncovalent interactions (NCIs)-driven photochemistry

The classification of forces that maintain atomic cohesion involves two primary categories: covalent interactions and noncovalent interactions (NCIs).[55] Although NCIs including hydrogen bonding, π-interactions, van der Waals, and Coulombic interactions are weaker compared to the relatively strong covalent bonds, they continue to maintain a fundamental role as the driving force within numerous processes, particularly exerting their significance in a majority of biochemical processes (**Figure 1.14**).[56, 57] For instance, precise conformational folding of proteins for functional efficacy significantly relies on NCIs. In addition, self-assembly has been considered as a consequence of NCIs. It is an inherent thermodynamic phenomenon characterized by the reduction of the system's free energy *via* intermolecular NCIs, resulting in the formation of precisely structured or organized nanoarchitectures.[58, 59] In the realm of catalyst design, NCIs also play a crucial role in the diminution of free energy barriers through the stabilization of transition states, making the catalytic systems more efficient.[60]

Among all the NCIs, π-interactions, encompassing π-π, lone pair-π, XH-π, and cation/anion-π interactions, have undergone comprehensive investigations within the realm of photochemical synthesis, particularly in association with aromatic functional moieties.[61-63] Considering factors such as the orientation, distance, and electronic effects that control or influence the NCIs, have been taken into account for the rational design of catalysts not only to achieve high catalytic reactivity but also high regio- or site-selectivity. In the following sections, selective examples of various π-interactions-mediated photocatalytic systems are introduced.

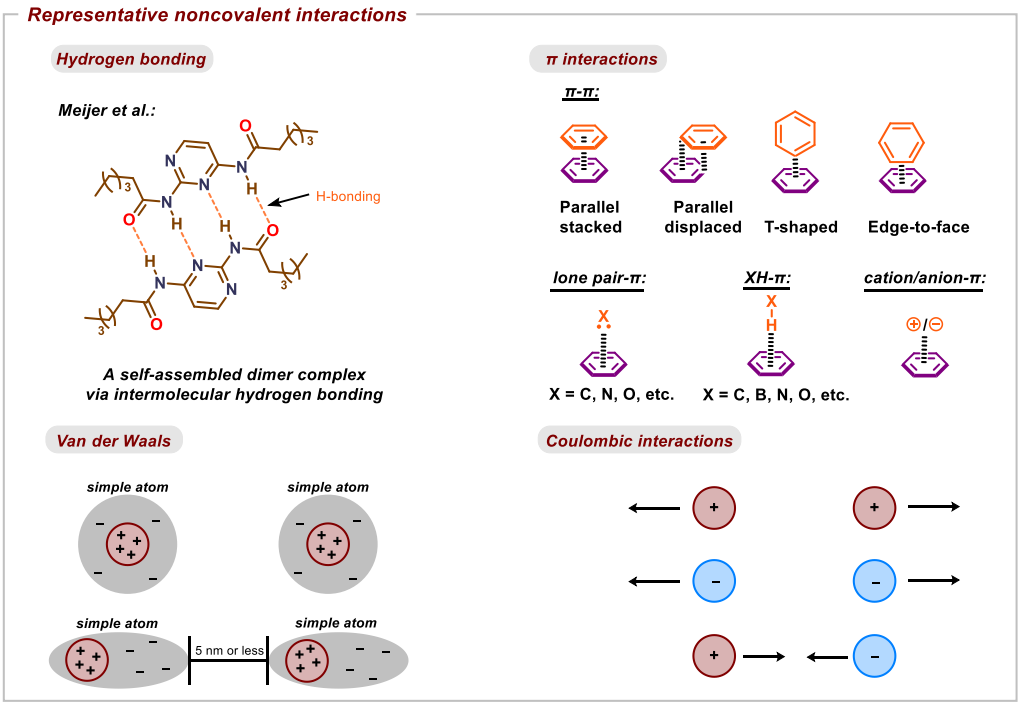

Figure 1.14. Representative noncovalent interactions and corresponding examples.

1.4.1 π-π interaction-induced photochemistry

C–S bonds are ubiquitously present within a range of pharmaceutical compounds, bioactive natural products, organic materials and polymers.[64] Consequently, there is a significant demand for facile and atom-economical methodologies to afford the formation of C–S bonds. In general, C–S cross-coupling reactions are conventionally catalyzed by transition metal catalysts, facilitating the coupling of thiols and aryl halides.[65] To accomplish the coupling reactions, strong bases, ligands and high temperature are essential in most of the reported systems. Since photochemistry has been emerged as a robust strategy to facilitating the advancement of chemical transformations under benign reaction conditions, methods for the formation of C–S bond have concurrently been developed. In 2017, Miyake group developed a visible light-mediated C–S cross-coupling reaction in the absence of both photoredox

catalysts and transition metals (**Figure 1.15**).[66] Based on the analysis of UV-vis spectroscopy and theoretical calculations, it suggested that the electron-poor aryl halide (acceptor) and the electron-rich thiolate (donor) formed a π-π interaction-induced electron donor-acceptor (EDA) complex. The intermolecular electron transfer between the donor and the acceptor provided the corresponding thiyl radical and aryl radical followed by the cross-coupling of these two radicals to provide the desired product.

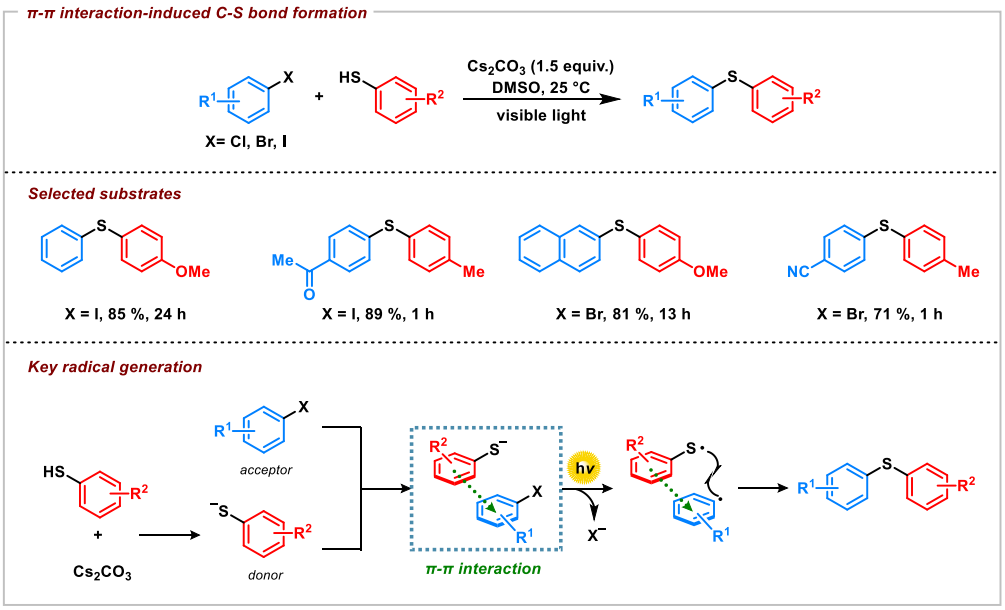

Figure 1.15. Photocatalytic C–S bond formation.

The transformation of carboxylic acids (CAs) is continuously attractive in both academia and industry since CAs are one of the extensively abundant and essential chemical feedstocks in nature.[67] Recently, photocatalytic decarboxylation of CAs has been well-developed and it has become a powerful method to generate various carbon-centered radicals.[68] In principle, photoinduced decarboxylation has both oxidative and reductive pathways. In oxidative pathway, the anion form of CAs ($RCOO^-$) undergoes the single-electron oxidation to provide the RCOO• followed by the release of CO_2 to the R•. In contrast,

CAs are able to bind with different redox auxiliaries such as *N*-hydroxyphthalimide to alter the intrinsic electronic properties, leading to a reductive pathway (**Figure 1.16**).[69]

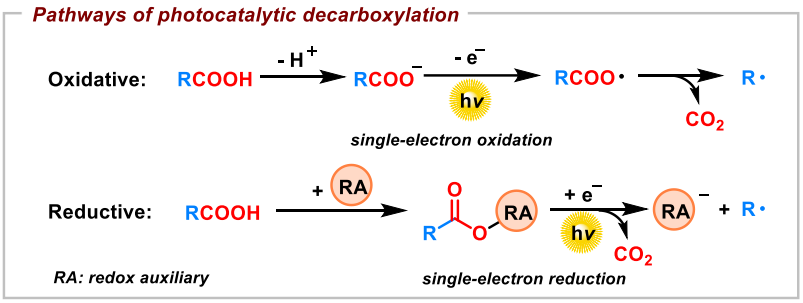

Figure 1.16. Oxidative and reductive photoinduced decarboxylation of CAs.

To realize the reactions based on two pathways, powerful photocatalysts or transition metals are required in the system since the redox potential of single-electron oxidation of $RCOO^-$ is around +1.6 V vs. SCE and the redox potential of single-electron reduction of RCOO-RA such as *N*-hydroxyphthalimide ester derivative is around -1.6 V vs. SCE. Among the commercially available photocatalysts, only few options can fulfil the required redox potentials, therefore, facile photoinduced decarboxylation is still intriguing.[70-72] In 2017, Aggarwal group has reported a photoinduced decarboxylative borylation of CAs in the absence of photocatalysts and transition metals (**Figure 1.17**).[73] The broad scope of CAs were firstly activated by *N*-hydroxyphthalimide as a redox auxiliary to form the *N*-hydroxyphthalimide ester derivative. Subsequently, the *N*-hydroxyphthalimide ester derivative were reduced by solvent-activated bis(catecholato)diboron (B_2cat_2) *via* an intermolecular charge transfer which was facilitated by a π-π interaction-induced EDA complex. After releasing the redox auxiliary and CO_2, the corresponding R• was further coupled with B_2cat_2 to form the borylated product.

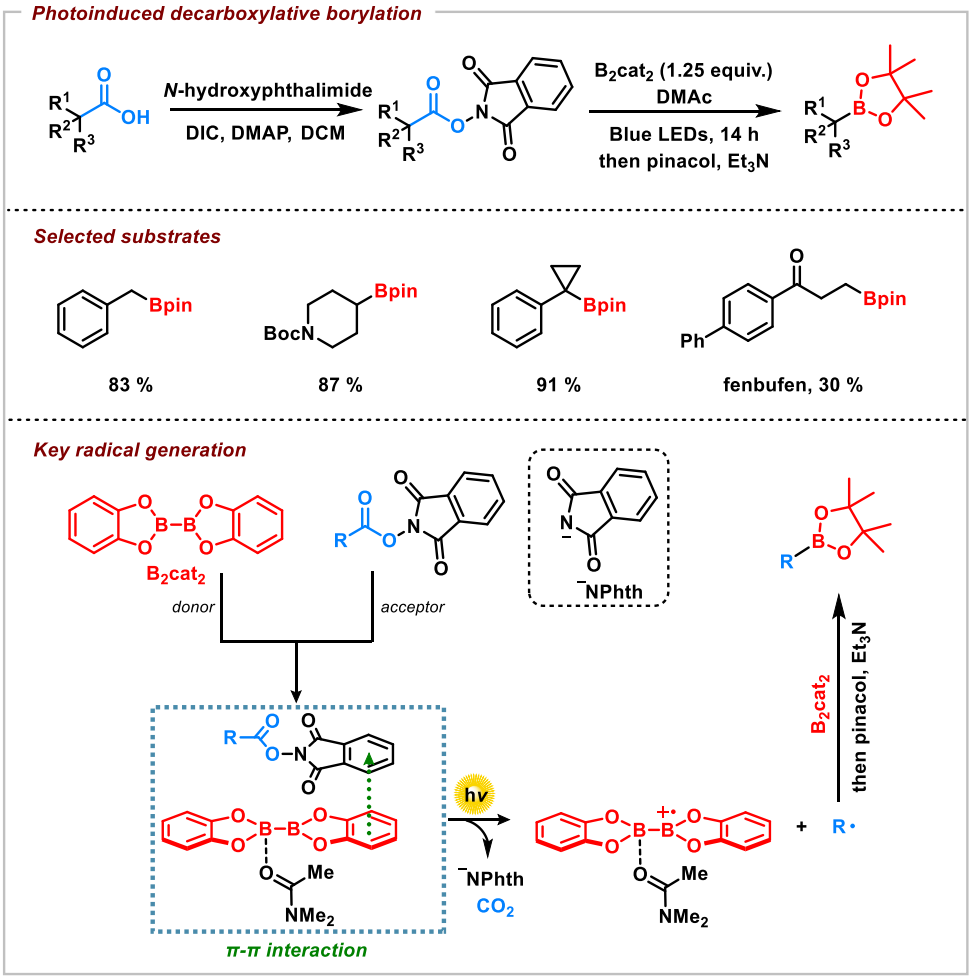

Figure 1.17. Photoinduced decarboyxlative borylation of CAs.

1.4.2 Cation/anion-π interaction-induced photochemistry

Inspired by the light-induced electron transfer process in organic synthesis, Fu et *al.* has reported a general photocatalytic strategy for promoting synthetically useful reactions by employing a combination of sodium iodide/triphenylphosphine (NaI/PPh_3) (**Figure 1.18**).[74] NaI as an easily available and inexpensive reagent and is recognized to reduce aryl bromides and triflates into their corresponding aryl radicals. This transformative process, however, requires the irradiation of high-energy UV light. To use the visible light instead of UV light, they estimated that

the energy of electron transfer between NaI and redox-active acceptors could be lowered in the presence of PPh_3 because they can form a three-component charge transfer complex (CTC) *via* coulombic and cation-π interaction.[75] The light-induced SET from iodide to *N*-hydroxyphthalimide ester derivative provided the $Na^+/Ph_3P–I•$ species and the corresponding R•, followed by the interception by acid-activated heteroarenes to deliver the product. The PPh_3 was significant in this system, because it not only facilitated the formation of CTC complex, but also stabilized the iodine radical as a $Ph_3P–I•$ species.

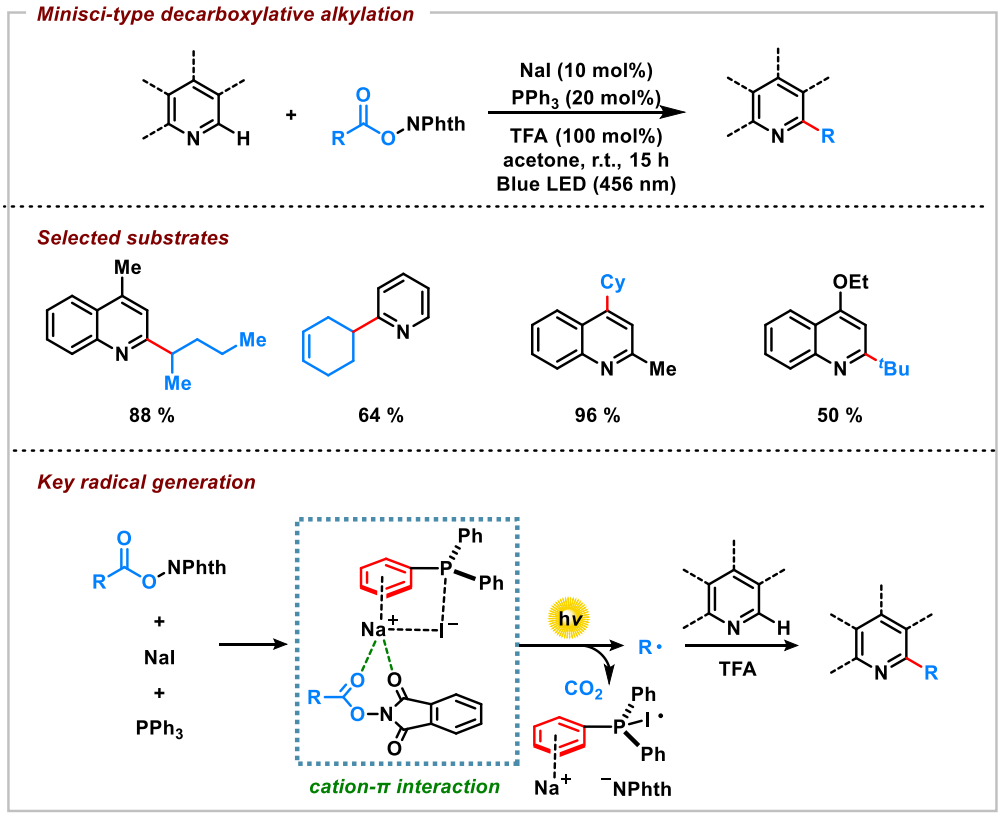

Figure 1.18. NaI/PPh_3-promoted photocatalytic Minisci-type decarboxylative alkylation.

To examine the general applicability of NaI/PPh_3 photoredox system, reactions for the generation of various radicals *via* photocatalytic SET reduction from different valuable precursors have been carried out. For

instance, the reduction of Katritzky's *N*-alkylpyridinium salts *via* SET is a well-known method to provide radicals (**Figure 1.19**).[76] The assembly of NaI and PPh_3 with Katritzky's *N*-alkylpyridinium salts to form a CTC *via* coulombic and anion-π interaction promoted the generation of R• under the irradiation of visible light, followed by trapping by electron-rich olefins to provide the alkenylated product.

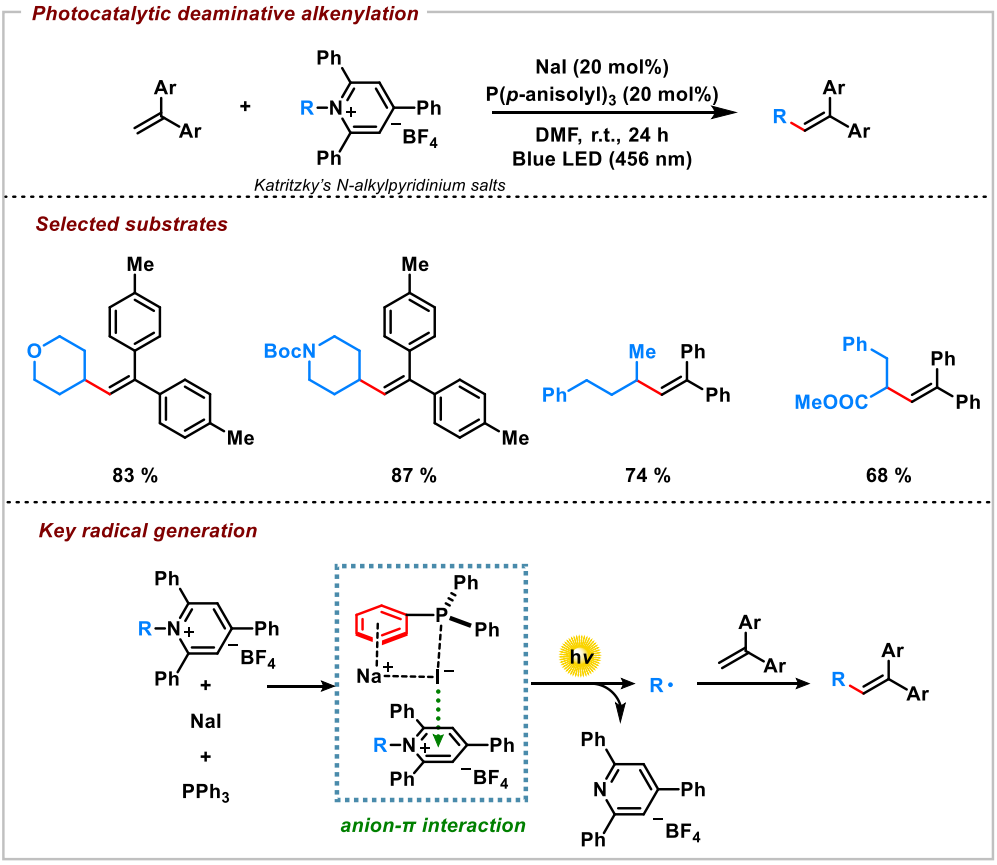

Figure 1.19. Photocatalytic deaminative alkenylation with Katritzkys *N*-alkylpyridinium salts.

1.4.3 Lone pair-π interaction-induced photochemistry

Amines as one of the most useful electron donors are frequently employed in the catalytic system. However, amines in catalytic cycles are typically used as a stoichiometric amount as a sacrificial reagent rather

than as a catalyst. Although electron-rich substrates with amine moieties have been reported to form an intramolecular EDA complex *via* iminium ion formation,[77] the use of amine as both the donor and the external catalytic species is still underdeveloped.

In 2019, Bosque and Bach employed 3-acetoxyquinuclidine (q-OAc) as a catalytic donor and tetrachlorophthalimide ester derivative as an acceptor to form a EDA complex *via* lone pair-π interaction, leading to amino/hydro-decarboxylation and the generation of R• from tetrachlorophthalimide ester derivative (**Figure 1.20**).[78] The formed R• was further oxidized by the catalyst radical cation (q-OAc$^{+\bullet}$) and was intercepted by the previously released NTClPhth^{-} to form the final product. Simultaneously, the catalyst q-OAc was regenerated. This strategy has extended the conceptual framework by employing of an external catalytic electron donor/acceptor species for the initiation of visible-light-driven radical reactions.

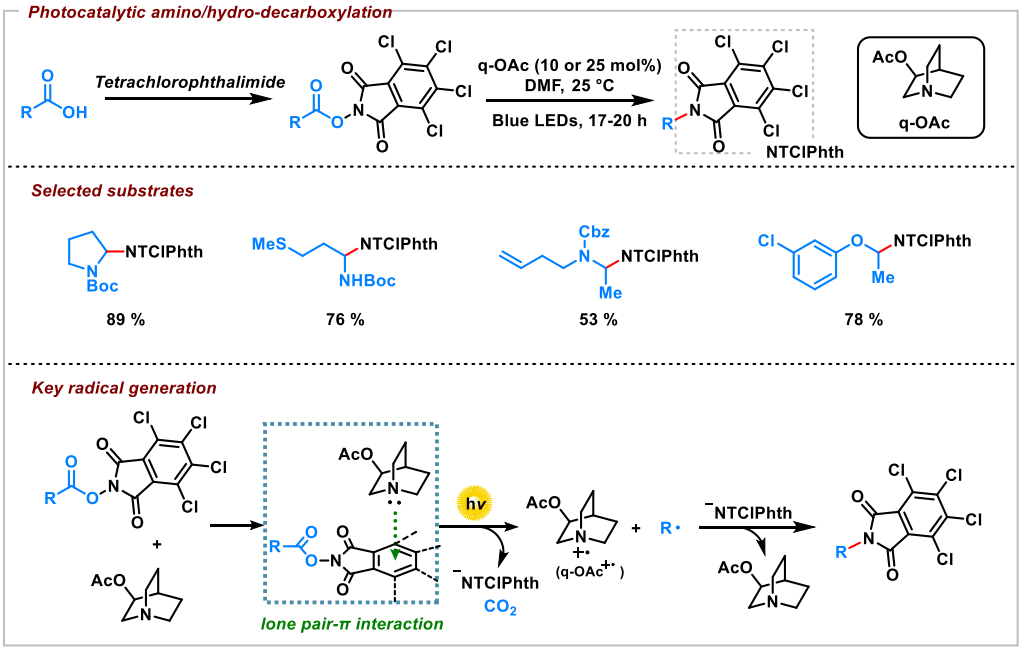

Figure 1.20. Photocatalytic amino/hydro-decarboxylation with q-OAc as a catalyst.

1.5 Synthetic photochemical reactions driven by red light

Photoredox reactions have become a powerful tool in organic synthesis over the past decade, especially the photocatalytic/chemical reactions mediated by visible light have drawn much attention due to their environmental sustainability and versatility. In principle, these photoinduced reactions widely use Ru-/ Ir-based or organic photocatalysts which are mainly activated under the irradiation of blue light. As discussed in **Figure 1.2**, the ground state (S_0) of the photocatalyst is activated by the irradiation of light to reach to its singlet excited state (S_1), followed by intersystem crossing (ISC) to its triplet excited state (T_1). Although the ISC of Ru-/Ir-photocatalysts is relatively rapid and efficient, ca. 25% of light energy is still wasted thermally due to the ISC process.[79] Furthermore, the scalability of the reaction under the irradiation of the visible light is another issue since the penetration of light plays a crucial role in the light-induced reaction.[80, 81] The penetration of blue light into the reaction medium with a $Ru(bpy)_3(PF_6)_2$ is ca. 0.17 cm. Therefore, multiple lamps or flow setups are required to increase the catalytic efficiency to upscale the reactions (**Figure1.21 Left**).

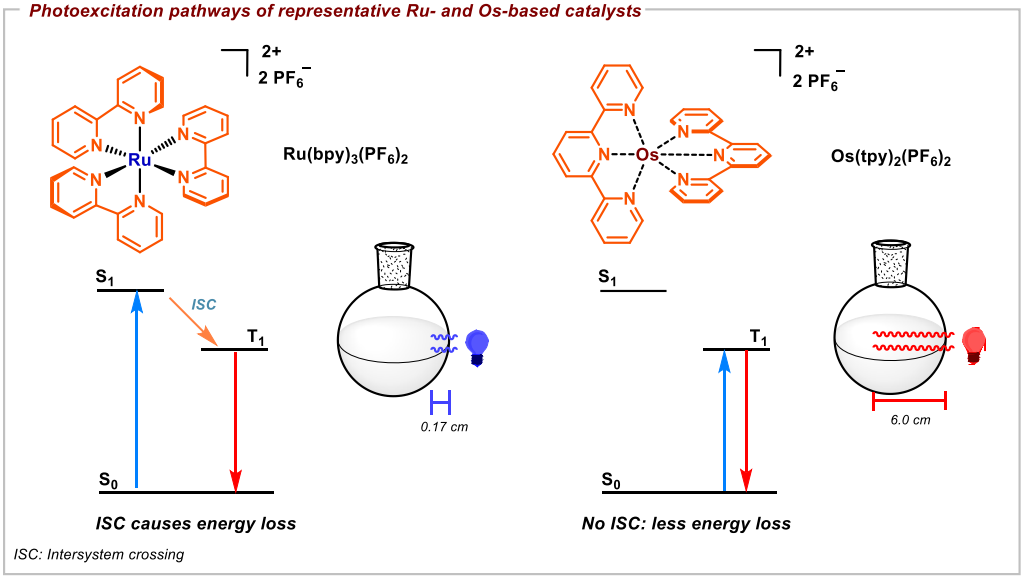

Figure 1.21. Schematic photoexcitation of $[Ru(bpy)_3]^{2+}$ and $[Os(tpy)_2]^{2+}$.

In 2020, Rovis group reported a series of osmium (Os)-based photocatalysts for synthetic organic reactions.[82] The Os-catalyst was directly excited by the red light or near-infrared (NIR) light from S_0 to T_1 without the excited state S_1. Compared to blue light, energy efficiency was increased by minimizing the energy loss as there was no ISC process. In addition, penetration of red light is also better, and the distance of red light irradiated in reaction medium with $Os(tpy)_2(PF_6)_2$ is ca. 6.0 cm (**Figure 1.21 Right**). The deep penetration of light is crucial for upscaling of reaction, since the photon flux on large-scale reactions exhibits a significant reduction. For instance, in order to maintain a consistent photon flux on a 1 mmol scale reaction, approximately 200 lamps were required for a 10 mmol scale reaction under the irradiation of blue light. However, only 8 lamps were necessary to obtain the comparable yield under the irradiation of red light.

To fulfil the catalytic requisite, Os-photocatalysts with different ligands were synthesized and their redox potentials were also measured for guiding the photocatalytic reactions. The representative Os-photocatalysts with redox potentials are shown in the **Figure 1.22**.[82] Since the energy of red light is low, the redox window of Os-catalysts are

comparably narrow, resulting in the better control of catalytic reactions to achieve high selectivity and the better tolerance of light-sensitive functional groups.

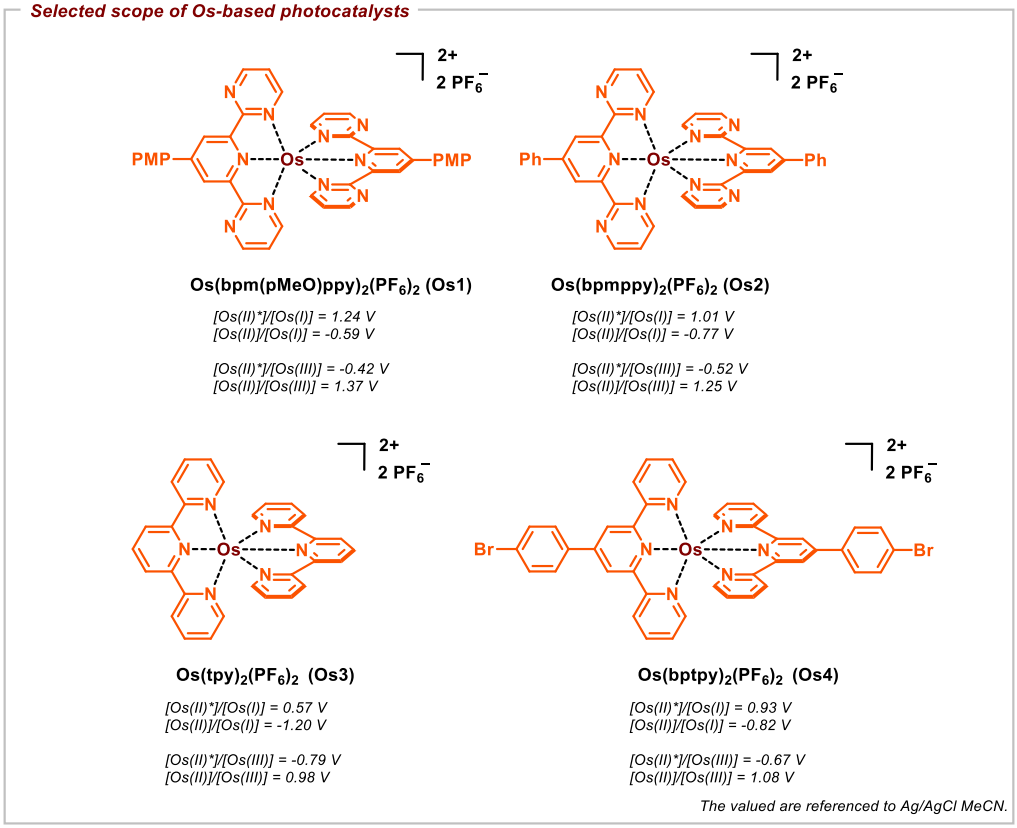

Figure 1.22. Representative Os-based photocatalysts.

To examine the catalytic efficiency of Os-photocatalysts, diverse photoredox reactions have been carried out (**Figure 1.23**). The successful and smooth execution of challenging transformations involving the photopolymerization of cyclohexene oxide, a cation radical [2+2] cycloaddition reaction, photocatalytic chlorotrifluoromethylation of olefins and the oxidation of aryl boronic acid has been demonstrated through the utilization of red/NIR photoredox catalysis.[82]

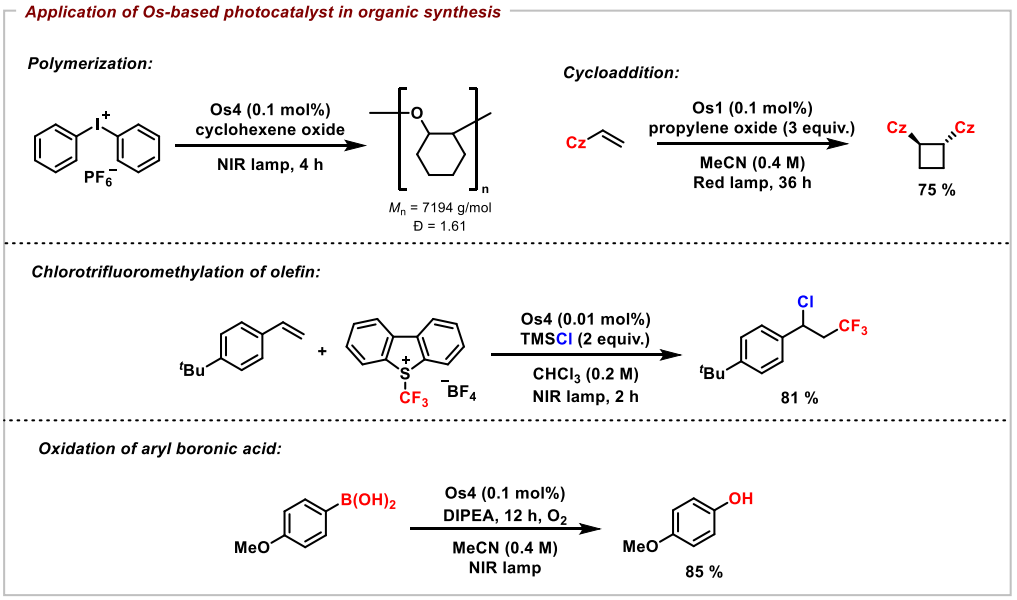

Figure 1.23. Photocatalytic reactions with Os-catalysts under the irradiation of red/NIR light.

To upscale the reaction, various quantity for Stephenson's trifluoromethylation reactions have been performed with both $Ru(bpy)_3(PF_6)_2$ and $Os(tpy)_2(PF_6)_2$ (Os3) under the irradiation of blue and NIR light, respectively (**Figure 1.24**). It was clearly observed that the catalytic efficiency of blue light system decreased with the increasing the reaction scale, while catalytic efficiency of NIR system maintained or even increased on larger scale. This difference could be attributed to the deeper light penetration of NIR light into the medium.

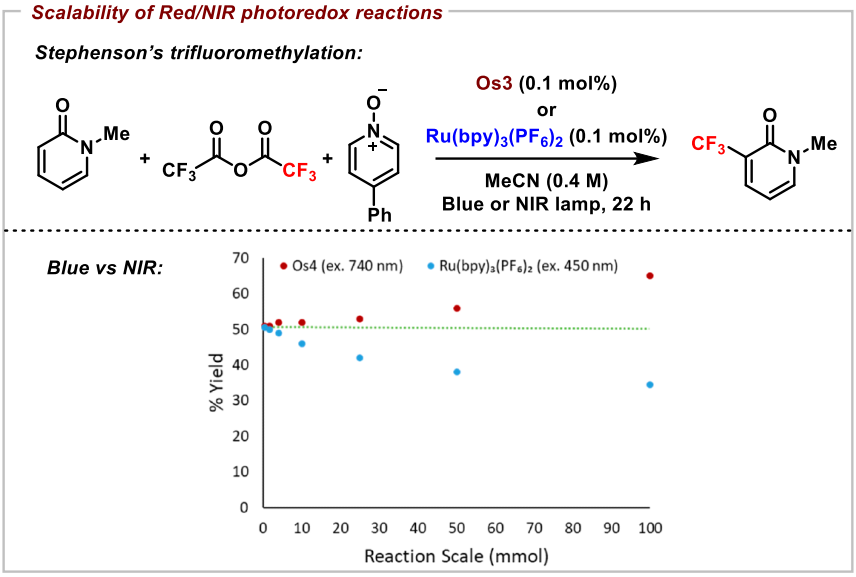

Figure 1.24. Top: Upscaling of Stephenson's trifluoromethylation with Os3 under NIR. **Bottom**: Comparison of scalability of catalytic systems with blue and red light.

1.6 References

1. Ekka, J. P.; Kumar, D. A review of industrial food processing using solar dryers with heat storage systems. *J. Stored Prod. Res.* **2023,** *101*, 102090.
2. Kumar, G. S.; Lin, Q. Light−triggered click chemistry. *Chem. Rev.* **2020,** *121* (12), 6991−7031.
3. Roth, H. D. The Beginnings of Organic Photochemistry. *Angew. Chem. Int. Ed.* **1989,** *28* (9), 1193−1207.
4. Roscoe, H. E. Bunsen, Kirchhoff, and Roscoe. In *The Life & Experiences of Sir Henry Enfield Roscoe... Written by Himself*, Macmillan Company: London, England, Vol. Courtesy of Science History Institute. Rights: Public Domain Mark 1.0.
5. Menzel, J. P.; Noble, B. B.; Lauer, A.; Coote, M. L.; Blinco, J. P.; Barner−Kowollik, C. Wavelength Dependence of Light−Induced Cycloadditions. *J. Am. Chem. Soc.* **2017,** *139* (44), 15812−15820.
6. Armaroli, N.; Balzani, V. The future of energy supply: Challenges and opportunities. *Angew. Chem. Int. Ed.* **2007,** *46*, 52−66.
7. Ciamician, G. The Photochemistry of the Future. *Science* **1912,** *36* (926), 385−394.
8. Protti, S.; Fagnoni, M. The sunny side of chemistry: green synthesis by solar light. *Photochem. Photobiol. Sci.* **2009,** *8* (11), 1499−1516.
9. Schultz, D. M.; Yoon, T. P. Solar synthesis: prospects in visible light photocatalysis. *Science* **2014,** *343* (6174), 1239176.
10. Yoon, T. P.; Ischay, M. A.; Du, J. Visible light photocatalysis as a greener approach to photochemical synthesis. *Nat. Chem.* **2010,** *2* (7), 527−532.
11. Marzo, L.; Pagire, S. K.; Reiser, O.; König, B. Visible-light photocatalysis: does it make a difference in organic synthesis? *Angew. Chem. Int. Ed.* **2018,** *57* (32), 10034−10072.
12. Stephenson, C. R.; Yoon, T. P.; MacMillan, D. W. *Visible light photocatalysis in organic chemistry*. John Wiley & Sons: 2018.

13. Prier, C. K.; Rankic, D. A.; MacMillan, D. W. Visible light photoredox catalysis with transition metal complexes: applications in organic synthesis. *Chem. Rev.* **2013,** *113* (7), 5322−5363.
14. Romero, N. A.; Nicewicz, D. A. Organic photoredox catalysis. *Chem. Rev.* **2016,** *116* (17), 10075−10166.
15. Kalyanasundaram, K. Photophysics, photochemistry and solar energy conversion with tris (bipyridyl) ruthenium (II) and its analogues. *Coord. Chem. Rev.* **1982,** *46*, 159−244.
16. Juris, A.; Balzani, V.; Barigelletti, F.; Campagna, S.; Belser, P. l.; von Zelewsky, A. v. Ru (II) polypyridine complexes: photophysics, photochemistry, eletrochemistry, and chemiluminescence. *Coord. Chem. Rev.* **1988,** *84*, 85−277.
17. Marian, C. M. Spin–orbit coupling and intersystem crossing in molecules. *Wiley Interdiscip. Rev. Comput. Mol. Sci.* **2012,** *2* (2), 187−203.
18. Serpone, N. Photocatalysis. *Kirk-Othmer Encyclopedia of Chemical Technology* **2000**.
19. Sumida, Y.; Ohmiya, H. Direct excitation strategy for radical generation in organic synthesis. *Chem. Soc. Rev.* **2021,** *50* (11), 6320−6332.
20. Strieth−Kalthoff, F.; James, M. J.; Teders, M.; Pitzer, L.; Glorius, F. Energy transfer catalysis mediated by visible light: principles, applications, directions. *Chem. Soc. Rev.* **2018,** *47* (19), 7190−7202.
21. Strieth−Kalthoff, F.; Glorius, F. Triplet energy transfer photocatalysis: unlocking the next level. *Chem* **2020,** *6* (8), 1888−1903.
22. Wang, P.; Zhang, H.; Nie, X.; Xu, T.; Liao, S. Photoredox catalytic radical fluorosulfonylation of olefins enabled by a bench−stable redox−active fluorosulfonyl radical precursor. *Nat. Commun.* **2022,** *13* (1), 3370.
23. Du, X.; Cheng−Sanchez, I.; Nevado, C. Dual Nickel/Photoredox−Catalyzed Asymmetric Carbosulfonylation of Alkenes. *J. Am. Chem. Soc.* **2023,** *145*, 12532–12540.
24. Hojo, R.; Bergmann, K.; Elgadi, S. A.; Mayder, D. M.; Emmanuel, M. A.; Oderinde, M. S.; Hudson, Z. M. Imidazophenothiazine−Based Thermally Activated Delayed Fluorescence Materials with

Ultra−Long−Lived Excited States for Energy Transfer Photocatalysis. *J. Am. Chem. Soc.* **2023,** *145* (33), 18366−18381.
25. Bond, G. C. Heterogeneous catalysis. **1987**.
26. Schlögl, R. Heterogeneous catalysis. *Angew. Chem. Int. Ed.* **2015,** *54* (11), 3465−3520.
27. Fechete, I.; Wang, Y.; Védrine, J. C. The past, present and future of heterogeneous catalysis. *Catal. Today* **2012,** *189* (1), 2−27.
28. Fujishima, A.; Rao, T. N.; Tryk, D. A. Titanium dioxide photocatalysis. *J. Photochem. Photobiol. C: Photochem. Rev.* **2000,** *1* (1), 1−21.
29. Khan, M. M.; Adil, S. F.; Al−Mayouf, A. Metal oxides as photocatalysts. Elsevier: 2015; Vol. 19, pp 462−464.
30. Velempini, T.; Prabakaran, E.; Pillay, K. Recent developments in the use of metal oxides for photocatalytic degradation of pharmaceutical pollutants in water—A review. *Mater. Today Chem.* **2021,** *19*, 100380.
31. Xie, W.; Xu, J.; Chen, J.; Wang, H.; Hu, P. Achieving theory−experiment parity for activity and selectivity in heterogeneous catalysis using microkinetic modeling. *Acc. Chem. Res.* **2022,** *55* (9), 1237−1248.
32. Jin, Z.; Xiao, M.; Bao, Z.; Wang, P.; Wang, J. A general approach to mesoporous metal oxide microspheres loaded with noble metal nanoparticles. *Angew. Chem. Int. Ed.* **2012,** *51* (26), 6406−6410.
33. Hou, W.; Cronin, S. B. A review of surface plasmon resonance-enhanced photocatalysis. *Adv. Funct. Mater.* **2013,** *23* (13), 1612−1619.
34. Hutter, E.; Fendler, J. H. Exploitation of localized surface plasmon resonance. *Advanced materials* **2004,** *16* (19), 1685−1706.
35. Wang, L.; Huang, W.; Li, R.; Gehrig, D.; Blom, P. W.; Landfester, K.; Zhang, K. A. Structural design principle of small-molecule organic semiconductors for metal-free, visible-light-promoted photocatalysis. *Angew. Chem. Int. Ed.* **2016,** *55* (33), 9783−9787.
36. Feng, X.; Ding, X.; Jiang, D. Covalent organic frameworks. *Chem. Soc. Rev.* **2012,** *41* (18), 6010−6022.
37. Ding, S.−Y.; Wang, W. Covalent organic frameworks (COFs): from design to applications. *Chem. Soc. Rev.* **2013,** *42* (2), 548−568.

38. Wang, H.; Wang, H.; Wang, Z.; Tang, L.; Zeng, G.; Xu, P.; Chen, M.; Xiong, T.; Zhou, C.; Li, X. Covalent organic framework photocatalysts: structures and applications. *Chem. Soc. Rev.* **2020,** *49* (12), 4135−4165.
39. Zhou, Z.; Zhang, Y.; Shen, Y.; Liu, S.; Zhang, Y. Molecular engineering of polymeric carbon nitride: advancing applications from photocatalysis to biosensing and more. *Chem. Soc. Rev.* **2018,** *47* (7), 2298−2321.
40. Zhang, J.; Guo, F.; Wang, X. An optimized and general synthetic strategy for fabrication of polymeric carbon nitride nanoarchitectures. *Adv. Funct. Mater.* **2013,** *23* (23), 3008−3014.
41. Wang, Y.; Li, H.; Yao, J.; Wang, X.; Antonietti, M. Synthesis of boron doped polymeric carbon nitride solids and their use as metal−free catalysts for aliphatic C–H bond oxidation. *Chem. Sci.* **2011,** *2* (3), 446−450.
42. Wang, X.; Maeda, K.; Thomas, A.; Takanabe, K.; Xin, G.; Carlsson, J. M.; Domen, K.; Antonietti, M. A metal−free polymeric photocatalyst for hydrogen production from water under visible light. *Nat. Mater.* **2009,** *8* (1), 76−80.
43. He, C.; Xia, W.; Zhou, C.; Huang, D.; Zhang, C.; Song, B.; Yang, Y.; Li, J.; Xu, X.; Shang, Y. Rational design to manganese and oxygen co−doped polymeric carbon nitride for efficient nonradical activation of peroxymonosulfate and the mechanism insight. *J. Chem. Eng.* **2022,** *430*, 132751.
44. Zhang, J.; Zhang, M.; Sun, R. Q.; Wang, X. A facile band alignment of polymeric carbon nitride semiconductors to construct isotype heterojunctions. *Angew. Chem.* **2012,** *124* (40), 10292−10296.
45. Zhang, T.; Schilling, W.; Khan, S. U.; Ching, H. Y. V.; Lu, C.; Chen, J.; Jaworski, A.; Barcaro, G.; Monti, S.; De Wael, K.; Slabon, A.; Das, S. Atomic−Level Understanding for the Enhanced Generation of Hydrogen Peroxide by the Introduction of an Aryl Amino Group in Polymeric Carbon Nitrides. *ACS Catal.* **2021,** *11* (22), 14087−14101.
46. Gopakumar, A.; Ren, P.; Chen, J.; Manzolli Rodrigues, B. V.; Vincent Ching, H. Y.; Jaworski, A.; Doorslaer, S. V.; Rokicinska, A.;

Kustrowski, P.; Barcaro, G.; Monti, S.; Slabon, A.; Das, S. Lignin–Supported Heterogeneous Photocatalyst for the Direct Generation of H2O2 from Seawater. *J. Am. Chem. Soc.* **2022,** *144* (6), 2603–2613.

47. Ren, P.; Zhang, T.; Jain, N.; Ching, H. Y. V.; Jaworski, A.; Barcaro, G.; Monti, S.; Silvestre–Albero, J.; Celorrio, V.; Chouhan, L.; Rokicinska, A.; Debroye, E.; Kustrowski, P.; Van Doorslaer, S.; Van Aert, S.; Bals, S.; Das, S. An Atomically Dispersed Mn–Photocatalyst for Generating Hydrogen Peroxide from Seawater via the Water Oxidation Reaction (WOR). *J. Am. Chem. Soc.* **2023,** *145* (30), 16584–16596.
48. Hou, H.; Zeng, X.; Zhang, X. Production of Hydrogen Peroxide by Photocatalytic Processes. *Angew. Chem. Int. Ed.* **2020,** *59* (40), 17356–17376.
49. Zhang, J.; Zhang, G.; Chen, X.; Lin, S.; Mohlmann, L.; Dolega, G.; Lipner, G.; Antonietti, M.; Blechert, S.; Wang, X. Co–monomer control of carbon nitride semiconductors to optimize hydrogen evolution with visible light. *Angew. Chem. Int. Ed.* **2012,** *51* (13), 3183–7.
50. Shiraishi, Y.; Kanazawa, S.; Kofuji, Y.; Sakamoto, H.; Ichikawa, S.; Tanaka, S.; Hirai, T. Sunlight–driven hydrogen peroxide production from water and molecular oxygen by metal–free photocatalysts. *Angew. Chem. Int. Ed.* **2014,** *53* (49), 13454–9.
51. Wang, B.; Cai, H.; Shen, S. Single metal atom photocatalysis. *Small Methods* **2019,** *3*, 1800447.
52. Wang, Y.; Hu, F.-L.; Mi, Y.; Yan, C.; Zhao, S. Single-metal-atom catalysts: an emerging platform for electrocatalytic oxygen reduction. *Chem. Eng. J.* **2021,** *406*, 127135.
53. Pei, Z.; Ding, L.; Hu, J.; Weng, S.; Zheng, Z.; Huang, M.; Liu, P. Defect and its dominance in ZnO films: A new insight into the role of defect over photocatalytic activity. *Appl. Catal. B* **2013,** *142*, 736–743.
54. Li, S.; Dong, G.; Hailili, R.; Yang, L.; Li, Y.; Wang, F.; Zeng, Y.; Wang, C. Effective photocatalytic H2O2 production under visible light irradiation at g–C3N4 modulated by carbon vacancies. *Appl. Catal. B* **2016,** *190*, 26–35.

55. Johnson, E. R.; Keinan, S.; Mori−Sánchez, P.; Contreras−García, J.; Cohen, A. J.; Yang, W. Revealing noncovalent interactions. *J. Am. Chem. Soc.* **2010,** *132* (18), 6498−6506.
56. Müller−Dethlefs, K.; Hobza, P. Noncovalent interactions: a challenge for experiment and theory. *Chem. Rev.* **2000,** *100* (1), 143−168.
57. Neel, A. J.; Hilton, M. J.; Sigman, M. S.; Toste, F. D. Exploiting non−covalent pi interactions for catalyst design. *Nature* **2017,** *543* (7647), 637−646.
58. Palmer, L. C.; Stupp, S. I. Molecular self−assembly into one−dimensional nanostructures. *Acc. Chem. Res.* **2008,** *41* (12), 1674−1684.
59. Claessens, C. G.; Stoddart, J. F. π–π Interactions in self-assembly. *J. Phys. Org. Chem.* **1997,** *10* (5), 254−272.
60. Davis, H. J.; Phipps, R. J. Harnessing non−covalent interactions to exert control over regioselectivity and site−selectivity in catalytic reactions. *Chem. Sci.* **2017,** *8* (2), 864−877.
61. Schottel, B. L.; Chifotides, H. T.; Dunbar, K. R. Anion−π interactions. *Chem. Soc. Rev.* **2008,** *37* (1), 68−83.
62. Gallivan, J. P.; Dougherty, D. A. Cation−π interactions in structural biology. *PNAS* **1999,** *96* (17), 9459−9464.
63. Tsuzuki, S. CH/π interactions. *Annual Reports Section" C"(Physical Chemistry)* **2012,** *108*, 69−95.
64. Shen, C.; Zhang, P.; Sun, Q.; Bai, S.; Hor, T. A.; Liu, X. Recent advances in C–S bond formation via C–H bond functionalization and decarboxylation. *Chem. Soc. Rev.* **2015,** *44* (1), 291−314.
65. Modha, S. G.; Mehta, V. P.; Van der Eycken, E. V. Transition metal−catalyzed C–C bond formation via C–S bond cleavage: an overview. *Chem. Soc. Rev.* **2013,** *42* (12), 5042−5055.
66. Liu, B.; Lim, C. H.; Miyake, G. M. Visible−Light−Promoted C–S Cross−Coupling via Intermolecular Charge Transfer. *J. Am. Chem. Soc.* **2017,** *139* (39), 13616−13619.
67. Gooßen, L. J.; Rodríguez, N.; Gooßen, K. Carboxylic acids as substrates in homogeneous catalysis. *Angew. Chem. Int. Ed.* **2008,** *47* (17), 3100−3120.

68. Cassani, C.; Bergonzini, G.; Wallentin, C.–J. Photocatalytic decarboxylative reduction of carboxylic acids and its application in asymmetric synthesis. *Org. Lett.* **2014,** *16* (16), 4228–4231.
69. Masui, M.; Ueshima, T.; Ozaki, S. N–Hydroxyphthalimide as an effective mediator for the oxidation of alcohols by electrolysis. *J. Chem. Soc. Chem. Commun.* **1983,** (8), 479–480.
70. Tan, X.; Liu, Z.; Shen, H.; Zhang, P.; Zhang, Z.; Li, C. Silver–Catalyzed Decarboxylative Trifluoromethylation of Aliphatic Carboxylic Acids. *J. Am. Chem. Soc.* **2017,** *139* (36), 12430–12433.
71. Bloom, S.; Liu, C.; Kolmel, D. K.; Qiao, J. X.; Zhang, Y.; Poss, M. A.; Ewing, W. R.; MacMillan, D. W. C. Decarboxylative alkylation for site–selective bioconjugation of native proteins via oxidation potentials. *Nat. Chem.* **2018,** *10* (2), 205–211.
72. Sun, X.; Chen, J.; Ritter, T. Catalytic dehydrogenative decarboxyolefination of carboxylic acids. *Nat. Chem.* **2018,** *10* (12), 1229–1233.
73. Fawcett, A.; Pradeilles, J.; Wang, Y.; Mutsuga, T.; Myers, E. L.; Aggarwal, V. K. Photoinduced decarboxylative borylation of carboxylic acids. *Science* **2017,** *357* (6348), 283–286.
74. Fu, M.–C.; Shang, R.; Zhao, B.; Wang, B.; Fu, Y. Photocatalytic decarboxylative alkylations mediated by triphenylphosphine and sodium iodide. *Science* **2019,** *363* (6434), 1429–1434.
75. Crisenza, G. E. M.; Mazzarella, D.; Melchiorre, P. Synthetic Methods Driven by the Photoactivity of Electron Donor–Acceptor Complexes. *J. Am. Chem. Soc.* **2020,** *142* (12), 5461–5476.
76. Jin, Y.; Ou, L.; Yang, H.; Fu, H. Visible–light–mediated aerobic oxidation of N–alkylpyridinium salts under organic photocatalysis. *J. Am. Chem. Soc.* **2017,** *139* (40), 14237–14243.
77. Arceo, E.; Jurberg, I. D.; Álvarez–Fernández, A.; Melchiorre, P. Photochemical activity of a key donor–acceptor complex can drive stereoselective catalytic α–alkylation of aldehydes. *Nat. Chem.* **2013,** *5* (9), 750–756.

78. Bosque, I.; Bach, T. 3−Acetoxyquinuclidine as catalyst in electron donor–acceptor complex−mediated reactions triggered by visible light. *ACS Catal.* **2019,** *9* (10), 9103−9109.
79. Bhasikuttan, A. C.; Suzuki, M.; Nakashima, S.; Okada, T. Ultrafast Fluorescence Detection in Tris(2,2'−bipyridine)ruthenium(II) Complex in Solution: Relaxation Dynamics Involving Higher Excited States. *J. Am. Chem. Soc.* **2002,** *124* (28), 8398−8405.
80. Byrne, A.; Dolan, C.; Moriarty, R. D.; Martin, A.; Neugebauer, U.; Forster, R. J.; Davies, A.; Volkov, Y.; Keyes, T. E. Osmium(ii) polypyridyl polyarginine conjugate as a probe for live cell imaging; a comparison of uptake, localization and cytotoxicity with its ruthenium(ii) analogue. *Dalton Trans.* **2015,** *44* (32), 14323−14332.
81. Szaciłowski, K.; Macyk, W.; Drzewiecka−Matuszek, A.; Brindell, M.; Stochel, G. Bioinorganic Photochemistry: Frontiers and Mechanisms. *Chem. Rev.* **2005,** *105* (6), 2647−2694.
82. Ravetz, B. D.; Tay, N. E. S.; Joe, C. L.; Sezen−Edmonds, M.; Schmidt, M. A.; Tan, Y.; Janey, J. M.; Eastgate, M. D.; Rovis, T. Development of a Platform for Near−Infrared Photoredox Catalysis. *ACS Cent. Sci.* **2020,** *6* (11), 2053−2059.

Chapter 2

Atomic Level Understanding for the Enhanced Generation of Hydrogen Peroxide by the Introduction of an Aryl Amino Group in Polymeric Carbon Nitrides

ABSTRACT: Heterogeneous catalysts are often 'black boxes' due to the insufficient understanding of the detailed mechanism at the catalytic sites. An atomic-level elucidation of the processes taking place in those regions is, thus, mandatory to produce robust and selective heterogeneous catalysts. We have improved the description of the whole reactive scenario for the polymeric carbon nitrides (PCN) by combining atomic-level characterizations with magic angle spinning (MAS) solid state nuclear magnetic resonance (NMR) spectroscopy, classical reactive molecular dynamics simulations (RMD), and quantum chemistry calculations (QC). We disclosed the structure-property relationships of an ad hoc modified PCN by inserting an arylamino group that turned out to be very efficient for the production of H_2O_2. The main advancement of this work was the development of a difluoromethylene-substituted aryl amino PCN to generate H_2O_2 at the rate of 2.0 mM h^{-1} under the irradiation of household blue LEDs and the identification of possible active catalytic sites with the aid of ^{15}N and ^{19}F MAS solid state NMR without using any expensive labeling reagent. RMD simulations and QC calculations confirmed and further extended the experimental descriptions by revealing the role and locations of the identified functionalities, namely NH linkers, $–NH_2$ terminal groups, and difluoromethylene units, reactants, and products.

This chapter is based on a published work: Zhang, T.; Schilling, W.; Khan, S. U.; Ching, H. Y. V.; Lu, C.; Chen, J.; Jaworski, A.; Barcaro, G.; Monti, S.; De Wael, K.; Slabon, A.; Das, S. *ACS Catal.* **2021**, *11*, 14087.

2.1 Introduction

Heterogeneous catalysts are essential for industrial synthesis because of their easy separation and reusability.[1] However, still, the traditional catalysts are poorly characterized and classified in terms of their active catalytic sites.[2] A clear understanding of these fundamental regions is essential to obtain a robust heterogeneous catalyst and to improve the structure-activity relationships of the whole process. Among the heterogeneous catalysts, polymeric carbon nitrides (PCN) have attracted much attention as metal-free catalysts with an appropriate band structure for various applications, such as water splitting, oxygen reduction reactions, C-C bond cleavage reactions (**Figure 2.1**).[3-4] Advantageously, fabrications and modifications of PCN are also feasible, and strategies such as morphology tuning such as mesoporous PCN (mpg-CN),[5] defect control,[6-7] elemental doping,[8-9] and hybridization[10] have been intensively investigated. Despite these improvements, characterization and structure determination of the active sites still remain inadequately explored. Although great efforts have been made to disclose the active site by the scanning transmission electron microscopy with energy-dispersive X-ray spectroscopy (STEM EDX) mapping, still the discrimination between the carbon and nitrogen is very difficult due to their close positions in the periodic table.

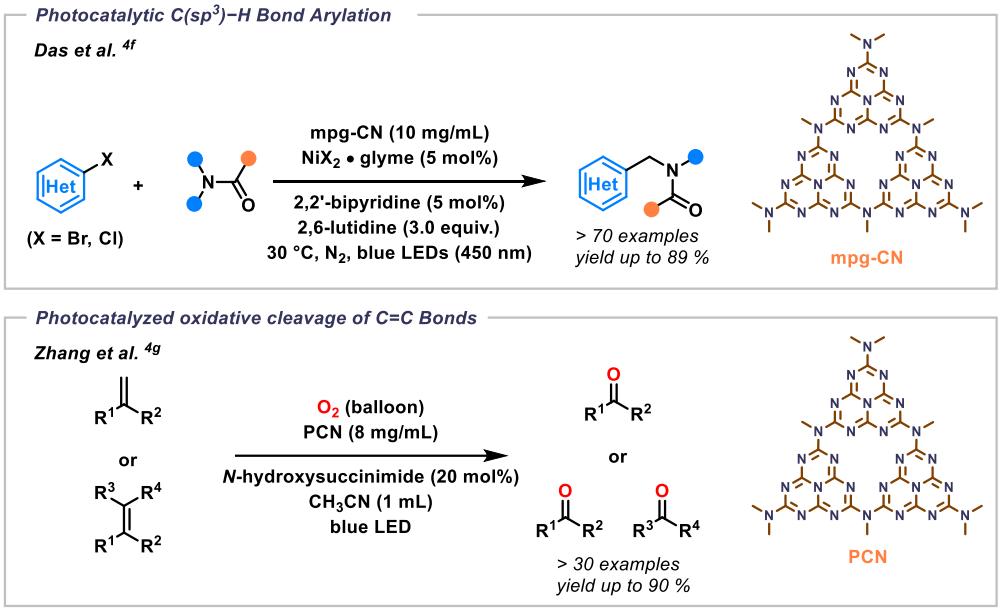

Figure 2.1. Selective examples of using PCN as a photocatalyst in organic synthesis.

This problem can be potentially overcome by the combination of experimental techniques and computational calculations. In this respect, solid-state NMR spectroscopy (ssNMR) can be very efficient for its atomic selectivity and ability to depict the local chemical environments regardless of the chemical/structural disorder or low species concentration. Indeed, among the nuclei relevant for this study, nitrogen is the most challenging one. This is because NMR active isotope ^{14}N exhibits severe spectral broadening due to quadrupolar interaction[11] (with exceptions for highly symmetric environments), and the other active isotope (^{15}N) suffers from low natural abundance and, therefore, sensitivity, which often requires isotope enrichment. However, it has been shown that ^{15}N NMR is capable of delivering crucial information for the nitrogen containing materials.[12] The examined catalysts are appropriate for cross-polarization (CPMAS) NMR experiments, a method utilizing ssNMR employs heteronuclear dipolar interactions to facilitate the transfer of nuclear magnetization

across distinct types of nuclei, at the natural ^{15}N isotope abundance due to the presence of protons (**Figure 2.2**).

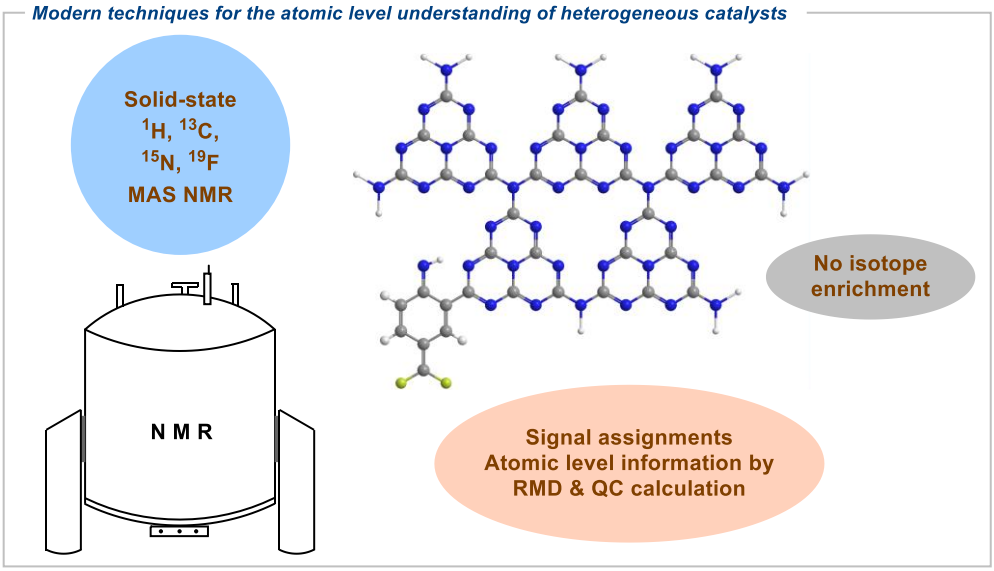

Figure 2.2. Atomic level characterizations of aryl amino PCN photocatalyst.

On the other hand, reactive molecular dynamics simulations (ReaxFF flavor [13]) of these types of materials based on efficient preparametrized potentials,[14] are a powerful tool to explore the most probable interactions and locations of the different species present in the complex environment on which the catalyst is inserted in to reproduce the reaction mechanisms realistically and, in conjunction with the nudged elastic band (NEB) approach, at the QC level, to identify the key intermolecular interactions which drive the reactants to crucial intermediates and products.[15]

Given these premises, we focused on the development of a novel metal-free heterogeneous photocatalyst for the production of hydrogen peroxide (H_2O_2). This is because hydrogen peroxide is considered as one of the 100 most essential chemicals.[16] The current global market size for H_2O_2 is reached to 1.49 billion USD with a compound annual growth rate forecast (CAGR) of more than 4.7% from 2020 to 2027.[17] Currently, more than 95% of the total industrial production of H_2O_2 relies on the anthraquinone

oxidation (AO) process which suffers from several drawbacks such as the use of an explosive gas mixture of H_2 and O_2, high energy consumption, and capital investments (**Figure 2.3**).[18]

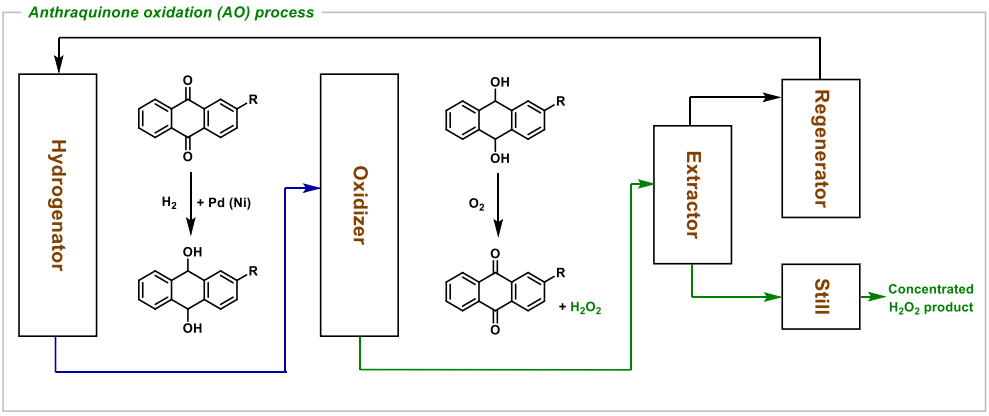

Figure 2.3. Schematic of the anthraquinone oxidation (AQ) process.

Therefore, there is an urgent need to develop new methods for the production of H_2O_2 under mild reaction conditions. To date, various photoactive materials have been investigated for photocatalytic H_2O_2 production.[19-31] For example, Fukuzumi et *al.* reported a photocatalytic process for the production of H_2O_2 from water and oxygen by using a mixture of $[Ru^{II}(Me_2phen)_3]^{2+}$ (Me_2phen = 4,7-dimethyl-1,10-phenanthroline) and $Ir(OH)_3$ (or cobalt catalyst).[19] In addition, Yerushalmi et *al.*[20] and Piao et *al.*[21] designed titanium oxide (TiO_2) doped with silicon or gold and Pt/TiO_2(anatase) for the production of H_2O_2 from water, respectively. Group of Shiraishi reported on resorcinol–formaldehyde resins[22] for the production of H_2O_2 from water and O_2 under the irradiation of solar energy. PCN-based-photocatalysts have also been used for the generation of H_2O_2. For example, the Shiraishi group described an excellent pyromellitic diimide (PDI) modified PCN photocatalyst to generate 50.6 *m*mol of H_2O_2 within 48 h.[23] It should be noted that these excellent photocatalysts facilitated the production of H_2O_2 directly from water, but one drawback of this H_2O_2 generation process

was to overcome the high kinetic barriers, that, as a consequence, limited the amount of H_2O_2 production.[24-25] Alternatively, mixtures of water and alcohols such as ethanol have become highly attractive since ethanol can be obtained directly *via* the hydrolysis of biomass.[26] Teranishi *et al.* demonstrated that an Au-doped TiO_2 catalyst was appropriate,[24c] and, subsequently, Moon *et al.* revealed an excellent TiO_2 catalyst with reduced graphene oxide (rGO).[27] Parallelly, Yamashita, and van Der Voort groups reported a hydrophobic metal-organic framework and a covalent organic frameworks (COFs) respectively for the generation of H_2O_2 from a mixture of water and alcohols.[28-29]

Table 2.1. Reported PCNs for the generation of H_2O_2 using the mixture of water and alcohols.

Entry	Materials	Sacrificial Reagent	Light source[a]	Production rate[c]	Ref.
1	g-C_3N_4	Ethanol[d]	2 kW Xe lamp	0.53 mM·h^{-1}	32
2	Mesoporous g-C_3N_4	Ethanol[d]	2 kW Xe lamp	0.83 mM·h^{-1}	33
3	(K, P, O)-g-C_3N_4	Ethanol[e]	300 W Xe arc lamp	0.23 mM·h^{-1}	34
4	CoP/g-C_3N_4	Ethanol[e]	300 W Xe lamp	0.07 mM·h^{-1}	35
5	Au/g-C_3N_4	2-Propanol[f]	300 W Xe lamp	0.47 mM·h^{-1}	36
6	3DOM g-C_3N_4-PW_{11}	Organic electron donors	300 W Xe lamp[b]	0.42 mM·h^{-1}	37
7	AQ-augmented g-C_3N_4	2-Propanol[e]	150 W Xe arc lamp	0.18 mM·h^{-1}	38
8	KPF_6/g-C_3N_4	Ethanol[e]	300 W Xe arc lamp	0.35 mM·h^{-1}	39
9	Nv-g-C_3N_4	Ethanol[g]	250 W sodium lamp	1.30 mM·h^{-1}	40
10	g-C_3N_4 with N vacancies	Ethanol[g]	250 W sodium lamp	2.00 mM·h^{-1}	41
11	g-C_3N_4-Carbon	2-Propanol[f]	300 W Xe lamp	0.38 mM·h^{-1}	42
12	Oxygen-enriched g-C_3N_4	2-Propanol[e]	300 W Xe lamp	1.20 mM·h^{-1}	43
13	g-C_3N_4–SiW_{11}	Methanol[f]	300 W Xe lamp	0.30 mM·h^{-1}	44
14	KH_2PO_4/g-C_3N_4	Ethanol[e]	300 W Xe arc lamp	0.75 mM·h^{-1}	45
15	g-C_3N_4-CoWO	Organic electron donors	300 W Xe arc lamp	0.09 mM·h^{-1}	46
16	Au/g-C_3N_4	Ethanol[e]	300 W Xe arc lamp	0.10 mM·h^{-1}	47
17	ACNN	2-Propanol[e]	300 W Xe lamp	5.10 mM·h^{-1}	48
18	Ti_3C_2/g-C_3N_4	2-Propanol[e]	300 W Xe lamp	0.11 mM·h^{-1}	49
19	BNQDs/UPCN	2-Propanol[e]	300 W Xe lamp	0.07 mM·h^{-1}	50
20	AKMT/C_3N_4	Ethanol[e]	300 W Xe lamp	1.37 mM·h^{-1}	51
21	*p*-TFAB-C_3N_4	Ethanol[d]	24 W household LED	2.00 mM·h^{-1}	This work

[a]The reaction systems were exposed to lamps with main emission from 420 nm ($\lambda \geq 420$ nm). [b]$\lambda > 320$ nm. [c]Production rates were determined based on slopes of graphs in initial time interval. [d]90 vol%. [e]10 vol%. [f]5 vol%. [g]0.789 g·L^{-1}.

In addition to all the above-mentioned catalysts, PCNs were also used to produce H_2O_2 from mixtures of water and alcohols (**Table 2.1**). More specifically, PCNs in conjunction with transition metal catalysts, nitrogen-vacancies, mesoporous morphologies, oxygen enrichment, or alkali metal dopants, have shown excellent reactivity. [32-51] Notwithstanding all these excellent photocatalysts, a high-power light source (at least >150 W) was essential to achieve high reactivity, and a higher production rate of the generated H_2O_2 was only possible with at least 250 W light power (very expensive lamps). From all these data, it is clear that a robust catalyst is essential to reduce costs and to increase production. Herein, we report on a difluoromethylene-substituted aryl amino PCN catalyst that reaches 2.0 mM h^{-1} of H_2O_2 production with a 24 W household LEDs and is stable for more than 30 h. The apparent quantum yield (AQY) is 36.7% at 456 nm (See supporting information). Compared to all the existing protocols using PCNs, this robust heterogeneous catalyst based on LEDs produces a higher concentration of H_2O_2 at a similar rate. Furthermore, to gain a comprehensive knowledge of its reactivity, we have characterized it with ^{1}H, ^{13}C, ^{15}N, and ^{19}F MAS solid state NMR spectroscopy, Fourier Transform Infrared Spectroscopy (FTIR), Diffuse-reflectance UV/Vis spectroscopy, Mott–Schottky plots, Brunauer–Emmett–Teller (BET) analysis and High-Resolution Transmission Electron Microscopy (HRTEM) and multiscale/level computational chemistry.

2.2 Results and Discussion

Different aryl amino PCNs were synthesized by heating the dicyandiamide (DCDA, 42 g) and the corresponding amino aryl nitriles (0.7 g, 1.6 wt%) in H_2O (160 mL) at 95 °C, until the mixture was completely dried (**Figure 2.4**). The resulting mixture was removed, grinded in an algae mortar, and loaded into a stainless steel chamber. Later, the chamber was heated to 585 °C in a GERO carbolite oven (type F70-200, power: 1.5 kW) for 244 minutes under air. The temperature was maintained for 4 h followed by cooling the chamber to room temperature in 6 h. The aryl amino-functionalized melem was generated from 2-aminobenzonitriles via condensation reaction, followed by thermal polycondensation of common and functionalized melem molecules to form the desired aryl amino-functionalized PCN.

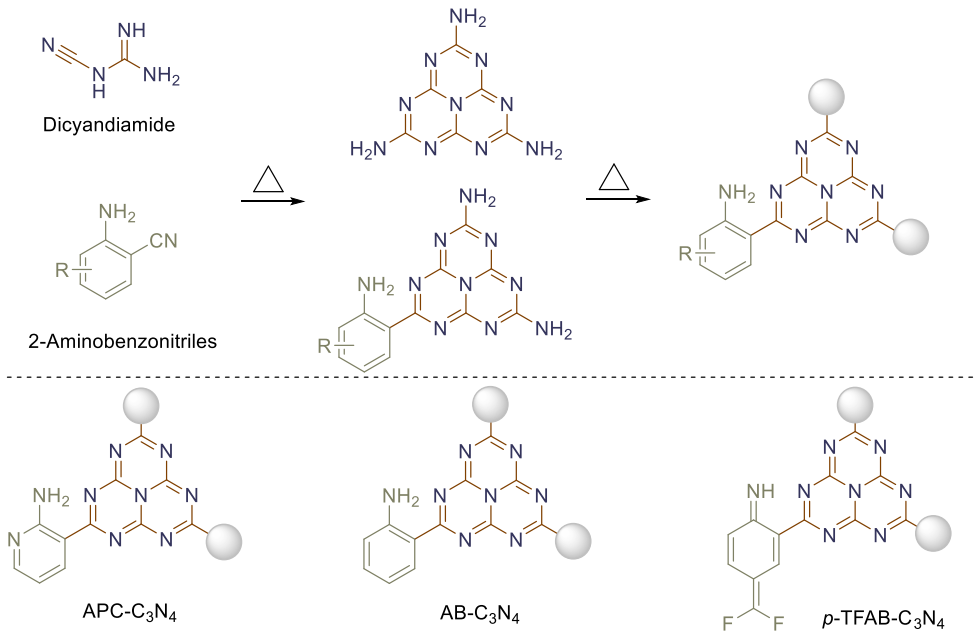

Figure 2.4. Synthesis of aryl amino PCNs.

After the synthesis of the aryl amino PCNs, Fourier Transform Infrared spectra (FTIR) were collected by using the Varian 610-IR FTIR spectrometer (USA). The sample was analyzed in the range of 400–4000

cm^{-1} with 16 scans at a 4 cm^{-1} resolution. As shown in **Figure 2.5**, all the stretching modes of the aromatic CN heterocycles around 1250 to 1600 cm^{-1} and the breathing mode of the triazine units at 800 cm^{-1} were observed. These signals clearly showed that the modification did not change the core of the polymeric structure of PCN and are similar to the pristine C_3N_4.[3a] Additionally, the Brunauer–Emmett–Teller (BET) specific surface area (S_{BET}) was determined from the low-temperature nitrogen adsorption/desorption isotherms and was approximately 12 $m^2 \cdot g^{-1}$ for the *p*-TFAB-C_3N_4, which was higher than the bulk g-C_3N_4 (**Figure 2.20**).[23]

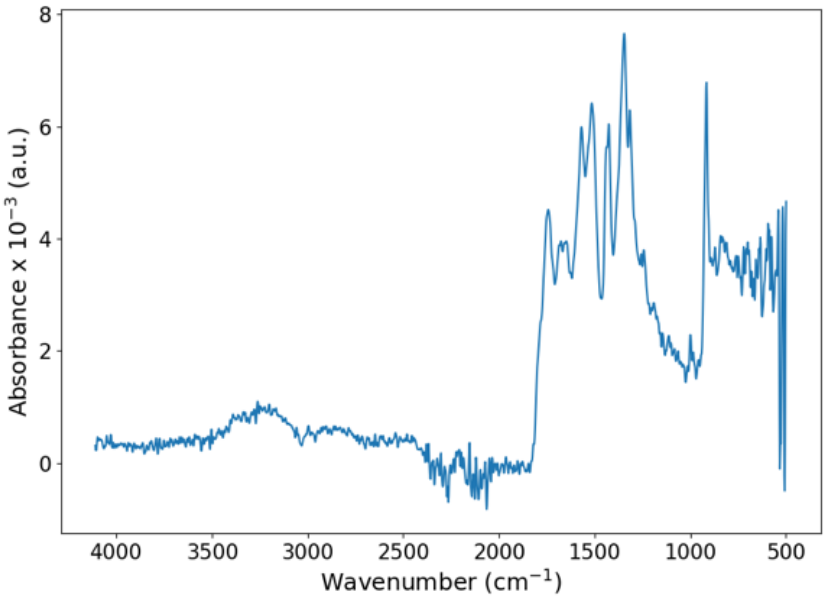

Figure 2.5. FTIR spectrum of *p*-TFAB-C_3N_4.

The bandgaps of all the arylamino PCNs were determined from the Tauc plots (ca. 2.8 eV), which were similar to the pristine C_3N_4 (**Figure 2.22**). Mott-Schottky experiments were also performed for the determination of flat band potentials (E_{fb}). The positive slope of the Mott-Schottky curve indicated the n-type nature of the arylamino PCNs. Based on the intersection between Mott–Schottky plot and the baseline, E_{fb} of

arylamino PCNs was approximately -0.69 V *vs.* RHE. It is generally considered that the bottom potential of the conduction band (CB) for an n-type semiconductor is approximately 0.2 V more negative than the E_{fb}. Therefore, CB of arylamino PCNs were ca. -0.89 V *vs.* RHE and valence band (VB) was 1.97 V *vs.* RHE (**Figure 2.23 and 2.24**).

To further obtain the structural information of arylamino PCNs, solid-state MAS NMR was performed (**Figure 2.6)**. To the best of our knowledge, high-resolution ^{1}H MAS NMR spectra of this type of material has not been reported before. The ^{1}H MAS NMR spectrum of the *p*-TFAB-C_3N_4 revealed two main signals: i) one from >NH linkers at 8.9 ppm and ii) another from $–NH_2$ terminal groups at 4.2 ppm. The high signal intensity from the >NH linkers in comparison to the low signal integral of the $–NH_2$ terminal groups (fitted ratio of ~0.8:0.2) reflected the high degree of polymerization among the melem monomers in the network. The two observed ^{13}C resonances originated from the "edge" (C_e; 165 ppm shift) and the "internal" (C_i; 157 ppm) carbon sites, as depicted in **Figure 2.6b.** The signal of C_e was expected to have a higher intensity than C_i as a consequence of closer distances to protons of the >NH and $–NH_2$ groups which enabled more efficient cross-polarization in the CPMAS experiment. This was in agreement with previously reported ^{1}H-^{13}C CPMAS spectra of g-C_3N_4.[3d,52] Noteworthy, the ^{13}C spectrum of *p*-TFAB-C_3N_4 sample revealed an additional partially resolved signal at 163 ppm, which had not been observed before. As this resonance originated from the carbon atoms adjacent to the >NH linkers, this indicated distinct network arrangements in the sample compared to the previous reports.

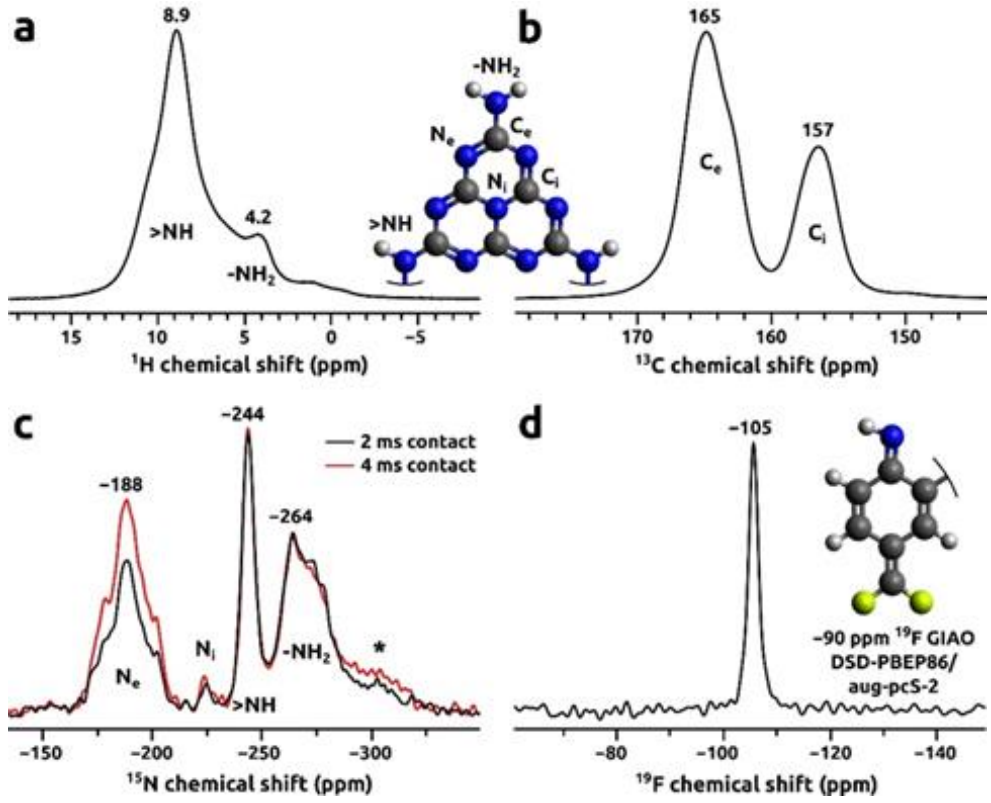

Figure 2.6. ^{1}H MAS NMR, ^{1}H- ^{13}C, ^{19}F and ^{1}H- ^{15}N CPMAS spectra of *p*-TFAB-C_3N_4 sample.

No other carbon signals from either the aromatic or non-aromatic species were observed in the ^{1}H-^{13}C CPMAS spectrum. However, the ^{1}H-^{15}N CPMAS spectrum revealed all the expected nitrogen resonances for the g-C_3N_4 structure being composed of melem monomeric units. The signals at -188 and -225 ppm correspond to the nitrogen atoms embedded at the edge (N_e) and inside (N_i) of the monomer units, respectively. The N_e/N_i signal intensity ratio was higher than the expected 6:1, because N_i was situated at a farther distance from the closest protons, which made cross-polarization less efficient for this nitrogen site. The intensities of both these signals increased when the contact time in the CPMAS experiment was increased from 2 to 4 ms, which corroborated signal

assignments. The resonances at -244 and approx. -264 ppm originated from linkers (>NH) and terminal –NH_2 groups, respectively. It is worth noting that the signal of the –NH_2 groups is over-represented in the ^{1}H-^{15}N CPMAS spectrum since there are two available protons to cross-polarize if compared to the >NH moiety. These signal assignments were in pair with the previous NMR study on $^{13}C/^{15}N$-isotope-enriched g-C_3N_4 and with theoretical predictions of $^{13}C/^{15}N$ NMR shifts in g-C_3N_4 by density-functional-theory (DFT).[52-53] The ^{19}F MAS NMR spectrum revealed a single resonance and consequently confirmed the successful incorporation of the fluorine atoms at a sole chemical site. The ^{19}F chemical shift of -105 ppm suggested the presence of the =CF_2 moiety [54-55], and it was corroborated further by the quantum chemical calculations. The ^{19}F chemical shift calculations at the robust DSD-PBEP86/aug-pcS-2 level of theory[56] for the model of the difluoromethylene functionality shown in **Figure 2.6d** (see SI for details), resulted in chemical shift prediction of -90 ppm, which was close to the experimental results given the wide chemical shift range of ^{19}F nucleus. Hence, we concluded that our combined NMR/DFT characterization confirmed the proposed chemical model of the catalyst.

After achieving all the characterizations of the arylamino PCNs, we became interested in observing their catalytic potential for the generation of H_2O_2 from a mixture of water and ethanol (**Table 2.2**). To our delight, initial evaluation of the photocatalytic performance from the (1/1, v/v) mixture of water and ethanol generated up to 1.2 mM of H_2O_2 within 1 h with the *p*-TFAB-C_3N_4. In general, the higher concentration of ethanol in the mixture, the higher contact possibility of ethanol and active sites which leads to better yield of H_2O_2. However, water can also increase the selectivity of H_2O_2 due to the hydration between H_2O_2 and water molecules.[32] Later, careful optimizations led to the best ethanol: water ratio as 9:1. Furthermore, the presence of an acid was essential because it prevented the decomposition of formed H_2O_2 under long reaction time.

Therefore, we have also screened the concentration of sulfuric acid in the system. Indeed, it was found that 0.5 M of H_2SO_4 was an ideal choice for this stabilization after screening. As oxygen and the light source are also crucial in the reaction system, reactions under N_2 atmosphere and the irradiation of blue lights with various intensities have been carried out, which have not shown any improvements. In addition, O_2 and a light source were essential to trigger the reaction, and without them, no formation of H_2O_2 was observed. The evaluation of all the optimization reactions led us to these optimal conditions (for detailed optimization studies, see **Table 2.3**): a mixture of ethanol (27 mL), H_2O (3 mL) and H_2SO_4 (0.5 M) containing the catalysts (45 mg) was irradiated under blue LED (> 420 nm, 24 W) at room temperature under O_2 saturation conditions. After achieving 25.64 mM of H_2O_2 in 30 h, *p*-TFAB-C_3N_4 catalyst was recollected by centrifugation and was reutilized for further reactions. Indeed, this catalyst was successfully recycled for at least four times (**Figure 2.26-2.27**).

Table 2.2. Generation of H_2O_2 from water and ethanol mixture by using aryl amino PCNs under the irradiation of blue LEDs.

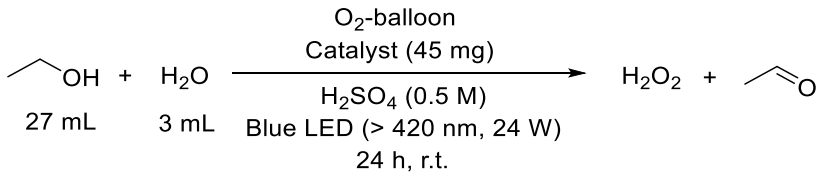

Entry	Catalyst	H_2O_2 (mM)[a]
1	APC-C_3N_4	15.89
2	AB-C_3N_4	24.44
3	*p*-TFAB-C_3N_4	25.64
4	g-C_3N_4	14.05

a: concentrations were determined by redox titration with $KMnO_4$ and results were the average value of two experiments under the same reaction conditions.

To further analyse the stability of the catalyst (***p*-TFAB-C_3N_4**) from **Table 2.2**, TEM studies on the catalyst before and after the reaction were performed (**Figure 2.7**). TEM images and HRTEM images of the *p*-TFAB-C_3N_4 (before reaction) revealed a two-dimensional structure, i.e. nanoflake structure with an amorphous phase (embedded SAED pattern). Even though the low-magnification TEM image of PCN after the reaction showed a denser and thicker morphology, the HRTEM showed the same nanoflake microstructure at the edge. As a result, the difference on the morphology was attributed to the observed thickness of particles, and it can be concluded that the reaction did not change the microstructure of the PCN, indicating a high stability during the reaction conditions. This clearly suggested the excellent recyclability of the *p*-TFAB-C_3N_4 photocatalyst under the reaction conditions (**Figure 2.26-2.27**).

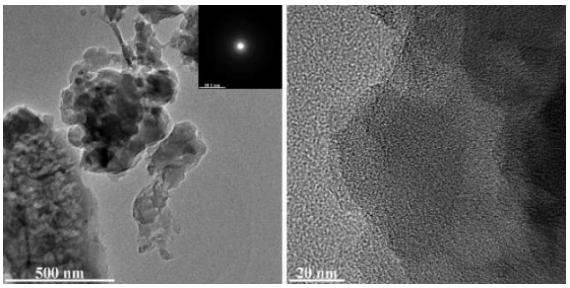

Before reaction

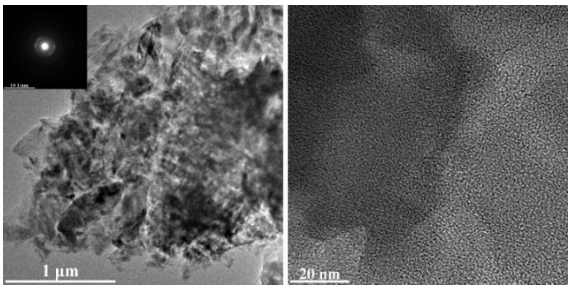

After reaction

Figure 2.7. TEM and HRTEM image of *p*-TFAB-C_3N_4 before and after the reaction. TEM image and selected area electron diffraction pattern (SAED) of PCN were recorded by JEOF-2100F.

To analyze, the kinetics of the photocatalytic H_2O_2 generation, experimentally, concentrations of the formed H_2O_2 and the decomposition of H_2O_2 under the irradiation of blue LEDs were measured. As shown in **Figure 2.8**, concentrations of the formed H_2O_2 with various aryl amino PCNs were increased linearly within 8 hours and accumulated slowly over time. Parallel to this, decomposition of H_2O_2 was also investigated and H_2O_2 was decomposed dramatically when its concentration was very high. All the aryl amino PCNs did not exhibit any obvious difference in the decomposition rate. It is worth noting that the decay rate of H_2O_2 was much slower in the presence of the acid compared to the absence of the acid. Therefore, we assumed that the formation and decomposition of H_2O_2 were in accordance with the zero-order and first-order reaction kinetics, respectively.

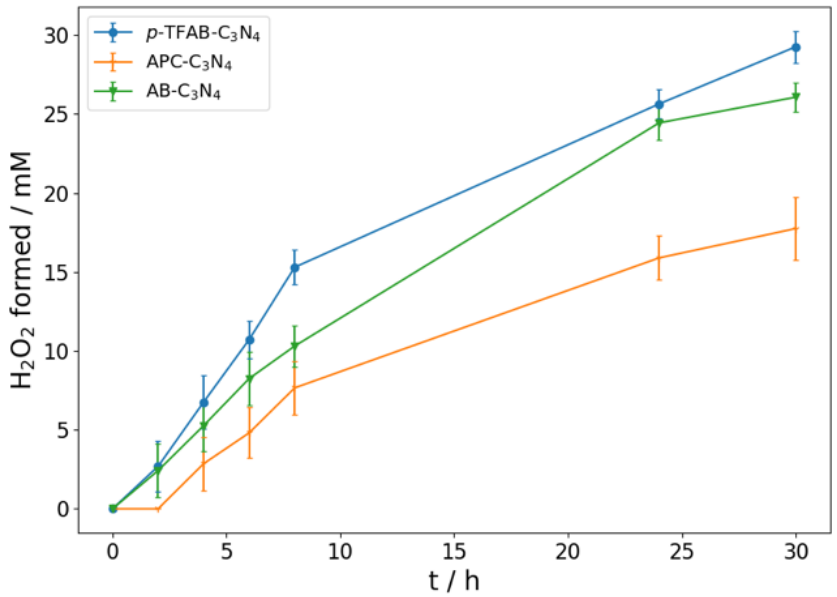

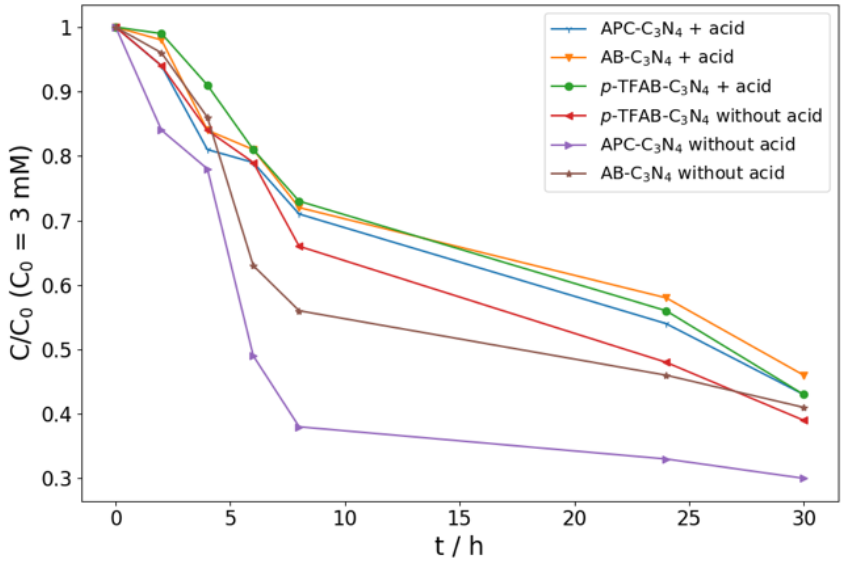

Figure 2.8. Photocatalytic H_2O_2 generation (top) and decomposition (down) with aryl amino PCNs under visible light. Concentrations were determined by redox titration with $KMnO_4$.

2.3 Mechanistic studies

Finally, to disclose the mechanism of this reaction, $^{18}O_2$-labelling experiment was carried out to investigate the oxygen source of the formed H_2O_2. The generated hydrogen peroxide from the mixture of O_2 gas ($^{16}O_2$) and labelled molecular oxygen ($^{18}O_2$) were subsequently reacted with PPh_3 and concomitantly analysed by GCMS. As shown in **Figure 2.9**, mixture of the phosphine oxides ($^{16}O{=}PPh_3$ and $^{18}O{=}PPh_3$) were observed which clearly proved the oxygen source of the formed H_2O_2 was the O_2 gas.

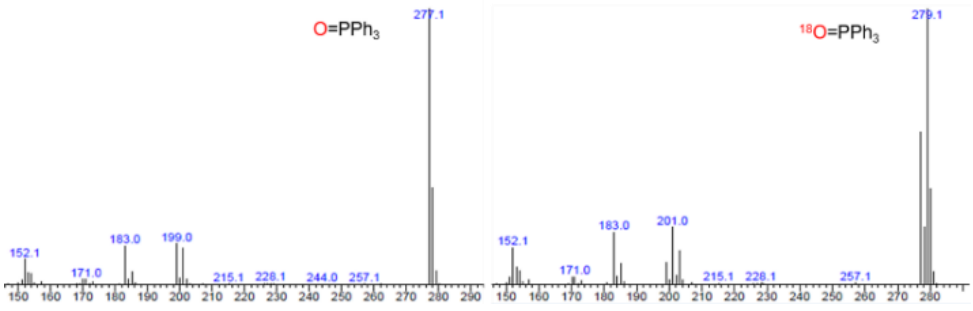

Figure 2.9. Mass spectra for labelling reaction.

To further investigate the performance of the photo-generated carriers transfer rate of the catalysts, Electrochemical Impedance Spectroscopy (EIS) measurements were carried out. As shown in **Figure 2.10**, following the Nyquist plots, the diameter of each of the semi-circle was related to the charge transfer resistance at the electrode surface of the catalyst. Therefore, smaller the diameter, faster the charge transfer and better the charge separation. Compared to the bare electrode, resistances at the electrode surfaces with the aryl amino PCNs were all smaller and the *p*-TFAB-C_3N_4 had the smallest resistance. It should be also clearly noted that all of these aryl amino PCNs exhibited smaller resistance compared to the g-C_3N_4 catalyst that suggested that these aryl amino PCNs had slower recombination of the photo-generated electron-hole pairs. Additionally, the electrode with *p*-TFAB-C_3N_4 was also investigated under the O_2 and N_2 atmosphere in the presence and absence of the light, respectively. It

was obvious that *p*-TFAB-C_3N_4 under the O_2 atmosphere in the presence of light exhibited much smaller resistance compared to that of N_2 atmosphere. The photo-generated electrons were consumed at the surface of the photocatalyst after being reduced by O_2, which indicated that O_2 facilitated the charge separation and prevented recombination of photoinduced charges and holes.

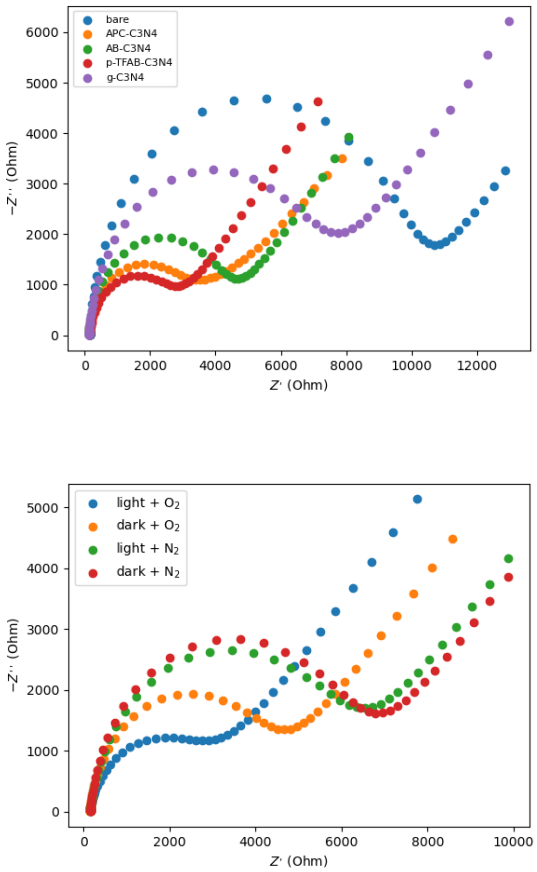

Figure 2.10. Electrochemical impedance spectroscopy Nyquist plots of various modified catalysts under air (top). Nyquist plots of *p*-TFAB-C_3N_4 under saturated N_2 or O_2 atmosphere (bottom). The measurements were performed in 80 µL solution containing 1 mM $K_3Fe(CN)_6$, 1 mM $K_4Fe(CN)_6$ and 150 mM NaCl. As a reference, one measurement was done on a bare working electrode.

Furthermore, to identify the possible radicals involved in this reaction, ESR analysis with 5,5-dimethyl-1-pyrroline N-oxide (DMPO) as a spin trapping reagent was carried out (**Figure 2.11**). The ESR spectra of an *in situ* photoreaction of *p*-TFAB-C_3N_4/EtOH/O_2 with DMPO system indicated that four radicals were identified in this photocatalytic system: 1) DMPO-•OOH; 2) radical of the catalyst; 3) DMPO-•OEt; 4) nitroxide degradation product of DMPO.[57] From the table below, parameters of the radical of the catalyst and DMPO-•OOH adduct were similar to the references.[58] Therefore, we suggested that oxygen was reduced *via* one-electron reduction due to the strong signal of DMPO-•OOH adduct. The signals of DMPO-•OEt adduct and nitroxide degradation radical of DMPO were weak and overlapped with DMPO-•OOH adduct signal. It is also worth noting that each of this reaction component played a crucial role for the generation of •OOH radical.

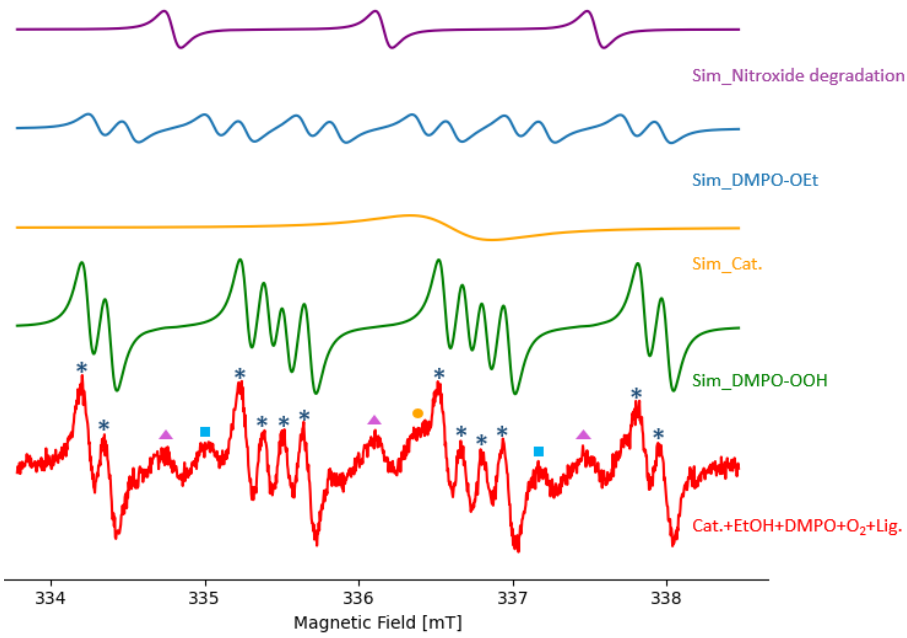

Radical	A_N [mT]	A_H [MT]	g_{iso}	Ref.
p-TFAB-C_3N_4	-	-	2.0038	This work
g-C_3N_4	-	-	2.0034	[3d]
DMPO-•OOH	1.30	1.03 (1H) 0.15 (1H)	2.0066	This work
DMPO-•OOH	1.31	1.03 (1H) 0.14 (1H)	2.0061	[58]
DMPO-•OEt	1.35	0.76 (1H) 0.21 (1H)	2.0065	This work
DMPO-•OEt	1.35	0.74 (1H) 0.17 (1H)	-	[59]

Figure 2.11. ESR spectra measured at room temperature for the reaction solution in the presence of a 200 mW solid state laser (447 nm). The EPR spectra was simulated with Matlab2018b using the EasySpin-6.0 module.

These data agree with the representative supramolecular models designed to disclose, computationally, possible reaction mechanisms and locations of the various species in relation to the catalysts. The main focus was on the edge regions of the nanoflakes where the functional group was attached. In the initial configurations of the reduction dynamics, the O_2 molecules were surrounded by the solvent, located far apart from one another and relatively close to the catalyst interfaces. After a few picoseconds RMD, most of the O_2 reached the catalyst regions where the NH or NH_2 groups were located, stabilizing their position there through intermolecular hydrogen bonding interactions. This is visible in **Figure 2.12**, where the O_2 maximum density maps, rendered as red contours, are superimposed to the molecular structures of the two catalysts (solvent molecules are also displayed as sticks).

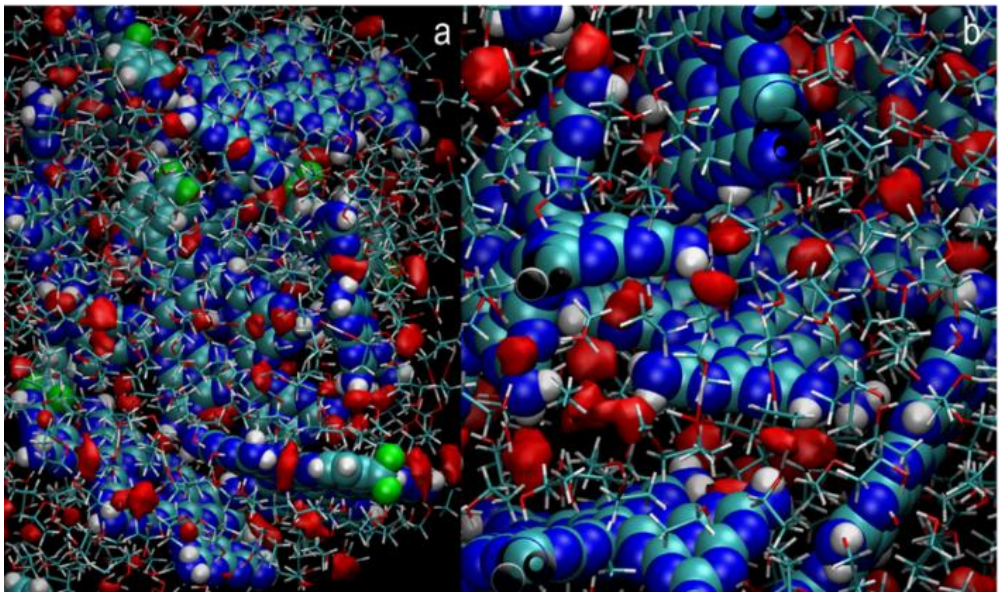

Figure 2.12. Simulations snapshots of the complex models comprising the catalyst with *p*-TFAB (a) and without it (b) (vdW spheres), ethanol and water molecules (sticks), and red high-density contours identifying the O_2 molecules. Color code: C cyan, O red, N blue, F green, H white.

The extension of these areas provided an idea of the motion of the oxygen near the interface, which was, apparently, very limited. This was in contrast with its high mobility in solution where the density contours were more extended. It was also noticed that the connections of the oxygens were sometimes reinforced by the cooperative action of various amine moieties close by and, when the *p*-TFAB fragment was present, by a relatively strong interaction with its nitrogen group (**Figure 2.13**).

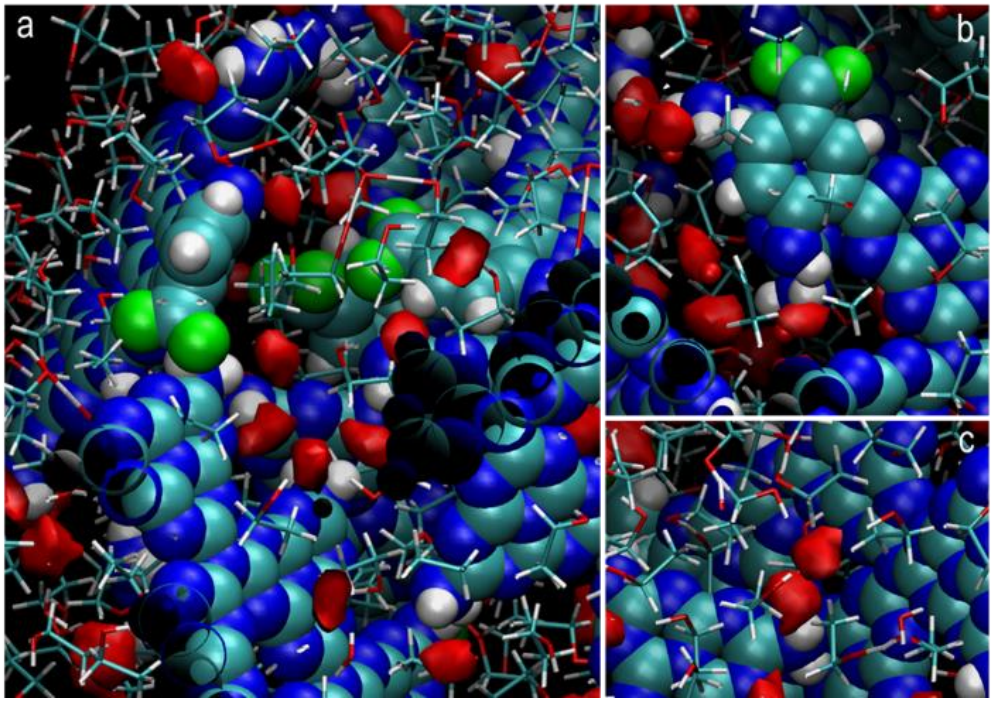

Figure 2.13. Catalyst with *p*-TFAB (vdW spheres), ethanol and water molecules (sticks), and red high-density contours identifying the O_2 molecules. Color code: C cyan, O red, N blue, F green, H white. a) Self-assembly of the various catalyst units and entrapment of the O_2 molecules interacting with the NH_2 groups. b) one of the *p*-TFAB groups. c) capture of the O_2 molecules inside the pores of the material.

A consequence of these local constraints on the O_2 was a sort of entrapment that induced a relocation of the surrounding solvent molecules. Practically, both ethanol and water adopted a more favourable orientation to interact/react with O_2. It is worth mentioning that the interfacial behaviour of the solvent was similar for the two catalysts. Indeed, the RDF plots shown in **Figure 2.14** confirmed the tendency of ethanol to exchange/release its H(OH) with/to the amine nitrogen or non-protonated nitrogens of both catalysts and to reorient its other hydrogens towards the π-density of the rings (peak centered at 2 Å in the carbon RDF plot). The *p*-TFAB functionalization represented another active O_2 binding

location at the catalyst edges that could be strengthened by the self-assembly of the graphitic-like sheets in T-shaped or parallel orientations (**Figures 2.13-2.14**).

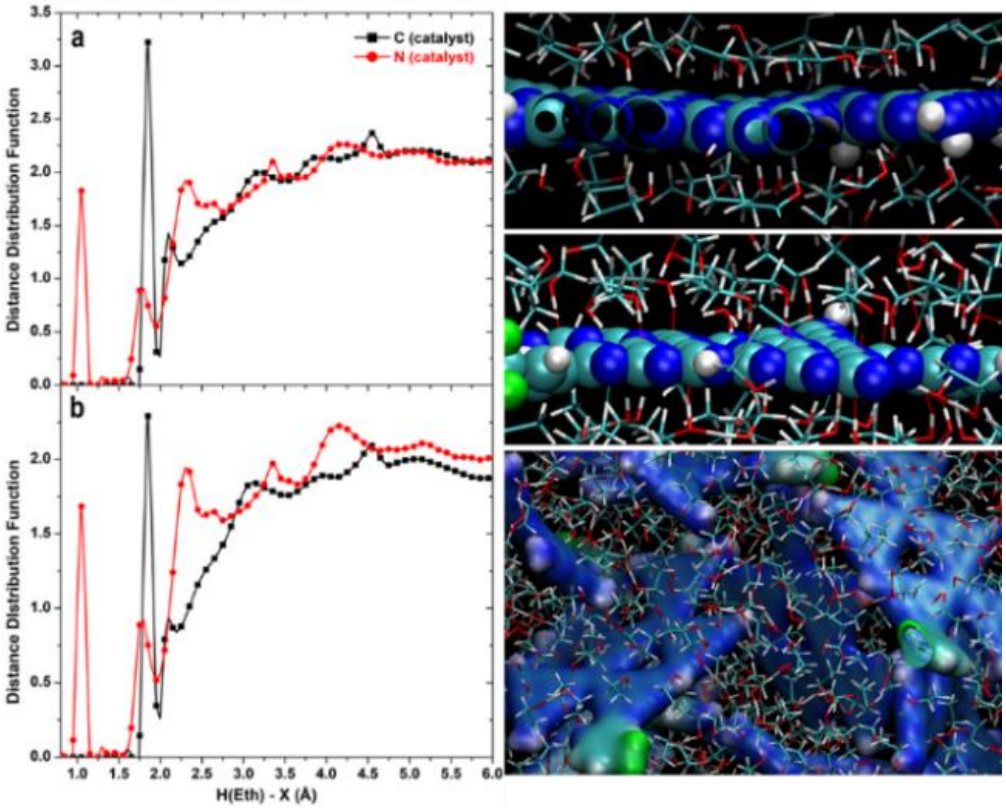

Figure 2.14. Ethanol hydrogens-C/N atoms of the catalyst distance distribution functions for the non-functionalized (a) and *p*-TFAB functionalized (b) systems. On the right-hand side, the molecular models depict the orientation of the ethanol molecules (sticks) in relation to the two supports (vdW or accessible surface representations). The red dash lines indicate the coordination of the OH groups to the interface.

A more straightforward characterization of the O_2 reduction mechanism, in general terms, was obtained through the examination of the atom-atom distance distribution functions of the O_2 with both nitrogen and carbon site of the catalysts and with the hydrogens of catalysts and solvent (**Figure 2.28**). The first RDFs confirmed again that the mechanism

started with the connection of O_2 to the -N sites through H-bond interactions (peak at 3.2 Å – red curve) and that the main actor was ethanol, which released its H(OH) to both or one of the oxygen atoms (red peak at about 1 Å in both a and b plots-right-hand side). However, the presence of the first peak at short distances (about 1.1 Å in the b plot) ascribed to the catalyst suggested that the *p*-TFAB played a role in the reduction process by providing the oxygen with the hydrogen that in the other case (non-functionalized melem) was released by water. The most striking effect of these interactions was an increase in H_2O_2 production, which was evident in the trend displayed in **Figure 2.15**.

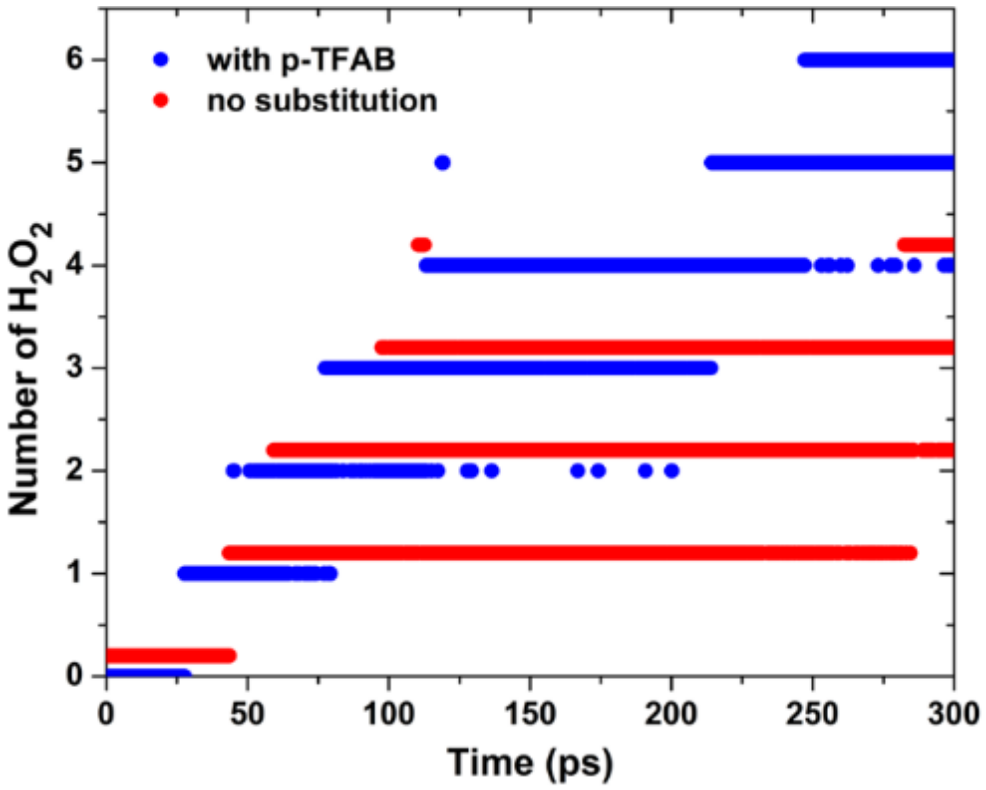

Figure 2.15. Evolution of the number of H_2O_2 produced during the RMD for the functionalized and non-functionalized supports.

As far as the reaction mechanism is concerned, two possible reaction models were identified, which are shown in **Figure 2.16**. The observed

phenomena were not induced by specific biases and happened spontaneously, suggesting that, in the presence of the catalysts, the energy barriers could be overcome at the simulated temperature. For both reaction models, it was apparent that a critical step was the restraint of the O_2 mobility by its hydrogen bonding to an edge -NH or -NH_2 group of the catalyst. This induced an ad hoc rearrangement of O_2 relative to the surrounding solvent species that started to reorient their active hydrogens towards each of the oxygens. As displayed in **Figure 2.16A** (Path a), the hydrogens released to the O_2 molecule came from ethanol. Another possible pathway observed during the simulation was the one where the -NH group of the catalyst functioned both as a mediator and as a proton donor (**Figure 2.16B**, Path b). Indeed, the -NH or -NH_2 of the linker was initially protonated and thus was prone to give a hydrogen atom to O_2, which almost simultaneously received another H atom from the ethanol adjacent to the other O (**Figure 2.30**). During the RMD simulations, we could not observe the formation of acetaldehyde, which was the main ethanol photooxidation product, because all the effects of visible light were not included in the models. Thus, we resorted to QC nudged elastic band (NEB) calculations on representative models of the catalysts (**Figure 2.31**) interacting with just an O_2 and an ethanol molecule to reproduce the whole reaction mechanism at the edges of the materials and to estimate the energy barriers involved in these processes (**Figure 2.3.9**).

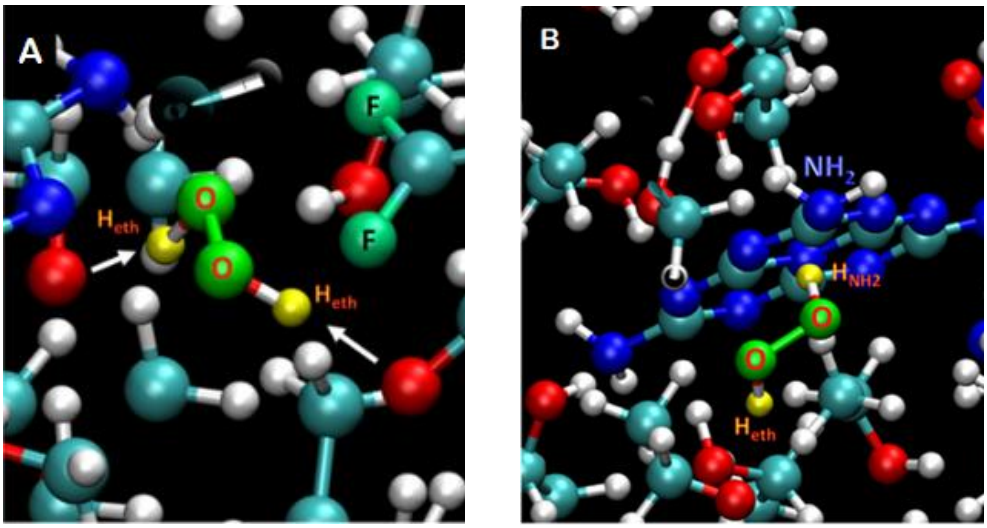

Figure 2.16. Two distinct reaction models where the hydrogens of the final product (H_2O_2) come from a) ethanol; b) the NH group of the catalyst and ethanol. O_2 and H_2O_2 are green, and the released hydrogens yellow.

The initial action was a sort of immobilization of O_2 *via* hydrogen-bonding interactions with the -NH or -NH_2 group of the catalyst and the ethanol -OH moiety (left panels in **Figure 2.17**, corresponding to reactants configuration). The transition state (TS in **Figure 2.17**) consists of the same OOH* intermediate obtained after the ethanol H(OH) migration on O_2 and, in the case of the incorporation of *p*-TFAB, in the addition of an H (from the CH_2 of ethanol) to the *p*-TFAB -NH moiety. The final stabilization was achieved by a simultaneous hydrogen transfer from the -NH_2 of the catalysts (and the CH_2 of ethanol in pristine melem) and the formation of H_2O_2 and acetaldehyde (right panels in **Figure 17**, corresponding to products configurations). The activation energies were approximately 28 and 23 kcal/mol for the Path a and Path b, respectively. Obviously, Path b showed lower activation energy, which was also consistent with our experimental results. However, it should be noted that catalysts were protonated by -H(CH_2) which was not the favourable step compared to H(OH). However, due to the instability of $CH_3CH_2O\cdot$ radical, -H(CH_2) was

used to estimate the activation energy and real activation energy was probably even less. Therefore, we proposed the catalysts acted as both proton donor and mediator.

Furthermore, to disclose the effects of light on the doped catalyst, we used the time-dependent extension of DFT (TDDFT) at the B3LYP/6-31G(d) level of theory, in line with Shiraishi and co-workers,[23] and simulated the UV/Vis spectrum of the *p*-TFAB-doped system. An intense absorption peak located at about 423 nm was identified (**Figure 2.32**), with its corresponding structure (See supporting information). In line with previous observations,[23,32] in the excited state conformation, the hydrogen of the *p*-TFAB was connected to the nearby nitrogen of the g-C_3N_4 unit, suggesting and confirming (in agreement with the RMD simulations) that the *p*-TFAB nitrogen was available for active hydrogen exchanges and thus a very efficient site in the H_2O_2 production mechanism.

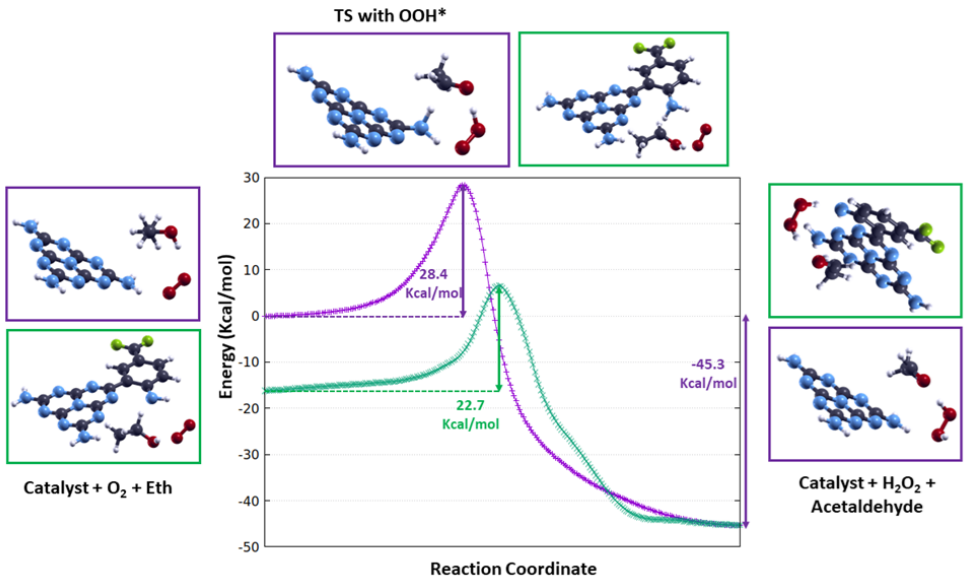

Figure 2.17. NEB simulations of the H_2O_2 generation process for two pathways. Hydrogens of the final product (H_2O_2) come from ethanol (path a, purple) or from the NH group of the catalyst and ethanol (path b, green). C, N, O, H, and F atoms are dark gray, blue, red, white, and green, respectively.

Based on all the above information, we proposed the mechanism of this reaction and robustness in the presence of the arylamino PCNs (**Figure 2.18**). Before the irradiation of light, the amino group of the *p*-TFAB fragment reinforced the interaction with O_2 through hydrogen bonding. This restrained O_2 mobility and facilitated the ad hoc rearrangement of ethanol surrounded by O_2 (**Step 1**). The -NH linker was further protonated by H(OH) in ethanol which was closed to the -NH linker (**2**). Upon photocatalyst activation by the blue LED, formation of photogenerated electron and holes occurred and consequently, ethanol as an electron donor was oxidized.[5e] At the same time, O_2 was reduced by the catalyst to form the superoxide radical anion *via* one-electron reduction (**Step 2**). Based on NEB calculations, H(NH) was more favourable than H(OH) to be deprotonated by superoxide radical anions (**3** and **4**). After protonation of superoxide radical anion, acetaldehyde radical and hydroperoxide radical were formed which were verified by ESR and the catalyst **1** was regenerated (**Step 3**). Finally, generation of H_2O_2 occurred in the final step (**Step 4**) by abstracting hydrogen atom radical and forming acetaldehyde. Due to the introduction of aryl amino groups in the PCN, the charge separation and oxygen reduction is more efficient compared to pristine PCN, which was verified by EIS and electronic energy levels measurements. In addition, the introduced aryl amino groups could also lower the energy barriers for the electron and proton transfer, thereby promoting the H_2O_2 generation.

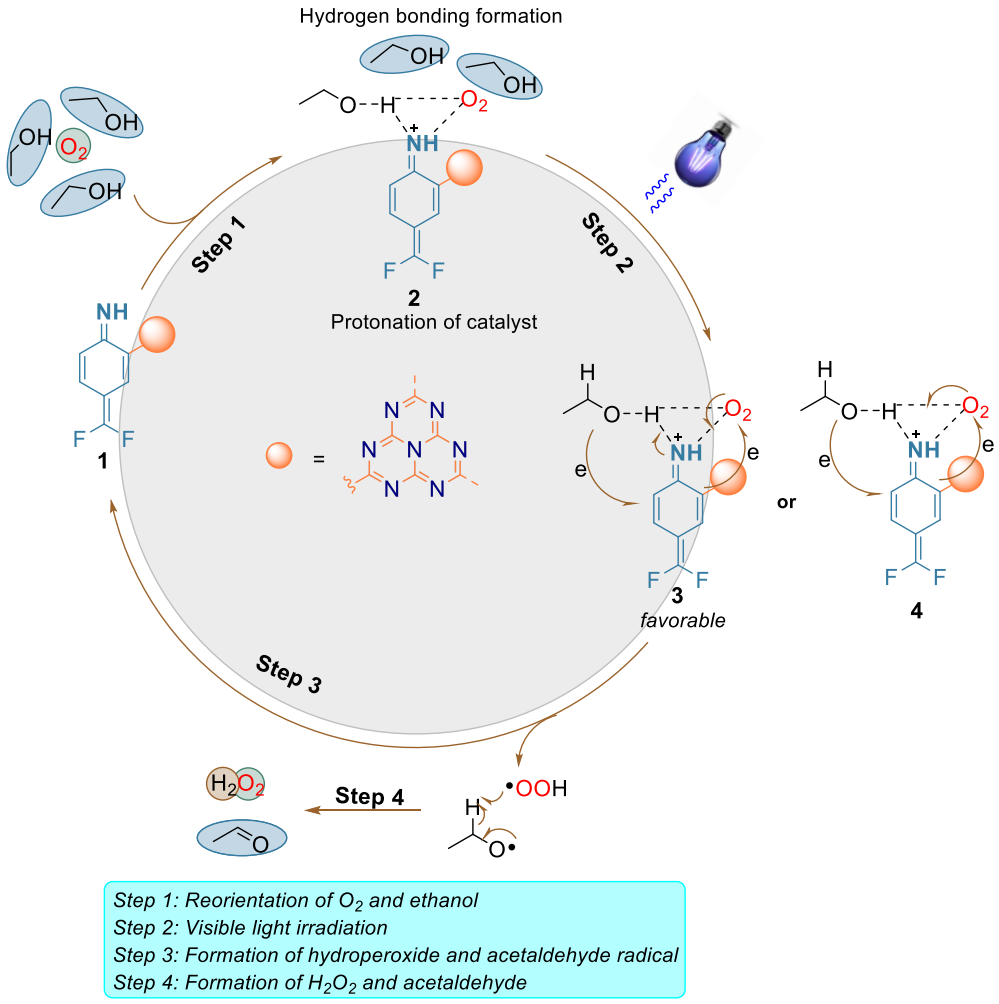

Figure 2.18. Proposed mechanism for photocatalytic H_2O_2 formation.

2.4 Conclusion

In conclusion, we constructed an effective photocatalytic system for the production of H_2O_2 in the presence of household LEDs. The novel aryl amino PCNs with more negative CB promoted O_2 reduction faster and facilitated higher concentration of H_2O_2. It is also worth noting that the aryl amino PCNs exhibited smaller resistance at the surface of the photocatalyst which suppressed the recombination of the photoinduced electrons and holes. Our work provides higher concentration of H_2O_2 (25.64 mM), which demonstrates that the modification with aryl amino moiety is a promising method to enhance the photocatalytic performance of H_2O_2 generation and facilitate O_2 reduction. The critical advancement of this work is the synthesis of an efficient H_2O_2 generation photocatalyst and its atomic level understanding by combined ^{19}F, ^{13}C, ^{1}H and ^{15}N solid state MAS NMR at natural abundance. This methodology reveals the chemical structure of the semiconducting PCNs contains both NH linkers, $–NH_2$ terminal groups and difluoro methylene functional group. Our study emphasizes the importance of the solid state NMR spectroscopy for the elucidation of structure-property relationships and is generally applicable to all the PCN-related materials. In addition, with the help of computational studies, we disclosed the possible reaction model in atomic level, which provided a new sight for the modification of photocatalysts for photocatalytic H_2O_2 production.

2.5 Supporting Information

2.5.1 Fourier Transform Infrared spectra (FTIR) Analysis

Fourier Transform Infrared spectra (FTIR) were collected using the JASCO FT/IR-4100 type A spectrometer (Germany). The sample was analyzed in the range of 500–4000 cm^{-1} with 32 scans at a 4 cm^{-1} resolution.

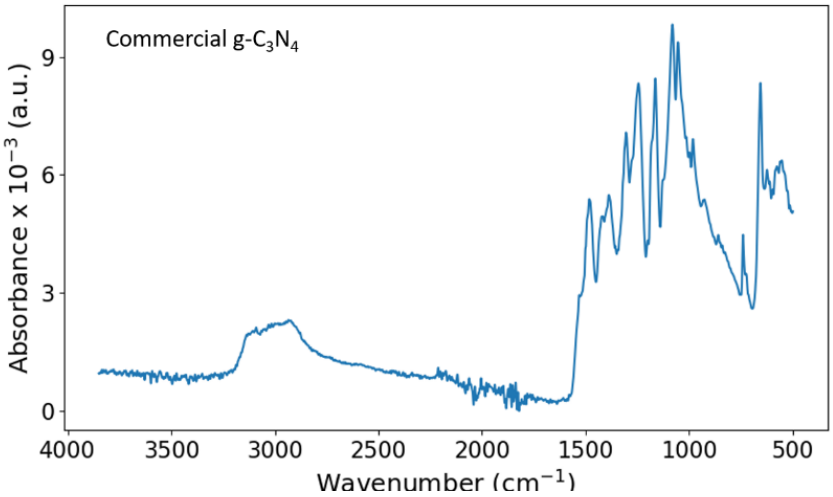

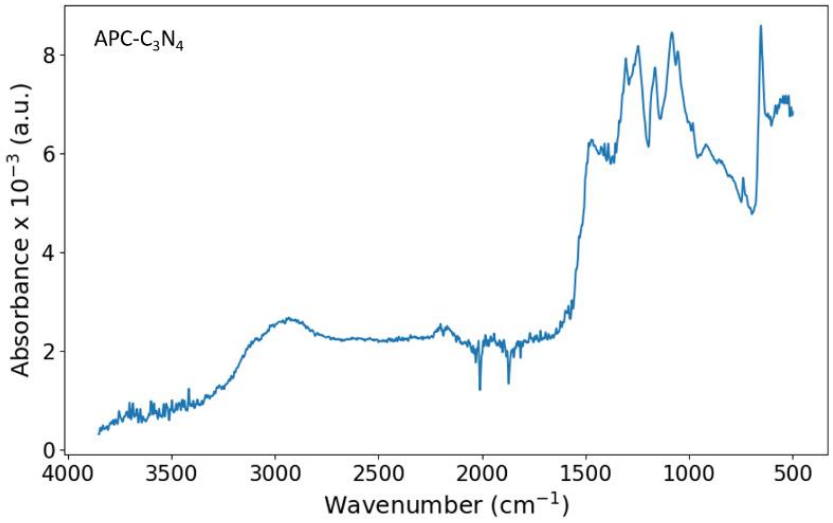

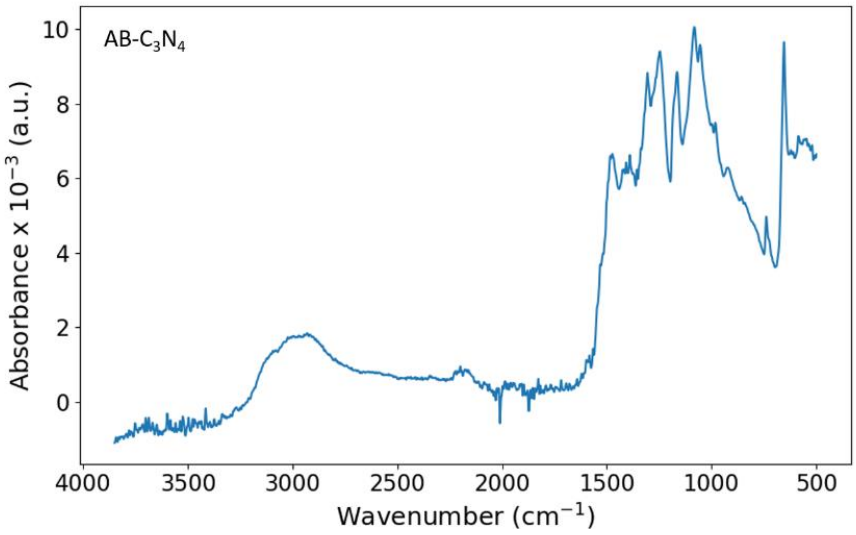

Figure 2.19. FTIR spectrum of commercial g-C_3N_4 (top), APC-C_3N_4 (middle) and AB-C_3N_4 (bottom).

2.5.2 Brunauer–Emmett–Teller (BET) specific surface area measurement

Brunauer–Emmett–Teller specific surface area (S_{BET}) was determined from the low-temperature nitrogen adsorption/desorption isotherms and found to be 12 $m^2 \cdot g^{-1}$ for the *p*-TFAB-C_3N_4. The shape of the isotherms corresponds to characteristic type II which is common for non-porous materials.[60] The hysteresis loop of isotherms belongs to type H3 which is referred to non-rigid aggregates of plate-like particles (slit-shaped pores).[1] However, some amount of micro and mesopores is presented on the surface of catalyst. According to Barret-Joyner-Halenda (BJH) analysis of adsorption and desorption branch of N_2 isotherm, an average pore diameter was 23 nm for *p*-TFAB-C_3N_4. The volume of pores up to 2 nm in diameter (micropore volume) was determined based on t-Plot and was found to be 0.000547 $cm^3 \cdot g^{-1}$ for *p*-TFAB-C_3N_4. The total pore volume of pores less than 95 nm in diameter (single point adsorption at $p/p° = 0.98$) was found 0.069 $cm^3 \cdot g^{-1}$ *p*-TFAB-C_3N_4.

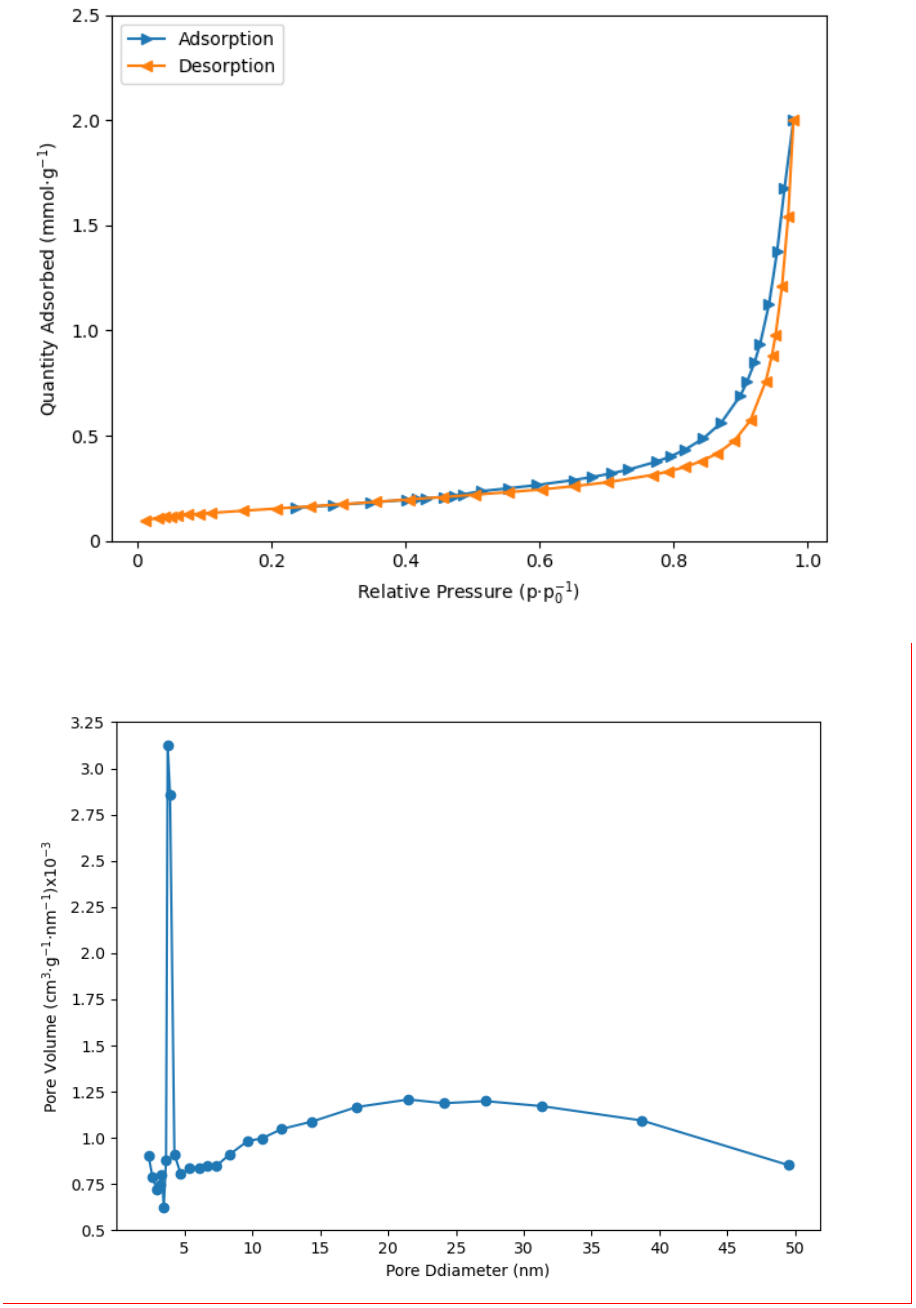

Figure 2.20. The N_2 adsorption/desorption isotherms (up) and BJH desorption dV/dD pore size distributions based on pore volume for *p*-TFAB-C_3N_4 (down).

2.5.3 Photoreaction for H_2O_2 production

The reaction has been carried out under O_2 atmosphere/air. The flasks were dried in an oven for four hours to remove the moisture. A 100 mL two-necked flask containing 45 mg of the photocatalyst with a stirring bar was evacuated and flushed with the inert gas for three times using SCHLENK techniques. After third time evacuating the flask, a O_2 balloon was connected with the flask. 27 mL of ethanol, 3 mL of O_2-bubbled H_2O and H_2SO_4 (0.5 M) were injected with O_2 gas-flushed syringes. The reaction mixture was stirred under the irradiation of blue LED at room temperature. Concentration of H_2O_2 was determined by redox titration with $KMnO_4$.[61]

The setup of the photocatalytic reactions is shown in **Figure 2.21**. An LED strip with power of 24 W was fixed on the inner surface of a round glass dish with a diameter of 140 mm. The emission spectra of the light setup was measured with a UV-Vis probe from Ocean optics (P200-5-UV-Vis). The emission spectra showed the clear wavelength band between 420 and 520 nm with a maximum at 456 nm. The light intensity was measured by Ophir StarLite power meter with 3A probe head. To avoid the heat produced by the irradiation of light, an electric fan was used for cooling. In general, the stirring was set from 250 rpm to 300 rpm. The oxygen balloon was used to main the O_2 atmosphere during the whole reaction.

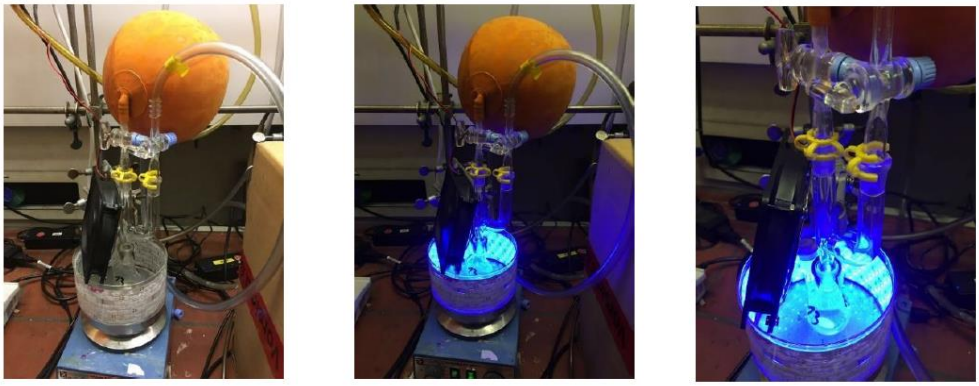

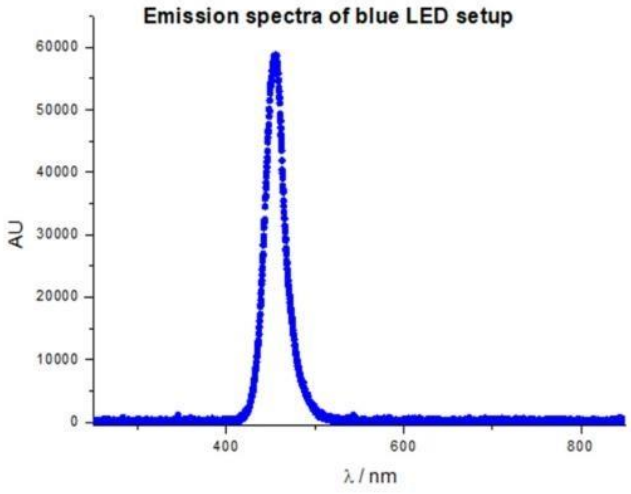

Figure 2.21. Setup for photocatalytic reactions under O_2 with an electric fan.

2.5.4 Optimization of reaction conditions for photocatalytic H_2O_2 production

Table 2.3. Optimization of reaction conditions for photocatalytic H_2O_2 production.

Starting materials		Catalyst(g-C3N4)/g	Additives	Atmos	Light/ W	Time/h	Yields/m M
EtOH (1 mL)	H_2O (1 mL)	*p*-TFAB-C_3N_4 (5 mg)	-	O_2	24	1	1.2
EtOH (0.1 mL)	H_2O (1.9 mL)	*p*-TFAB-C_3N_4 (5 mg)	-	O_2	24	1	0.05
EtOH (0.2 mL)	H_2O (1.8 mL)	*p*-TFAB-C_3N_4 (5 mg)	-	O_2	24	1	0.71
EtOH (1.8 mL)	H_2O (0.2 mL)	*p*-TFAB-C_3N_4 (5 mg)	-	O_2	24	1	1.34
EtOH (2 mL)	-	*p*-TFAB-C_3N_4 (5 mg)	-	O_2	24	1	0.95
EtOH (1.8 mL)	H_2O (0.2 mL)	*p*-TFAB-C_3N_4 (2 mg)	-	O_2	24	1	1.05
EtOH (1.8 mL)	H_2O (0.2 mL)	*p*-TFAB-C_3N_4 (3 mg)	-	O_2	24	1	1.36
EtOH (1.8 mL)	H_2O (0.2 mL)	*p*-TFAB-C_3N_4 (6 mg)	-	O_2	24	1	1.33
EtOH (1.8 mL)	H_2O (0.2 mL)	*p*-TFAB-C_3N_4 (10 mg)	-	O_2	24	1	1.37
EtOH (1.8 mL)	H_2O (0.2 mL)	*p*-TFAB-C_3N_4 (3 mg)	H_2SO_4 (0.2 M)	O_2	24	1	1.52
EtOH (1.8 mL)	H_2O (0.2 mL)	*p*-TFAB-C_3N_4 (3 mg)	H_2SO_4 (0.5 M)	O_2	24	1	2.03
EtOH (1.8 mL)	H_2O (0.2 mL)	*p*-TFAB-C_3N_4 (3 mg)	H_2SO_4 (1 M)	O_2	24	1	2.04

EtOH (1.8 mL)	H_2O (0.2 mL)	*p*-TFAB-C_3N_4 (3 mg)	H_2SO_4 (2 M)	O_2	24	1	2.01
EtOH (1.8 mL)	H_2O (0.2 mL)	*p*-TFAB-C_3N_4 (3 mg)	H_2SO_4 (0.5 M)	N_2	24	1	<0.1
EtOH (1.8 mL)	H_2O (0.2 mL)	*p*-TFAB-C_3N_4 (3 mg)	H_2SO_4 (0.5 M)	O_2	12	1	0.85
EtOH (1.8 mL)	H_2O (0.2 mL)	*p*-TFAB-C_3N_4 (3 mg)	H_2SO_4 (0.5 M)	O_2	-	1	0
EtOH (1.8 mL)	H_2O (0.2 mL)	APC-C_3N_4 (3 mg)	H_2SO_4 (0.5 M)	O_2	24	1	0.51
EtOH (1.8 mL)	H_2O (0.2 mL)	AB-C_3N_4 (3 mg)	H_2SO_4 (0.5 M)	O_2	24	1	1.89
EtOH (1.8 mL)	H_2O (0.2 mL)	*p*-TFAB-C_3N_4 (3 mg)	H_2SO_4 (0.5 M)	O_2	24	24	22.05
EtOH (1.8 mL)	H_2O (0.2 mL)	*p*-TFAB-C_3N_4 (3 mg)	H_2SO_4 (0.5 M)	O_2	24	30	27.11
EtOH (27 mL)	H_2O (3 mL)	*p*-TFAB-C_3N_4 (30 mg)	H_2SO_4 (0.5 M)	O_2	24	24	20.06
EtOH (27 mL)	H_2O (3 mL)	*p*-TFAB-C_3N_4 (45 mg)	H_2SO_4 (0.5 M)	O_2	24	24	25.64
EtOH (27 mL)	H_2O (3 mL)	*p*-TFAB-C_3N_4 (90 mg)	H_2SO_4 (0.5 M)	O_2	24	24	24.22
EtOH (27 mL)	H_2O (3 mL)	*p*-TFAB-C_3N_4 (45 mg)	H_2SO_4 (0.5 M)	O_2	24	30	29.26

2.5.5 Electrochemical impedance spectroscopy (EIS) measurement

Electrochemical impedance spectroscopy (EIS) measurements were carried out using Autolab Potentiostat/Galvanostat PGSTAT 302N from Metrohm (Utrecht, The Netherlands), operated with the PC equipped by NOVA 2.1.4 software. As an illumination source, home-made LED was used.

Experiments were conducted at screen printed electrodes (Ital-Sens IS-C) which were purchased from PalmSens. The working and counter electrode consist of carbon, the reference electrode consists of silver. The working electrode was first washed with a 5 µL drop of 80% ethanol solution and dried at room temperature. Then, 4.5 mg of each catalyst was mixed with 60 µL of 5% nafion solution and diluted with 390 µL of distilled water. To modify the electrode, 5 µL of this suspension was drop casted on the working electrode and dried at room temperature for approximately 1 h. The measurements were performed in 80 µL solution containing 1 mM $K_3Fe(CN)_6$, 1 mM $K_4Fe(CN)_6$ and 150 mM NaCl. As a reference, one measurement was done on a bare working electrode.

2.5.6 Diffuse-reflectance UV/Vis spectra for bandgap determination

The optical bandgaps of all the samples are determined from Tauc plots of the $(\alpha hv)^{1/2}$ as a function of photonic energy (**Figure 2.22**). The band gaps of APC-C_3N_4, AB-C_3N_4, *p*-TFAB-C_3N_4 and commercial C_3N_4 are estimated to be 2.87, 2.87, 2.86 and 2.82 eV, respectively. Therefore, electronic structural information for all arylated PCNs are gathered (**Figure 2.24**).

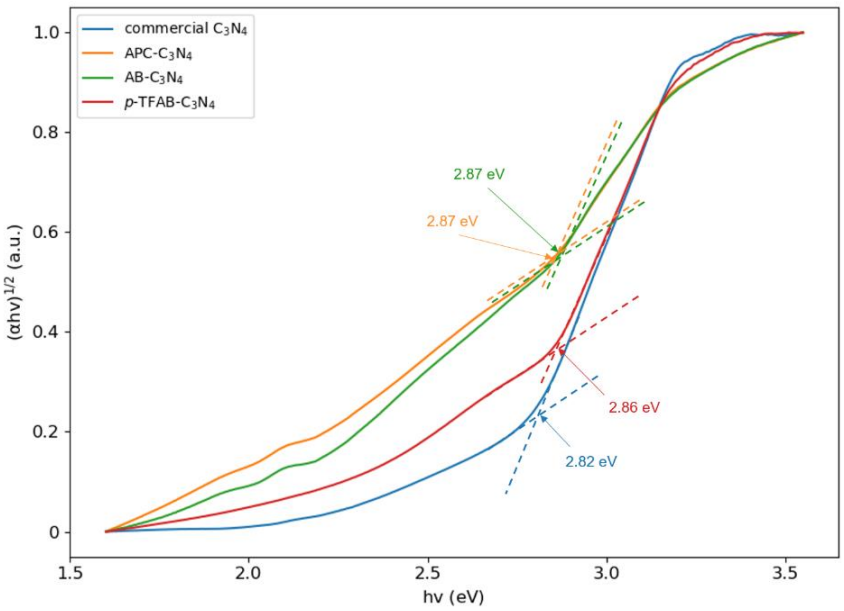

Figure 2.22. Tauc plots of all arylated PCNs employed to determine the band gaps.

2.5.7 Mott–Schottky measurements

Thin film electrodes were prepared by electrophoretic deposition (EPD) method reported elsewhere.[62] Typically, 23 mg of the C_3N_4 derivative was mixed with 7 mg of iodine in 30 mL acetone under ultrasonication for 15 min. Two pre-cleaned fluorine-doped tin oxide (FTO) glasses were immersed vertically in the aforementioned suspension with 1 cm in distance. 50 V potential was subsequently applied for 5 min to allow the deposition of the particles on the FTO, which was then dried in air.

Mott-Schottky experiments were performed in a three-electrode configuration, with as-obtained thin film electrode as working electrode, Pt electrode as counter electrode, and 1 M Ag/AgCl electrode as reference electrode, respectively. 0.1 M potassium phosphate (KP_i) solution degassed by N_2 was used as electrolyte. The measurements were conducted by using a Gamry INTERFACE 1010T Potentiostat/Galvanostat/ZRA workstation in dark, at AC amplitude of 5 mV and a frequency of 10 Hz.

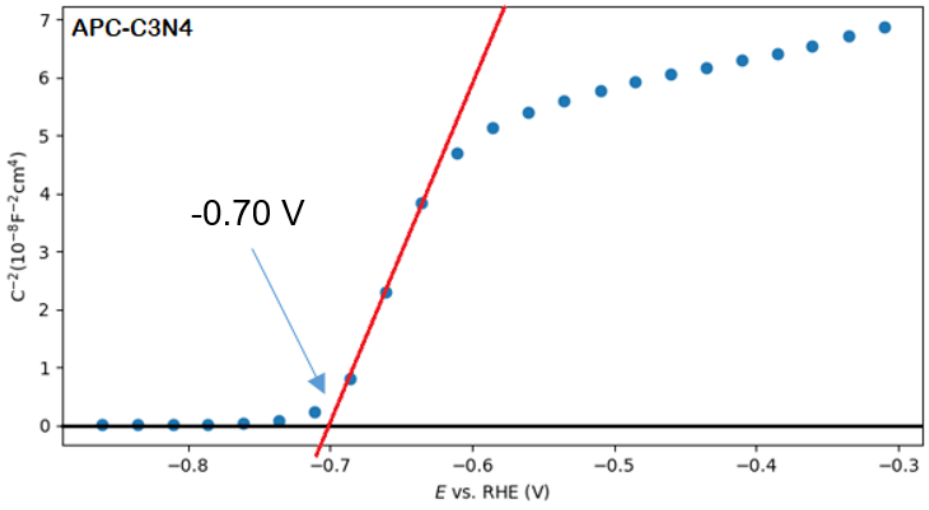

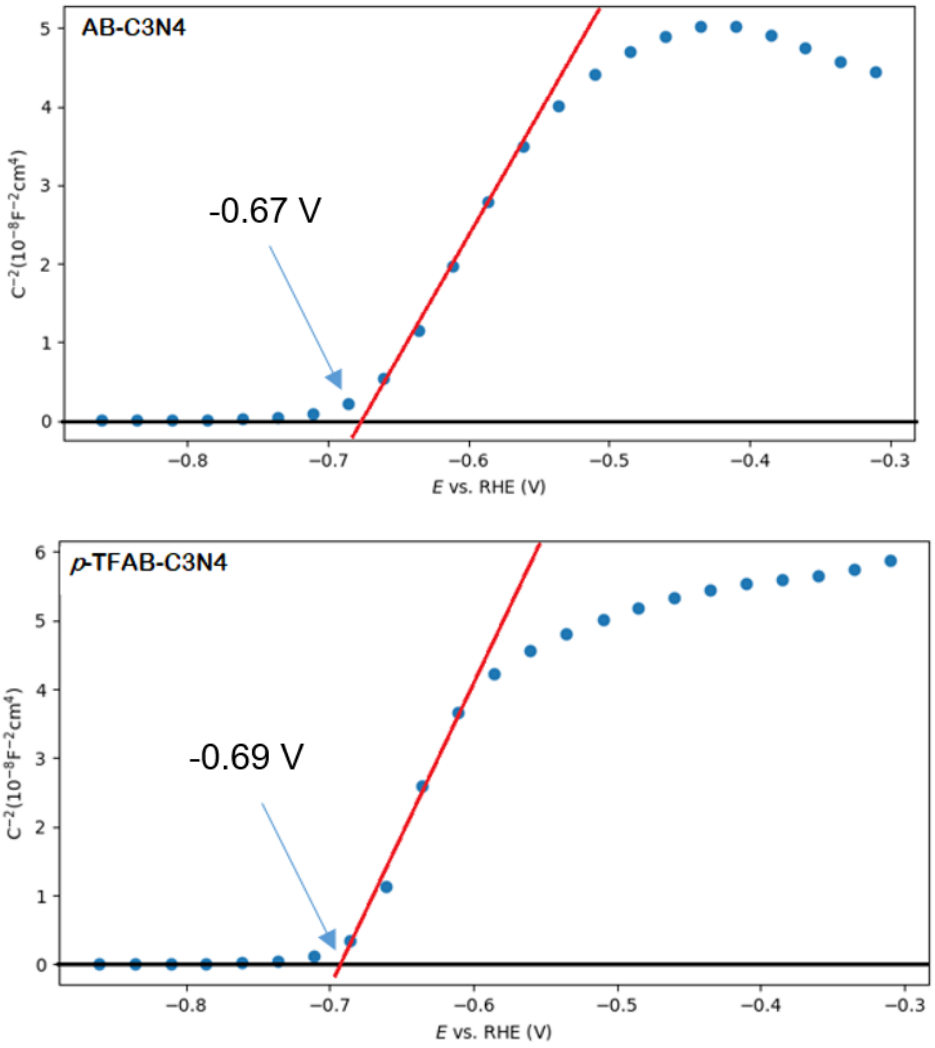

Figure 2.23. Electrochemical Mott-Schottky plots of modified C_3N_4.

The positive slope of the Mott-Schottky curve indicates the n type nature of the sample. All the recorded potentials were converted to the potentials vs. reversible hydrogen electrode (RHE) via Nernst equation ($E_{RHE} = E^{\theta}_{Ag/AgCl} + 0.059\ pH + E_{Ag/AgCl}$). Therefore, the flat band potential (E_{fb}) of *p*-TFAB-C_3N_4 is determined to be -0.69 V *vs.* RHE based on the intersection between Mott–Schottky plot and the baseline. It is generally considered that the bottom potential of conduction band (CB) for an n type

semiconductor is approximately 0.2 V more negative than the E_{fb};[63] the E_{CB} is therefore estimated to be ca. -0.89 V *vs.* RHE.

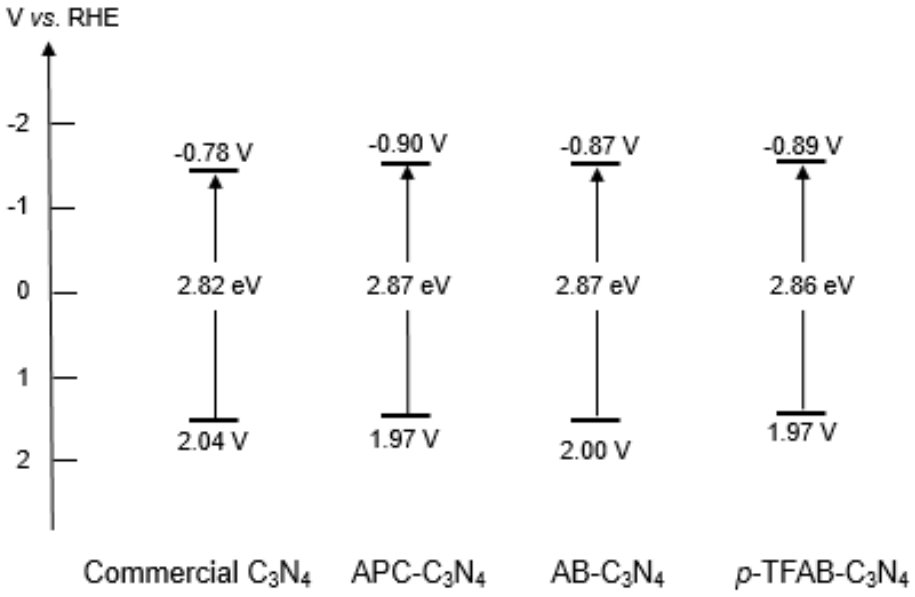

Figure 2.24. Schematic illustration of the electronic energy levels.

2.5.8 Solid-State NMR

Magic-angle-spinning (MAS) NMR experiments were performed at a magnetic field of 14.1 T (Larmor frequencies of 600.12, 150.92, and 60.83 MHz for ^{1}H, ^{13}C, and ^{15}N, respectively) on a Bruker Avance-III spectrometer. The ^{1}H MAS NMR spectrum was acquired using a 1.3 mm probehead and a 60 kHz MAS rate. This acquisition involved a use of a rotor-synchronized, double-adiabatic spin-echo sequence with a 90° excitation pulse of 1.25 μs followed by a pair of 50.0 μs tanh/tan short high-power adiabatic pulses (SHAPs) with 5 MHz frequency sweep.[64-65] All pulses operated at the nutation frequency of 200 kHz, and 128 signal transients were acquired using a relaxation delay of 5 s. Cross-polarization (CP) ^{1}H-^{13}C and ^{1}H-^{15}N CPMAS NMR spectra were recorded using a 7 mm probehead with a 7 kHz MAS rate and 65 kHz spinal64 proton decoupling. For ^{1}H-^{13}C CPMAS acquisition Hartmann-Hahn matched radiofrequency

fields were applied for a contact interval of 1.5 ms and 2048 signal transients were collected using a relaxation delay of 5 s. The ^{1}H-^{15}N CPMAS acquisitions involved contact intervals of 2 and 4 ms, and 16384 scans collected with relaxation time of 5 s. Chemical shifts were referenced with respect to TMS (^{1}H, ^{13}C) and nitromethane (^{15}N). Experiments were performed at natural isotope abundance.

2.5.9 Electron Spin Resonance (ESR) analysis

Unless otherwise stated, samples were prepared in capillaries and sealed under an anhydrous N_2 atmosphere. Room temperature continuous wave (cw) ESR measurements were carried out using a Bruker ESP300E spectrometer equipped with a rectangular cavity with optical access. The ESR spectra were recorded at X-band microwave frequency (~ 9.44 GHz) in cw mode using 5 mW micro-wave power, 0.05 mT modulation amplitude and 100 kHz modulation frequency. A solid state 447 nm laser operating at ~ 200 mW was used for illumination experiments. The ESR spectra were simulated with Matlab2018b using the EasySpin-6.0 module.[66]

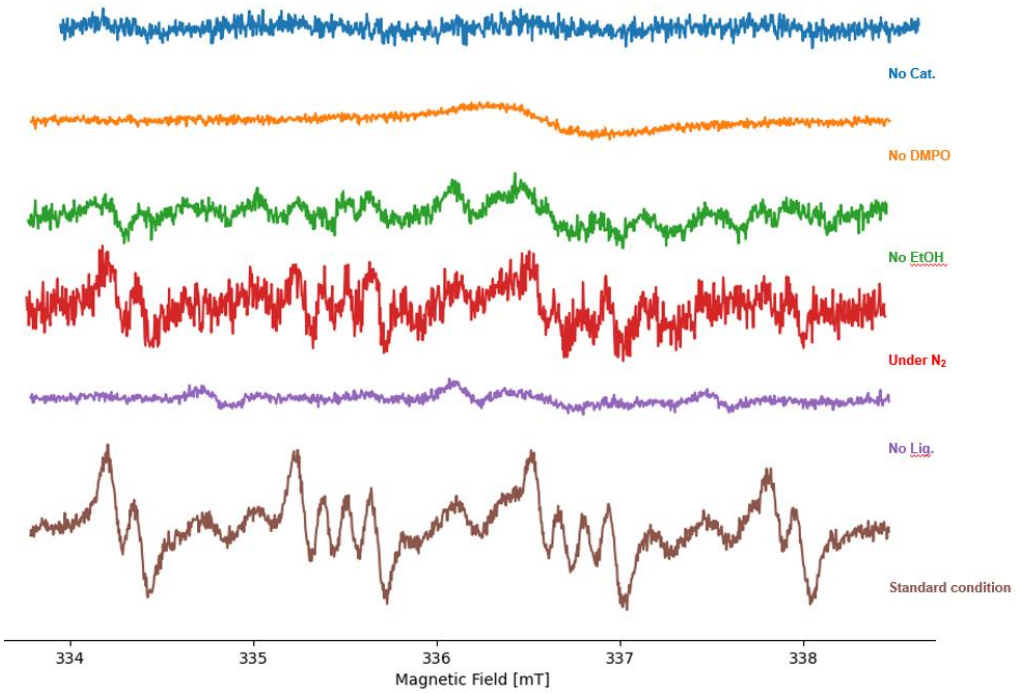

Figure 2.25. Time-dependent ESR measurements at room temperature for reaction mixture (top). ESR measurements at room temperature for reaction mixture in the absence of each parameter (down).

2.5.10 On-Off reaction

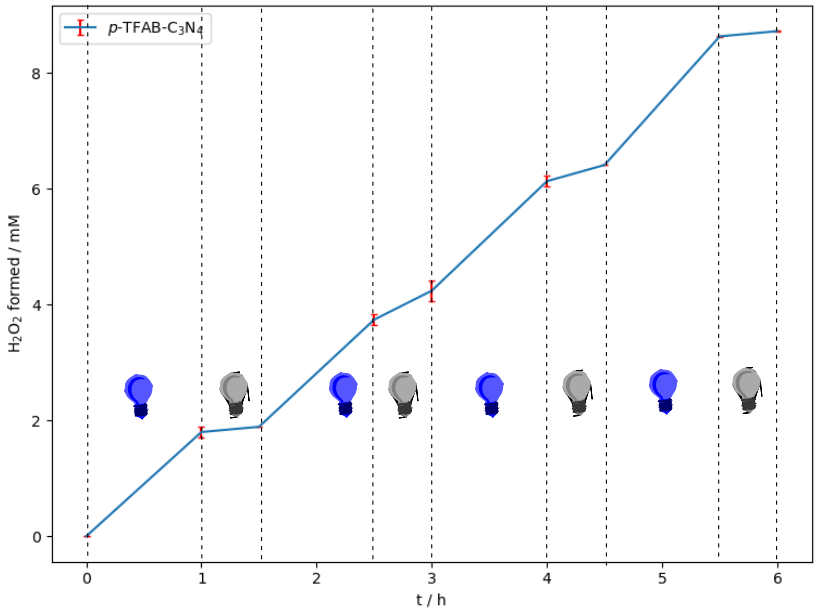

Time (h)	Measurement I (mM)	Measurement II (mM)	Average (mM)
1	1.89	1.71	1.80
1.5	1.89	1.89	1.89
2.5	3.83	3.64	3.74
3	4.42	4.06	4.24
4	6.22	6.04	6.13
4.5	6.41	6.40	6.41
5.5	8.63	8.62	8.63
6	8.72	8.71	8.72

Figure 2.26. Measurements of On-Off reaction.

2.5.11 Cycling test of *p*-TFAB-C_3N_4

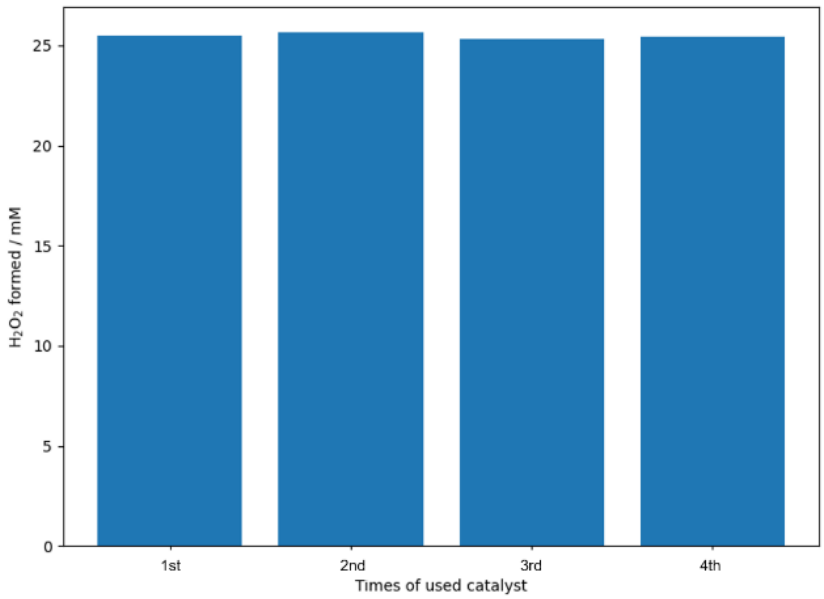

Figure 2.27. Recycling test of *p*-TFAB-C_3N_4.

2.5.12 Apparent quantum yield (AQY) measurement

The light intensity of LED (λ = 456 nm) was 0.0076 W/cm^2. AQY for photocatalytic production of H_2O_2 was calculated using the following formula:[48]

$$\eta = \frac{N_e}{N_p} \times 100\ \% = \frac{2 \times M \times N_a}{\frac{S \times P \times t}{h \times \frac{c}{\lambda}}} \times 100\ \% = \frac{2 \times M \times N_a \times h \times c}{S \times P \times t \times \lambda} \times 100\ \%$$

Where, M represents the amount of formed H_2O_2 (mol), N_a is the Avogadro constant 6.02x10^{23} mol^{-1}, h is the Planck constant 6.63x10^{-34} J·s, c is the light speed 3x10^8 m·s^{-1}, S is the irradiation area (cm^2), P is the light intensity (W·cm^{-2}), t is irradiation time (s), λ is the wavelength of light (m)

2.5.13 Computational Chemistry

Model Building. To gain an atomic-level understanding of the various steps of possible reaction mechanisms leading to the formation of the final H_2O_2 product, we complemented the experimental characterization with a multiscale/level computational protocol, which could simulate dynamically, at the atomic resolution, the complex environment surrounding the catalyst and the evolution of all the species present there. To this aim, a simplified representative molecular model of the polymeric carbon nitrides photocatalyst was built by assembling five melem units according to the scheme shown in **Figure 1**. Then, one of the NH_2 groups of this basic structure was replaced with the *p*-TFAB fragment to compare the catalytic behavior of these two different compositions.

First, the two models were optimized at the DFT level using both the M06-2X functional and 6-31(d) basis set [67] and the Perdew-Burke-Ernzerhof (PBE) functional [68] with the D2-Grimme correction,[69] which accounts for dispersion forces, and plane waves UltraSoft (US) pseudopotentials [70] (Quantum Espresso),[71] to check the reliability of the functional performance.

Both optimizations produced very similar planar structures, which were then employed to prepare more representative supramolecular arrangements in a complex environment such as the one considered in this investigation.

ReaxFF Molecular Dynamics Simulations. To identify a variety of O_2 adsorption/entrapment modes and reaction mechanisms, eight sheets were assembled randomly in parallel and T-shaped orientations, one relative to the other ones, and surrounded by solvent molecules, namely ethanol and water, in an 8 to 1 ratio, which is very close to the ideal experimental finding. The simulation box (approximately 38×49x40 $Å^3$) contained 550 ethanol and 70 water molecules and was replicated in all directions (PBC).

Reactive molecular dynamics simulations (RMD - ReaxFF methodology),[13b] based on a force field used earlier for these types of materials,[14b] were carried out in the NVT ensemble at ambient temperature and pressure (300 K and 1 atm) to equilibrate the systems and prepare them for the subsequent O_2 reduction simulations. Indeed, representative structures were extracted at the end of a 250 ps production phase and used as starting configurations of the catalyst-solvent environment in the reduction of O_2 to H_2O_2. In all the RMD runs, the time step was set to 0.2 fs, and the temperature was controlled through the Hoover-Nosé thermostat with a relaxation constant of 0.1 ps. RMDs were carried out with the ReaxFF code implemented in the Amsterdam Density Functional (ADF)/ReaxFF package.[72] The O_2 molecules (100 in all) were injected in the two catalyst+mixed solvent boxes in the proximity of the catalyst (to speed up the simulation times of adsorption/reaction), and RMD simulations were carried out for hundreds of picoseconds to disclose possible reaction mechanisms, the most probable reaction sites and the role played by the mixed solvent.

During the dynamics, system configurations were collected every 0.02 ps, and the evolution of the species was examined every 0.01 ps to estimate the efficiency of the catalyst+solvent combination and to identify the various steps of the H_2O_2 formation. The total simulation time was approximately 300 ps. No constraints were imposed on the systems, and all their components could relax and explore different locations inside the simulation box.

Several reaction mechanisms were identified, and the corresponding configurations were collected, size-reduced to the essential components, and used as starting arrangements in the quantum mechanics calculations.

The analysis of the RMD trajectories was focused on the last 20 ps (1000 configurations) to extract information on the O_2 and solvent relative locations, considering mainly atom-atom distance distribution (RDFs) and

spatial distribution functions (SDF). The H_2O_2 production was also monitored as a function of the simulation time.

Quantum Chemistry Calculations. As done in a previous investigation,[15] quantum mechanics calculations were carried out to reveal the details of the reaction mechanisms, such as the Minimum Energy Paths, transition states, energy barriers, and final products. The one-electron wave functions were expanded in a plane-wave basis set up with a kinetic energy cutoff of 40 Ry (400 Ry for the density). All the calculations were spin-unpolarized, and single-particle wave functions were calculated through Gaussian smearing of about 0.002 Ry. The Brillouin zone sampling was restricted to the gamma point. The nudged-elastic-band (NEB) method [73] was employed to find energy profiles along possible reaction paths (MEP), and the saddle states between the relaxed initial and final configurations along the reaction coordinate. The energy barriers were estimated considering 25 intermediate images between the identified local minima, and a convergence criterion of 0.05 eV $Å^{-1}$for the force orthogonal to the path was defined.

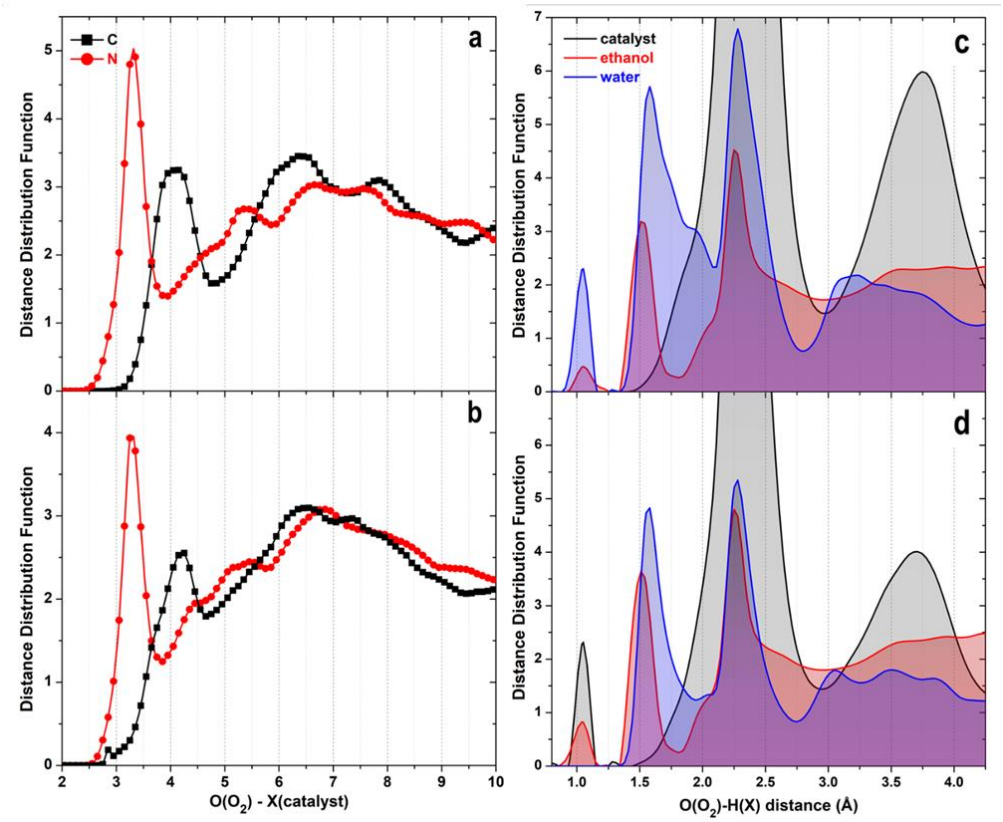

Figure 2.28. Distance distribution functions between the O_2 atoms and the C/N atoms of the non-functionalized (a) and *p*-TFAB functionalized (b) catalyst. Distance distribution functions between the O_2 atoms and the hydrogen atoms of the catalyst, ethanol, and water for the non-functionalized (c) and *p*-TFAB functionalized (d) materials.

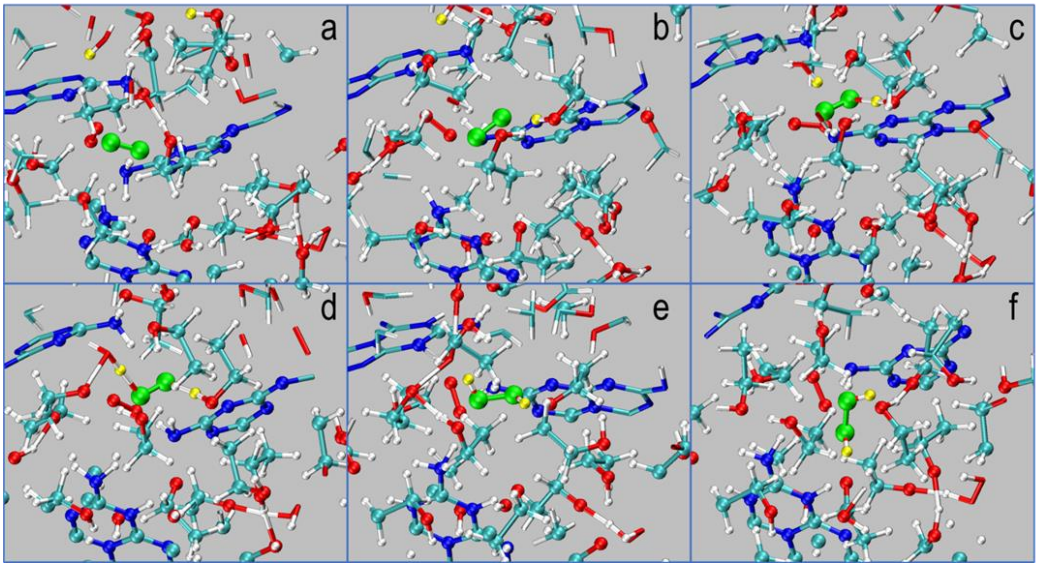

Figure 2.29. Sequential snapshots (ball and stick models) illustrating a few steps of the first reaction mechanism shown in **Figure 10a**. The hydrogens released to the target O_2 molecule (green spheres) are yellow and come from water and an ethanol molecule.

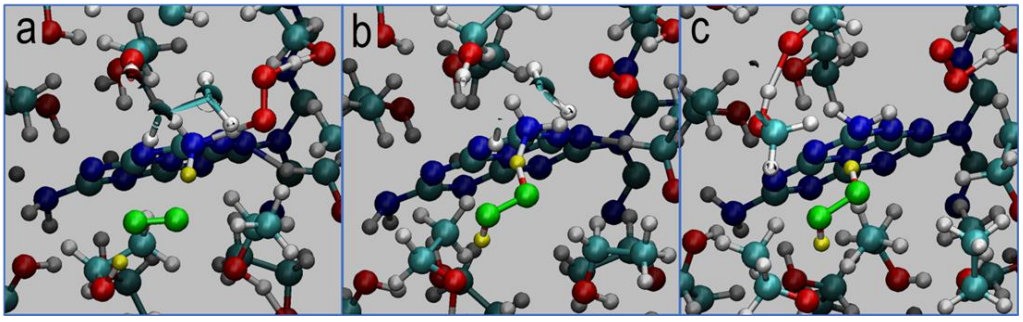

Figure 2.30. Sequential snapshots (ball and stick models) illustrating the main steps of the second reaction mechanism shown in **Figure 10b**. The hydrogens released to the target O_2 molecule (green spheres) are yellow and come from an edge NH_2 group (protonated) of the catalyst and an ethanol molecule.

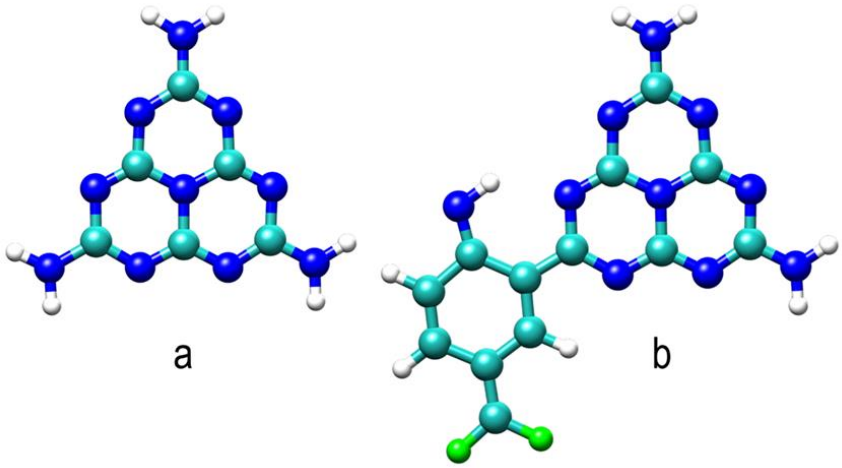

Figure 2.31. Reduced models of the catalysts. (a) undoped and (b) *p*-TFAB-doped system. C, N, H, F atoms are cyan, blue, white, and green, respectively.

2.5.14 Simulation of the UV/Visible Spectrum of *p*-TFAB

By using the time-dependent extension of DFT (TDDFT) at the B3LYP/6-31G(d) level of theory in g09 package,[67] we simulated the UV/Vis spectrum of the *p*-TFAB-doped system (15 states), and carried out excited-state geometry optimization.

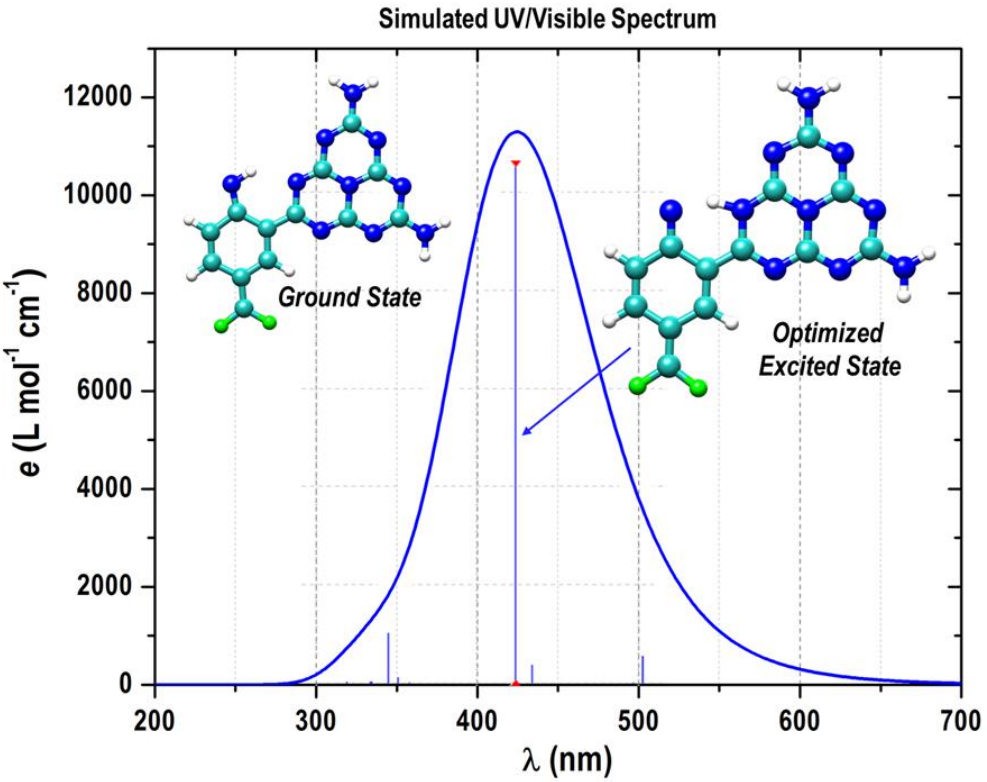

Figure 2.32. Simulated UV/Vis absorption spectrum of *p*-TFAB-C_3N_4 with the calculated excitation wavelengths (vertical lines).

Chemical Shifts - DFT calculations on a reduced model system

Cartesian coordinates (in Å) of the model used for ^{19}F chemical shift calculations. The $CFCl_3$ molecule was used as a chemical shift reference (coordinates provided below as well).[54]

Cartesian coordinates

C	-0.437397	1.356014	0.000036
C	-1.654987	0.542346	0.000201
C	-1.627742	-0.812230	0.000221
C	-0.355900	-1.509870	0.000077
C	0.865902	-0.726612	-0.000089
C	0.849866	0.633436	-0.000113
C	-0.316055	-2.868201	0.000100
N	-0.419416	2.660484	0.000013
F	-1.386539	-3.660045	0.000241
F	0.798236	-3.595376	-0.000015
H	-1.384564	3.018380	0.000129
H	-2.610145	1.072001	0.000312
H	-2.550527	-1.391294	0.000347
H	1.818485	-1.256263	-0.000201
C	2.110092	1.447399	-0.000285
H	2.997417	0.802226	-0.000395
H	2.141706	2.109766	0.876572
H	2.141477	2.109750	-0.877162

$CFCl_3$

F	-0.794588	1.696741	0.172498
C	-0.342799	0.428887	0.008437

Cl	1.443147	0.459818	0.012162
Cl	-0.952633	-0.191664	-1.551438
Cl	-0.952845	-0.569171	1.358341

2.6 References

1. a) Maeda, K.; Teramura, K.; Lu, D.; Takata, T.; Saito, N.; Inoue, Y.; Domen, K. Photocatalyst releasing hydrogen from water. *Nature*, **2006**, *440*, 295; b) Kudo, A.; Miseki, Y. Heterogeneous photocatalyst materials for water splitting. *Chem. Soc. Rev.*, **2009**, *38*, 253—278; c) Walter, M. G.; Warren, E. L.; McKone, J. R.; Boettcher, S. W.; Mi, Q.; Santori, E. A.; Lewis, N. S. Solar water splitting cells. *Chem. Rev.*, **2010**, *110*, 6446—6473.

2. a) Vallejo, F. C.-; Tymoczko, J.; Colic, V.; Vu, Q. H.; Pohl, M. D.; Morgenstern, K.; Loffreda, D.; Sautet, P.; Schuhmann, W.; Albiter, Bandarenka, A. S. Finding optimal surface sites on heterogeneous catalysts by counting nearest neighbors. *Science*, **2015**, *350*, 185—189; b) Van Santen, R. A. Complementary Structure Sensitive and Insensitive Catalytic Relationships. *Acc. Chem. Res.* **2009**, *42*, 57—66; c) Lee, I.; Delbecq, F.; Morales, R. M. A.; Zaera, F. Tuning selectivity in catalysis by controlling particle shape. *Nat. Mater.*, **2009**, *8*, 132 — 138; d) Stamenkovic, V. R.; Fowler, B.; Mun, B. S.; Wang, G.; Ross, P. N.; Lucas, C. A.; Marković, N. M. Improved Oxygen Reduction Activity on Pt3Ni(111) via Increased Surface Site Availability. *Science*, **2007**, *315*, 493—497; e) Behrens, M.; Studt, F.; Kasatkin, I.; Kühl, S.; Hävecker, M.; Pedersen, F. A.-; Zander, S.; Girgsdies, F.; Kurr, P.; Kniep, B.-L.; Tovar, M.; Fischer, R. W.; Nørskov, J. K.; Schlögl, R. The Active Site of Methanol Synthesis over Cu/ZnO/Al2O3 Industrial Catalysts. *Science*, **2012**, *336*, 893—897.

3. a) Wang, X.; Maeda, K.; Thomas, A.; Takanabe, K.; Xin, G.; Carlsson, J. M.; Domen, Antonietti, K. M. A metal-free polymeric photocatalyst for hydrogen production from water under visible light. *Nat. Mater*. **2009**, *8*, 76—80; b) Maeda, K.; Wang, X. C.; Nishihara, Y.; Lu, D. L.; Antonietti, M.; Domen, K. Photocatalytic Activities of Graphitic Carbon Nitride Powder for Water Reduction and Oxidation under Visible Light. *J.*

Phys. Chem. C, **2009**, *113*, 4940—4947; c) Zhang, J. S.; Sun, J. H.; Maeda, K.; Domen, K.; Liu, P.; Antonietti, M.; Fu, X. Z.; Wang, X. C. Sulfur-mediated synthesis of carbon nitride: Band-gap engineering and improved functions for photocatalysis. *Energy Environ. Sci.* **2011**, *4*, 675—678; d) Zhang, J.; Zhang, G.; Chen, X.; Lin, S.; Mçhlmann, L.; Dołęga, G.; Lipner, G.; Antonietti, M.; Blechert, S.; Wang, X. C. Co-Monomer Control of Carbon Nitride Semiconductors to Optimize Hydrogen Evolution with Visible Light. *Angew. Chem. Int. Ed*. **2012**, *51*, 3183—3187.

4. a) Giusto, P.; Arazoe, H.; Cruz, D.; Lova, P.; Heil, T.; Aida, T.; Antonietti, M. Boron Carbon Nitride Thin Films: From Disordered to Ordered Conjugated Ternary Materials. *J. Am. Chem. Soc.* **2020**, *142*, *49*, 20883—20891; b) Giusto, P.; Kumru, B.; Zhang, J.; Rothe, R.; Antonietti, M. Let a Hundred Polymers Bloom: Tunable Wetting of Photografted Polymer-Carbon Nitride Surfaces. *Chem. Mater*. **2020**, *32*, 7284—7291; c) Giusto, P.; Cruz, D.; Heil, T.; Arazoe, H.; Lova, P.; Aida, T.; Comoretto, D.; Patrini, M.; Antonietti, M. Shine Bright Like a Diamond: New Light on an Old Polymeric Semiconductor. *Adv. Mater.* **2020**, *32*, 1908140; d) Xia, Y.; Tian, Z.; Heil, T.; Meng, A.; Cheng, B.; Cao,S.; Yu, J.; Antonietti, M. Highly Selective CO2 Capture and Its Direct Photochemical Conversion on Ordered 2D/1D Heterojunctions. *Joule*, **2019**, *3*, 2792—2805; e) Li, A.; Cao, Q.; Zhou, G.; Schmidt, B. V.; Zhu, W.; Yuan, X.; Huo, H.; Gong, J.; Antonietti, M. Three-Phase Photocatalysis for the Enhanced Selectivity and Activity of CO2 Reduction on a Hydrophobic Surface. *Angew. Chem., Int. Ed*., **2019**, *58*, 14549—14697; f) Das, S.; Murugesan, K.; Rodríguez, G. J. V.; Kaur, J.; Barham, J. P.; Savateev, A.; Antonietti, M.; König, B. Photocatalytic (Het)arylation of C(sp3)–H Bonds with Carbon Nitride. *ACS Catal*. **2021**, *11*, 1593—1603; g) Zhang, Y.; Hatami, N.; Lange, N.; Schilling, W.; Ronge, E.; Jooss, C.; Das, S. A metal-free heterogeneous photocatalyst

for the selective oxidative cleavage of C—C bonds in aryl olefins via harvesting direct solar energy. *Green Chem*. **2020**, *22*, 4516—4522.

5. a) Mohamed, M. A.; Zain, M.; Minggu, L. J.; Kassim, M. B.; Amin, N. A. S.; Salleh, W.; Salehmin, M. N. I.; Nasir, M. F. M.; Hir, Z. A. M. Constructing bio-templated 3D porous microtubular C-doped g-C3N4 with tunable band structure and enhanced charge carrier separation. *Appl. Catal. B*, **2018**, *236*, 265—279; b) Xu, Q.; Zhang, L.; Yu, J.; Wageh, S.; Al-Ghamdi, A. A.; Jaroniec, M. Direct Z-scheme photocatalysts: Principles, synthesis, and applications. *Mater. Today*, **2018**, *21*, 1042—1063; c) Liao, G.; Gong, Y.; Zhang, L.; Gao, H.; Yang, G.-J.; Fang, B. Semiconductor polymeric graphitic carbon nitride photocatalysts: the "holy grail" for the photocatalytic hydrogen evolution reaction under visible light. *Energy Environ. Sci*. **2019**, *12*, 2080—2147; d) Ou, H.; Yang, P.; Lin, L.; Anpo, M.; Wang, X. Carbon Nitride Aerogels for the Photoredox Conversion of Water. *Angew. Chem.* **2017**, *56*, 10905—10910; e) Hou, H.; Zeng, X.; Zhang, X. Production of Hydrogen Peroxide by Photocatalytic Processes. *Angew. Chem., Int. Ed*., **2020**, *59*, 17356—17376.

6. a) Pei, Z.; Ding, L.; Hu, J.; Weng, S.; Zheng, Z.; Huang, M.; Liu, P. Defect and its dominance in ZnO films: A new insight into the role of defect over photocatalytic activity. *Appl. Catal. B*, **2013**, *142*, 736—743; b) Xiong, J.; Di, J.; Xia, J.; Zhu, W.; Li, H. Surface Defect Engineering in 2D Nanomaterials for Photocatalysis. *Adv. Funct. Mater*. **2018**, *28*, 1801983; c) Li, Y.; Ho, W.; Lv, K.; Zhu, B.; Lee, S. C. Carbon vacancy-induced enhancement of the visible light-driven photocatalytic oxidation of NO over g-C3N4 nanosheets. *Appl. Surf. Sci*. **2018**, *430*, 380—389.

7. a) Goclon, J.; Winkler, K. Computational insight into the mechanism of O2 to H2O2 reduction on amino-groups-containing g-C3N4. *Appl. Surf. Sci*. **2018**, *462*, 134—141; b) Li, X.; Zhang, J.; Zhou, F.; Zhang, H.; Bai, J.;

Wang, Y.; Wang, H. Preparation of N-vacancy-doped g-C3N4 with outstanding photocatalytic H2O2 production ability by dielectric barrier discharge plasma treatment. *Chin. J. Catal*. **2018**, *39*, 1090—1098; c) Shi, L.; Yang, L.; Zhou, W.; Liu, Y.; Yin, L.; Hai, X.; Song, H.; Ye, J. Photoassisted Construction of Holey Defective g-C3N4 Photocatalysts for Efficient Visible-Light-Driven H2O2 Production. *Small*, **2018**, *14*, 1703142.

8. a) Cai, J.; Huang, J.; Wang, S.; Iocozzia, J.; Sun, Z.; Sun, J.; Yang, Y.; Lai, Y.; Lin, Z. Crafting Mussel-Inspired Metal Nanoparticle-Decorated Ultrathin Graphitic Carbon Nitride for the Degradation of Chemical Pollutants and Production of Chemical Resources. *Adv. Mater*. **2019**, *31*, 1806314; b) Bellardita, M.; García-López, E. I.; Marcì, G.; Krivtsov, I.; García, J. R.; Palmisano, L. Selective photocatalytic oxidation of aromatic alcohols in water by using P-doped g-C3N4. *Appl. Catal. B*, **2018**, *220*, 222—233; c) Hu, J.; Zhang, P.; An, W.; Liu, L.; Liang, Y.; Cui, W. In-situ Fe-doped g-C3N4 heterogeneous catalyst via photocatalysis-Fenton reaction with enriched photocatalytic performance for removal of complex wastewater. *Appl. Catal. B*, **2019**, *245*, 130—142; d) Hu, S.; Qu, X.; Li, P.; Wang, F.; Li, Q.; Song, L.; Zhao, Y.; Kang, X.Photocatalytic oxygen reduction to hydrogen peroxide over copper doped graphitic carbon nitride hollow microsphere: The effect of Cu(I)-N active sites. *Chem. Eng. J*. **2018**, *334*, 410—418.

9. a) Qu, X.; Hu, S.; Bai, J.; Li, P.; Lu, G.; Kang, X. Synthesis of band gap-tunable alkali metal modified graphitic carbon nitride with outstanding photocatalytic H2O2 production ability via molten salt method. *J. Mater. Sci. Technol*. **2018**, *34*, 1932—1938; b) Zhang, C.; Bai, J.; Ma, L.; Lv, Y.; Wang, F.; Zhang, X.; Yuan, X.; Hu, S. Synthesis of halogen doped graphite carbon nitride nanorods with outstanding photocatalytic H2O2 production ability via saturated NH4X (X = Cl, Br) solution-hydrothermal post-treatment. *Diamond Relat. Mater*. **2018**, *87*,

215—222; c) Kim, S.; Moon, G.-h.; Kim, H.; Mun, Y.; Zhang, P.; Lee, J.; Choi, W. Selective charge transfer to dioxygen on KPF6-modified carbon nitride for photocatalytic synthesis of H2O2 under visible light. *J. Catal*. **2018**, *357*, 51—58.

10. a) Zhao, S.; Guo, T.; Li, X.; Xu, T.; Yang, B.; Zhao, X. Carbon nanotubes covalent combined with graphitic carbon nitride for photocatalytic hydrogen peroxide production under visible light. *Appl. Catal. B*, **2018**, 224, 725—732; b) Tasis, D.; Tagmatarchis, N.; Bianco, A.; Prato, M. Chemistry of Carbon Nanotubes. *Chem. Rev*. **2006**, *106*, 1105—1136; c) Zhao, S.; Zhao, X. Polyoxometalates-derived metal oxides incorporated into graphitic carbon nitride framework for photocatalytic hydrogen peroxide production under visible light. *J. Catal*. **2018**, *366*, 98 — 106; d) Kofuji, Y.; Ohkita, S.; Shiraishi, Y.; Sakamoto, H.; Ichikawa, S.; Tanaka, S.; Hirai, T. Mellitic Triimide-Doped Carbon Nitride as Sunlight-Driven Photocatalysts for Hydrogen Peroxide Production. *ACS Sustainable Chem. Eng*. **2017**, *5*, 6478—6485; e) Yang, L.; Dong, G.; L. Jacobs, D.; Wang, Y.; Zang, L.; Wang, C. Two-channel photocatalytic production of H2O2 over g-C3N4 nanosheets modified with perylene imides. *J. Catal*. **2017**, *352*, 274—281.

11. a) Ma, Z.; Lu, C.; Chen, J.; Rokicinska, A.; Kustrowski, P.; Coridan, R.; Dronskowski, R.; Slabon, A.; Jaworski, A. CeTiO2N oxynitride perovskite : paramagnetic 14N MAS NMR without paramagnetic shifts. *Z. Naturforsch*, **2021**, *76*, 275—280; b) Chen, Z.; Jaworski, A.; Chen, J.; Budnyak, T.; Szewczyk, I.; Rokicinska, A.; Dronskowski, R.; Hedin, N.; Kuśtrowski, P.; Slabon, A. Graphitic nitrogen in carbon catalysts is important for the reduction of nitrite as revealed by naturally abundant 15N NMR spectroscopy. *Dalton Trans.*, **2021**, *50*, 6857—6866.

12. a) Fang, X.; Mao, J.; Levin, E. M.; Rohr, K. S.- Nonaromatic Core−Shell Structure of Nanodiamond from Solid-State NMR Spectroscopy. *J. Am. Chem. Soc*. **2009**, *131*, 1426—1435; b) Rossini, A. J.; Zagdoun, A.; Lelli, M.; Canivet, J.; Aguado, S.; Ouari, O.; Tordo, P.; Rosay, M.; Maas, W. E.; Copéret, C.; Farrusseng, D.; Emsley, L.; Lesage, A. Dynamic Nuclear Polarization Enhanced Solid-State NMR Spectroscopy of Functionalized Metal–Organic Frameworks. *Angew. Chem., Int. Ed*., **2012**, *51*, 123—127; c) J. Rossini, A.; Widdifield, C. M.; Zagdoun, A.; Lelli, M.; Schwarzwälder, M.; Copéret, C.; Lesage, A.; Emsley, L. Dynamic Nuclear Polarization Enhanced NMR Spectroscopy for Pharmaceutical Formulations. *J. Am. Chem. Soc*. **2014**, *136*, 2324—2334; d) Szewczyk, I.; Rokicińska, A.; Michalik, M.; Chen, J.; Jaworski, A.; Aleksis, R.; Pell, A. J.; Hedin, N.; Slabon, A.; Kuśtrowski, P. Electrochemical Denitrification and Oxidative Dehydrogenation of Ethylbenzene over N-doped Mesoporous Carbon: Atomic Level Understanding of Catalytic Activity by 15N NMR Spectroscopy. *Chem. Mater.* **2020**, *32*, 7263—7273; e) Wei, Z.; Becwar, S. M.; Chmelka, B. F.; Sautet, P. Atomic Environments in N-Containing Graphitic Carbon Probed by First-Principles Calculations and Solid-State Nuclear Magnetic Resonance. *J. Phys. Chem. C,* **2021**, *125*, 8779—8787.

13. a) van Duin, A. C. T.; Dasgupta, S.; Lorant , F.; Goddard III, W. A. ReaxFF: A Reactive Force Field for Hydrocarbons. *J. Phys. Chem. A*, **2001**, *105*, 9396—9409; b) Chenoweth, K.; van Duin, A. C. T.; Goddard III, W. A. ReaxFF Reactive Force Field for Molecular Dynamics Simulations of Hydrocarbon Oxidation. *J. Phys. Chem. A*, **2008**, *112*, 1040—1053.

14. a) Ma, Y.; Yang, Y.; Lu, C.; Wen, X.; Liu, X.; Wu, S.; Lu, K.; Yin, J. Enhanced thermal resistance of carbon/phenolic composites by addition of novel nano-g-C3N4. *Compos. Sci. Technol.*, **2019**, *180*, 60—70; b) de Sousa, J. M.; Botari, T.; Perim, E.; Bizao, R. A.; Galvao, D. S.

Mechanical and structural properties of graphene-like carbon nitride sheets. *RSC Adv.*, **2016**, *6*, 76915—76921.

15. De Santi, A.; Monti, S.; Barcaro, G.; Zhang, Z.; Barta, K.; Deuss, P. J. New Mechanistic Insights into the Lignin β-O-4 Linkage Acidolysis with Ethylene Glycol Stabilization Aided by Multilevel Computational Chemistry. *ACS Sus. Chem. Eng.* **2021**, *9*, 2388—2399.

16. a) Campos-Martin, J. M.; Blanco-Brieva, G.; Fierro, J. L. Hydrogen Peroxide Synthesis: An Outlook beyond the Anthraquinone Process. *Angew. Chem., Int. Ed*. **2006**, *45*, 6962—6984; b) Ksibi, M. Chemical oxidation with hydrogen peroxide for domestic wastewater treatment. *Chem. Eng. J*. **2006**, *119*, 161—165; c) Gurram, R. N.; Al-Shannag, M.; Lecher, N. J.; Duncan, S. M.; Singsaas, E. L.; Alkasrawi, M. Bioconversion of paper mill sludge to bioethanol in the presence of accelerants or hydrogen peroxide pretreatment. *Bioresour. Technol*. **2015**, *192*, 529—539; d) Zhan, W.; Ji, L.; Ge, Z.-m.; Wang, X.; Li, R.-t. A continuous-flow synthesis of primary amides from hydrolysis of nitriles using hydrogen peroxide as oxidant. *Tetrahedron*, **2018**, *74*, 1527—1532.

17. https://www.grandviewresearch.com/industry-analysis/hydrogen-peroxide-market (accessed 2021-07-06).

18. a) Edwards, J. K.; Hutchings, G. J. Palladium and Gold–Palladium Catalysts for the Direct Synthesis of Hydrogen Peroxide. *Angew. Chem., Int. Ed*. **2008**, *47*, 9192—9198; b) García-Serna, J.; Moreno, T.; Biasi, P.; Cocero, M. J.; Mikkola, J.-P.; Salmi, T. O. Engineering in direct synthesis of hydrogen peroxide: targets, reactors and guidelines for operational conditions. *Green Chem*. **2014**, *16*, 2320—2343; c) Yang, S.; Verdaguer-Casadevall, A.; Arnarson, L.; Silvioli, L.; Čolić, V.; Frydendal, R.; Rossmeisl, J.; Chorkendorff, I.; Stephens, I. E. L. Toward the Decentralized Electrochemical Production of H2O2: A Focus on the

Catalysis. *ACS Catal*. **2018**, *8*, 4064—4081; d) Haider, Z.; Cho, H.-i.; Moon, G.-h.; Kim, H.-i. Minireview: Selective production of hydrogen peroxide as a clean oxidant over structurally tailored carbon nitride photocatalysts. *Catal. Today*, **2018**, *335*, 55—64.

19. Kato, S.; Jung, J.; Suenobua, T.; Fukuzumi, S. Production of hydrogen peroxide as a sustainable solar fuel from water and dioxygen. *Energy Environ. Sci.*, **2013**, *6*, 3756—3764.

20. Kaynan, N.; Berke, B. A.; Hazut, O.; Yerushalmi, R. Sustainable photocatalytic production of hydrogen peroxide from water and molecular oxygen. *J. Mater. Chem. A*, **2014**, *2*, 13822—13826.

21. Wang, L.; Cao, S.; Guo, K.; Wu, Z.; Ma, Z.; Piao, L. Simultaneous hydrogen and peroxide production by photocatalytic water splitting. *Chin. J. Catal*. **2019**, *40*, 470—475.

22. Shiraishi, Y.; Takii, T.; Hagi, T.; Mori, S.; Kofuji, Y.; Kitagawa, Y.; Tanaka, S.; Ichikawa, S.; Hirai, T. Resorcinol–formaldehyde resins as metal-free semiconductor photocatalysts for solar-to-hydrogen peroxide energy conversion. *Nat. Mater.*, **2019**, *18*, 985—993.

23. Shiraishi, Y.; Kanazawa, S.; Kofuji, Y.; Sakamoto, H.; Ichikawa, S.; Tanaka. S.; Hirai, T. Sunlight-Driven Hydrogen Peroxide Production from Water and Molecular Oxygen by Metal-Free Photocatalysts. *Angew. Chem., Int. Ed*. **2014**, *53*, 13454—13459.

24. a) Maurino, V.; Minero, C.; Mariella, G.; Pelizzetti, E. Sustained production of H2O2 on irradiated TiO2 – fluoride systems. *Chem. Commun*. **2005**, *20*, 2627—2629; b) Maurino, V.; Minero, C.; Pelizzetti, E.; Mariella, G.; Arbezzano, A.; Rubertelli, F. Influence of Zn(II) adsorption on the photocatalytic activity and the production of H2O2 over irradiated TiO2. *Res. Chem. Intermed*. **2007**, *33*, 319 — 332; c) Teranishi, M.; Naya, S.; Tada, H. In Situ Liquid Phase Synthesis of

Hydrogen Peroxide from Molecular Oxygen Using Gold Nanoparticle-Loaded Titanium(IV) Dioxide Photocatalyst. *J. Am. Chem. Soc*. **2010**, *132*, 7850—7851.

25. a) Zeng, X.; Wang, Z.; Meng, N.; McCarthy, D. T.; Deletic, A.; Pan, J.-h.; Zhang, X. Highly dispersed TiO2 nanocrystals and carbon dots on reduced graphene oxide: Ternary nanocomposites for accelerated photocatalytic water disinfection. *Appl. Catal. B,* **2017**, *202*, 33—41; b) Zeng, X.; Wang, Z.; Wang, G.; Gengenbach, T. R.; McCarthy, D. T.; Deletic, A.; Yu, J.; Zhang, X. Highly dispersed TiO2 nanocrystals and WO3 nanorods on reduced graphene oxide: Z-scheme photocatalysis system for accelerated photocatalytic water disinfection. *Appl. Catal. B*, **2017**, *218*, 163—173; c) Zheng, L.; Su, H.; Zhang, J.; Walekar, L. S.; Vafaei Molamahmood, H.; Zhou, B.; Long, M.; Hu, Y. H. Highly selective photocatalytic production of H2O2 on sulfur and nitrogen co-doped graphene quantum dots tuned TiO2. *Appl. Catal. B,* **2018**, *239*, 475—484.

26. a) Sun, Y.; Cheng, J. Hydrolysis of lignocellulosic materials for ethanol production: a review. *BioresourTechnol*, **2002**, *83*, 1—11; b) Álvarez, C.; Sosa, F. M. R.-; Díez, B. Enzymatic hydrolysis of biomass from wood. *Microbial Biotechnology*, **2016**, *9*, 149—156.

27. Moon, G.-h.; Kim, W.; Bokare, A. D.; Sung, N.-e.; Choi, W. Solar production of H2O2 on reduced graphene oxide–TiO2 hybrid photocatalysts consisting of earth-abundant elements only. *Energy Environ. Sci*. **2014**, *7*, 4023—4028.

28. Isaka, Y.; Kawase, Y.; Kuwahara, Y.; Mori, K.; Yamashita, Y. Two-Phase System Utilizing Hydrophobic Metal–Organic Frameworks (MOFs) for Photocatalytic Synthesis of Hydrogen Peroxide. *Angew. Chem., Int. Ed*. **2019**, *58*, 5402—5406.

29. Krishnaraj, C.; Jena, H. S.; Bourda, L.; Laemont, A.; Pachfule, P.; Roeser, J.; Chandran, C. V.; Borgmans, S.; Rogge, S. M. J.; Leus, K.; Stevens, C. V.; Martens, J. A.; Speybroeck, V. V.; Breynaert, E.; Thomas, A.; Voort, P. V. D. Strongly Reducing (Diarylamino)benzene-Based Covalent Organic Framework for Metal-Free Visible Light Photocatalytic H2O2 Generation. *J. Am. Chem. Soc*. **2020**, *142*, 20107—20116.

30. a) Zeng, X.; Liu, Y.; Kang, Y.; Li, Q.; Xia, Y.; Zhu, Y.; Hou, H.; Uddin, H.; Gengenbach, T. R.; Xia, D.; Sun, C.; Mccarthy, D. T.; Deletic, A.; Yu, J.; Zhang, X. Simultaneously Tuning Charge Separation and Oxygen Reduction Pathway on Graphitic Carbon Nitride by Polyethylenimine for Boosted Photocatalytic Hydrogen Peroxide Production. *ACS Catal.*, **2020**, *10*, 3697—3706; b) Ye, Y.-X.; Pan, J.; Xie, F.; Gong, L.; Huang, S.; Ke, Z.; Zhu, F.; Xu, J.; Ouyang, G. Highly efficient photosynthesis of hydrogen peroxide in ambient conditions. *PNAS*, **2021**, *118*, e2103964118; c) Fu, Y.; Liu, C.; Zhang, M.; Zhu, C.; Li, H.; Wang, H.; Song, Y.; Huang, H.; Liu, Y.; Kang, Z. Photocatalytic H2O2 and H2 Generation from Living Chlorella vulgaris and Carbon Micro Particle Comodified g-C3N4. *Adv. Energy Mater*. **2018**, *8*, 1802525.

31. a) Chu, C.; Zhu, Q.; Pan, Z.; Gupta, S.; Huang, D.; Du, Y.; Weon, S.; Wu, Y.; Muhich, C.; Stavitski, E.; Domen, K.; Kim, J.-H. Spatially separating redox centers on 2D carbon nitride with cobalt single atom for photocatalytic H2O2 production. *PNAS*, **2020**, *117*, 6376—6382; b) Oka, K.; Nishide, H.; Jensen, B. W.- Copolymer of Phenylene and Thiophene toward a Visible-Light-Driven Photocatalytic Oxygen Reduction to Hydrogen Peroxide. *Adv. Sci*. **2021**, *8*, 2003077; c) Chen, L.; Wang, L.; Wan, Y.; Zhang, Y.; Qi, Z.; Wu, X.; Xu, H. Acetylene and Diacetylene Functionalized Covalent Triazine Frameworks as Metal-Free Photocatalysts for Hydrogen Peroxide Production: A New Two-Electron Water Oxidation Pathway. *Adv. Mater.* **2020**, *32*, 1904433; d) Gryszel, M.; Rybakiewicz, R.; Głowacki, E. D.Water-Soluble Organic

Dyes as Molecular Photocatalysts for H2O2 Evolution. *Adv. Sustainable Syst*., **2019**, *3*, 1900027.

32. Shiraishi, Y.; Kanazawa, S.; Sugano, Y.; Tsukamoto, D.; Sakamoto, H.; Ichikawa, S.; Hirai, T. Highly Selective Production of Hydrogen Peroxide on Graphitic Carbon Nitride (g-C3N4) Photocatalyst Activated by Visible Light. *ACS Catal*. **2014**, *4*, 774—780.

33. Shiraishi, Y.; Kofuji, Y.; Sakamoto, H.; Tanaka, S.; Ichikawa, S.; Hirai, T. Effects of Surface Defects on Photocatalytic H2O2 Production by Mesoporous Graphitic Carbon Nitride under Visible Light Irradiation. *ACS Catal*. **2015**, *5*, 3058—3066.

34. Moon, G.-h.; Fujitsuka, M.; Kim, S.; Majima, T.; Wang, X.; Choi, W. Eco-Friendly Photochemical Production of H2O2 through O2 Reduction over Carbon Nitride Frameworks Incorporated with Multiple. *ACS Catal*. **2017**, *7*, 2886—2895.

35. Peng, Y.; Wang, L.; Liu, Y.; Chen, H.; Lei, J.; Zhang, J.Visible-Light-Driven Photocatalytic H2O2 Production on g-C3N4 Loaded with CoP as a Noble Metal Free Cocatalyst. *Eur. J. Inorg. Chem*. **2017**, *2017*, 4797—4802.

36. Chang, X.; Yang, J.; Han, D.; Zhang, B.; Xiang, X.; He, J. Enhancing Light-Driven Production of Hydrogen Peroxide by Anchoring Au onto C3N4 Catalysts. *Catalysts*. **2018**, *8*, 147.

37. Zhao, S.; Zhao, X.; Zhang, H.; Li, J.; Zhu, Y. Covalent combination of polyoxometalate and graphitic carbon nitride for light-driven hydrogen peroxide production. *Nano Energy* **2017**, *35*, 405—414.

38. Kim, H.-i.; Choi, Y.; Hu, S.; Choi, W.; Kim, J.-H. Photocatalytic hydrogen peroxide production by anthraquinone-augmented polymeric carbon nitride. *Appl. Catal., B* **2018**, *229*, 121—129.

39. Kim, S.; Moon, G.-h.; Kim, H.; Mun, Y.; Zhang, P.; Lee, J.; Choi, W. Selective charge transfer to dioxygen on KPF6-modified carbon nitride for photocatalytic synthesis of H2O2 under visible light. *J. Catal*. **2018**, *357*, 51—58.

40. Li, X.; Zhang, J.; Zhou, F.; Zhang, H.; Bai, J.; Wang, Y.; Wang, H. Preparation of N-vacancy-doped g-C3N4 with outstanding photocatalytic H2O2 production ability by dielectric barrier discharge plasma treatment. *Chin. J. Catal*. **2018**, *39*, 1090—1098.

41. Qu, X.; Hu, S.; Li, P.; Li, Z.; Wang, H.; Ma, H.; Li, W. The effect of embedding N vacancies into g-C3N4 on the photocatalytic H2O2 production ability via H2 plasma treatment. *Diamond Relat. Mater*. **2018**, *86*, 159—166.

42. Wang, R.; Zhang, X.; Li, F.; Cao, D.; Pu, M.; Han, D.; Yang, J.; Xiang, X. Energy-level dependent H2O2 production on metal-free, carbon-content tunable carbon nitride photocatalysts. *J. Energy Chem*. **2018**, *27*, 343—350.

43. Wei, Z.; Liu, M.; Zhang, Z.; Yao, W.; Tan, H.; Zhu, Y. Efficient visible-light-driven selective oxygen reduction to hydrogen peroxide by oxygen-enriched graphitic carbon nitride polymers. *Energy Environ. Sci*. **2018**, *11*, 2581—2589.

44. Zhao, S.; Zhao, X.; Ouyang, S.; Zhu, Y. Polyoxometalates covalently combined with graphitic carbon nitride for photocatalytic hydrogen peroxide production. *Catal. Sci. Technol*. **2018**, *8*, 1686—1695.

45. Tian, J.; Wu, T.; Wang, D.; Pei, Y.; Qiao, M.; Zong, B. One-pot synthesis of potassium and phosphorus-doped carbon nitride catalyst derived from urea for highly efficient visible light-driven hydrogen peroxide production. *Catal. Today* **2019**, *330*, 171—178.

46. Zhao, S.; Zhao, X. Insights into the role of singlet oxygen in the photocatalytic hydrogen peroxide production over polyoxometalates-derived metal oxides incorporated into graphitic carbon nitride framework. *Appl. Catal., B* **2019**, *250*, 408—418.

47. Zuo, G.; Liu, S.; Wang, L.; Song, H.; Zong, P.; Hou, W.; Li, B.; Guo, Z.; Meng, X.; Du, Y.; Wang, T.; Roy, V. A. L. Finely dispersed Au nanoparticles on graphitic carbon nitride as highly active photocatalyst for hydrogen peroxide production. *Catal. Commun*. **2019**, *123*, 69—72.

48. Wu, S.; Yu, H.; Chen, S.; Quan, X. Enhanced Photocatalytic H2O2 Production over Carbon Nitride by Doping and Defect Engineering. *ACS Catal.* **2020**, *10*, 14380—14389.

49. Yang, Y.; Zeng, Z.; Zeng, G.; Huang, D.; Xiao, R.; Zhang, C.; Zhou, C.; Xiong, W.; Wang, W.; Cheng, M.; Xue, W.; Guo, H.; Tang, X.; He, D. Ti3C2 Mxene/porous g-C3N4 interfacial Schottky junction for boosting spatial charge separation in photocatalytic H2O2 production. *Appl. Catal. B,* **2019**, *258*, 117956.

50. Yang, Y.; Zhang, C.; Huang, D.; Zeng, G.; Huang, J.; Lai, C.; Zhou, C.; Wang, W.; Guo, H.; Xue, W.; Deng, R.; Cheng, M.; Xiong, W. Boron nitride quantum dots decorated ultrathin porous g-C3N4: Intensified exciton dissociation and charge transfer for promoting visible-light-driven molecular oxygen activation. *Appl. Catal. B,* **2019**, *245*, 87—99.

51. Zhang, P.; Tong, Y.; Liu, Y.; Vequizo, J. J. M.; Sun, H.; Yang, C.; Yamakata, A.; Fan, F.; Lin, W.; Wang, X.; Choi, W. Heteroatom Dopants Promote Two-Electron O2 Reduction for Photocatalytic Production of H2O2 on Polymeric Carbon Nitride. *Angew. Chem. Int. Ed*. **2020**, *59*, 16209—16217.

52. Hu, Y.; Shim, Y.; Oh, J.; Park, S.; Park, S.; Ishii, Y. Synthesis of 13C-,15N-Labeled Graphitic Carbon Nitrides and NMR-Based Evidence of Hydrogen-Bonding Assisted Two-Dimensional Assembly. *Chem. Mater*. **2017**, *29*, 5080—5089.

53. Sehnert, J.; Baerwinkel, K.; Senker, J. Ab Initio Calculation of Solid-State NMR Spectra for Different Triazine and Heptazine Based Structure Proposals of g-C3N4. *J. Phys. Chem. B*, **2007**, *111*, 10671—10680.

54. Fukaya, H.; Ono, T. DFT-GIAO calculations of 19F NMR chemical shifts for perfluoro compounds. *J. Comput. Chem.* **2003**, *25*, 51—60.

55. Sun, Y.-N.; Yang, J.; Ding, X.; Ji, W.; Jaworski, A.; Hedin, N.; Han, B.-H. Synergetic contribution of nitrogen and fluorine species in porous carbons as metal-free and bifunctional oxygen electrocatalysts for zinc–air batteries. *Appl. Catal. B,* **2021**, *297*, 120448.

56. a) Stoychev, G. L.; Auer, A. A.; Neese, F.; *J. Chem. Theory Comput.* **2018**, *14*, 4756; b) Rzepka, P.; Bacsik, Z.; Pell, A. J.; Hedin, N.; Jaworski, A. Nature of Chemisorbed CO2 in Zeolite A. *J. Phys. Chem. C,* **2019**, *123*, 21497—21503.

57. Sobańska, K.; Pietrzyk, P.; Sojka, Z. Generation of Reactive Oxygen Species via Electroprotic Interaction of H2O2 with ZrO2 Gel: Ionic Sponge Effect and pH-Switchable Peroxidase- and Catalase-Like Activity. *ACS Catal.* **2017**, *7*, 2935—2947.

58. Reszka, K.; Chignell, C. F. *Spectroscopic studies of cutaneous photosensitizing agents-IV. The photolysis of benoxaprofen, an anti-inflammatory drug with phototoxic properties*. **1983**, 281.

59. Bilski, P.; Chignell, C. F.; Szychlinski, J.; Borkowski, A.; Oleksy, E.; Reszka, K. Photooxidation of organic and inorganic substrates during

UV photolysis of nitrite anion in aqueous solution. *J. Am. Chem. Soc*. **1992**, *114*, 549—556.

60. Sing, K.S.W. Reporting physisorption data for gas/solid systems with special reference to the determination of surface area and porosity (Recommendations 1984). *Pure & App. Chem.*, **1985**, *57*, 603—619.

61. Tsukamoto, D.; Ikeda, M.; Shiraishi, Y.; Hara, T.; Ichikuni, N.; Tanaka, S.; Hirai, T. Selective Photocatalytic Oxidation of Alcohols to Aldehydes in Water by TiO2 Partially Coated with WO3. *Chem. Eur. J.* **2011**, *17*, 9816—9824.

62. Ma, Z.; Jaworski, A.; George, J.; Rokicinska, A.; Thersleff, T.; Budnyak, T. M.; Hautier, G.; Pell , A. J.; Dronskowski, R.; Kuśtrowski, P.; Slabon, A. Exploring the Origins of Improved Photocurrent by Acidic Treatment for Quaternary Tantalum-Based Oxynitride Photoanodes on the Example of CaTaO2N. *J. Phys. Chem. C*., **2020**, *124*, 152—160.

63. Dong, B.; Cui, J.; Gao, Y.; Qi, Y.; Zhang, F.; Li, C. Heterostructure of 1D Ta3N5 Nanorod/BaTaO2N Nanoparticle Fabricated by a One-Step Ammonia Thermal Route for Remarkably Promoted Solar Hydrogen Production. *Adv. Mater*. **2019**, *31*, 1808185.

64. Hwang, T.-L.; van Zijl, P. C.; Garwood, M. Fast Broadband Inversion by Adiabatic Pulses. *J. Magn. Reson.* **1998**, *133*, 200—203.

65. Kervern, G.; Pintacuda, G.; Emsley, L. Fast adiabatic pulses for solid-state NMR of paramagnetic systems. *Chem. Phys. Lett.* **2007**, *435*, 157—162.

66. Stoll, S.; Schweiger, A. EasySpin, a comprehensive software package for spectral simulation and analysis in EPR. *J. Magn. Res.* **2006**, *178*, 42—55.

67. *Gaussian 09, Revision A.02,* M. J. Frisch, G. W. Trucks, H. B. Schlegel, G. E. Scuseria, M. A. Robb, J. R. Cheeseman, G. Scalmani, V. Barone, G. A.

Petersson, H. Nakatsuji, X. Li, M. Caricato, A. Marenich, J. Bloino, B. G. Janesko, R. Gomperts, B. Mennucci, H. P. Hratchian, J. V. Ortiz, A. F. Izmaylov, J. L. Sonnenberg, D. Williams-Young, F. Ding, F. Lipparini, F. Egidi, J. Goings, B. Peng, A. Petrone, T. Henderson, D. Ranasinghe, V. G. Zakrzewski, J. Gao, N. Rega, G. Zheng, W. Liang, M. Hada, M. Ehara, K. Toyota, R. Fukuda, J. Hasegawa, M. Ishida, T. Nakajima, Y. Honda, O. Kitao, H. Nakai, T. Vreven, K. Throssell, J. A. Montgomery, Jr., J. E. Peralta, F. Ogliaro, M. Bearpark, J. J. Heyd, E. Brothers, K. N. Kudin, V. N. Staroverov, T. Keith, R. Kobayashi, J. Normand, K. Raghavachari, A. Rendell, J. C. Burant, S. S. Iyengar, J. Tomasi, M. Cossi, J. M. Millam, M. Klene, C. Adamo, R. Cammi, J. W. Ochterski, R. L. Martin, K. Morokuma, O. Farkas, J. B. Foresman, D. J. Fox, *Gaussian, Inc., Wallingford CT,* **2016**.

68. Perdew, J. P.; Burke, K.; Ernzerhof, M. Generalized Gradient Approximation Made Simple. *Phys. Rev. Lett.* **1996**, *77*, 3865.

69. Grimme, S. Semiempirical GGA-type density functional constructed with a long-range dispersion correction. *J. Comput. Chem.* **2006**, *27*, 1787—1799.

70. Vanderbilt, D. Soft self-consistent pseudopotentials in a generalized eigenvalue formalism. *Phys. Rev. B: Condens. Matter Mater. Phys.* **1990**, *41*, 7892.

71. Giannozzi, P.; Baseggio, O.; Bonfà, P.; Brunato, D.; Car, R.; Carnimeo, I.; Cavazzoni, C.; de Gironcoli, S.; Delugas, P.; Ferrari Ruffino, F.; Ferretti, A.; Marzari, N.; Timrov, I.; Urru, A.; Baroni, S. Quantum ESPRESSO toward the exascale. *J. Chem. Phys.* **2020**, *152*, 154105.

72. Baerends, E. J.; *et al. ADF, adf2019.106 SCM, Theoretical Chemistry, Vrije Universiteit, Amsterdam, The Netherlands,* http://www.scm.com (accessed 2021-07-06).

73. Sheppard, D.; Terrell, R.; Henkelman, G. Optimization methods for finding minimum energy paths. *J. Chem. Phys.* **2008**, *128*, 134106.

Chapter 3

Π–Π Stacking Complex Induces Three-Component Coupling Reactions to Synthesize Functionalized Amines

ABSTRACT: π–π stacking and ion-pairing interactions induced the generation of α-amino radicals under the irradiation of visible light without the requirement of an expensive photocatalyst. This strategy provided access to the construction of functionalized amines *via* three-component coupling reactions with broad scopes (we reported > 50 examples with an up to 90% yield). This synthetic pathway also delivered the synthesis of complex functionalized amines with a very high yield. Advanced Quantum mechanical calculations identified the π-π stacked ionic complexes; Time-Dependent DFT simulated the absorption spectra and with the nudged elastic band (NEB) methodology provided a possible interaction/reaction picture of the selected species.

This chapter is based on the published work: Zhang, T.; Vanderghinste, J.; Guidetti, A.; Van Doorslaer, S.; Barcaro, G.; Monti, S.; Das, S. *Angew. Chem. Int. Ed*. **2022**, *61*, e202212083.

3.1 Introduction

Noncovalent interactions (NCIs) such as hydrogen bonding, π-interactions, van der Waals, and Coulombic interactions play crucial roles in enzyme catalysis, supramolecular chemistry, biocatalysis, and organic synthesis.[1-2] Although NCIs are relatively weak, they still play an essential role in reducing free energy barriers by the stabilization of the transition-state, making the catalytic systems more efficient.[3] In addition, NCIs have been taken into account in the rational designing of catalysts, considering factors such as the orientation, distance, and electronic effects that control or influence the NCIs to achieve high regio- or site-selectivity.[4-5]

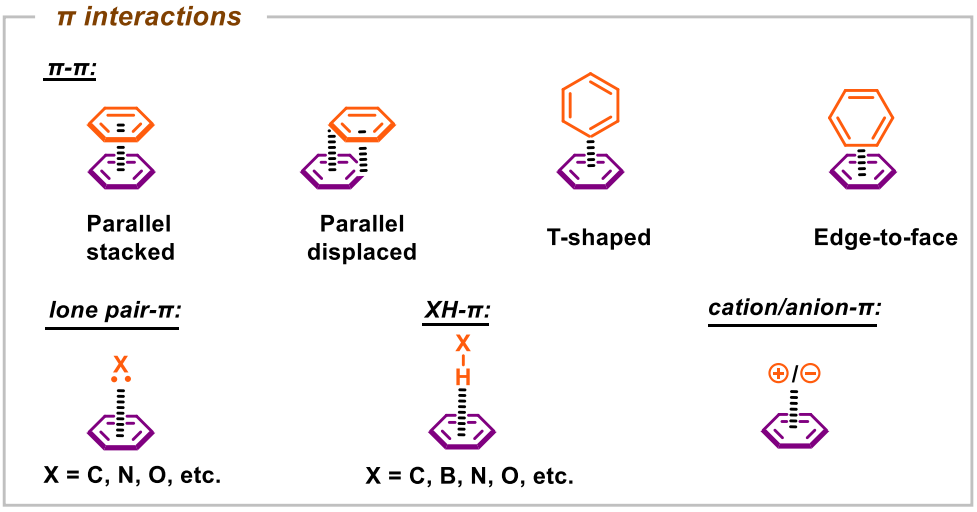

Figure 3.1. Schematic forms of various π-interactions.

Among all the NCIs, π-interactions, including π-π, lone pair-π, XH-π, and cation/anion-π interactions have been intensively studied with aromatic functional groups in photochemical synthesis (**Figure 3.1**).[6-7] In fact, the design of catalysts based on π-interactions has also been achieved, for example, Yoon *et al.* reported a chiral iridium-photosensitizer for the generation of intramolecular [2+2] cycloaddition products (**Figure 3.2**).[8] In addition, π-interactions also assisted the

formation of electron donor-acceptor (EDA) and ion-pair charge-transfer (IPCT) complexes which had been used in photochemical synthesis.[9-11] These unique adducts showed the potential for activating substrates under the irradiation of visible light. Recently, Bach *et al*. reported that 3-acetoxyquinuclidine could act as the electron donor and formed the EDA complex by combining with tetrachlorophthalimide ester, followed by a single electron transfer (SET) process under the irradiation of blue light (**Figure 3.2**).[12] Later, Melchiorre *et al.* designed radical-based catalytic systems with two EDA complexes involving π-π and anion-π interactions for the generation of alkyl and sulfur-centered radicals (**Figure 3.2**).[13b,13c] It was demonstrated that the selection of molecules that could form π-interaction complexes enriched the synthetic photochemical approaches and provided new reactivity principles.[13]

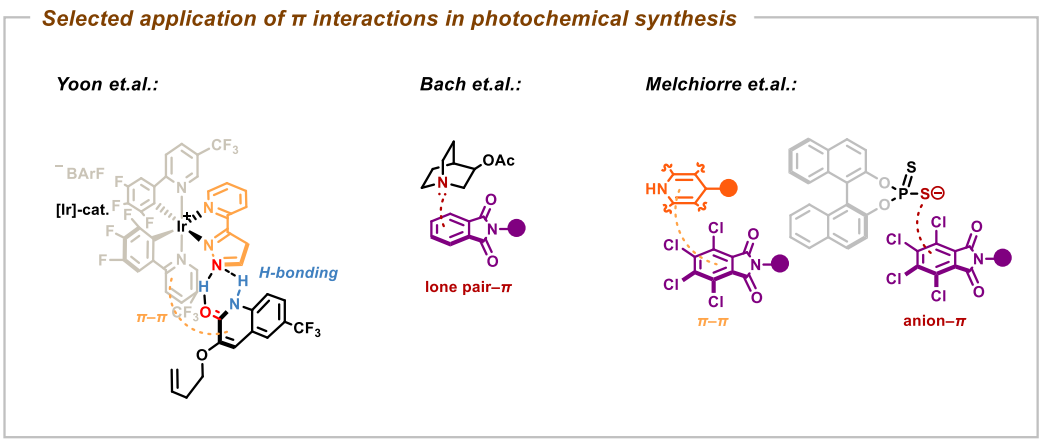

Figure 3.2. Applications of π-interactions in synthetic photochemical approaches.

Strategies for the synthesis of functionalized amines have attracted much attention because they are considered as one of the synthetically essential compounds in the areas of pharmaceuticals, natural products, and fine chemicals.[14-15] To meet these demands, a plethora of procedures, such as C-H bond functionalization, reductive amination, and other techniques, have been developed.[16-17] In this respect, the generation of α-

amino radicals to synthesize functionalized amines has gained tremendous priority.[18-20] While these radicals can be prepared from amino acids (by releasing CO_2), or directly from an amine substrate,[21-24] their generation from an imine offers higher scope and versatility for the synthesis of functionalized amines.[25-29]

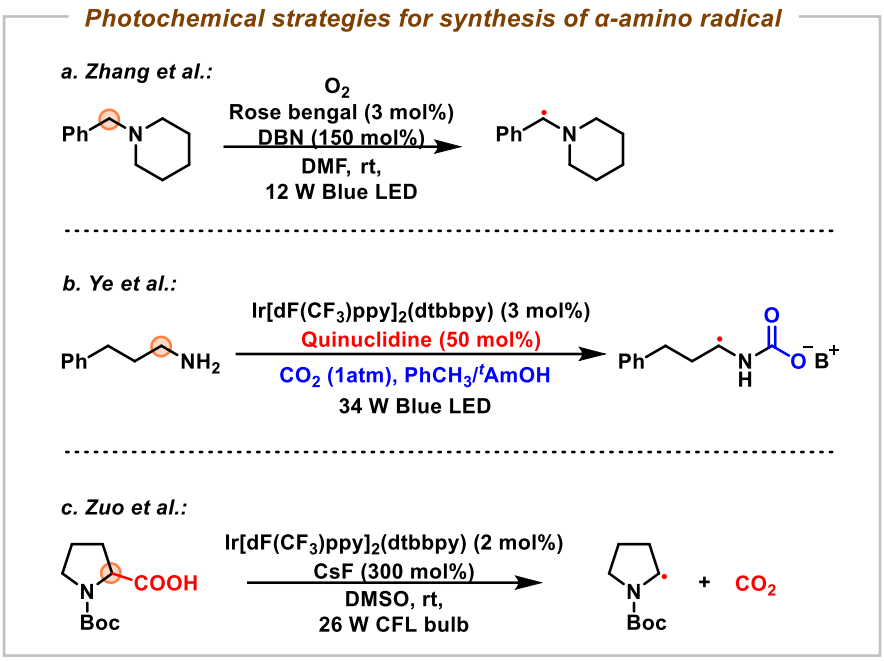

Figure 3.3. Strategies for the formation of α-amino radical via photochemistry.

For instance, our group has reported an elegant methodology for the production of amides from tertiary amines.[30a] In this approach, the alpha-amino radical was produced through a sequential mechanism involving the oxidation and subsequent deprotonation of amines (**Figure 3.3a**). In 2018, Rovis group reported a highly selective CO_2-catalyzed system to generate alpha-amino radical from an amine substrate via hydrogen atom transfer step.[30b] The quinuclidine acted as HAT reagent and preferably abstracted hydrogen closed to amine rather than the hydrogen at the benzylic position (**Figure 3.3b**). In addition, alpha-amino radical was also formed *via* decarboxylation from alpha-amino acids.[30c]

MacMillan group reported this strategy with Ir- catalysts and cesium base under the irradiation of light irradiation (**Figure 3.3c**).

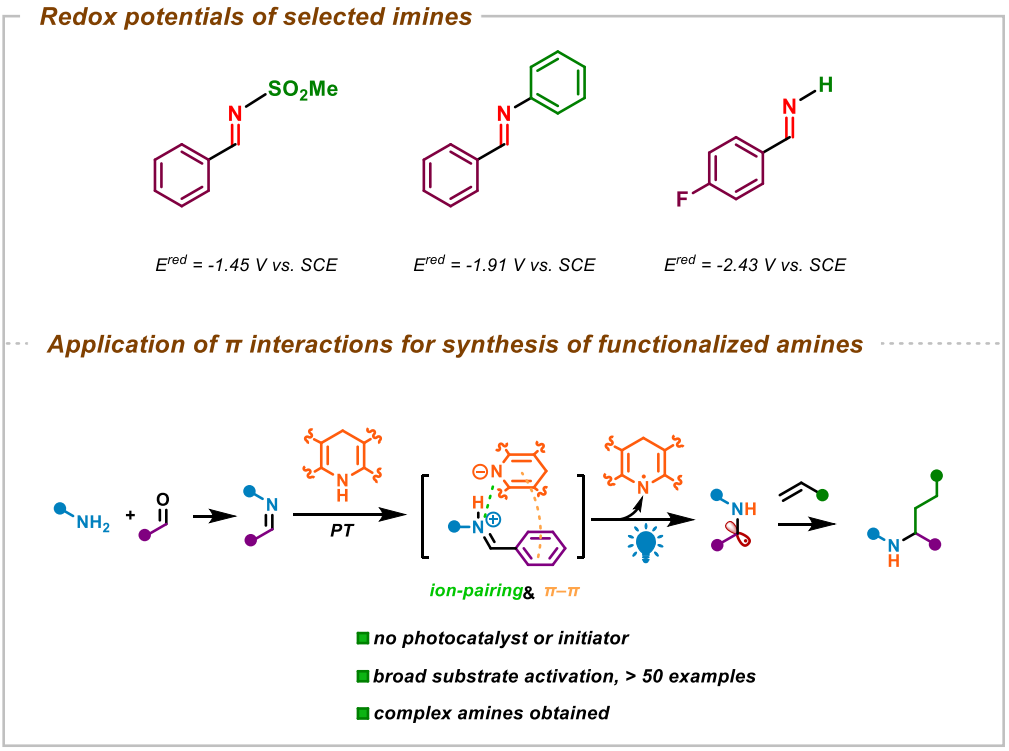

Figure 3.4. **Top**: The redox potentials of selected imines. **Bottom**: π interaction-induced photochemical synthesis of functionalized amines.

Compared to aforementioned methods, generation of alpha-amino radicals via imine reduction is more challenging, as the redox potentials of imines are relatively much negative, which means they are difficult to be reduced (**Figure 3.4 Top**). Therefore, only strong reducing photocatalysts such as *fac*-Ir(ppy)$_3$ (Ir(II)/Ir(III) = -2.19 *vs.* SCE) or strong sacrificial reducing additives such as silane reagents are essential to reduce the imine to afford alpha-amino radicals.[15a] In general, Hantzsch ester (HE) has been applied as an electron/proton donor to synthesize various organic compounds.[31] We rationalized that the lone-pair electrons on the aromatic imine nitrogen atom and the π-system of HE ring could establish π interactions, which should be able to facilitate an

electron/proton transfer between them under blue light. Considering this possibility, we took the challenge[32] and designed a photochemical system for the formation of α-amino radicals under the irradiation of visible light (**Figure 3.4 Bottom**).

3.2 Results and Discussion

At the beginning of this project, we conducted a three-component coupling reaction by using *p*-anisidine (**1**), benzaldehyde (**2**) and *n*-butyl acrylate (**3**) in the presence of Hantzsch ester (**4a**) under the irradiation of blue light (**Table 3.1**) and obtained the Giese-type product butyl 4-((4-methoxyphenyl)amino)-4-phenylbutanoate (**5a**) in 50% yield. To further increase the yield of **5a**, we tried to modify the amount of **3** and **4a**, but these changes did not provide better yields (**Table 3.1, entries 3-4**). Considering the crucial role of the Hantzsch ester in this reaction, we investigated various HE (**Table 3.1, entries 5-7**)[28d] and among them, only the methoxyethyl-HE (**4b**) provided the product in 58% yield, whereas 4-phenyl- and 4-cyclohexyl-substituted HEs did not provide any outcome. Even though the use of DCM as a solvent promoted the *in situ* formation of imine from the corresponding aldehyde and amine, it also promoted reductive amination and oligomerization (**Table 3.1, 5b,** and **5c**) as side products, which were detected by the GC-MS. To avoid by-product formation, we checked the behaviour of various solvents, and we found that a mixture of DCM and DMSO (1:1) was the optimal choice for this reaction. Not surprisingly, no product was formed in the absence of HE or light irradiation (**Table 3.1, entries 8-9**), suggesting that these two ingredients were essential for the whole process. Interestingly, when a pre-formed imine was introduced into the reaction, the yield of **5a** was slightly decreased due to the formation of the reductive amination products (**Table 3.1**, **entries 10**).

Table 3.1. Optimization of three-component coupling reactions.

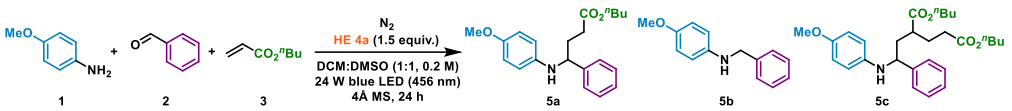

Entry[a]	Variations	Yield of 5a (%)[b]
1	none	72(63[c])
2	DCM (1 mL)	50
3	1.5 equiv. acrylate	62
4	HE (2 equiv.)	72
5	HE 4b (1.5 equiv.)	58
6	4-Ph-HE (1.5 equiv.)	n.ob.
7	4-Cyclohexane-HE (1.5 equiv.)	n.ob.
8	No HE	n.ob.
9	No light	n.ob.
10	Pre-formed imine	35

[a]Reaction conditions: amine (0.2 mmol), aldehyde (0.2 mmol), acrylate (0.4 mmol), solvent (1 mL). [b]Yield was determined by ^{1}H NMR with 1,3,5-trimethoxybenzene as internal standard. [c]Isolated yields.

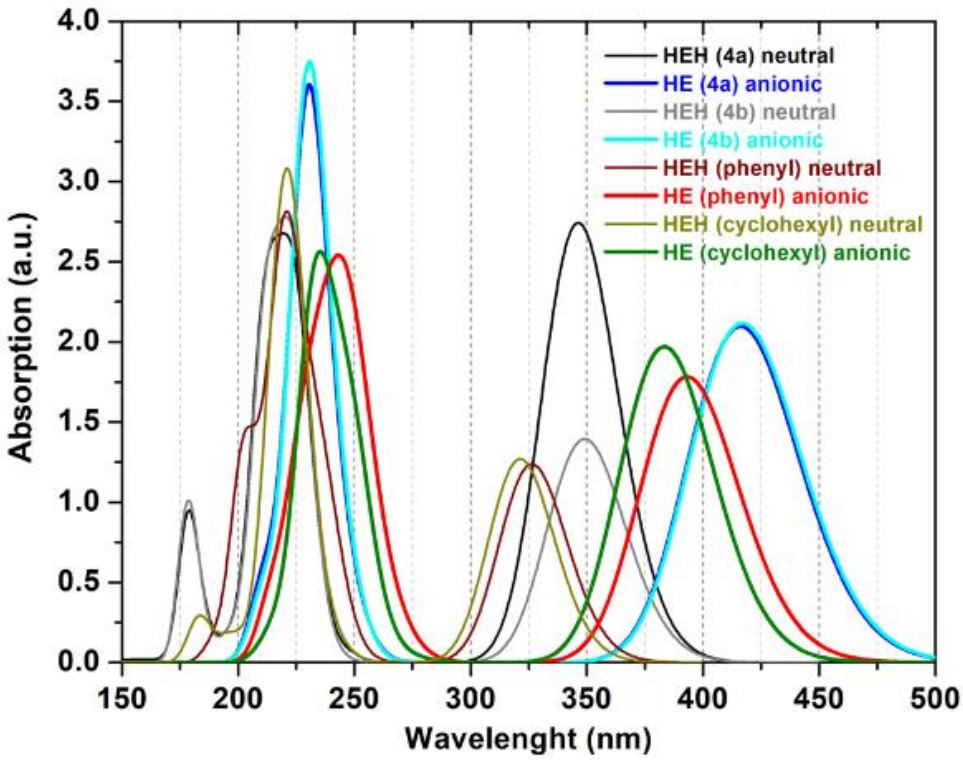

Figure 3.5. CAM-B3LYP/6-311+G(d,p)/DMSO absorption spectra of the Hantzsch ester structures optimized at the B3LYP/6-311+G(d,p) level in DMSO (artificially broadened with gaussian peaks – HWHH = 0.15 eV).

To explain these unprecedented results at the molecular/atomic/electronic levels, we estimated the UV-vis absorption lengths of the selected HE species in their neutral and anionic forms using quantum chemistry (QC) calculations (**Figure 3.5**), and we proposed the possible intermediate molecular complexes involving the HE species with a representative imine structure (**Figure 3.6**). We found, in agreement with experiments, that all the neutral HE species exhibited relatively strong absorption in the near-ultraviolet region (between 300 and 400 nm), as well as their neutral complexes with the selected imine (red curve in **Figure 3.6**).[33] Instead, the HE anionic forms extended their absorption bands in the blue part of the spectrum. Thus, we speculated that, most probably, these were the species activated by the blue LED

light that induced an electron transfer between the photoexcited HE and the imine ion, leading to the corresponding radical species.

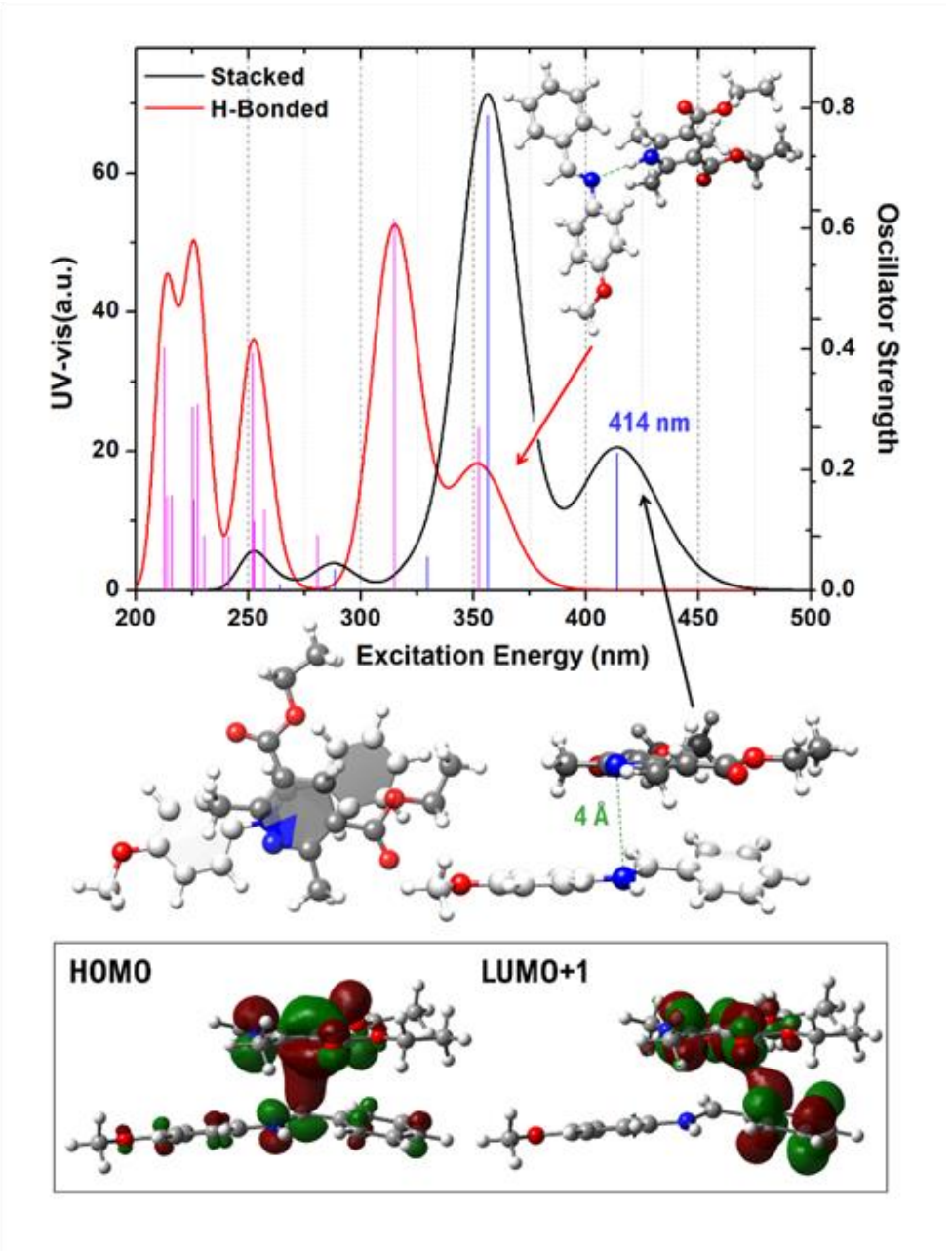

Figure 3.6. **Top**. CAM-B3LYP/6-311+G(d,p)/DMSO absorption spectra computed for the stacked complex and T-shaped complexes optimized at the B3LYP/6-311+G(d,p) level in DMSO (artificially broadened with gaussian peaks

– HWHH = 0.15 eV). The corresponding geometries are shown in the inset T-shaped) and below the plot (stacked) in two different orientations. **Bottom**. Representation of the molecular orbitals involved in the bright transition for the stacked complex system (HOMO—LUMO+1 transition).

To check this assumption, we hypothesized the formation of two complexes between the imine and the HE; one was a T-shaped complex (top in **Figure 3.6**), and another one was a π-π stacked adduct (bottom in **Figure 3.6**). The QC calculations predicted the T-shaped complex to have a dipole moment of about 7 Debye, and a distance between the nitrogen atoms of 3.11 Å. Compared to the T-shaped complex, the stacked complex with a dipole moment of about 16 Debye was an ionic pair, in which the HE had already released its H(N) hydrogen. The ionic pair was linked by a π-system with a distance between the nitrogen atoms of approximately 4 Å. The calculated energy difference of - 8.5 kcal/mol between the π-π stacked ionic complex and the sum of the energy of the isolated species validated the stability of this assembly (bottom in **Figure 3.6)**. From a computational point of view, this complex was a stable minimum energy configuration but could not be experimentally detected.[34]

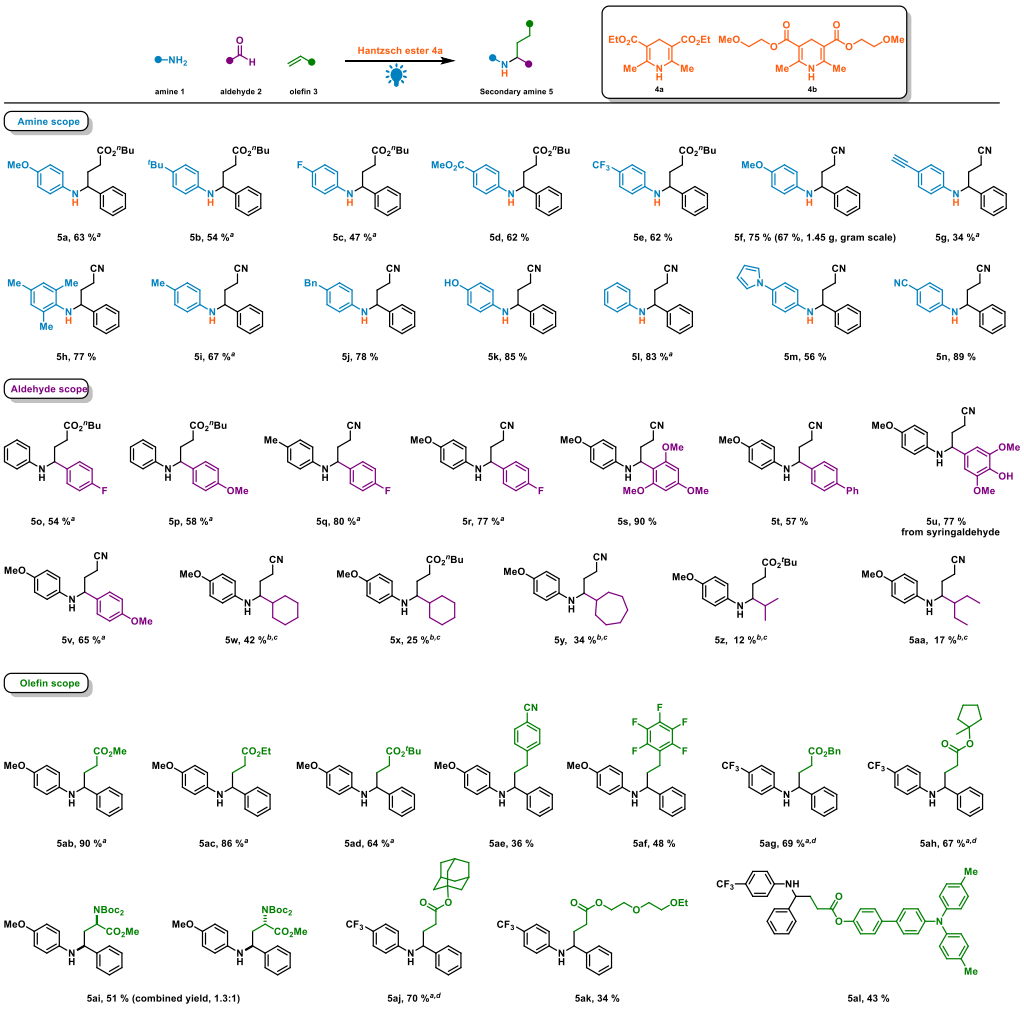

Figure 3.7. Scope of amines, aldehydes and olefins. Standard reaction conditions: amines (0.2 mmol), aldehyde (0.2 mmol), olefin (0.4 mmol), **4a** (0.3 mmol), DCM:DMSO (1:1, 0.2 M), 24 W blue LED (456 nm), 4Å MS, 24 h; [a]**4b** (0.3 mmol); [b]amines (0.2 mmol), aldehyde (0.4 mmol), olefin (0.4 mmol); [c]additional 10 mol% acetic acid; [d]pre-formed imine.

Based on the formation of the π-π stacked complex, we speculated that a radical catalysis pathway could be initiated by a blue-light activated intermolecular single-electron transfer (SET) from the HE reductant to the electrophilic iminium ion. Such a process took place in the intermediate ion-pair charge-transfer complex shown in **Figure 3.6** (black line) and **Figure 3.24**.

Considering these suggestions, we evaluated the scope of our three-component coupling reaction (**Figure 3.7**). To our delight, various electron-rich and electron-poor aniline derivatives (**5a-5e**) reacted smoothly, providing the desired products in moderate to good yields. It is worth noting that the products formed by electron-rich substituted anilines and *n*-butyl acrylate were not stable; instead, they readily formed the substituted pyrrolidones *via* intramolecular cyclization.[29a,35] To avoid this cyclization reaction, acrylonitrile was selected as model olefin to investigate the scope further. Indeed, the presence of acrylonitrile improved the yield of the corresponding noncyclic amines, and diverse classes of anilines (**5f-5n**) were efficiently transformed to the desired secondary amines in moderate to excellent yields (up to 89%).

Intrigued by these results, we examined the scope of different aldehydes under the model reaction conditions. As expected, benzaldehydes containing electron-donating groups such as methoxy, phenyl, and hydroxyl groups and weak electron-deficient groups such as fluorine (**5o-5r**) performed well under the applied reaction conditions. To intensify the scope of this reaction, we examined unactivated aldehydes, particularly aliphatic and alicyclic aldehydes, as the coupling partners. However, that led to the unstable alkyl imines by reacting with the amines present in the reaction.[27b] It is well known that the formation of alkyl imines is complex, and they can be obtained only by adding a catalytic amount of acetic acid.[28c] The addition of acetic acid not only promoted the formation of imine but also assisted the formation of the corresponding iminium salts, which, due to their less negative reduction

potential, facilitated the reduction by the HE.[15a,36] Following this strategy, the aldehydes of cyclohexane and cycloheptane worked smoothly without forming side products *via* the ring-opening, albeit in decreased yields of ca. 40%. Similarly, aliphatic aldehydes also reacted with the acrylate and acrylonitrile to provide **5z and 5aa**.

Further diversification of this concept was achieved by varying the olefins under the model reaction conditions. Our results suggested that this three-component coupling reaction could be efficiently carried out in the presence of electron-deficient alkenes. In fact, the performance of alkenes was related to their electrophilicity (*E*): for example, methyl acrylate (**5ab**, *E* = -18.84) and ethyl acrylate (**5ac**, *E* = -19.07) exhibited higher yields than *tert*-butyl acrylate (**5ad**, *E* = -20.22) due to the less negative electrophilicity.[37] Acrylonitrile (*E* = -19.05) was expected to be a more suitable coupling candidate due to its very close electrophilicity of the ethyl acrylate. However, *ca.* 20% lower yield of the resulting product was obtained due to the oligomerization in radical reaction.[28c] Furthermore, 4-vinylbenzonitrile and 2,3,4,5,6-pentafluorostyrene were viable alkenes to deliver the corresponding secondary amines (**5ae-5af**). We could also observe that various acrylates from natural products such as estrone, α-tocopherol, *etc*., provided complex secondary amine products in moderate to good yields (**5am-5aq**). These results demonstrated the strong potential of this methodology for the synthesis of complex secondary amines *via* three-component coupling reactions (**Figure 3.8**).

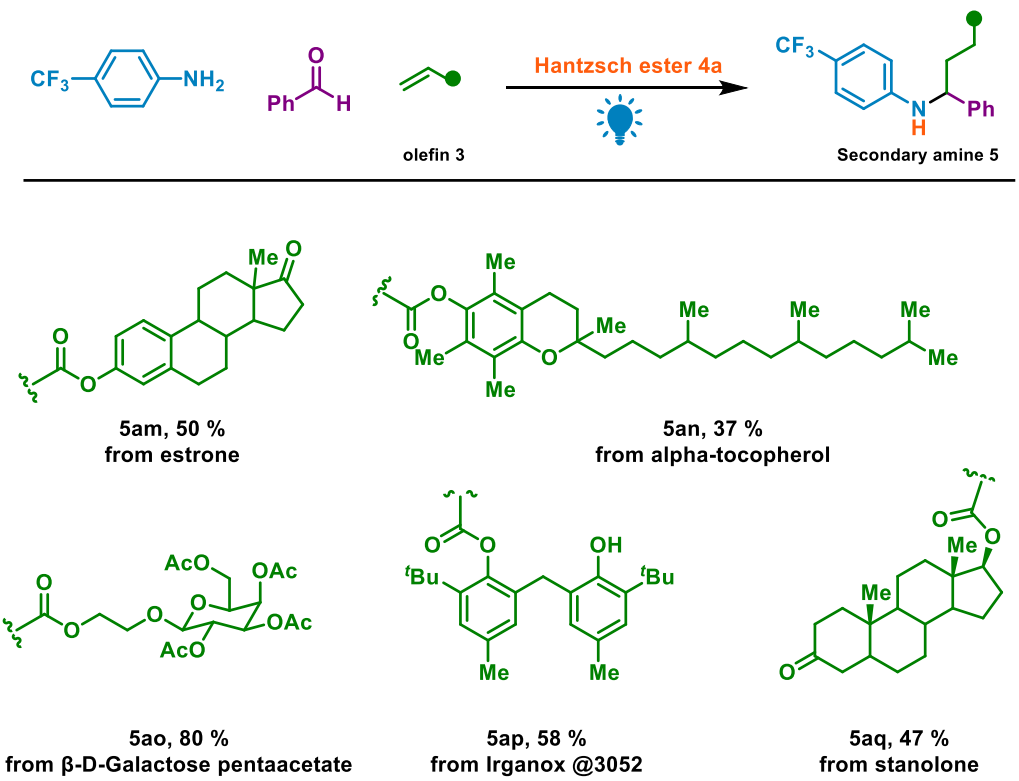

Figure 3.8. Scope of complex olefins. Standard reaction conditions: amines (0.2 mmol), aldehyde (0.2 mmol), olefin (0.24 mmol), **4a** (0.3 mmol), DCM: DMSO (1:1, 0.2 M), 24 W blue LED (456 nm), 4Å MS, 24 h.

The formation of complex amines *via* three-component reactions intrigued us to achieve cyclic amines *via* intramolecular C-C bond formation reactions. For this purpose, under the model reaction conditions, α,β-unsaturated ester-tethered benzaldehydes were investigated to assess 1-aminoindanes, which can be used as intermediates for the construction of pharmaceutical compounds.[29d] Indeed, the reaction system was effective in providing *trans*-1-aminoindanes in moderate yields with both electron-rich and -deficient aniline derivatives (**Figure 3.9**, **7a-7f**). According to the substrate scope, we observed that if the nucleophilicity of α-amino radicals matched well with the electrophilicity of olefins, better yields of coupling products could be obtained. In comparison with amines, methyl acrylate (E = -

18.84) had less negative electrophilicity than *tert*-butyl acrylate (E = -20.22), and the former reacted more smoothly with electron-rich functionalized amines (**7a** and **7d**). Then, we compared the action of two acrylates, namely methyl and tert-butyl acrylates. These showed different trends: methyl acrylate preferred reacting with electron-rich functionalized amines (see yields for **7a-7c)**, whereas *tert*-butyl acrylate preferred reacting with the electron-deficient functionalized amines (see corresponding yields in **7d-7f**).

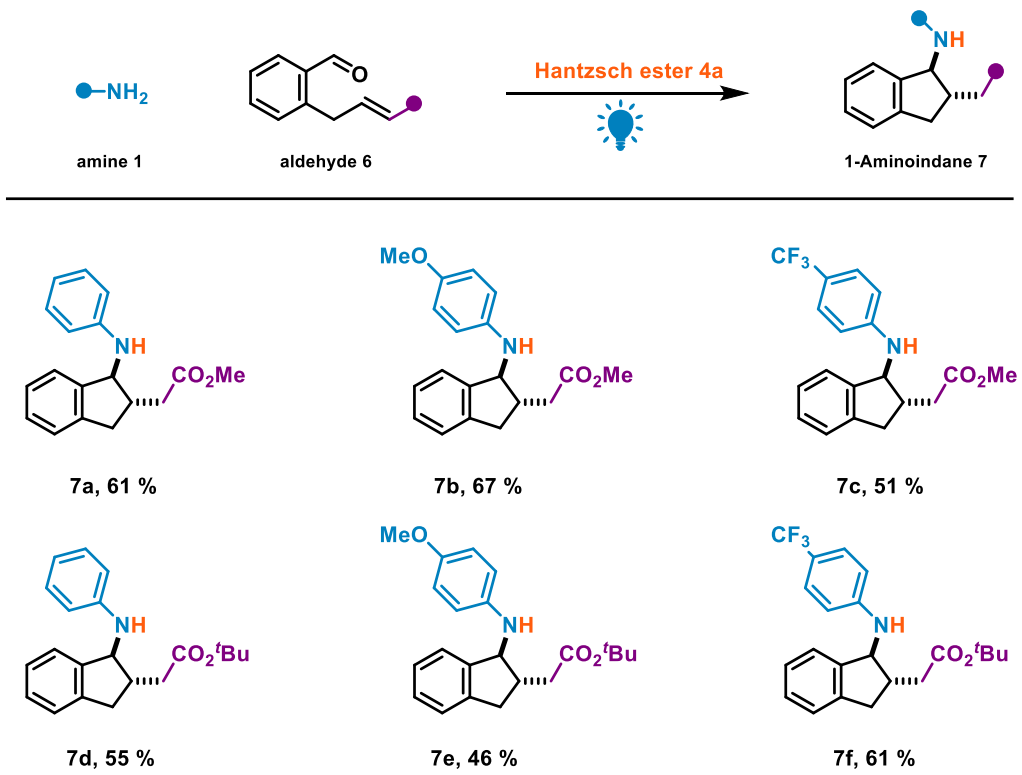

Figure 3.9. Scope of complex olefins. Standard reaction conditions: amines **1** (0.2 mmol), aldehyde **6** (0.2 mmol), **4a** (0.3 mmol), DCM:DMSO (1:1, 0.2 M), 24 W blue LED (456 nm), 4Å MS, 24 h.

To simulate these cyclization reactions, we used QC models and managed to identify possible minimum-energy paths (MEPs) and activation energies (transition states-TS) in line with the experimental yield. As already done in other studies,[38] we used the nudged elastic

band (NEB) methodology (**See SI 3.5.4.6.2**), and we found that all the energy barriers were connected to the concomitant hydrogen transfer from HE to the reactant, and the C-C bond formation (cyclization reactions, **Figures 3.25-3.26**), were relatively low (at most 10 kcal/mol, **Table 3.6**) and in agreement with the experimental yield.

3.3 Mechanistic studies

After achieving the scope of this reaction and considering all the results of the QC calculations, we proposed the mechanism in **Figure 3.10**. At first, the Hantzsch ester (**I**) and *in-situ*-generated imine (**II**) formed the π-π stacked ionic complex (**III**), followed by the proton transfer (PT). Upon the irradiation of blue light (456 nm), an electron transfer process occurred to provide α-amino radical (**VI**) and Hantzsch ester intermediate (**IV**). α-Amino radical (**VI**) further reacted with the polarity-matched olefin to deliver the open-shell intermediate (**VII**), which abstracted an atom of H(D) from (**IV**) to provide the final product (**VIII**) and Hantzsch pyridine (**V**).

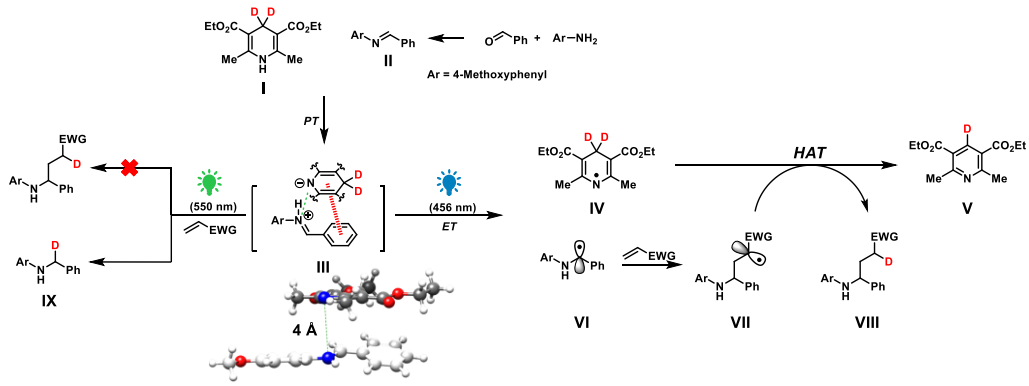

Figure 3.10. Proposed mechanism for three-component coupling reactions.

We measured the UV-absorption bands of both the imine substrate and the Hantzsch ester to confirm the existence of π-π stacked complex

III (**Figure 3.14**). The absorption band of their mixture did not display any shift. In addition, cyclic voltammetry (CV) titration has been carried out to detect the transient complex. When HE **4a** added in solution of model imine (10 mM), new peak has shown and the current of new peak was linearly increased with increasing concentration of HE **4a** (**Figure 3.22**). At last, we carried out the model reaction under green light (550 nm) to find the proof for **III**. Although the desired product **VIII** was not obtained, we obtained the direct hydrogenation product **IX** in 44% yield (7% yield under dark, see **SI 3.5.4.3**). Since **I** and **II** cannot be directly excited by green light, along with the CV titration we can speculate that a π-π stacking complex between **I** and **II** was present.

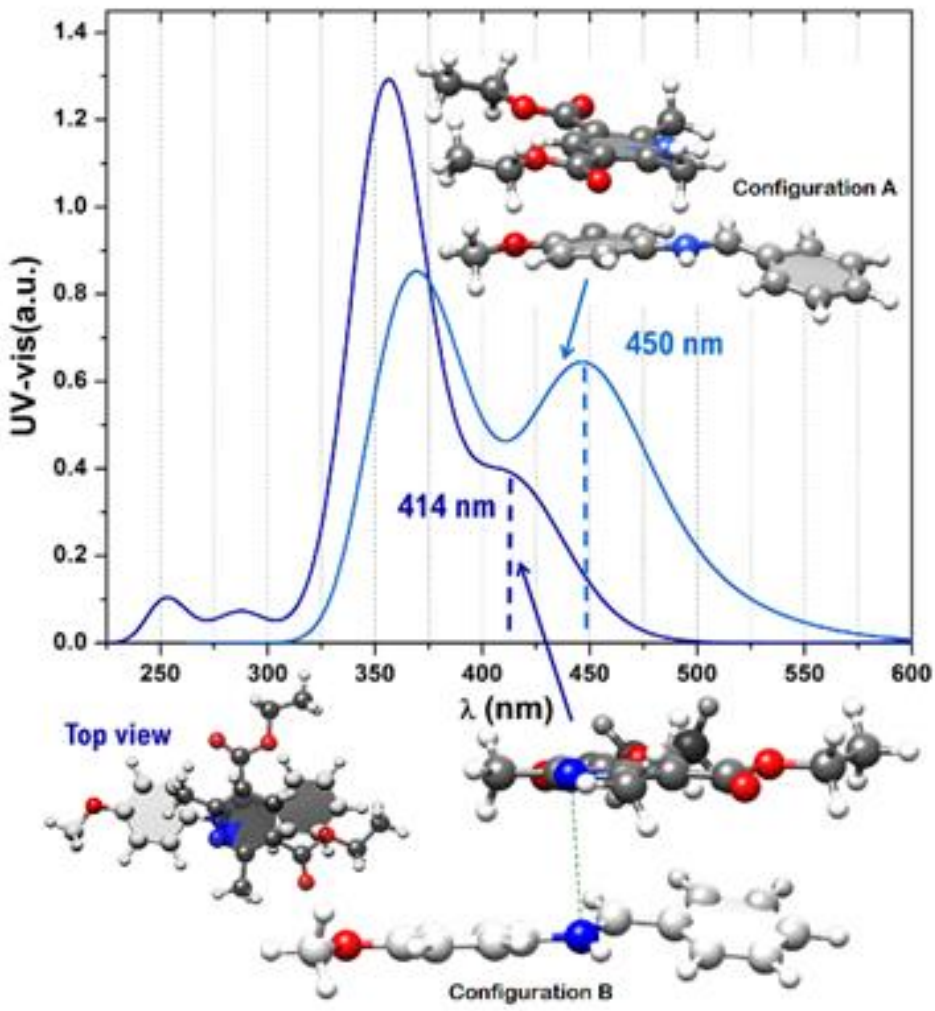

Figure 3.11. CAM-B3LYP/6-311+G(d,p) absorption spectrum of the stacked-rings ionic complexes of an iminium cation and **4a** anions optimized at the B3LYP/6-311+G(d,p) level in solution. In the geometry corresponding to the light blue curve, the Hantzsch ester has already released one of the H(C) (configuration A), whereas, in the other configuration below the plot, the H(N) was released (configuration B).

Among the ionic complexes identified through QC calculations, two promising configurations, presenting UV-vis spectra in agreement with the experiments, are shown in **Figure 3.11**. Only configuration B could be stabilized, as demonstrated by the labelling experiment (**Figure 3.12,**

B-C). On the contrary, configuration A consisting of an HE that had lost one of its H(C) which was stacked on the iminium ion, could not be stabilized and evolved towards a final configuration made of neutral species. We could speculate that, most probably, **III** (configuration B) is the species activated by blue light that induces an electron transfer to obtain the corresponding radical species.

Furthermore, Stern-Volmer fluorescence quenching experiments revealed that the Hantzsch ester was quenched neither by the aldehyde nor by the amine but rather by the imine **II** (**Figure 3.13**). In fact, the fluorescence intensity decreased with the increase of imine concentration, while only slight changes were observed for aldehyde and amine. In order to prove the generation of **VI** in the system, the model reaction was further carried out without the presence of *n*-butyl acrylate, and the dimer of **II** was observed (**Figure 3.12, A**). Furthermore, we expected the presence of a HAT process between **IV** and **VII** to provide product **VIII**. Hence, labelling reactions were carried out with deuterated-Hantzsch esters (**4c** and **4d**). As shown in **Figure 3.12**, **5s** was formed in dramatically decreased yield, and no deuterated product was observed. This was due to the fact that N-D bond was not stable and was easily exchanged with a hydrogen atom (**Figure 3.12, B**). In contrast, **5s-D** was successfully obtained in slightly decreased yield, and no H/D exchange occurred since only the deuterated product was detected (**Figure 3.12, C**). To further verify the HAT, process, an intermolecular competition reaction was carried out and 55% combined yield of **5s** and **5s-D** was obtained; the ratio of **5s** and **5s-D** was 9:1 (**Figure 3.12, D**). This intermolecular competition reaction suggested that this procedure was going *via* a HAT pathway.[39] *N*-methyl Hantzsh ester (**4e**) was also examined under standard reaction conditions, and only a trace amount of the product was obtained. As expected, deuterated solvents had no apparent effect on the product (see **SI 3.5.4.3**).

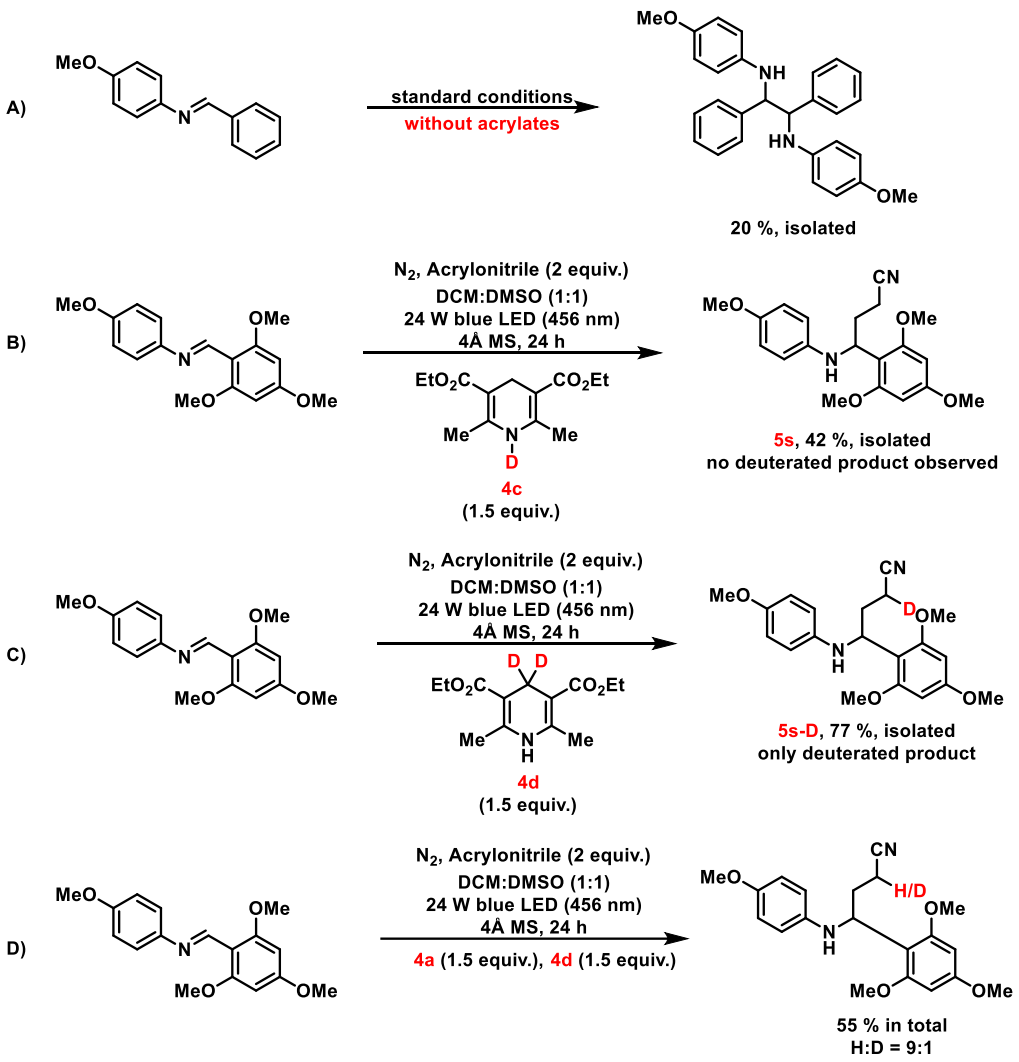

Figure 3.12. Control experiments and labelling reactions.

3.4 Conclusion

We have explored a novel visible-light-induced procedure for the reductive generation of synthetically important α-amino radicals *via* a π-π stacked ionic complex. Notably, multiple π interactions stabilized the reactive intermediate, and neither photocatalysts nor initiators were required in this Giese-type three-component coupling system. A wide range of amines, aldehydes, and olefins displayed reactivity. We believe this protocol could find more opportunities for synthesizing underexplored amines in both academic and industrial branches of organic synthesis.

3.5 Supporting Information

3.5.1 Chemicals and solvents

All reagents and solvents were purchased from certified chemical vendors and used without prior purification. Demineralized water was obtained through deionization of tap water using a EUROTEC L4 reverse osmosis installation. This instrument filters out salts by means of a semi-permeable membrane. Water that was used never exceeded a conductivity of 0.5 μS/cm. Gases were purchased in high-pressured cylinders (200 bar) and converted to the desired pressure by means of a pressure regulator.

3.5.2 Analysis

3.5.2.1 Nuclear magnetic resonance

^{1}H NMR (400 MHz) and ^{13}C NMR (101 MHz) spectra were recorded using a Bruker Avance III Fourier Transform NMR spectrometer at 300 K unless explicitly stated otherwise, using deuterated solvents as internal standard (^{1}H: δ 7.26 ppm and ^{13}C {^{1}H}: δ 77.2 ppm in $CDCl_3$; ^{1}H: δ 2.50 ppm and 13C {^{1}H}: δ 39.52 in DMSO-d6). Chemical shifts (δ) were expressed in ppm and coupling constants (*J*) in Hertz (Hz). Splitting patterns are reported as: s (singlet), d (doublet), t (triplet), q (quadruplet),

p (pentuplet), m (multiplet) or combinations thereof. Integration of the signals is presented as the number of hydrogen atoms.

3.5.2.2 Chromatography

Thin-layer chromatography was performed using a heptane/ethyl acetate (EtOAc) solvent system as mobile phase and a 0.20 mm silica gel on an aluminium plate (Machery-Nagel Precoated TLC sheets Alugram® SIL G/UV254) as stationary phase. Visualization of the 'spots' was enhanced by illumination with UV-light (254 nm).

Flash chromatography was performed using an automatic chromatographic system (Biotage® or Combiflash®) with on-line UV-detection (254 nm and 280 nm unless explicitly stated otherwise). A heptane/EtOAc solvent system was used as mobile phase and commercial silica cartridges (12-80 g, Grace®) as stationary phase.

3.5.3 Optimization of reaction conditions

Table 3.2. Optimization of three-component coupling reactions.

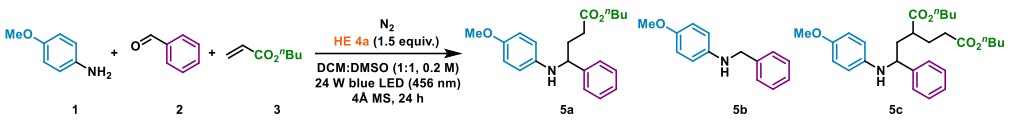

Entry[a]	Variations	Yield of 5a (%)[b]
1	none	72(63[c])
2	DCM (1 mL)	50
3	1.5 equiv. acrylate	62
4	HE (2 equiv.)	72
5	HE 4b (1.5 equiv.)	58
6	4-Ph-HE (1.5 equiv.)	n.ob.
7	4-Cyclohexane-HE (1.5 equiv.)	n.ob.
8	DMSO (1 mL)	61

9	MeCN (1 mL)	60
10	No HE	n.ob.
11	No light	n.ob.
12	Pre-formed imine	35
13	40 W 390 nm Kessil lamp	30
14	40 W 427 nm Kessil lamp	39

[a]Reaction conditions: amine (0.2 mmol), aldehyde (0.2 mmol), acrylate (0.4 mmol), solvent (1 mL). [b]Yield was determined by ^{1}H NMR with 1,3,5-trimethoxybenzene as internal standard. [c]Isolated yields.

Table 3.3. Acid screening for coupling reactions with unactivated aldehydes.

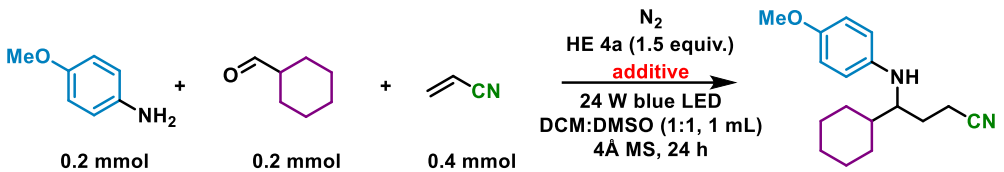

0.2 mmol 0.2 mmol 0.4 mmol

Entry	additives	Yield (%)[a]
1	TFA (0.1 equiv.)	n. ob.
2	Octanic acid (0.1 equiv.)	31
3	Octanic acid (0.1 equiv.), 2 equiv. aldehyde	34
4	Acetic acid (0.1 equiv.)	45(42[b])
5	Butyric acid (0.1 equiv.)	n. ob.
6	Valeric acid (0.1 equiv.)	n. ob.
7	Hexanoic acid (0.1 equiv.)	trace
8	4-Methylpentanoic acid (0.1 equiv.)	n. ob.

[a]Yield was determined by ^{1}H NMR with 1,3,5-trimethoxybenzene as internal standard. [b]Isolated yields.

3.5.4 Mechanistic studies

3.5.4.1 Quenching experiment

Table 3.4. Quenching experiments.

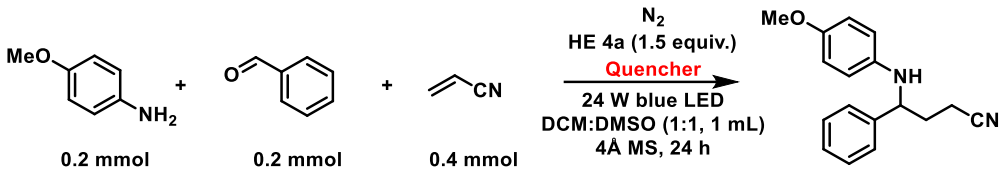

Entry	Quencher (2 equiv.)	Yield (%)[a]
1	TEMPO	13
2	$CuCl_2$	19
3	Under air	8

[a]Yield was determined by ^1H NMR with 1,3,5-trimethoxybenzene as internal standard.

3.5.4.2 Stern-Volmer plot

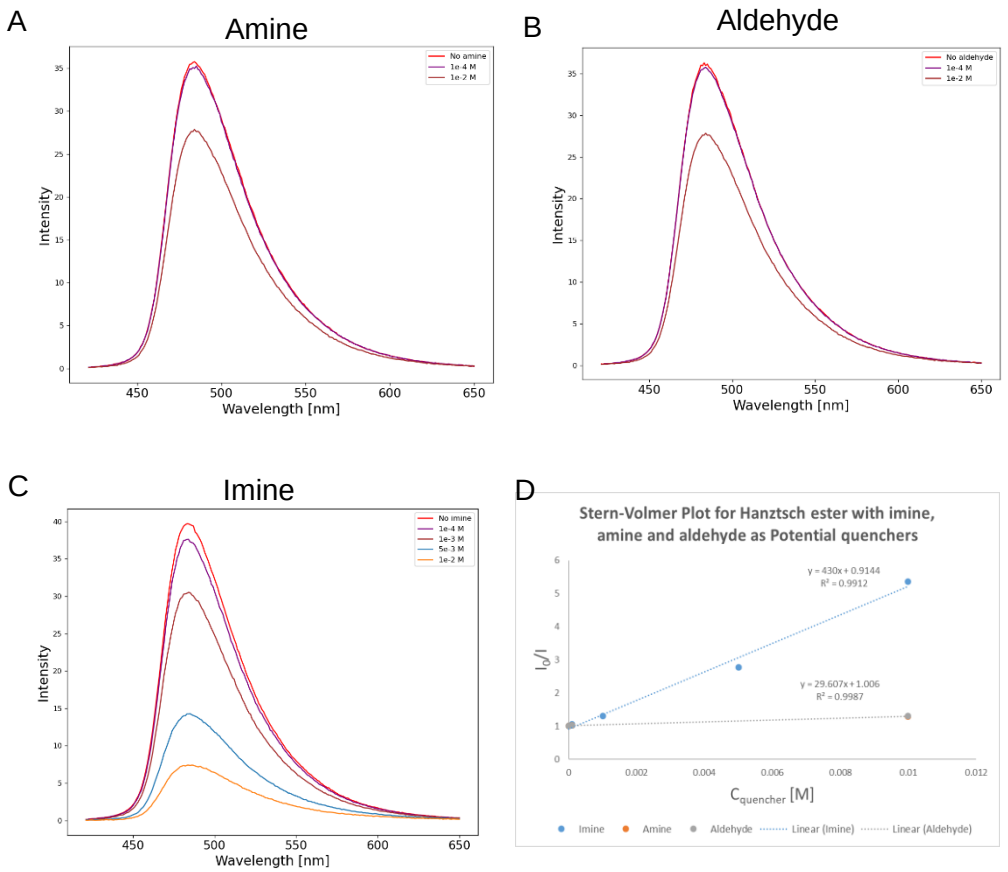

Figure 3.13. Fluorescence quenching experiments were carried out with Cary Eclipse Fluorescence Spectrometer. Amine: *p*-anisidine (A), aldehyde: benzaldehyde (B), imine: *N*-(4-methoxyphenyl)-1-phenylmethanimine (C) as fluorescence quenchers. Stern-Volmer plot with potential quenchers (D).

3.5.4.3 Labeling/control experiments and KIE analysis

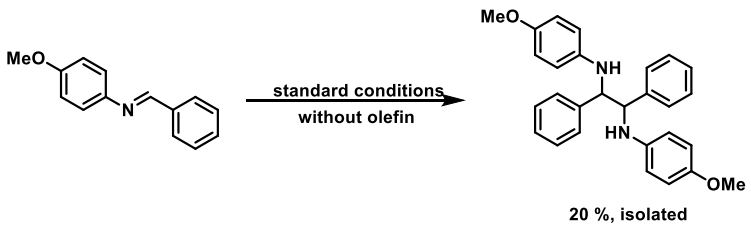

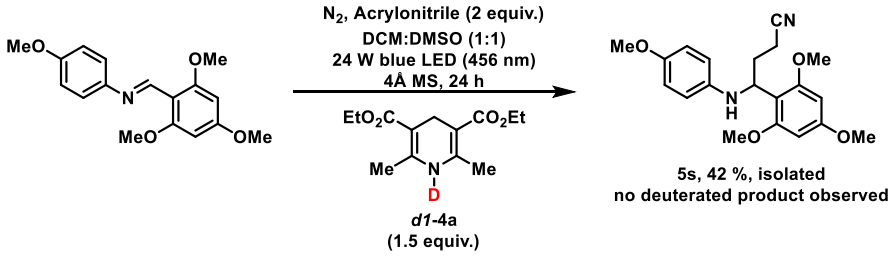

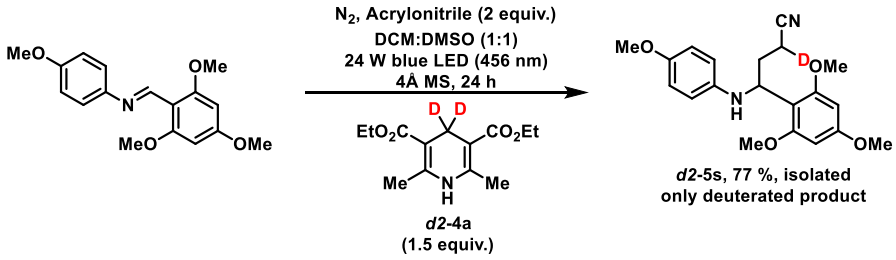

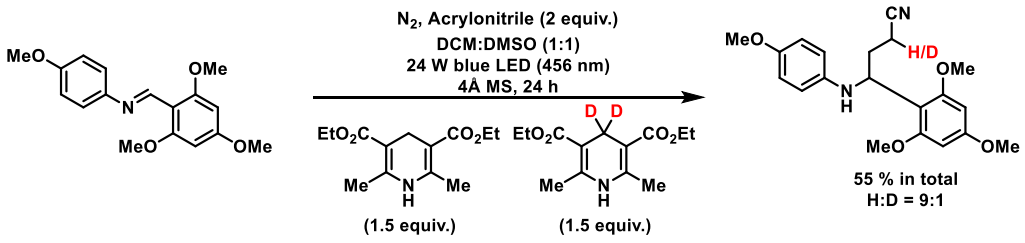

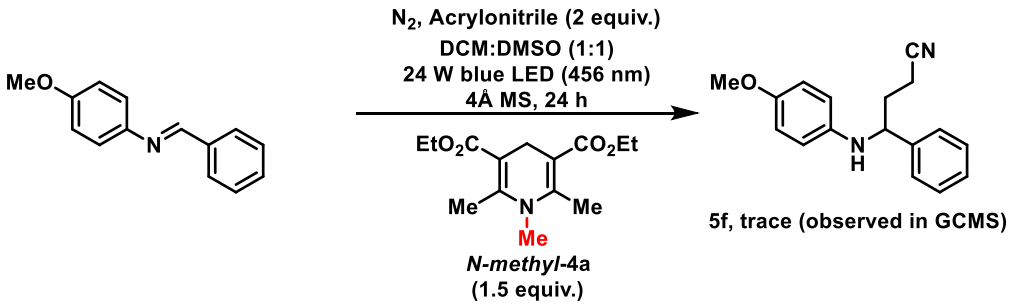
N2, Acrylonitrile (2 equiv.)
DCM:DMSO (1:1)
24 W blue LED (456 nm)
4Å MS, 24 h
MeO
N
EtO2C
CO2Et
Me
N
Me
Me
N-methyl-4a
(1.5 equiv.)
CN
MeO
N
H
5f, trace (observed in GCMS)

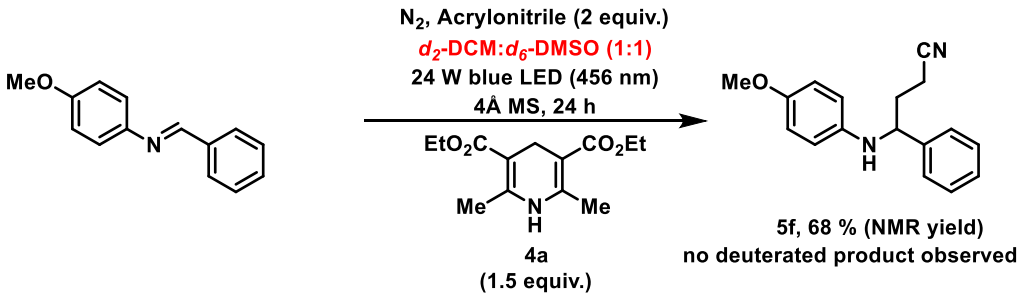
N2, Acrylonitrile (2 equiv.)
d2-DCM:d6-DMSO (1:1)
24 W blue LED (456 nm)
4Å MS, 24 h
MeO
N
EtO2C
CO2Et
Me
N
H
Me
4a
(1.5 equiv.)
CN
MeO
N
H
5f, 68 % (NMR yield)
no deuterated product observed

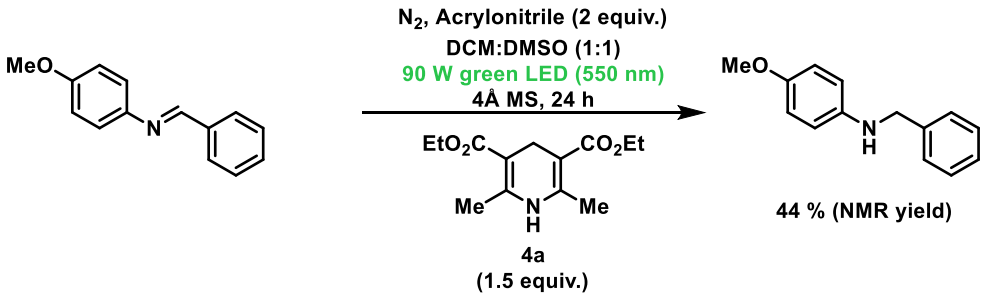
N2, Acrylonitrile (2 equiv.)
DCM:DMSO (1:1)
90 W green LED (550 nm)
4Å MS, 24 h
MeO
N
EtO2C
CO2Et
Me
N
H
Me
4a
(1.5 equiv.)
MeO
N
H
44 % (NMR yield)

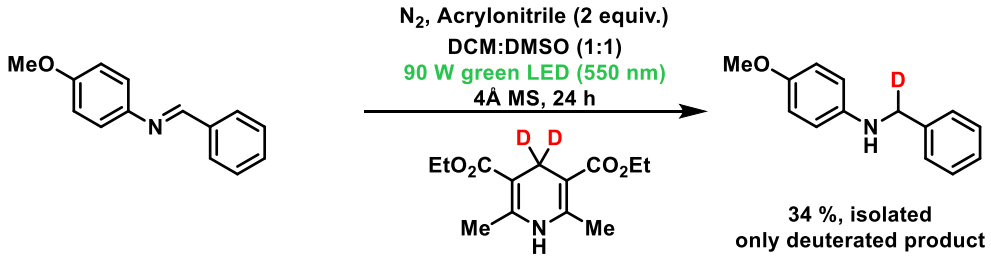
N2, Acrylonitrile (2 equiv.)
DCM:DMSO (1:1)
90 W green LED (550 nm)
4Å MS, 24 h
MeO
N
D
D
EtO2C
CO2Et
Me
N
H
Me
d2-4a
(1.5 equiv.)
MeO
D
N
H
34 %, isolated
only deuterated product

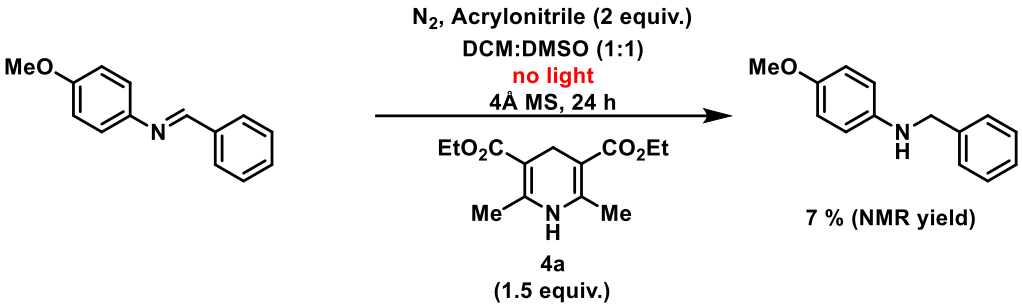

3.5.4.4 UV-Vis absorption studies

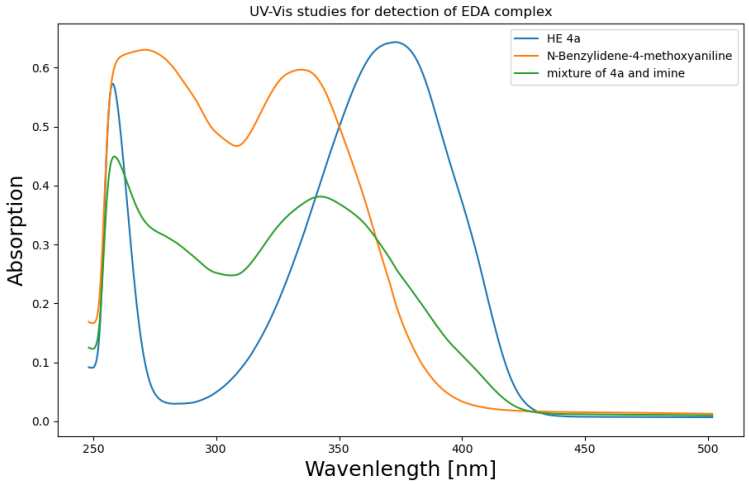

Figure 3.14. UV-Vis absorption studies were performed on a Shimadzu UV-2600 spectrophotometer.

Stock solutions of *N*-benzylidene-4-methoxyaniline and Hantzsch ester were prepared in vials, respectively. From the UV-Vis spectra, the mixture of imine and Hantzsch ester showed no observable 'red shift'. We assumed that the lifetime of ionic complex is short and it is difficult to be experimentally detected via UV-Vis absorption analysis.

3.5.4.5 Electrochemical Measurements

The electrochemical redox potentials were obtained using a Metrohm Autolab potentiostat-galvanostat PGSTAT204 fitted with a glassy carbon (GC) working electrode (diameter = 3 mm), an Ag/AgCl (3 M KCl) reference electrode and a Pt-foil counter electrode, attached to a PC using Nova v2.1.5 software. 0.2 mmol samples were dissolved in 20 mL 0.1 M tetra-*n*-butylammonium hexafluorophosphate in dry, degassed acetonitrile. Reductions were measured by scanning potentials in the negative direction and oxidations in the positive direction. The obtained value was referenced to Ag/AgCl (3 M KCl).

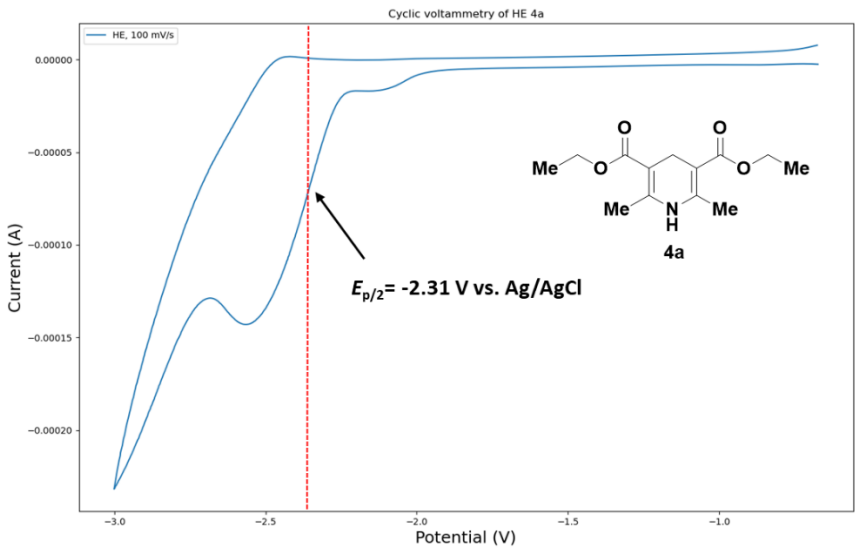

Figure 3.15. Cyclic voltammogram of Hantzsch ester **4a**.

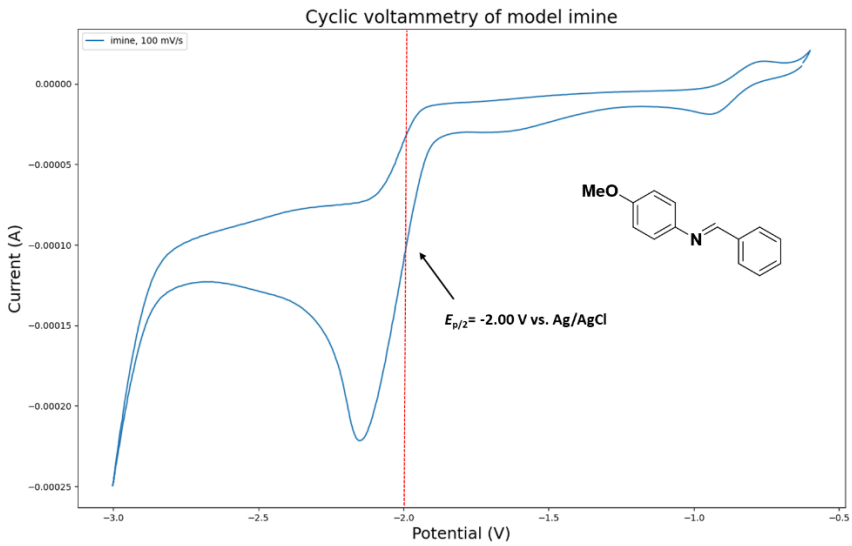

Figure 3.16. Cyclic voltammogram of *N*-(4-methoxyphenyl)-1-phenylmethanimine.

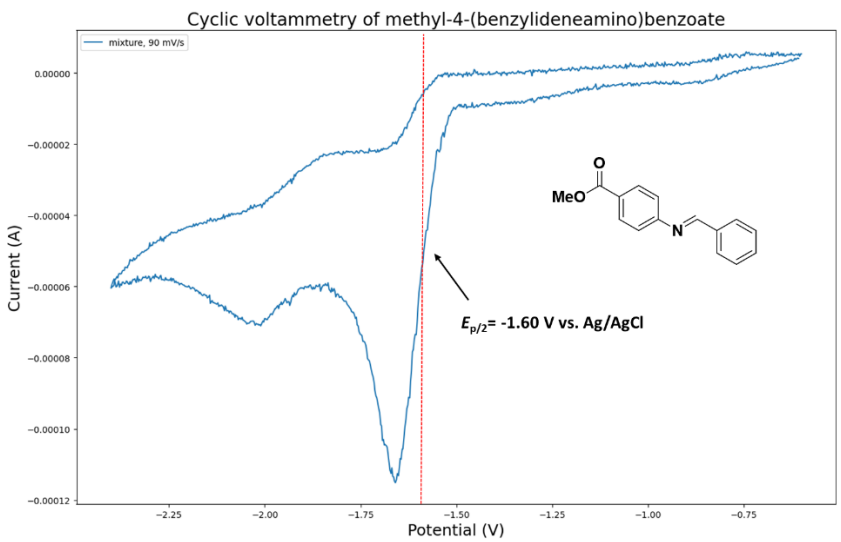

Figure 3.17. Cyclic voltammogram of methyl-4-(benzylideneamino)benzoate.

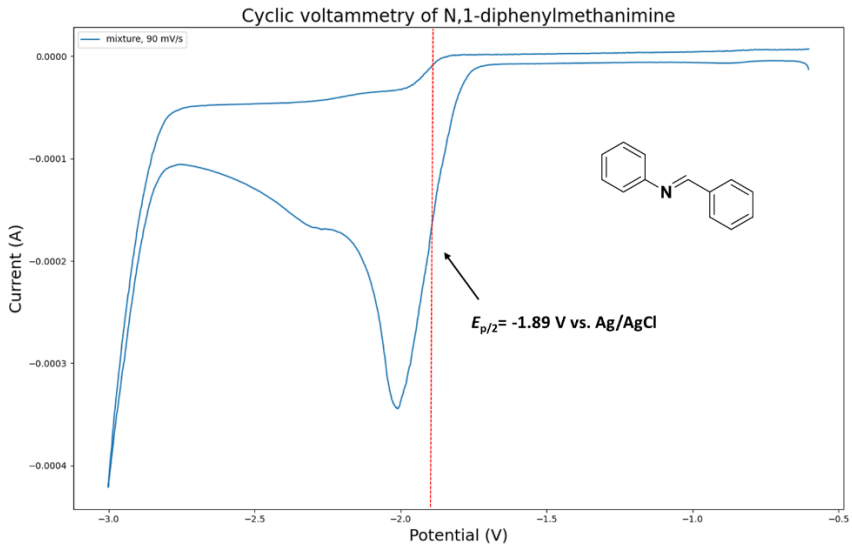

Figure 3.18. Cyclic voltammogram of *N*,1-diphenylmethanimine.

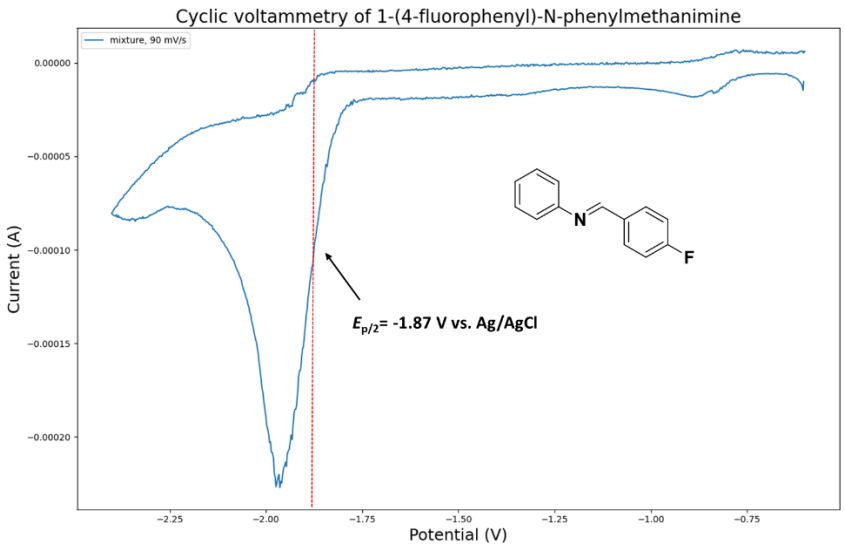

Figure 3.19. Cyclic voltammogram of 1-(4-fluorophenyl)-*N*-phenylmethanimine.

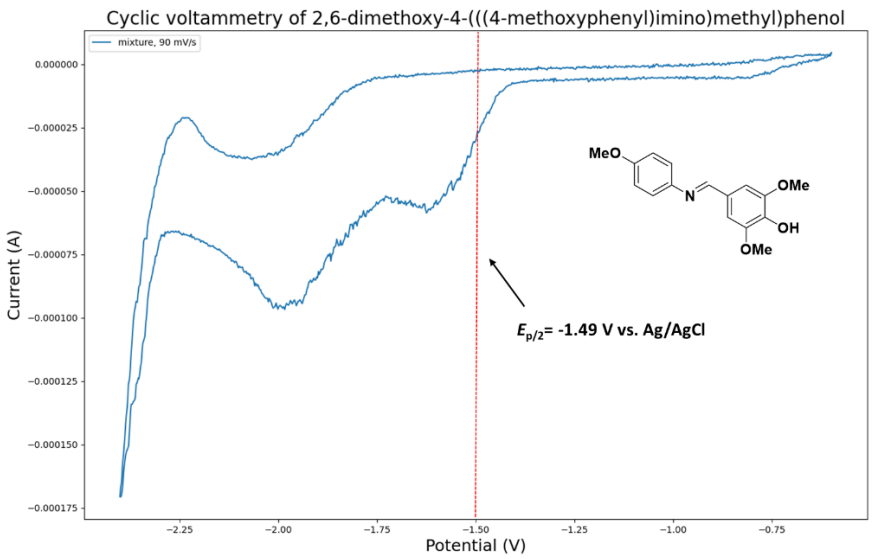

Figure 3.20. Cyclic voltammogram of 2,6-dimethoxy-4-(((4-methoxyphenyl)imino)methyl)phenol.

The redox potentials of Hantzsch ester and representative imines were measured. The redox potentials of imines with electron-donating groups or electron-withdrawing groups on the both amine part or aldehyde part are all located within the potential range between ca. -1.5 V to -2.0 V vs. Ag/AgCl, which are consistent with the literatures.[40,15a] Therefore, the reported imines in the manuscript can be reduced by HE **4a** by single-electron transfer via EDA complexes.

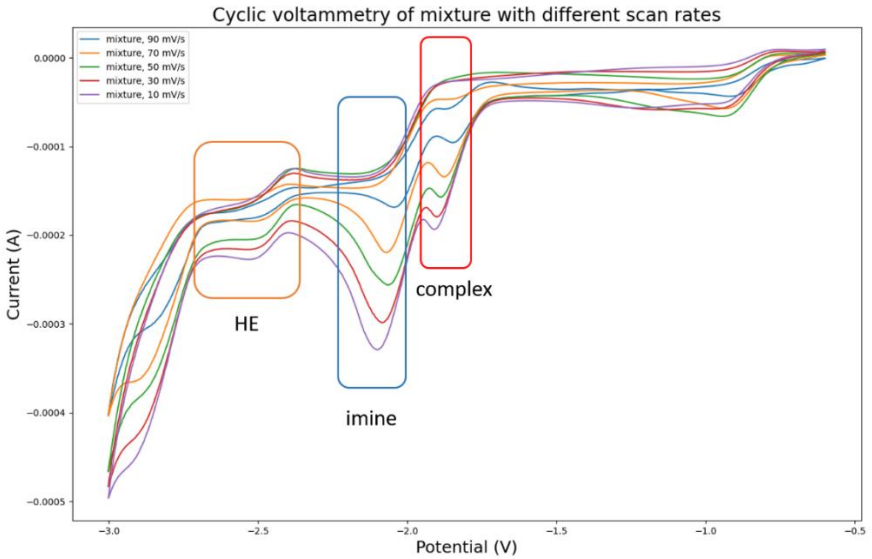

Figure 3.21. Cyclic voltammogram of mixture of HE and model imine (1:1) with different scan rates.

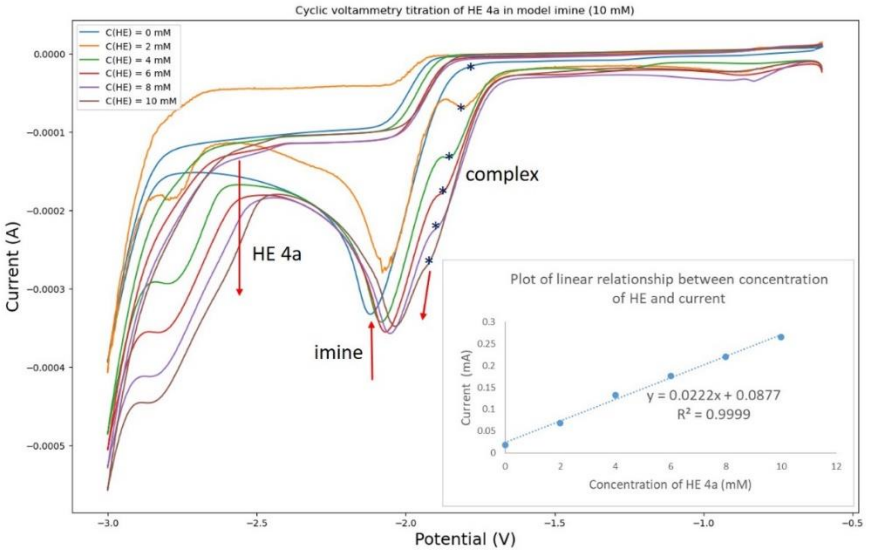

Figure 3.22. Cyclic voltammogram titration of HE in model imine (10 mM).

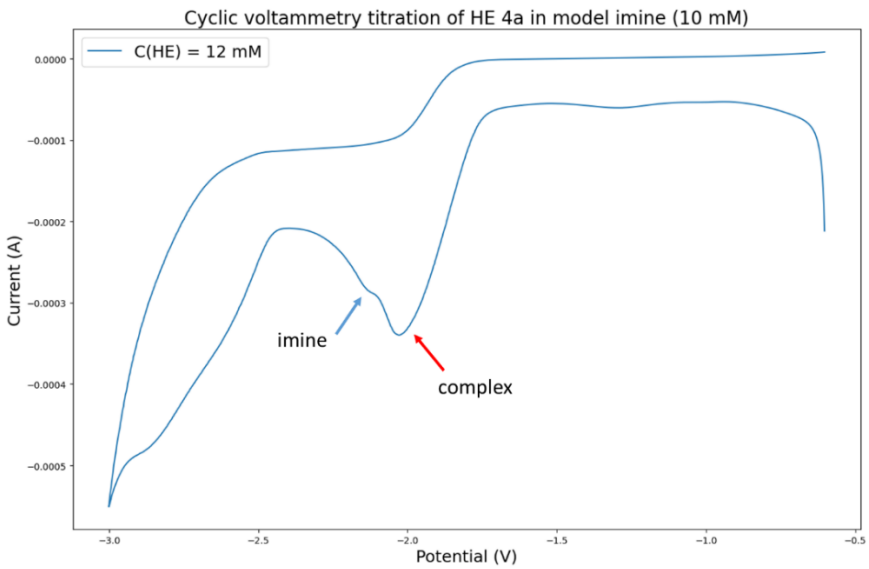

Figure 3.23. Cyclic voltammogram titration of HE in model imine (10 mM).

As shown in **Figure 3.21**, the cyclic voltammetry of mixture of HE and model imine showed not only peaks of HE and imine but also one new peak with lower reduction potential. To further analyze the new peak, cyclic voltammetry titration of HE in imine (10 mM) has been carried out. It is clear that the current of new peak increased linearly with increasing concentration of added HE (**Figure 3.22**). The peak changes of imine and HE were difficult to see since the influence of peak overlap. However, when the concentration of HE **4a** reached 12 mM, the current of imine peak was clearly dropped and the concentration of new peak was further increased (**Figure 3.23**). Therefore, we proposed that this new peak was generated by the complex of HE and imine.

3.5.4.6 Computational Chemistry and NEB calculations

3.5.4.6.1 Computational Chemistry calculations

We investigated the effect of blue light LED on imine-Hantzsch ester complexes in different protonation states, namely neutral molecules or ionic forms, by considering that the Hantzsch esters were extensively used in hydrogen transfer reactions as an electron donor and a proton source in several photoredox processes.

First, we generated possible structures of the complex by a multiobjective genetic algorithm based on a classical force field [41] and optimized all of them (198 in all) at the B3LYP/6-311+G(d,p) level of theory in a continuum solvent description rendered through the polarizable continuum model (PCM) in its integral equation formalism (IEF),[42] choosing dimethyl sulfoxide (DMSO, $\epsilon = 46.70$) as the dominant solvent species acting on the supermolecule. We identified two prevalent arrangements where the phenyl ring of the aldehyde and the ring of the Hantzsch ester were parallel (stacked but shifted) or almost perpendicular (T-shaped) (**Figure 3.24**). In the stacked ring configuration (ester and 4-methoxyphenyl rings), where both of the molecules are neutral, the distance between the ring planes is approximately 5 Å, and the Hantzsch ester NH bond points toward the methoxy oxygen of the imine molecule. The dipole moment of the complex is around 3 Debye. Instead, in the stacked ionic complex, which is made of electron-donating-accepting moieties linked by a π-system with a separation of the planes of about 4 Å (which is shorter than in the neutral molecules case), a distance between the nitrogens of 4.04 Å, and a dipole moment of about 16 Debye, the rings are shifted, and the two nitrogens are on top of each other (**Figure 3.24**). As done by other authors,[43] we calculated the energy difference between the complex and the sum of the energy of the isolated species and found that it was approximately -8.5 kcal/mol. This

validated the stability of this particular assembly. In the hydrogen-bonded complex, where the molecules are in perpendicular orientation, the nitrogen atoms' distance is about 3.11 Å, and each species is neutral because the only stable configuration is the one with the hydrogen linked to the ester. Indeed, although it was linked to the imine in the starting structure, the hydrogen of this bond migrated onto the nitrogen of the Hantzsch ester during the optimization, producing a complex with a relatively low dipole moment of about 7 Debye.

To simulate the UV-vis spectra, we chose the TD-DFT method, combined with the continuum solvent approach, because it was benchmarked on many different systems, which included compounds similar to the molecules examined in this study, and it was used by other authors such as Gaunt and co-workers in their work [11a] to reasonably reproduce the main experimental features of the absorption (CAM-B3LYP/6-311+G(d,p) level of theory). Reliable reference values directly comparable with the molecular models were not available. We checked our choice by examining the experimental UV-vis spectra of the Hantzsch ester (HE) available in the supporting matterials.[33] There, the spectrum of HE in DMSO showed an absorption peak at about 370 nm (**Figure 3.24**). In our case, the peak of HE is at about 350 nm. This 5% discrepancy can be considered acceptable.

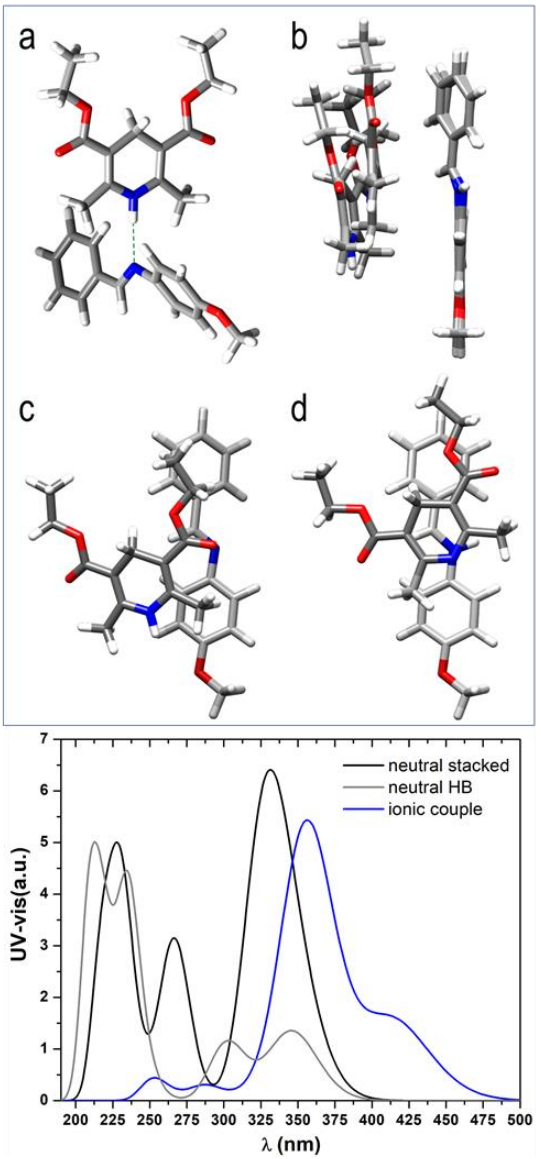

Figure 3.24. **Top**. Optimized geometries of the H-bonded and stacked structures (a, b). The neutral stacked and ionic complexes are superimposed for comparison (b) and shown separately (c, d - top view) to highlight the position of the N atoms. **Bottom**. CAM-B3LYP/6-311+G(d,p)/DMSO absorption spectrum of the H-bonded (gray line) and stacked-rings complexes optimized at the B3LYP/6-311+G(d,p) level in DMSO.

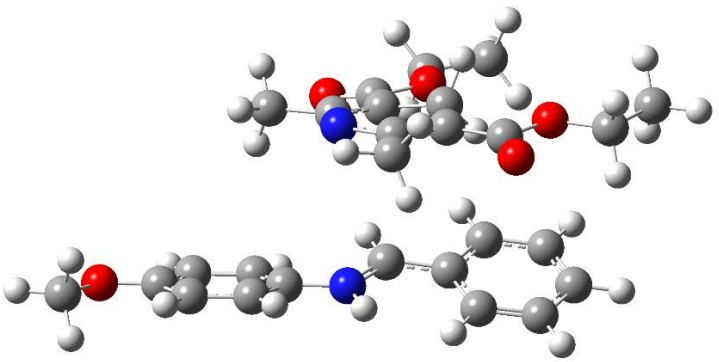

Stacked Configuration (Figure 3) – cartesian coordinates

C	-4.33802800	-0.64660500	0.91540400
C	-3.23996500	-1.17106000	1.82422100
C	-3.55234000	-1.60485200	3.10113200
N	-4.82398100	-1.64648800	3.59490100
C	-5.86698600	-1.37084200	2.77703600
C	-5.72251100	-0.97488600	1.44768100
C	-2.51742300	-2.07875000	4.09675700
C	-7.21164000	-1.52363200	3.45230900
C	-1.87512900	-1.13525500	1.33929100
O	-1.79403200	-0.53144500	0.10834200
C	-0.48478600	-0.43909600	-0.48991300
C	-0.63056300	0.28266800	-1.81559600
C	-6.86375300	-0.71434200	0.59886800
O	-6.48216500	-0.18164500	-0.61161900
C	-7.53391900	0.12786300	-1.54904200

C	-6.89167300	0.71639100	-2.79036600
O	-0.85763500	-1.56048600	1.88670500
O	-8.05734800	-0.91234300	0.83394500
N	-5.52758700	-5.05483100	1.53671600
C	-5.56951500	-4.32609000	0.45078900
C	-4.51179700	-4.21812800	-0.51766900
C	-3.30522000	-4.94767400	-0.44189100
C	-2.35257600	-4.81563800	-1.43798100
C	-2.58210800	-3.96456600	-2.52616600
C	-3.77024700	-3.24131700	-2.61428300
C	-4.73000100	-3.36344600	-1.61714600
C	-6.58788700	-5.32286700	2.44270900
C	-6.25896000	-5.76146200	3.72463400
C	-7.25669300	-6.04133100	4.65181700
C	-8.60064100	-5.88330700	4.29191300
C	-8.92565300	-5.45783600	2.99315100
C	-7.93142900	-5.18507500	2.07195500
H	-5.21947500	-5.87457100	4.01093000
H	-6.97558300	-6.37443000	5.64069000
H	-9.96898900	-5.36234300	2.71964200
H	-8.20929900	-4.88953400	1.06839700
H	-3.10623900	-5.62558700	0.38006400

H	-5.65464500	-2.80289600	-1.68295100
H	-1.42973300	-5.37922800	-1.37664200
H	-3.94810300	-2.58402900	-3.45639700
H	-1.83300900	-3.87232400	-3.30370500
H	-6.49617700	-3.80153100	0.25633200
H	-4.23181300	0.44223800	0.77479900
H	-4.21273400	-1.05529300	-0.09177100
H	-7.78822300	-2.34421100	3.02045600
H	-7.04798700	-1.72202500	4.51177200
H	-7.82388800	-0.62733400	3.33506500
H	-3.01090300	-2.26232200	5.05152700
H	-2.03607100	-3.00085400	3.76060500
H	-1.71570900	-1.35011900	4.22988200
H	-0.08095000	-1.44593900	-0.62472200
H	0.18178200	0.10023400	0.18752700
H	0.34820700	0.37027500	-2.29478300
H	-1.29363400	-0.26371700	-2.49062200
H	-1.03193100	1.28899600	-1.67274700
H	-8.08963000	-0.78458500	-1.78074300
H	-8.22960800	0.83267900	-1.08696100
H	-7.66649200	0.96673700	-3.51995000
H	-6.33965000	1.62892200	-2.55232300

H	-6.20397700	0.00484400	-3.25386300
O	-9.64911000	-6.12691700	5.11302200
C	-9.39295100	-6.57546800	6.45000500
H	-8.81911300	-5.83149400	7.00838800
H	-10.37088300	-6.70182800	6.90854800
H	-8.86269800	-7.53127100	6.44641900
H	-4.64637000	-5.49990400	1.77471400

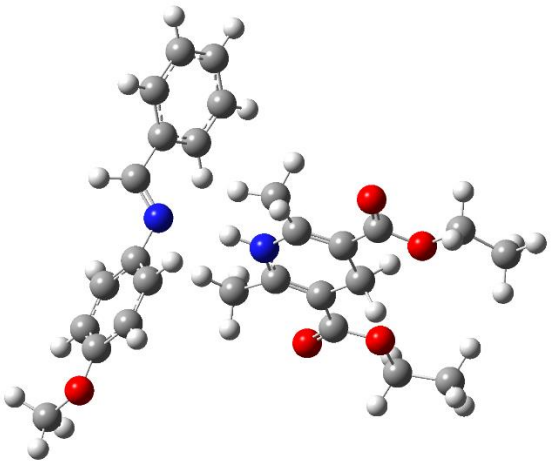

HB-bonded Configuration (Figure 3) – cartesian coordinates

C	-3.49433800	0.05398100	0.46374700
C	-3.28449800	-0.30129400	1.80457400
C	-3.89382400	-1.42557900	2.34145400
C	-4.70906800	-2.24135500	1.54493000
C	-4.90686300	-1.90919200	0.20315700
C	-4.29976200	-0.76705900	-0.32699900
H	-2.65001400	0.31856900	2.42761200
H	-3.74342900	-1.69114100	3.38142700
H	-5.52086200	-2.52261800	-0.44204600
H	-4.45108300	-0.52646600	-1.37301500
O	-5.25370000	-3.33059500	2.16538800
C	-6.08836700	-4.20244400	1.40051600
H	-6.40788100	-4.98458200	2.08629500
H	-6.96581200	-3.67396500	1.01644900

H	-5.53569200	-4.65012200	0.56923200
N	-2.79833600	1.16518500	-0.08270900
C	-2.58729300	3.32337700	-1.06546000
C	-1.54676200	2.98280400	-1.94195100
C	-2.83810200	4.68121100	-0.81374400
C	-0.76986200	3.96980300	-2.54264900
H	-1.36343600	1.93919600	-2.16504100
C	-2.04940100	5.66727500	-1.40168600
H	-3.63224100	4.97591200	-0.13909200
C	-1.01589200	5.31537700	-2.26988900
H	0.02219800	3.68916200	-3.22753100
H	-2.24249700	6.71095300	-1.18161300
H	-0.41076300	6.08507400	-2.73504000
C	0.58037100	-0.76821600	-0.90584800
C	1.01139400	0.88004800	0.84466300
C	1.85642900	-1.24139100	-0.84364400
C	2.30368500	0.46394400	0.98233000
N	0.18319600	0.25679600	-0.06923000
H	-0.77894200	0.60682000	-0.15920300
C	2.86606700	-0.67233400	0.14043400
H	3.23863900	-1.47058400	0.79238500
H	3.75298700	-0.32390400	-0.39990000

C	0.34316300	1.99044900	1.61018300
H	0.87537800	2.93199600	1.47071800
H	-0.68839800	2.11033100	1.27858400
H	0.35070000	1.78493000	2.68141500
C	-0.50857800	-1.24161100	-1.82979800
H	-1.44215600	-0.75375000	-1.55384600
H	-0.27004000	-1.00281700	-2.86780500
H	-0.63654300	-2.32165300	-1.77219300
C	2.28883500	-2.31997600	-1.73229700
C	3.19695800	1.10408700	1.94837600
O	1.62695300	-2.88594800	-2.59226900
O	2.94561900	2.04607000	2.68808000
O	3.58503700	-2.66230300	-1.49451300
O	4.44601100	0.56569700	1.89106400
C	4.14421000	-3.72584500	-2.30061700
H	4.07545800	-3.44401300	-3.35377900
H	3.54944800	-4.63029000	-2.15416100
C	5.58284100	-3.92603900	-1.86810200
H	6.03365700	-4.72521600	-2.46211500
H	6.16894300	-3.01635800	-2.01857300
H	5.64122100	-4.20903100	-0.81446200
C	5.44892000	1.13635200	2.76454700

H	5.54735200	2.20108300	2.54084200
H	5.11391100	1.03934000	3.79975300
C	6.74770600	0.39276400	2.52520800
H	7.52695400	0.80309100	3.17259500
H	6.63964200	-0.67046900	2.75230700
H	7.07491100	0.49714900	1.48805900
C	-3.40149500	2.24525400	-0.42631100
H	-4.46070002	2.30991722	-0.22555397

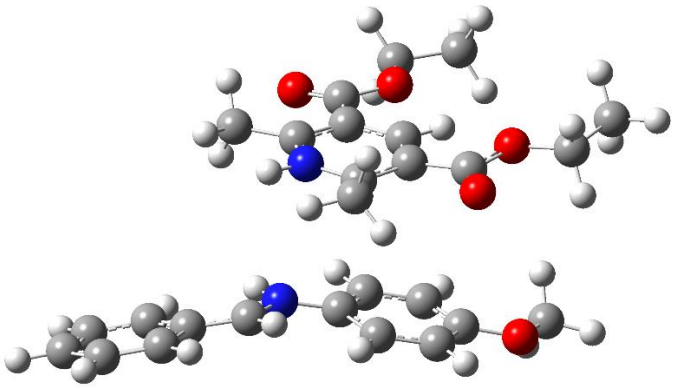

Configuration A (Figure 8) – cartesian coordinates

N	-5.970000	-4.457000	1.993000
C	-6.103000	-3.993000	0.693000
C	-5.029000	-3.714000	-0.171000
C	-3.647000	-3.865000	0.163000
C	-2.645000	-3.606000	-0.764000
C	-2.940000	-3.169000	-2.060000
C	-4.292000	-3.000000	-2.408000
C	-5.303000	-3.267000	-1.503000
C	-6.940000	-5.135000	2.724000
C	-6.636000	-5.600000	4.016000
C	-7.558000	-6.317000	4.773000
C	-8.831000	-6.585000	4.257000
C	-9.147000	-6.130000	2.976000
C	-8.222000	-5.423000	2.215000
H	-5.656000	-5.399000	4.437000

H	-7.269000	-6.655000	5.759000
H	-10.129000	-6.345000	2.569000
H	-8.502000	-5.110000	1.218000
H	-3.356000	-4.206000	1.152000
H	-6.341000	-3.162000	-1.813000
H	-1.610000	-3.747000	-0.466000
H	-4.554000	-2.667000	-3.408000
H	-2.151000	-2.971000	-2.777000
H	-7.103000	-3.859000	0.332000
O	-9.817000	-7.279000	4.921000
C	-9.524000	-7.775000	6.225000
H	-9.286000	-6.963000	6.919000
H	-10.426000	-8.284000	6.562000
H	-8.694000	-8.489000	6.204000
H	-5.045000	-4.443000	2.399000
C	-7.470000	-2.782000	6.141000
C	-8.367000	-2.648000	5.097000
C	-7.899000	-2.262000	3.810000
N	-6.572000	-1.854000	3.773000
C	-5.671000	-1.912000	4.771000
C	-6.101000	-2.377000	6.023000
C	-8.709000	-1.818000	2.633000

C	-4.300000	-1.422000	4.430000
C	-9.825000	-2.891000	5.310000
O	-10.131000	-3.125000	6.592000
C	-11.537000	-3.348000	6.907000
C	-11.641000	-3.562000	8.401000
C	-5.175000	-2.511000	7.157000
O	-5.818000	-2.888000	8.283000
C	-5.002000	-3.105000	9.466000
C	-5.924000	-3.539000	10.586000
O	-10.658000	-2.840000	4.423000
O	-3.966000	-2.327000	7.123000
H	-3.601000	-2.260000	4.418000
H	-4.294000	-0.946000	3.448000
H	-3.938000	-0.717000	5.178000
H	-8.052000	-1.590000	1.789000
H	-9.424000	-2.576000	2.316000
H	-9.283000	-0.912000	2.864000
H	-11.876000	-4.219000	6.343000
H	-12.100000	-2.472000	6.579000
H	-12.688000	-3.731000	8.667000
H	-11.064000	-4.435000	8.712000
H	-11.287000	-2.687000	8.950000

H	-4.255000	-3.868000	9.235000
H	-4.482000	-2.175000	9.705000
H	-5.336000	-3.708000	11.492000
H	-6.670000	-2.770000	10.802000
H	-6.439000	-4.469000	10.335000
H	-6.243000	-1.482000	2.891000
H	-7.826000	-3.123000	7.103000

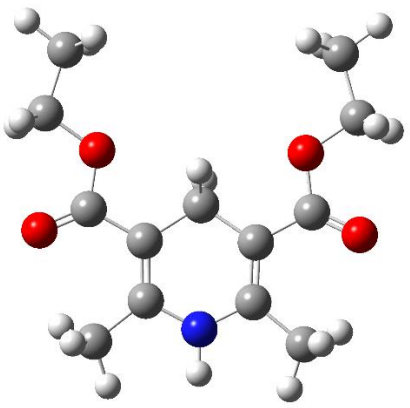

Hantzsch ester (4a) – cartesian coordinates

C	-3.06402100	1.67582000	3.09817900
C	-0.83685500	2.19487800	2.20713800
C	-3.47383300	2.96413600	2.94107900
C	-1.17018900	3.50053000	2.01630800
C	-2.50498200	4.05077100	2.49808700
H	-2.96270800	4.64411600	1.70320900
H	-2.34174900	4.76310800	3.31764800
C	0.45864900	1.52607000	1.83744300
C	-3.89251500	0.51486600	3.57677500
H	-3.25941700	-0.35393400	3.76806600
H	-4.43504800	0.76627800	4.48652200
H	-4.63916500	0.23984200	2.82869300
C	-4.85658800	3.34644200	3.23597600
C	-0.23170100	4.42420500	1.37362700
O	-5.77771200	2.60554700	3.55296500

O	0.84666600	4.14901500	0.86448500
O	-5.03130200	4.68749100	3.11799700
O	-0.70307600	5.69674400	1.39567400
C	-6.36003600	5.20382500	3.37723800
H	-6.64921300	4.93254300	4.39486000
H	-7.06148800	4.72905000	2.68767100
C	-6.31560800	6.70621700	3.18770700
H	-7.30670900	7.12563700	3.37872000
H	-5.60935400	7.16940400	3.88071400
H	-6.02574500	6.96595900	2.16690800
C	0.12196100	6.71612000	0.77942200
H	1.09321900	6.73038700	1.27858200
H	0.28277800	6.45086900	-0.26782100
C	-0.60072700	8.04018300	0.91932900
H	-0.00094700	8.83120900	0.46188700
H	-1.57102500	8.01389100	0.41797400
H	-0.75660400	8.29426900	1.97037600
H	0.51807300	1.37345300	0.75701500
H	1.31360100	2.13700200	2.11905000
H	0.53691900	0.55243900	2.32563300
H	-1.48273700	0.38053300	2.91542000
N	-1.75659900	1.34351900	2.79301400

Other structures are available from the corresponding authors upon request.

Table 3.5. Calculated Absorption Energies (eV, and in the corresponding Wavelength, nm) and oscillator strengths for the different Hantzsch Ester (HE) species and the selected HE complexes.

Molecule	Energy (eV)	Wavelength (nm)	Oscillator strength
HEH(4a) neutral	3.56	348.5	0.2003
HE (4a) anionic	2.96	418.3	0.3013
HEH (4b) neutral	3.55	349.1	0.2068
HE (4b) anionic	2.97	417.0	0.3138
HEH (phenyl) neutral	3.80	326.4	0.1835
HE (phenyl) anionic	3.15	393.1	0.2643
HEH (cyclohexyl) neutral	3.86	321.3	0.1883
HE (cyclohexyl) anionic	3.23	383.4	0.2921
Stacked complex (Figure 3)	2.99	414.1	0.2281
T-shaped complex (Figure 3)	3.50	354.2	0.1999
Configuration A (Figure 8)	2.74	452.6	0.1559

CAM-B3LYP/6-311+G(d,p)/DMSO absorption spectra computed for the stacked complex and T-shaped complexes optimized at the B3LYP/6-311+G(d,p) level in DMSO (artificially broadened with gaussian peaks – HWHH = 0.1 eV).

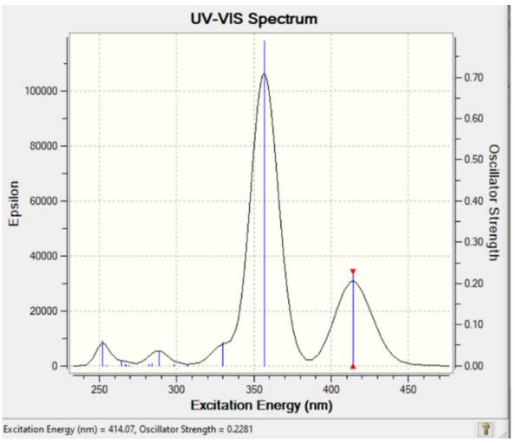

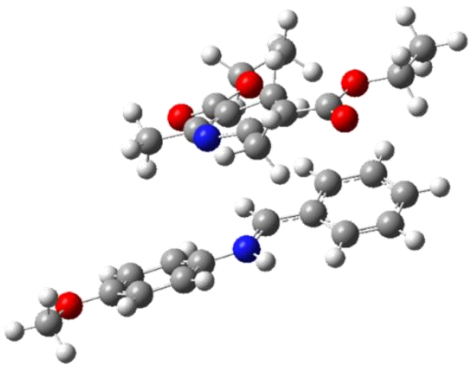

Stacked Complex

Excited State	1:	1.6608 eV	746.51 nm	f=0.0450
Excited State	2:	2.9943 eV	414.07 nm	f=0.2281
Excited State	3:	3.4770 eV	356.58 nm	f=0.7886
Excited State	4:	3.7611 eV	329.65 nm	f=0.0562
Excited State	5:	4.0385 eV	307.00 nm	f=0.0013
Excited State	6:	4.1586 eV	298.14 nm	f=0.0024
Excited State	7:	4.2956 eV	288.63 nm	f=0.0342
Excited State	8:	4.3663 eV	283.96 nm	f=0.0056
Excited State	9:	4.3960 eV	282.04 nm	f=0.0035
Excited State	10:	4.6040 eV	269.29 nm	f=0.0005
Excited State	11:	4.6383 eV	267.30 nm	f=0.0004
Excited State	12:	4.6448 eV	266.93 nm	f=0.0021
Excited State	13:	4.6957 eV	264.04 nm	f=0.0101
Excited State	14:	4.8666 eV	254.77 nm	f=0.0009
Excited State	15:	4.9189 eV	252.06 nm	f=0.0594

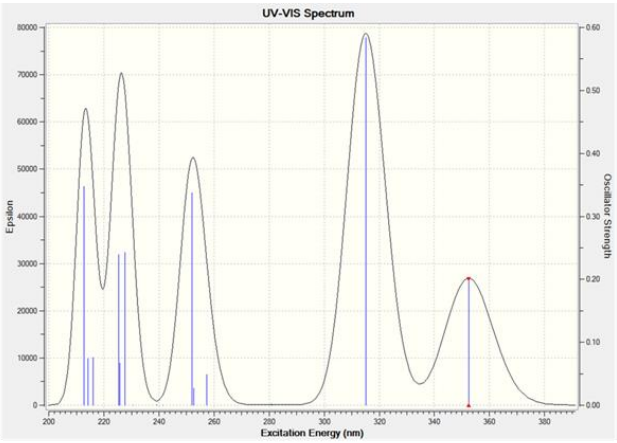

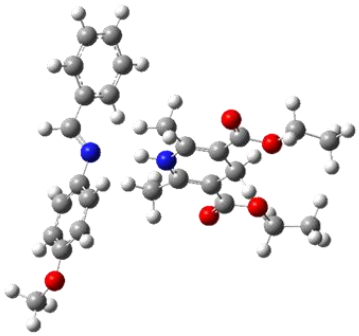

H-bonded Complex

Excited State	1:	3.5177 eV	352.46 nm	f=0.2001
Excited State	2:	3.9351 eV	315.08 nm	f=0.5841
Excited State	3:	4.4153 eV	280.80 nm	f=0.0016
Excited State	4:	4.8173 eV	257.37 nm	f=0.0488
Excited State	5:	4.9100 eV	252.51 nm	f=0.0275
Excited State	6:	4.9210 eV	251.95 nm	f=0.3377
Excited State	7:	5.1341 eV	241.49 nm	f=0.0002
Excited State	8:	5.1844 eV	239.15 nm	f=0.0012
Excited State	9:	5.3771 eV	230.58 nm	f=0.0002
Excited State	10:	5.4469 eV	227.62 nm	f=0.2428
Excited State	11:	5.4915 eV	225.77 nm	f=0.0669
Excited State	12:	5.5041 eV	225.26 nm	f=0.2388
Excited State	13:	5.7408 eV	215.97 nm	f=0.0754
Excited State	14:	5.7892 eV	214.16 nm	f=0.0736
Excited State	15:	5.8266 eV	212.79 nm	f=0.3474

M062X/6-311+G(d,p)/DMSO absorption spectra computed for the stacked complex and T-shaped complexes optimized at the B3LYP/6-311+G(d,p) level in DMSO (artificially broadened with gaussian peaks – HWHH = 0.15 eV).

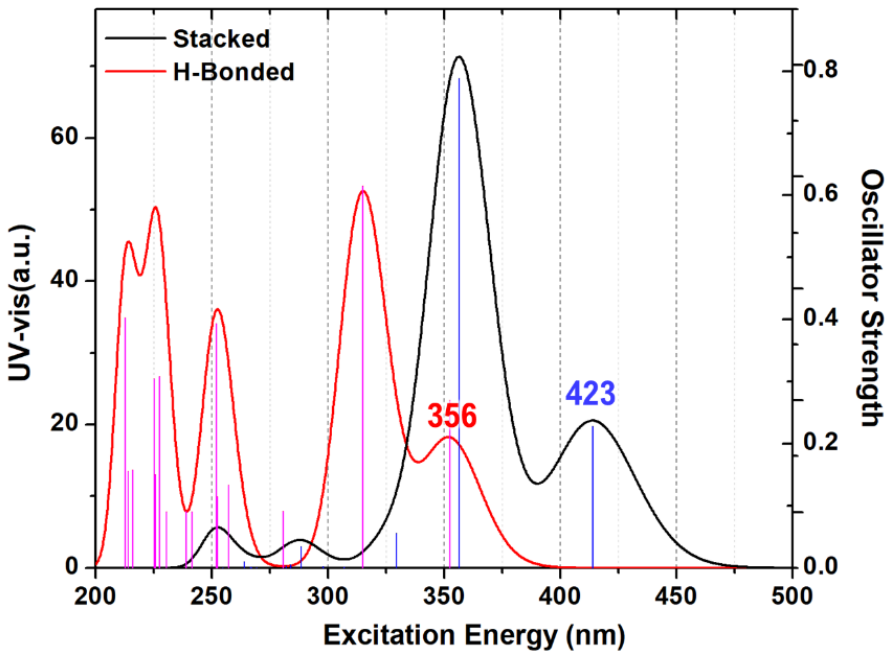

B3LYP/6-311+G(d,p)/DMSO absorption spectra computed for the stacked complex and T-shaped complexes optimized at the B3LYP/6-311+G(d,p) level in DMSO (artificially broadened with gaussian peaks – HWHH = 0.15 eV).

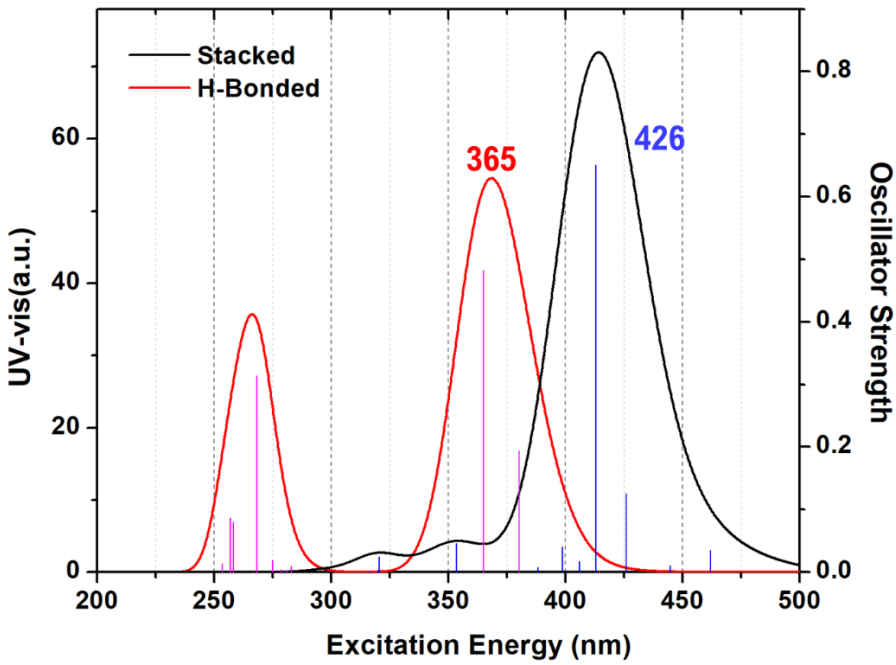

CAM-B3LYP/6-311+G(d,p)/DMSO absorption spectra computed for HEH (4a) and HE (4a) optimized at the B3LYP/6-311+G(d,p) level in DMSO (artificially broadened with gaussian peaks – HWHH = 0.15 eV).

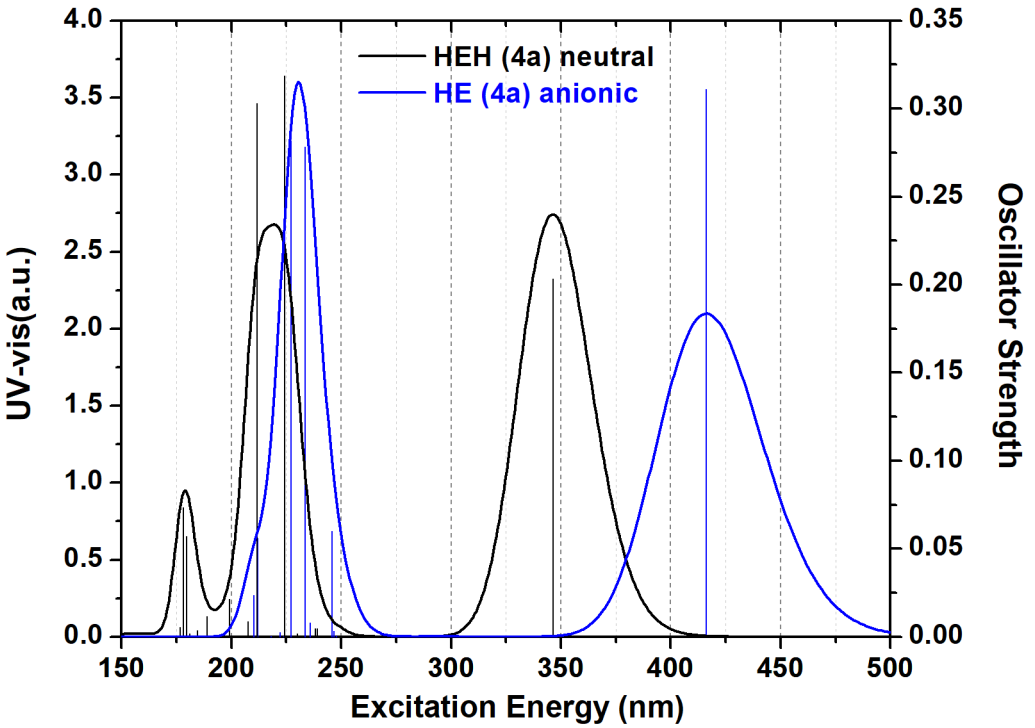

3.5.4.6.2 NEB calculations

To disclose possible minimum-energy paths (MEPs) for the cyclization reactions and estimate the activation energies (transition states -TS) that could be connected to the experimental yield, we used the nudged elastic band (NEB) methodology[44] implemented in the Quantum Espresso [45] software package. The calculations were based on a plane-wave basis set; the projector augmented wave (PAW) method with Perdew–Burke–Ernzerhof (PBE) functional, and kinetic energy cutoffs of 40 Ry and 400 Ry for the wave functions and the charge density, respectively. Single-particle wave functions were calculated through Gaussian smearing of 0.002 Ry. The Brillouin zone sampling was restricted to the gamma point, and all the calculations were spin-polarized. Long-range nonlocal effects were included by applying van der Waals corrections (Grimme-D2 approach).

The energy barriers were estimated considering 8-15 intermediate images between the identified local minima, and a convergence cutoff of 0.05 eV $Å^{-1}$ for the force orthogonal to the path was employed.

After activating the molecules through the blue light (which induces the formation of two radicals, as described above), sets of NEB calculations were carried out to disclose the steps of cyclization. The central panels of **Figures 3.25-3.26** show the energy profiles along the different reaction paths and the structure of the transition states, whereas the left and right panels display the geometries of reactants and products, respectively. In **Table 3.6,** we have reported energy barriers and final energies relative to the starting configuration of the different complexes.

As shown in **Figure 3.25-3.26**, in the starting configurations, the two radicals are rotated with respect to each other, and the HE is near the aldehydic side chain, pointing its ring hydrogens to the C atom connected to the CO_2Me group. During cyclization, one of these Hs is transferred to that C, and the other carbon atom close by gets close to the ring, forming a bond with the radical carbon of the molecule. Eight steps were required to form the final products in all cases, and the energy barriers were relatively low (at most 10 kcal/mol) and in line with the yield results obtained with experiments.

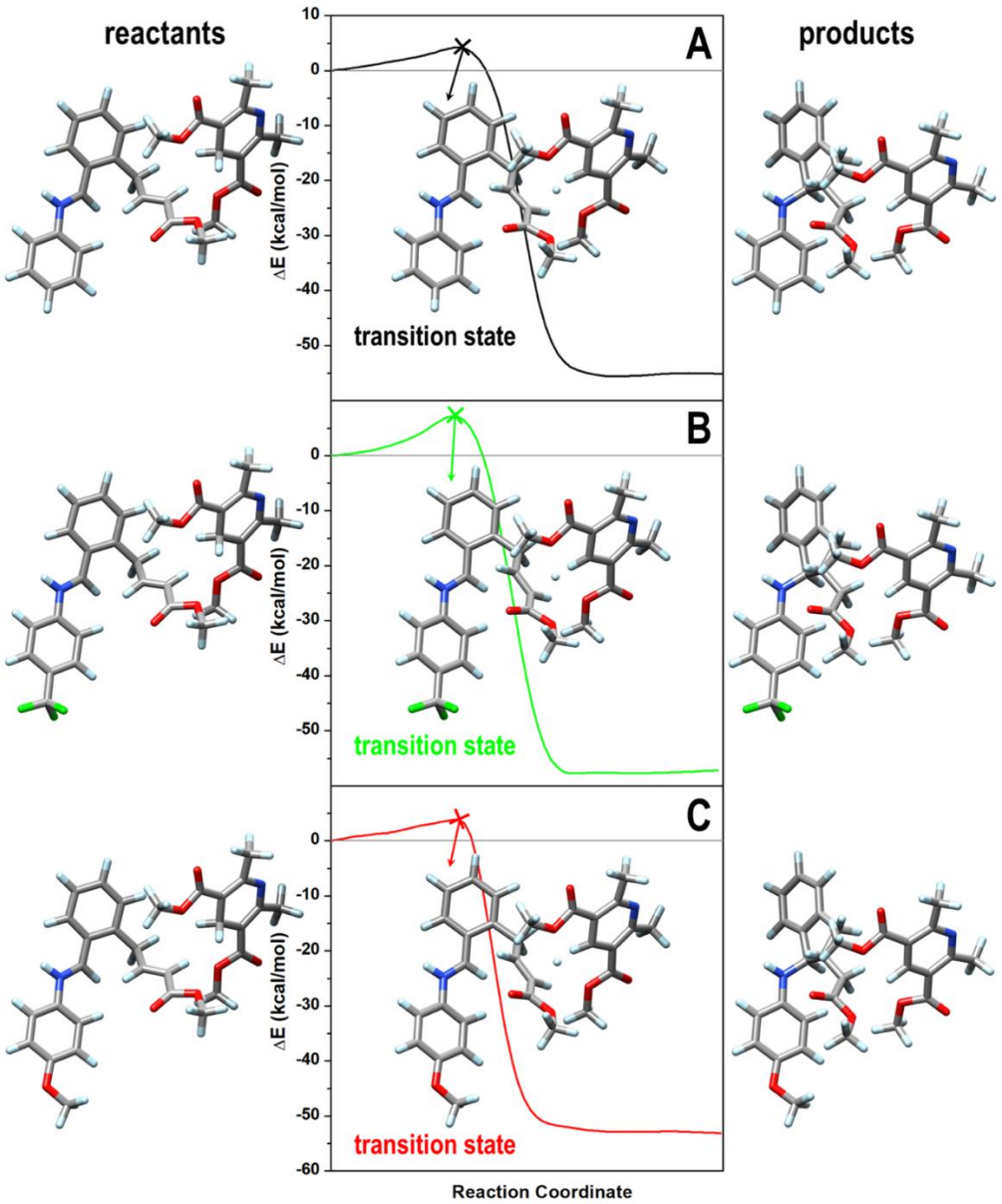

Figure 3.25. Cyclization of compound 7 from NEB calculations. (a) **7a**; (b) **7c**; (c) **7b**.

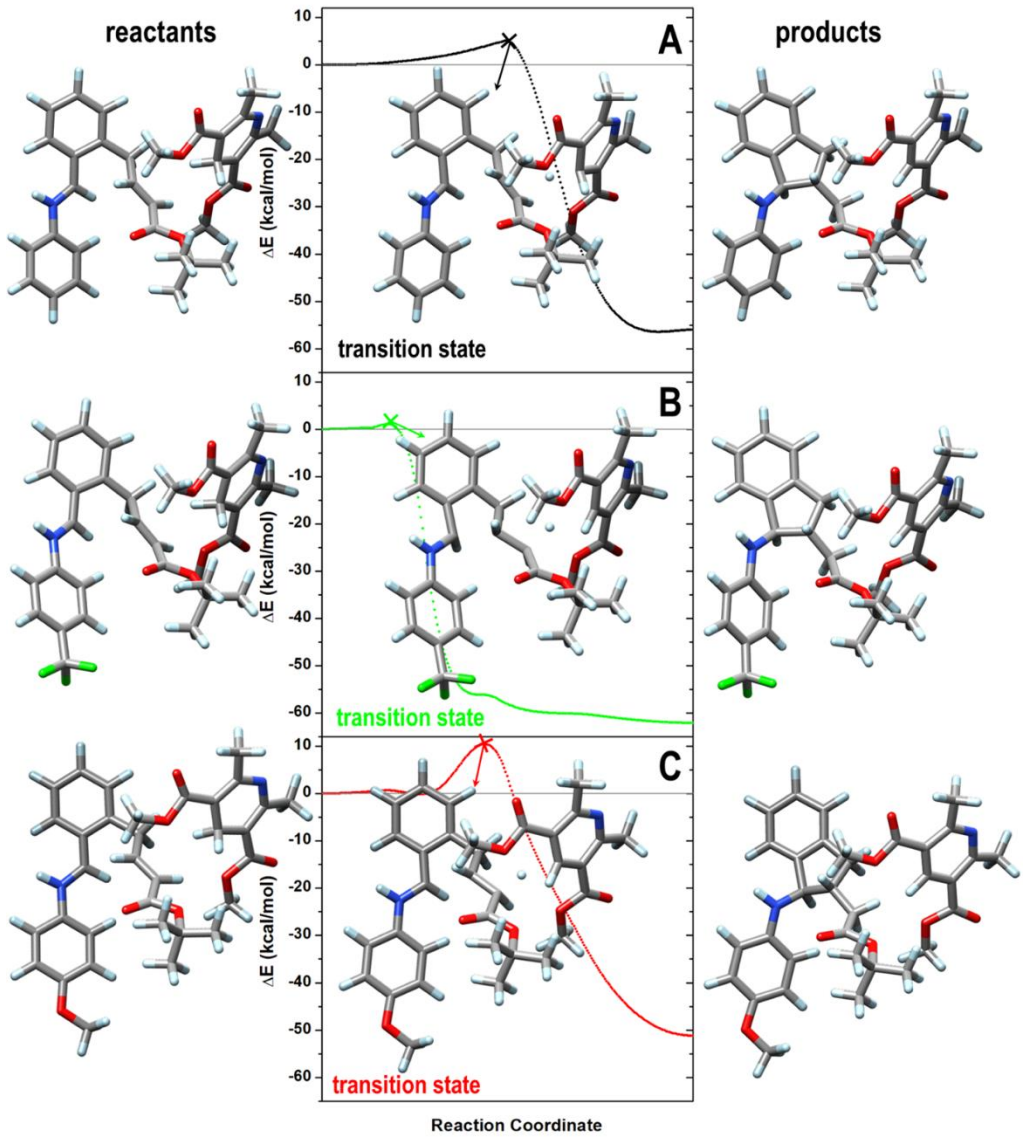

Figure 3.26. Cyclization of compound 7 from NEB calculations. (a) **7d**; (b) **7f**; (c) **7e**.

Table 3.6. Energy barriers (TS) and final energy differences (Products) relative to the starting configuration of the different complexes (**Figures 3.25-3.26**).

compound	Reactant (kcal/mol)	TS (kcal/mol)	Products (kcal/mol)
7a	0	4.2	-55.1
7b	0	3.8	-53.1
7c	0	7.0	-57.2
7d	0	5.1	-56.0
7e	0	10.4	-51.2
7f	0	1.1	-62.1

3.5.5 Experiments

3.5.5.1 Photocatalytic reaction setup

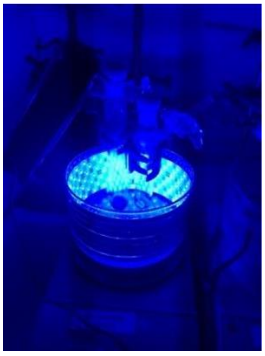

The inner surface of a round glass dish with a diameter of 140 mm was fixed with a blue LED strip with a total power of 24 W (**Figure 3.5.5.1.1**). A switch can control the intensity of illumination. An electric fan was placed over the glass dish to avoid heating by the LED irradiation. Inside the glass dish, two Schlenk flasks were placed. The reaction mixture was stirred using a magnetic stirring plate and stirring bar at 400 rpm on average.

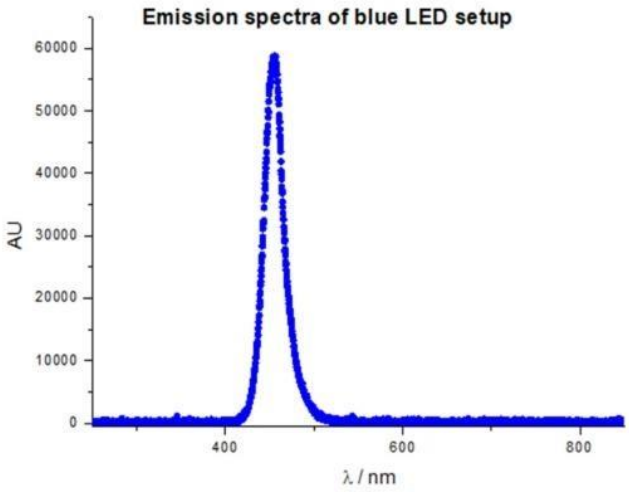

Figure 3.5.5.1.1. Setup for visible-light-mediate photocatalytic reactions under N_2 with an electric fan.

3.5.5.2 General procedure for the three-component coupling

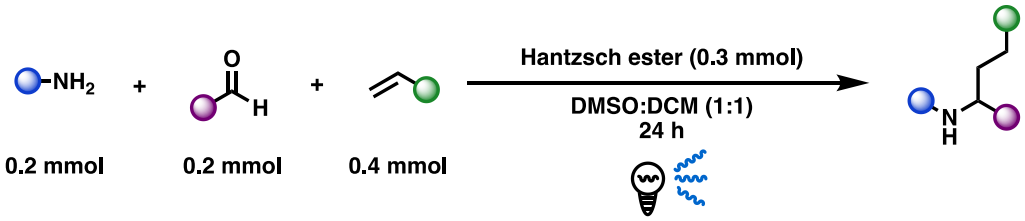

A dried Schlenk flask with magnetic stirring bar was charged with [amine] (0.2 mmol, 1 equiv.) and [Hantzsch ester] (0.3 mmol, 1.5 equiv.), after which the vessel was evacuated using Schlenk techniques and flushed with N_2 three times. Under nitrogen gas flow, [aldehyde (if liquid, otherwise added before flushing cycle)] (0.2 mmol, 1 equiv.), [Michael acceptor (if liquid, otherwise added before flushing cycle)] (0.4 mmol, 2 equiv.), dry DMSO (0.5 mL), and dry CH_2Cl_2 (0.5 mL) were added using a syringe flushed with inert gas. The resulting mixture was stirred for 24 h under irradiation of blue LED light (24 W) at room temperature. After 24 h, the reaction mixture was quenched by adding distilled water (3 mL) and ethyl acetate (3 mL). The organic phase was extracted and concentrated in vacuo. 1,3,5-Trimethoxybenzene was added as internal standard to determine the NMR yield of the functionalised product through ^{1}H NMR. Purification proceeded via flash column chromatography.

3.5.5.3 General procedure for the cyclization reaction

A dried Schlenk flask with magnetic stirring bar was charged with [amine] (0.2 mmol, 1 equiv.) and [Hantzsch ester] (0.3 mmol, 1.5 equiv.), and [aldehyde/olefin substrate] (0.2 mmol, 1 equiv.) after which the vessel was evacuated using Schlenk techniques and flushed with N_2 three times. Under nitrogen gas flow, dry DMSO (0.5 mL), and dry CH_2Cl_2 (0.5 mL) were added using a syringe flushed with inert gas. The resulting mixture was stirred for 24 h under irradiation of blue LED light (24 W) at room temperature. After 24 h, the reaction mixture was quenched by adding distilled water (3 mL) and ethyl acetate (3 mL). The organic phase was extracted and concentrated in vacuo. 1,3,5-

Trimethoxybenzene was added as internal standard to determine the NMR yield of the functionalised product through ^{1}H NMR. Purification proceeded via flash column chromatography.

3.5.5.4 General procedure for the synthesis of cyclization aldehyde/olefin substrates

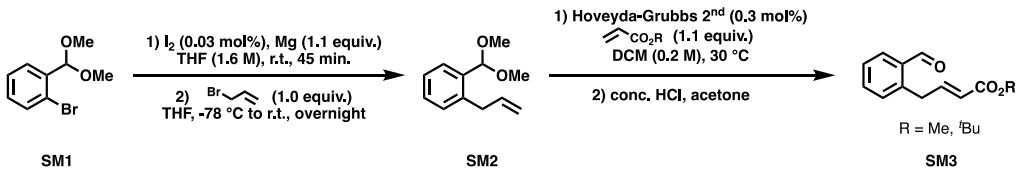

A dried two-necked flask with stirring bar was charged with fresh magnesium (1.1 equiv.) and iodine (0.03 mol%), after which the vessel was evacuated and the solid mixtures were vigorously stirred for 10 minutes. A solution of 1-bromo-2-(dimethoxymethyl)benzene (**SM1**, 1 equiv.) in anhydrous THF (1.6 M) was added dropwise over 15 minutes. The mixture was allowed to stir for further 30 minutes and cool to -78 ^{0}C, followed by the dropwise addition of allyl bromide (1 equiv.) over 15 minutes. After that, the solution was allowed to warm to room temperature and stir overnight. The mixture was then quenched with saturated aqueous NH_4Cl solution and stirred for 10 minutes. The product was extracted with EtOAc and washed with H_2O and brine. The combined organic phase was dried with $MgSO_4$, followed by filtration and concentration in vacuo. The pure product **SM2** as a colorless oil was obtained via distillation under reduced pressure (67 ^{0}C, 0.5 mbar).

A dried two-necked flask with stirring bar was charged with **SM2** (1 equiv.) and alkyl acrylate (1.1 equiv.), after which the vessel was evacuated using Schlenk techniques and flushed with N_2 three times. The mixture was dissolved in anhydrous DCM (0.2 M) and warmed to 30 ^{0}C. A solution of Hoveyda-Grubbs 2nd Generation catalyst (0.3 mol%) in anhydrous toluene (10^{-3} M) was added dropwise over 1 h. After reaction, the solvent was evaporated in vacuo and the residue was dissolved in conc. HCl (20 mol%) and acetone (0.25 M). After further stirring for 10

minutes, the reaction mixture was quenched with aqueous Na_2CO_3 (1 M), followed by evaporation of acetone in vacuo. The crude product was extracted with EtOAc and washed with H_2O and brine. The combined organic phase was dried with $MgSO_4$, followed by filtration and concentration in vacuo. Flash column chromatography was applied to obtain pure product **SM3**.

3.5.5.5 General procedure for the reductive functionalization with pre-formed imine

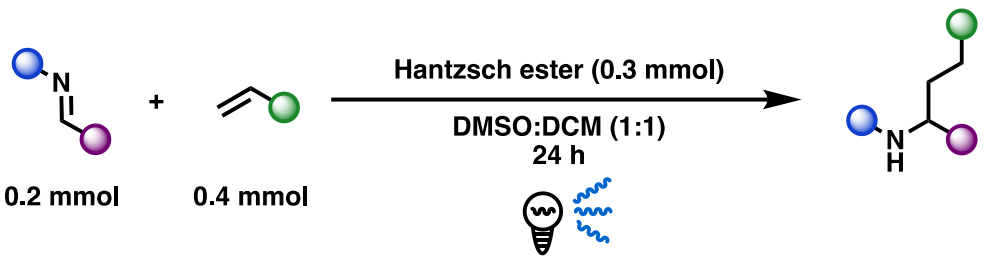

A dried Schlenk flask with magnetic stirring bar was charged with [imine] (0.2 mmol, 1 equiv.) and [Hantzsch ester] (0.3 mmol, 1.5 equiv.), after which the vessel was evacuated using Schlenk techniques and flushed with N_2 three times. Under nitrogen gas flow, [Michael acceptor (if liquid, otherwise added before flushing cycle)] (0.4 mmol, 2 equiv.) and dry DMSO (1 mL) were added using a syringe flushed with inert gas. The resulting mixture was stirred for 24 h under irradiation of blue LED light (24 W) at room temperature. After 24 h, the reaction mixture was quenched by adding distilled water (3 mL) and ethyl acetate (3 mL). The organic phase was extracted and concentrated in vacuo. 1,3,5-Trimethoxybenzene was added as internal standard to determine the NMR yield of the functionalised product through ^1H NMR. Purification proceeded via flash column chromatography.

3.5.5.6 General procedure for synthesis of imines

A dried two-necked flask with stirring bar was charged with [amine (if solid, otherwise added after flushing cycle)] (2 mmol, 1 equiv.) and $MgSO_4$ (960 mg, 8 mmol, 4 equiv.), after which the vessel was evacuated using Schlenk techniques and flushed with N2 three times. Under nitrogen gas flow, [aldehyde (if liquid, otherwise added before flushing cycle)] (2 mmol, 1 equiv.) and CH_2Cl_2 (8 mL) were added using a syringe flushed with inert gas. The resulting mixture was stirred for 2 h (unless explicitly stated otherwise) at room temperature. After 2 h, the mixture was filtered over Celite® and concentrated in vacuo. In most cases, the product was dried under high vacuum (< 0.5 mbar) while cooled with liquid nitrogen.

3.5.5.7 General procedure for synthesis of complex olefins

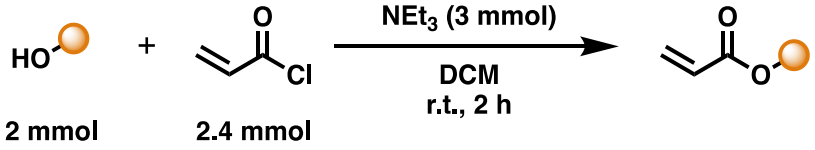

The following procedure was obtained from literature.[40] Acryloyl chloride (217 mg, 2.4 mmol, 1.2 equiv.) was added to a stirred solution of [complex alcohol] (2 mmol, 1 equiv.), triethylamine (417 µL, 3 mmol, 1.5 equiv.) in DCM (7 mL) at 0 °C. The reaction was warmed to room temperature and stirred for 2 hours. The solvent was removed in vacuo and the residue was purified by flash chromatography (silica, EtOAc in heeptane). Ultimately, the desired fractions were collected and concentrated in vacuo.

3.5.6 Characterization

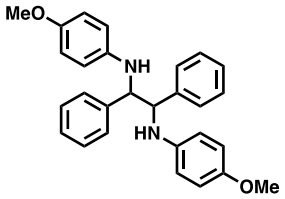

N^1,N^2-bis(4-methoxyphenyl)-1,2-diphenylethane-1,2-diamine

Following procedure **3.5.5.2** with *p*-anisidine (0.2 mmol, 24.6 mg), benzaldehyde (0.2 mmol, 20 µL), and *n*-butyl acrylate (0.4 mmol, 29 µL). The dimer by-product was observed and purified using flash column chromatography in a EtOAc/heptane eluent system. **Yield:** 20 %. **^{1}H NMR** (400 MHz, $CDCl_3$) δ 7.21-7.16 (m, 6H), 7.15-7.09 (m, 2H), 6.94 (dd, *J* = 6.4, 2.9 Hz, 2H), 6.66 (dd, *J* = 7.7, 5.5 Hz, 4H), 6.47 (dd, *J* = 8.7, 6.1 Hz, 4H), 4.86 (s, 1H), 4.45 (s, 1H), 4.33 (s, 2H), 3.67 (d, *J* = 3.2 Hz, 6H) ppm. **^{13}C NMR** (101 MHz, $CDCl_3$) δ 158.4, 152.5, 152.3, 141.3, 140.7, 140.3, 138.7, 131.0, 128.7, 128.6, 128.34, 128.2, 127.6, 127.5, 127.4, 122.2, 115.5, 115.1, 114.9, 114.8, 114.4, 65.0, 62.9, 55.7 ppm.

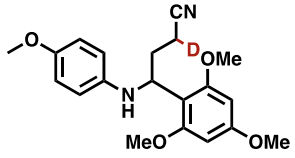

4-((4-Methoxyphenyl)amino)-4-(2,4,6-trimethoxyphenyl)butanenitrile-2-d ***5s-D***

Following procedure **3.5.5.2** with *p*-anisidine (0.2 mmol, 24.6 mg), 2,4,6-trimethoxybenzaldehyde (0.2 mmol, 39.2 mg), acrylonitrile (0.4 mmol, 26 µL), and **4d** as the sole photoreductant. The crude product was purified using flash column chromatography in a EtOAc/heptane eluent system. **Yield:** 77 %. **^{1}H NMR** (400 MHz, $CDCl_3$) δ 6.73-6.66 (m, 2H), 6.64-6.58 (m,

2H), 6.08 (s, 2H), 5.00 (t, *J* = 7.4 Hz, 1H), 3.83 (s, 6H), 3.76 (s, 3H), 3.69 (s, 3H), 2.47-2.22 (m, 2H), 2.18-1.99 (m, 1H) ppm. **HRMS** (ESI^+, *m*/*z*) [$M+H^+$] calcd. for $C_{20}H_{23}N_2O_4D$ 358.1872, found 358.1883.

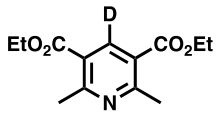

Diethyl 2,6-dimethylpyridine-3,5-dicarboxylate-4-d

Following procedure **3.5.5.2** with *p*-anisidine (0.2 mmol, 24.6 mg), 2,4,6-trimethoxybenzaldehyde (0.2 mmol, 39.2 mg), acrylonitrile (0.4 mmol, 26 μL), and **4d** as the sole photoreductant. The crude product was purified using flash column chromatography in a EtOAc/heptane eluent system. **Yield:** 70 %. **^{1}H NMR** (400 MHz, $CDCl_3$) δ 4.40 (q, *J* = 7.1 Hz, 4H), 2.85 (s, 6H), 1.42 (t, *J* = 7.1 Hz, 6H) ppm.

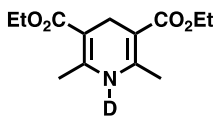

Diethyl 2,6-dimethyl-1,4-dihydropyridine-3,5-dicarboxylate-1-d ***4c***

According to the literature,[46] a dried two-necked flask with stirring bar was charged with diethyl 2,6-dimethyl-1,4-dihydropyridine-3,5-dicarboxylate, after which the vessel was evacuated using Schlenk techniques and flushed with argon three times. CD_3OD (0.3 M) was added and stirred overnight. The solvent was removed under reduced pressure and the desired compound was obtained as a pale green solid. **Yield:** 95 %. **^{1}H NMR** (400 MHz, $CDCl_3$) δ 4.17 (dd, *J* = 13.4, 6.5 Hz, 4H), 3.27 (s, 2H), 2.19 (s, 6H), 1.28 (t, *J* = 6.8 Hz, 6H) ppm.

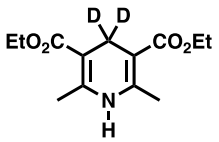

Diethyl 2,6-dimethylpyridine-1,4-dihydropyridine-3,5-dicarboxylate-4,4-d$_2$ ***4d***

According to the literature,[46] a dried two-necked flask with stirring bar was charged with ethyl acetoacetate (4 equiv.), d$_2$-paraformaldehyde (1 equiv.) and ammonium acetate (2 equiv.), after which the vessel was evacuated using Schlenk techniques and flushed with N_2 three times.Then, water (0.15 M) was added and stirred at 90 °C for 3 h. Later, the mixture was cooled to room temperature and filtered, followed by evaporation in vacuo and the desired product was obtained as a yellow solid. **Yield:** 44 %. **^{1}H NMR** (400 MHz, $CDCl_3$) δ 5.08 (s, 1H), 4.17 (q, *J* = 7.1 Hz, 4H), 2.19 (s, 6H), 1.28 (t, *J* = 7.1 Hz, 6H) ppm.

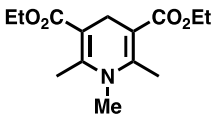

Diethyl 1,2,6-trimethyl-1,4-dihydropyridine-3,5-dicarboxylate ***4e***

According to the literature,[47] a dried two-necked flask with stirring bar was charged with Hantzsch ester, after which the vessel was evacuated using Schlenk techniques and flushed with argon three times. The solid was dissolved in anhydrous THF (0.11 M) and stirred at 0 °C, followed by the addition of sodium hydride. After further stirring for 10 minutes, iodomethane was dropwise added. The reaction mixture was warmed to room temperature and stirred for 15 minutes. Later, the mixture was refluxed overnight. The addition of water and extraction of EtOAc were required and combined organic phases were dried with $MgSO_4$.

Purification proceeded via flash column chromatography (heptane/ethyl acetate as eluent). **Yield:** 54 %. **^{1}H NMR** (400 MHz, $CDCl_3$) δ 4.18 (q, *J* = 7.1 Hz, 4H), 3.15 (m, 5H), 2.38 (s, 6H), 1.29 (t, *J* = 7.1 Hz, 6H) ppm.

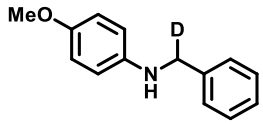

4-Methoxy-N-(phenylmethyl-d)aniline

Following procedure **3.5.5.2** with *p*-anisidine (0.2 mmol, 24.6 mg), and benzaldehyde (0.2 mmol, 20 µL). The green LED (90 W, 525 nm) was used instead of blue LED. The crude product was purified using flash column chromatography in a EtOAc/heptane eluent system. **Yield:** 34 %. **^{1}H NMR** (400 MHz, $CDCl_3$) δ 7.41 – 7.22 (m, 5H), 6.77 (d, *J* = 8.9 Hz, 2H), 6.60 (d, *J* = 8.9 Hz, 2H), 4.26 (s, 1H), 3.74 (s, 3H).

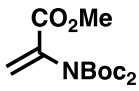

*Methyl 2-(bis(t-butoxycarbonyl)amino)acrylate **3ai***

According to the literature,[48] the desired product can be obtained in 36 % yield over three steps. **^{1}H NMR** (400 MHz, $CDCl_3$) δ 6.34 (s, 1H), 5.64 (s, 1H), 3.79 (s, 3H), 1.47 (s, 18H) ppm.

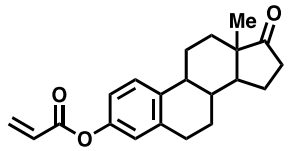

*13-Methyl-17-oxo-7,8,9,11,12,13,14,15,16,17-decahydro-6H-cyclopenta[a]phenantren-3-yl acrylate **3am***

Following procedure **3.5.5.7** with estrone (2 mmol, 540.8 mg. The crude product was purified using flash column chromatography in a EtOAc/heptane eluent system. **Yield:** 54 %. **^{1}H NMR** (400 MHz, $CDCl_3$) δ 7.29 (t, *J* = 6.9 Hz, 1H), 6.95-6.82 (m, 2H), 6.59 (d, *J* = 17.3 Hz, 1H), 6.31 (dd, *J* = 17.3, 10.4 Hz, 1H), 5.99 (d, *J* = 10.4 Hz, 1H), 2.98-2.87 (m, 2H), 2.51 (dd, *J* = 18.8, 8.6 Hz, 1H), 2.40 (m, 1H), 2.31 (m, 1H), 2.20-1.94 (m, 4H), 1.69-1.41 (m, 6H), 0.91 (s, 3H).

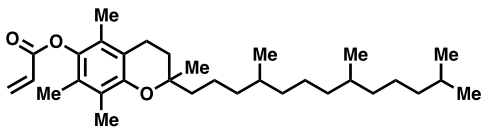

2,5,7,8-tetramethyl-2-(4,8,12-trimethyltridecyl)chroman-6-yl acrylate ***3an***

Following procedure **3.5.5.7** with 2,5,7,8-tetramethyl-2-(4,8,12-trimethyltridecyl)chroman-6-ol (2 mmol, 861.4 mg. The crude product was purified using flash column chromatography in a EtOAc/heptane eluent system. **Yield:** 66 %. **^{1}H NMR** (400 MHz, $CDCl_3$) δ 6.62 (dd, *J* = 17.3, 1.2 Hz, 1H), 6.37 (dd, *J* = 17.3, 10.4 Hz, 1H), 6.00 (dd, *J* = 10.5, 1.2 Hz, 1H), 2.59 (t, *J* = 6.8 Hz, 2H), 2.09 (s, 3H), 2.01 (s, 3H), 1.97 (s, 3H), 1.88-1.70 (m, 2H), 1.63-1.45 (m, 2H), 1.43-1.34 (m, 3H), 1.33-0.99 (m, 19H), 0.86 (dd, *J* = 8.9, 6.1 Hz, 12H) ppm.

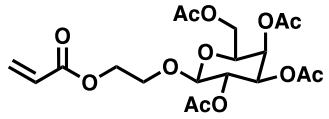

2-(Acetoxymethyl)-6-(2-(acryloyloxy)ethoxy)tetrahydro-2H-pyran-3,4,5-triyl triacetate ***3ao***

Following procedure **3.5.5.7** with 2-(acetoxymethyl)-6-(2-hydroxyethoxy)tetrahydro-2*H*- pyran-3,4,5-triyl triacetate (2 mmol, 784.8 mg. The crude product was purified using flash column chromatography

in a EtOAc/heptane eluent system. **Yield:** 78 %. **^{1}H NMR** (400 MHz, $CDCl_3$) δ 6.43 (dd, *J* = 17.3, 1.4 Hz, 1H), 6.14 (dd, *J* = 17.3, 10.4 Hz, 1H), 5.86 (dd, *J* = 10.4, 1.4 Hz, 1H), 5.42-5.36 (m, 1H), 5.22 (dd, *J* = 10.5, 8.0 Hz, 1H), 5.02 (dd, *J* = 10.5, 3.4 Hz, 1H), 4.53 (d, *J* = 8.0 Hz, 1H), 4.38-4.25 (m, 2H), 4.22-4.10 (m, 2H), 4.09-4.01 (m, 1H), 3.91 (td, *J* = 6.6, 0.9 Hz, 1H), 3.86-3.79 (m, 1H), 2.15 (s, 3H), 2.05 (s, 3H), 2.03 (s, 3H), 1.98 (s, 3H) ppm.

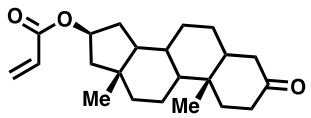

(10S,13R,16S)-10,13-Dimethyl-3-oxohexadecahydro-1H-cyclopenta[a]phenanthren-16-yl acrylate ***3aq***

Following procedure **3.5.5.7** with (10S,13R,16S)-16-hydroxy-10,13-dimethylhexadecahydro-3*H*-cyclopenta[*a*]phenanthren-3-one (2 mmol, 580.8 mg. The crude product was purified using flash column chromatography in a EtOAc/heptane eluent system. **Yield:** 36 %. **^{1}H NMR** (400 MHz, $CDCl_3$) δ 6.37 (d, *J* = 17.3 Hz, 1H), 6.11 (dd, *J* = 17.3, 10.4 Hz, 1H), 5.80 (d, *J* = 10.4 Hz, 1H), 4.68 (t, *J* = 8.4 Hz, 1H), 2.46-1.96 (m, 6H), 1.81-1.61 (m, 4H), 1.57-1.06 (m, 10H), 1.02 (s, 3H), 0.93 (ddd, *J* = 25.0, 12.5, 5.4 Hz, 1H), 0.84 (s, 3H), 0.80-0.71 (m, 1H) ppm.

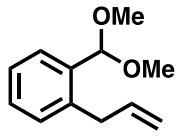

1-Allyl-2-(dimethoxymethyl)benzene ***SM2***

Following procedure **3.5.5.4** with 1-Allyl-2-(dimethoxymethyl)benzene (2 mmol, 580.8 mg. The crude product was purified using distillation under reduced pressure. **Yield:** 56 %. **^{1}H NMR** (400 MHz, $CDCl_3$) δ = 7.58

(dd, *J* = 7.4, 1.6, 1H), 7.34 -7.18 (m, 3H), 6.04-5.93 (m, 1H), 5.47 (s, 1H), 5.17-4.97 (m, 2H), 3.54 (m, 2H), 3.35 (s, 6H).

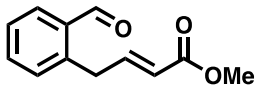

Methyl (E)-4-(2-formylphenyl)but-2-enoate ***6a***

Following procedure **3.5.5.4** with **SM2** (1 equiv.) and methyl acrylate (1.1 equiv.). The crude product was purified using flash column chromatography in a EtOAc/heptane eluent system. **Yield:** 53 %. **^{1}H NMR** (400 MHz, $CDCl_3$) δ 10.15 (s, 1H), 7.83 (d, *J* = 7.6 Hz, 1H), 7.55 (t, *J* = 7.5 Hz, 1H), 7.46 (t, *J* = 7.5 Hz, 1H), 7.27 (d, *J* = 8.2 Hz, 1H), 7.14 (dt, *J* = 15.6, 6.4 Hz, 1H), 5.73 (dd, *J* = 15.7, 1.5 Hz, 1H), 3.98 (d, *J* = 6.4 Hz, 2H), 3.70 (s, 3H).

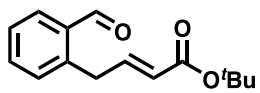

tert-Butyl (E)-4-(2-formylphenyl)but-2-enoate ***6b***

Following procedure **3.5.5.4** with **SM2** (1 equiv.) and *tert*-butyl acrylate (1.1 equiv.). The crude product was purified using flash column chromatography in a EtOAc/heptane eluent system. **Yield:** 75 %. **^{1}H NMR** (400 MHz, $CDCl_3$) δ 10.17 (s, 1H), 7.84 (dd, *J* = 7.6, 1.1 Hz, 1H), 7.55 (td, *J* = 7.5, 1.4 Hz, 1H), 7.45 (t, *J* = 7.5 Hz, 1H), 7.28 (s, 1H), 7.02 (dt, *J* = 15.6, 6.4 Hz, 1H), 5.63 (dt, *J* = 15.6, 1.6 Hz, 1H), 3.95 (dd, *J* = 6.4, 1.4 Hz, 2H), 1.45 (s, 9H).

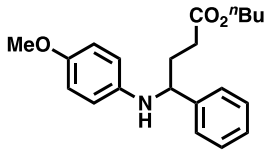

Butyl 4-((4-methoxyphenyl)amino-4-phenylbutanoate ***5a***

Following procedure **3.5.5.2** with *p*-anisidine (0.2 mmol, 24.6 mg), benzaldehyde (0.2 mmol, 20 μL), and *n*-butyl acrylate (0.4 mmol, 29 μL). The crude product was purified using flash column chromatography in a EtOAc/heptane eluent system. For isolation, **4b** (0.3 mmol, 94.0 mg) was used as the photoreductant. **Yield:** 63 %. **^{1}H NMR** (400 MHz, $CDCl_3$) δ 7.32-7.19 (m, 5H), 6.69-6.67 (m, 2H), 6.49-6.46 (m, 2H), 4.32-4.29 (t, *J* = 6.8 Hz, 1H), 4.09-4.05 (t, *J* = 6.7 Hz, 2H), 3.69 (s, 3H), 2.41-2.38 (t, *J* = 7.2 Hz, 2H), 2.14-2.09 (m, 2H), 1.61-1.57 (m, 2H), 1.39-1.33 (m, 2H), 0.94-0.90 (t, *J* = 7.4 Hz, 3H) ppm. **^{13}C NMR** (101 MHz, $CDCl_3$) δ 173.7, 152.1, 143.4, 141.4, 128.7, 127.2, 126.5, 114.8, 114.6, 64.5, 58.7, 55.8, 33.3, 31.3, 30.7, 19.1, 13.7 ppm.

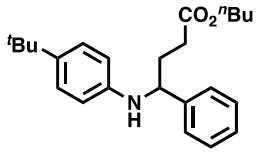

Butyl 4-((4-(t-butyl)phenyl)amino-4-phenylbutanoate ***5b***

Following procedure **3.5.5.2** with 4-*t*-butylaniline (0.2 mmol, 32 μL), benzaldehyde (0.2 mmol, 20 μL), and *n*-butyl acrylate (0.4 mmol, 29 μL). The crude product was purified using flash column chromatography in a EtOAc/heptane eluent system. For isolation, **4b** (0.3 mmol, 94.0 mg) was used as the photoreductant. **Yield:** 54 %. **^{1}H NMR** (400 MHz, $CDCl_3$) δ

7.35-7.31 (m, 4H), 7.22 (t, *J* = 6.9 Hz, 1H), 7.10 (d, *J* = 8.6 Hz, 2H), 6.47 (d, *J* = 8.6 Hz, 2H), 4.34 (t, *J* = 6.8 Hz, 1H), 4.18 (s, 1H), 4.06 (t, *J* = 6.7 Hz, 2H), 2.39 (t, *J* = 7.2 Hz, 2H), 2.10 (dt, *J* = 13.7, 7.2 Hz, 2H), 1.64-1.53 (m, 2H), 1.36 (m, 2H), 1.22 (s, 9H), 0.92 (t, *J* = 7.4 Hz, 3H) ppm. **^{13}C NMR** (101 MHz, $CDCl_3$) δ 173.7, 144.9, 143.6, 140.0, 128.7, 127.1, 126.4, 125.9, 112.9, 64.5, 58.1, 33.8, 33.4, 31.5, 31.3, 30.7, 19.1, 13.7 ppm. **HRMS** (ESI^+, *m*/*z*) [$M+H^+$] calcd. for $C_{24}H_{33}NO_2$ 368.2584, found 368.2728.

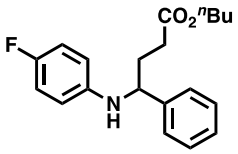

Butyl 4-((4-fluorophenyl)amino-4-phenylbutanoate ***5c***

Following procedure **3.5.5.2** with 4-fluoroaniline (0.2 mmol, 19 μL), benzaldehyde (0.2 mmol, 20 μL), and *n*-butyl acrylate (0.4 mmol, 29 μL). The crude product was purified using flash column chromatography in a EtOAc/heptane eluent system. For isolation, **4b** (0.3 mmol, 94.0 mg) was used as the photoreductant. **Yield:** 47 %. **^{1}H NMR** (400 MHz, $CDCl_3$) δ 7.32-7.18 (m, 5H), 6.80-6.75 (m, 2H), 6.45-6.41 (m, 2H), 4.32-4.29 (t, *J* = 6.8 Hz, 1H), 4.09-4.05 (t, *J* = 6.7 Hz, 2H), 2.41-2.38 (t, *J* = 6.9 Hz, 2H), 2.17-2.07 (m, 2H), 1.61-1.57 (m, 2H), 1.38-1.33 (m, 2H), 0.94-0.90 (t, *J* = 7.4 Hz, 3H) ppm. **^{19}F NMR** (376 MHz, $CDCl_3$) δ -128.22 ppm. **^{13}C NMR** (101 MHz, $CDCl_3$) δ 173.7, 143.0, 128.8, 127.3, 126.4, 115.6, 115.4, 114.2, 114.1, 64.6, 58.5, 33.3, 31.3, 30.7, 19.1, 13.7 ppm. **HRMS** (ESI^+, *m*/*z*) [$M+H^+$] calcd. for $C_{20}H_{24}NO_2F$ 330.1864, found 330.1878.

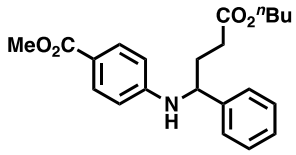

Methyl 4-((4-butoxy-4-oxo-1-phenylbutyl)amino)benzoate ***5d***

Following procedure **3.5.5.2** with methyl 4-aminobenzoate (0.2 mmol, 30.2 mg), benzaldehyde (0.2 mmol, 20 μL), and *n*-butyl acrylate (0.4 mmol, 29 μL). The crude product was purified using flash column chromatography in a EtOAc/heptane eluent system. **Yield:** 62 %. **^{1}H NMR** (400 MHz, $CDCl_3$) δ 7.77 (d, *J* = 8.8 Hz, 2H), 7.38-7.27 (m, 4H), 7.25-7.19 (m, 1H), 6.48 (d, *J* = 8.8 Hz, 2H), 4.87 (d, *J* = 5.9 Hz, 1H), 4.46 (dd, *J* = 13.3, 6.2 Hz, 1H), 4.09 (t, *J* = 6.7 Hz, 2H), 3.81 (s, 3H), 2.41 (td, *J* = 6.9, 2.0 Hz, 2H), 2.27-2.00 (m, 2H), 1.67-1.50 (m, 2H), 1.36 (dd, *J* = 15.0, 7.5 Hz, 2H), 0.92 (t, *J* = 7.4 Hz, 3H) ppm. **^{13}C NMR** (101 MHz, $CDCl_3$) δ 173.7, 167.2, 151.0, 142.2, 131.4, 128.9, 127.5, 126.28, 118.6, 112.2, 64.7, 57.6, 51.5, 32.9, 31.2, 30.7, 19.1, 13.7 ppm. **HRMS** (ESI^+, *m*/*z*) [$M+H^+$] calcd. for $C_{22}H_{27}NO_4$ 370.2013, found 370.2016.

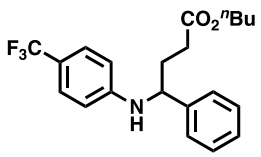

Butyl 4-((4-(trifluoromethyl)phenyl)amino-4-phenylbutanoate ***5e***

Following procedure **3.5.5.2** with 4-(trifluoromethyl)aniline (0.2 mmol, 25 μL), benzaldehyde (0.2 mmol, 20 μL), and *n*-butyl acrylate (0.4 mmol, 29 μL). The crude product was purified using flash column chromatography in a EtOAc/heptane eluent system. **Yield:** 62%. **^{1}H NMR** (400 MHz, $CDCl_3$) δ 7.34-7.21 (m, 7H), 6.51 (d, *J* = 8.5 Hz, 2H), 4.76 (s, 1H), 4.41 (dd, *J* = 12.2, 5.7 Hz, 1H), 4.08 (t, *J* = 6.7 Hz, 2H), 2.41 (td, *J* = 6.9, 3.5 Hz, 2H), 2.26-2.04 (m, 2H), 1.59 (dt, *J* = 14.6, 6.8 Hz, 2H), 1.43-1.27 (m, 2H),

0.92 (t, *J* = 7.4 Hz, 3H) ppm. **^{19}F NMR** (376 MHz, $CDCl_3$) δ -61.11 ppm. **^{13}C NMR** (101 MHz, $CDCl_3$) δ 173.7, 149.7, 142.3, 128.9, 127.5, 126.5, 126.5, 126.3, 119.1-118.8 (d, CF_3), 112.5, 64.7, 57.7, 32.9, 31.2, 30.7, 19.1, 13.7 ppm.

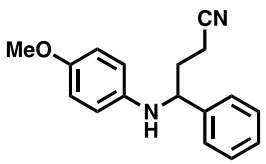

*4-((4-Methoxyphenyl)amino)-4-phenylbutanenitrile **5f***

Following procedure **3.5.5.2** with *p*-anisidine (0.2 mmol, 24.6 mg), benzaldehyde (0.2 mmol, 20 μL), and acrylonitrile (0.4 mmol, 26 μL). The crude product was purified using flash column chromatography in a EtOAc/heptane eluent system. **Yield:** 67%. **^{1}H NMR** (400 MHz, $CDCl_3$) δ 7.35-7.29 (m, 4H), 7.28-7.22 (m, 1H), 6.73-6.63 (m, 2H), 6.53 (dd, *J* = 9.6, 2.7 Hz, 2H), 4.41 (t, *J* = 7.0 Hz, 1H), 3.68 (s, 3H), 2.49-2.25 (m, 2H), 2.23-1.95 (m, 2H) ppm. **^{13}C NMR** (101 MHz, $CDCl_3$) δ 152.6, 141.9, 140.7, 129.0, 127.8, 126.3, 119.4, 115.3, 114.9, 57.9, 55.7, 33.6, 14.5 ppm.

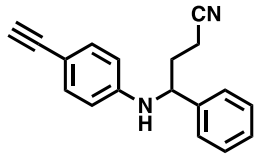

*4-((4-Ethynylphenyl)amino)-4-phenylbutanenitrile **5g***

Following procedure **3.5.5.2** with 4-ethynylaniline (0.2 mmol, 23.4 mg), benzaldehyde (0.2 mmol, 20 μL), and acrylonitrile (0.4 mmol, 26 μL). The crude product was purified using flash column chromatography in a EtOAc/heptane eluent system. For isolation, **4b** (0.3 mmol, 94.0 mg) was used as the photoreductant. **Yield:** 34%. **^{1}H NMR** (400 MHz, $CDCl_3$) δ

7.39-7.27 (m, 5H), 7.23 (m, 2H), 6.49 (d, *J* = 8.7 Hz, 2H), 4.51 (t, *J* = 6.7 Hz, 1H), 4.19 (s, 1H), 2.92 (s, 1H), 2.52-2.29 (m, 2H), 2.26-2.00 (m, 2H) ppm. **^{13}C NMR** (101 MHz, $CDCl_3$) δ 146.9, 141.0, 133.4, 129.2, 128.1, 126.3, 119.1, 113.3, 111.1, 84.3, 75.0, 56.8, 33.4, 14.5 ppm.

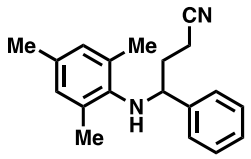

4-(Mesitylamino)-4-phenylbutanenitrile ***5h***

Following procedure **3.5.5.2** with 2,4,6-trimethylaniline (0.2 mmol, 28 μL), benzaldehyde (0.2 mmol, 20 μL), and acrylonitrile (0.4 mmol, 26 μL). The crude product was purified using flash column chromatography in a EtOAc/heptane eluent system. **Yield:** 77%. **^{1}H NMR** (400 MHz, $CDCl_3$) δ 7.32-7.26 (m, 3H), 7.15 (dd, *J* = 7.7, 1.5 Hz, 2H), 6.75 (s, 2H), 4.11 (dt, *J* = 6.5, 4.0 Hz, 1H), 2.49-2.38 (m, 1H), 2.33 (ddt, *J* = 18.3, 11.7, 4.7 Hz, 2H), 2.19 (s, 3H), 2.18-2.11 (m, 1H), 2.09 (s, 6H) ppm. **^{13}C NMR** (101 MHz, $CDCl_3$) δ 141.9, 141.1, 131.7, 130.1, 129.6, 128.9, 127.9, 126.6, 119.4, 60.8, 31.9, 20.5, 18.7, 14.9 ppm. **HRMS** (ESI$^+$, *m*/*z*) [M+H$^+$] calcd. for $C_{19}H_{22}N_2$ 279.1856, found 279.1847.

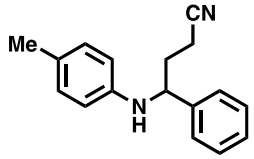

4-Phenyl-4-(p-tolylamino)butanenitrile ***5i***

Following procedure **3.5.5.2** with *p*-toluidine (0.2 mmol, 21.4 mg), benzaldehyde (0.2 mmol, 20 μL), and acrylonitrile (0.4 mmol, 26 μL). The crude product was purified using flash column chromatography in a

EtOAc/heptane eluent system. For isolation, **4b** (0.3 mmol, 94.0 mg) was used as the photoreductant. **Yield:** 67%. **^{1}H NMR** (400 MHz, $CDCl_3$) δ 7.39-7.28 (m, 4H), 7.29-7.19 (m, 1H), 6.92 (d, *J* = 8.2 Hz, 2H), 6.50 (d, *J* = 8.4 Hz, 2H), 4.47 (t, *J* = 7.0 Hz, 1H), 2.53-2.30 (m, 2H), 2.26-2.05 (m, 5H) ppm. **^{13}C NMR** (101 MHz, $CDCl_3$) δ 144.3, 141.8, 129.8, 129.0, 127.8, 127.5, 126.3, 119.3, 113.9, 57.3, 33.6, 20.3, 14.5 ppm.

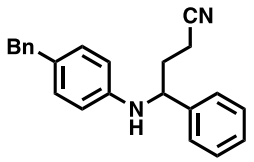

4-((4-Benzylphenyl)amino)-4-phenylbutanenitrile ***5j***

Following procedure **3.5.5.2** with 4-benzylaniline (0.2 mmol, 36.7 mg), benzaldehyde (0.2 mmol, 20 μL), and acrylonitrile (0.4 mmol, 26 μL). The crude product was purified using flash column chromatography in a EtOAc/heptane eluent system. **Yield:** 78%. **^{1}H NMR** (400 MHz, $CDCl_3$) δ 7.38-7.30 (m, 4H), 7.28 (d, *J* = 2.0 Hz, 1H), 7.23 (d, *J* = 7.5 Hz, 2H), 7.19-7.10 (m, 3H), 6.93 (d, *J* = 8.5 Hz, 2H), 6.51 (d, *J* = 8.5 Hz, 2H), 4.46 (t, *J* = 7.0 Hz, 1H), 4.00 (s, 1H), 3.82 (s, 2H), 2.50-2.27 (m, 2H), 2.24-2.02 (m, 2H) ppm. **^{13}C NMR** (101 MHz, $CDCl_3$) δ 144.8, 141.8, 141.7, 130.9, 129.7, 129.0, 128.8, 128.4, 127.8, 126.3, 125.9, 119.3, 113.9, 57.2, 41.0, 33.6, 14.5 ppm. **HRMS** (ESI^+, *m*/*z*) [M+H^+] calcd. for $C_{23}H_{22}N_2$ 327.1856, found 327.1852.

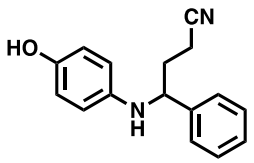

4-((4-Hydroxyphenyl)amino)-4-phenylbutanenitrile ***5k***

Following procedure **3.5.5.2** with 4-aminophenol (0.2 mmol, 21.8 mg), benzaldehyde (0.2 mmol, 20 μL), and acrylonitrile (0.4 mmol, 26 μL). The crude product was purified using flash column chromatography in a EtOAc/heptane eluent system. **Yield:** 85%. **^{1}H NMR** (400 MHz, $CDCl_3$) δ 7.38-7.26 (m, 4H), 7.25-7.22 (m, 1H), 6.66-6.57 (m, 2H), 6.49 (dd, *J* = 9.4, 2.7 Hz, 2H), 4.40 (t, *J* = 7.0 Hz, 1H), 4.07 (m, 2H), 2.51-2.29 (m, 2H), 2.23-2.00 (m, 2H) ppm. **^{13}C NMR** (101 MHz, $CDCl_3$) δ 148.2, 141.8, 140.7, 129.0, 127.8, 126.3, 119.4, 116.2, 115.5, 58.0, 33.6, 14.5 ppm. **HRMS** (ESI^+, *m*/*z*) [$M+H^+$] calcd. for $C_{16}H_{16}N_2O$ 253.1335, found 253.1335.

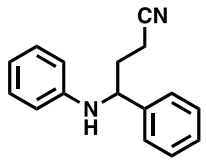

4-Phenyl-4-(phenylamino)butanenitrile ***5l***

Following procedure **3.5.5.2** with aniline (0.2 mmol, 18 μL), benzaldehyde (0.2 mmol, 20 μL), and acrylonitrile (0.4 mmol, 26 μL). The crude product was purified using flash column chromatography in a EtOAc/heptane eluent system. For isolation, **4b** (0.3 mmol, 94.0 mg) was used as the photoreductant. **Yield:** 83%. **^{1}H NMR** (400 MHz, $CDCl_3$) δ 7.38-7.23 (m, 5H), 7.11 (dd, *J* = 8.4, 7.5 Hz, 2H), 6.69 (t, *J* = 7.3 Hz, 1H), 6.57 (d, *J* = 7.7 Hz, 2H), 4.50 (t, *J* = 7.0 Hz, 1H), 4.00 (s, 1H), 2.55-2.27 (m, 2H), 2.23-1.92 (m, 2H) ppm. **^{13}C NMR** (101 MHz, $CDCl_3$) δ 146.6, 141.6, 129.3, 129.0, 127.8, 126.3, 119.3, 118.2, 113.7, 57.0, 33.6, 14.5 ppm.

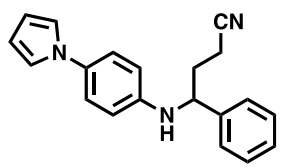

4-((4-(1H-Pyrrol-1-yl)amino)-4-phenylbutanenitrile ***5m***

Following procedure **3.5.5.2** with 4-(*1H*-pyrrol-1-yl)aniline (0.2 mmol, 31.6 mg), benzaldehyde (0.2 mmol, 20 μL), and acrylonitrile (0.4 mmol, 26 μL). The crude product was purified using flash column chromatography in a EtOAc/heptane eluent system. **Yield:** 56%. **^{1}H NMR** (400 MHz, $CDCl_3$) δ 7.41-7.26 (m, 5H), 7.13 (d, *J* = 8.7 Hz, 2H), 6.91 (t, *J* = 2.0 Hz, 2H), 6.60 (d, *J* = 8.7 Hz, 2H), 6.26 (t, *J* = 2.0 Hz, 2H), 4.49 (t, *J* = 7.0 Hz, 1H), 4.08 (s, 1H), 2.53-2.28 (m, 2H), 2.28-2.01 (m, 2H) ppm. **^{13}C NMR** (101 MHz, $CDCl_3$) δ 144.8, 141.4, 132.6, 129.1, 128.0, 126.3, 122.4, 119.6, 119.2, 114.3, 109.4, 57.3, 33.6, 14.5 ppm.

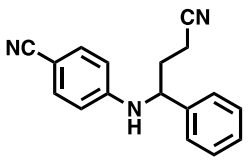

4-((3-Cyano-1-phenylpropyl)amino)benzonitrile ***5n***

Following procedure **3.5.5.2** with 4-aminobenzonitrile (0.2 mmol, 23.6 mg), benzaldehyde (0.2 mmol, 20 μL), and acrylonitrile (0.4 mmol, 26 μL). The crude product was purified using flash column chromatography in a EtOAc/heptane eluent system. **Yield:** 89%. **^{1}H NMR** (400 MHz, $CDCl_3$) δ 7.44-7.31 (m, 7H), 6.58 (d, *J* = 8.8 Hz, 2H), 4.59 (dt, *J* = 20.4, 6.7 Hz, 2H), 2.52-2.31 (m, 2H), 2.30-2.10 (m, 2H) ppm. **^{13}C NMR** (101 MHz, $CDCl_3$) δ 149.8, 140.2, 133.7, 129.4, 128.4, 126.2, 120.0, 118.9, 113.3, 100.2, 56.6, 33.2, 14.5 ppm.

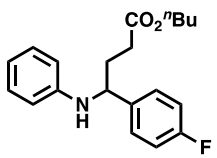

Butyl 4-((4-fluorophenyl)-4-(phenylamino)butanoate ***5o***

Following procedure **3.5.5.2** with aniline (0.2 mmol, 18 μL), 4-fluorobenzaldehyde (0.2 mmol, 21 μL), and *n*-butyl acrylate (0.4 mmol, 29 μL). The crude product was purified using flash column chromatography in a EtOAc/heptane eluent system. For isolation, **4b** (0.3 mmol, 94.0 mg) was used as the photoreductant. **Yield:** 54%. **^{1}H NMR** (400 MHz, $CDCl_3$) δ 7.30 (dd, *J* = 8.6, 5.4 Hz, 2H), 7.08 (dd, *J* = 8.4, 7.5 Hz, 2H), 7.00 (t, *J* = 8.7 Hz, 2H), 6.64 (t, *J* = 7.3 Hz, 1H), 6.48 (d, *J* = 7.7 Hz, 2H), 4.42-4.28 (t, *J* = 6.8 Hz, 1H), 4.26 (s, 1H), 4.07 (t, *J* = 6.7 Hz, 2H), 2.40 (t, *J* = 7.5 Hz, 2H), 2.15-2.03 (m, 2H), 1.59 (dt, *J* = 14.7, 6.9 Hz, 2H), 1.35 (dt, *J* = 14.6, 7.5 Hz, 2H), 0.92 (t, *J* = 7.4 Hz, 3H) ppm. **^{19}F NMR** (376 MHz, $CDCl_3$) δ -115.71 ppm. **^{13}C NMR** (101 MHz, $CDCl_3$) δ 173.6, 160.7, 147.0, 138.9, 129.1, 127.9, 127.8, 117.5, 115.7, 115.4, 113.3, 64.6, 57.2, 33.4, 31.2, 30.7, 19.1, 13.7 ppm. **HRMS** (ESI^+, *m*/*z*) [$M+H^+$] calcd. for $C_{20}H_{24}NO_2F$ 330.1864, found 330,1878.

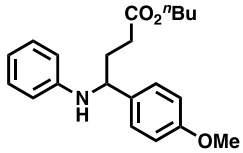

Butyl 4-((4-methoxyphenyl)-4-(phenylamino)butanoate ***5p***

Following procedure **3.5.5.2** with aniline (0.2 mmol, 18 μL), 4-methoxybenzaldehyde (0.2 mmol, 24 μL), and *n*-butyl acrylate (0.4 mmol). The crude product was purified using flash column chromatography in a EtOAc/heptane eluent system. For isolation, **4b** (0.3 mmol, 94.0 mg) was used as the photoreductant. **Yield:** 58%. **^{1}H NMR** (400 MHz, $CDCl_3$) δ 7.25-7.23 (m, 2H), 7.07 (dd, *J* = 8.3, 7.5 Hz, 2H), 6.86-6.84 (m, 2H), 6.64 -6.61(dt, *J* = 7.3 , 1.0 Hz, 1H), 6.52-6.50 (d, *J* = 7.7 Hz, 2H), 4.34-4.31 (t, *J* = 6.8 Hz, 1H), 4.20 (s, 1H), 4.07-4.05 (t, *J* = 6.7 Hz, 2H), 3.77 (s, 3H), 2.38 (t, *J* = 7.2 Hz, 2H), 2.20-1.98 (m, 2H), 1.65-1.48 (m, 2H), 1.43-1.23 (m, 1H), 0.92 (t, *J* = 7.4 Hz, 2H) ppm. **^{13}C NMR** (101 MHz, $CDCl_3$) δ 173.7, 158.7, 147.3, 135.2, 129.1, 127.5, 117.3, 114.1, 113.3, 64.5, 57.2, 55.3,

33.3, 31.3, 30.7, 19.1, 13.7 ppm. **HRMS** (ESI$^+$, *m*/*z*) [M+H$^+$] calcd. for $C_{21}H_{27}NO_3$ 342.2064, found 342.2071.

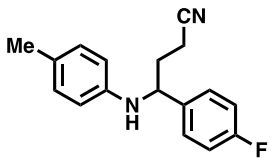

4-(4-Fluorophenyl)-4-(p-tolylamino)butanenitrile ***5q***

Following procedure **3.5.5.2** with *p*-toluidine (0.2 mmol, 22 μL), 4-fluorobenzaldehyde (0.2 mmol, 21 μL), and acrylonitrile (0.4 mmol, 26 μL). The crude product was purified using flash column chromatography in a EtOAc/heptane eluent system. For isolation, **4b** (0.3 mmol, 94.0 mg) was used as the photoreductant. **Yield:** 80%. **^{1}H NMR** (400 MHz, $CDCl_3$) δ 7.32-7.26 (m, 1H), 7.02 (dd, *J* = 12.0, 5.3 Hz, 1H), 6.92 (d, *J* = 8.2 Hz, 1H), 6.47 (d, *J* = 8.4 Hz, 1H), 4.46 (t, *J* = 7.0 Hz, 1H), 3.84 (s, 1H), 2.51-2.29 (m, 1H), 2.19 (s, 1H), 2.09 (ddt, *J* = 32.5, 13.9, 7.0 Hz, 1H) ppm. **^{19}F NMR** (376 MHz, $CDCl_3$) δ -114.54 ppm. **^{13}C NMR** (101 MHz, $CDCl_3$) δ 163.4, 161.0, 144.1, 137.6, 137.6, 129.8, 127.9, 127.8, 127.7, 119.2, 116.0, 115.8, 114.0, 56.6, 33.7, 20.3, 14.5 ppm.

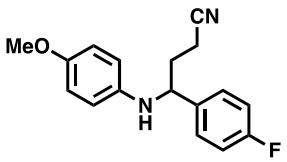

4-(4-Fluorophenyl)-4-((4-methoxyphenyl)amino)butanenitrile ***5r***

Following procedure **3.5.5.2** with *p*-anisidine (0.2 mmol, 24.6 mg), 4-fluorobenzaldehyde (0.2 mmol, 21 μL), and acrylonitrile (0.4 mmol, 26 μL). The crude product was purified using flash column chromatography in a EtOAc/heptane eluent system. For isolation, **4b** (0.3

mmol, 94.0 mg) was used as the photoreductant. **Yield:** 77%. **^{1}H NMR** (400 MHz, $CDCl_3$) δ 7.34-7.25 (m, 2H), 7.02 (t, *J* = 8.6 Hz, 2H), 6.70 (d, *J* = 8.9 Hz, 2H), 6.51 (d, *J* = 8.9 Hz, 2H), 4.41 (t, *J* = 7.0 Hz, 1H), 3.70 (s, 3H), 2.41 (ddt, *J* = 50.4, 17.0, 7.1 Hz, 2H), 2.24-1.97 (m, 2H) ppm. **^{19}F NMR** (376 MHz, $CDCl_3$) δ -114.50 ppm. **^{13}C NMR** (101 MHz, $CDCl_3$) δ 163.4, 161.0, 152.8, 140.4, 137.7, 137.6, 128.0, 127.9, 119.2, 116.0, 115.8, 115.4, 114.9, 57.3, 55.7, 33.7, 14.5 ppm. **HRMS** (ESI^+, *m*/*z*) [$M+H^+$] calcd. for $C_{17}H_{17}N_2OF$ 285.1398, found 285.1393.

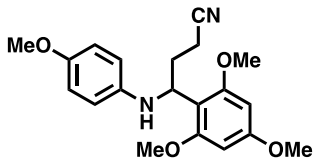

4-((4-Methoxyphenyl)amino)-4-(2,4,6-trimethoxyphenyl)butanenitrile ***5s***

Following procedure **3.5.5.2** with *p*-anisidine (0.2 mmol, 24.6 mg), 2,4,6-trimethoxybenzaldehyde (0.2 mmol, 39.2 mg), and acrylonitrile (0.4 mmol, 26 μL). The crude product was purified using flash column chromatography in a EtOAc/heptane eluent system. **Yield:** 90%. **^{1}H NMR** (400 MHz, $CDCl_3$) δ 6.70 (d, *J* = 8.9 Hz, 2H), 6.62 (d, *J* = 9.0 Hz, 2H), 6.09 (s, 2H), 5.00 (t, *J* = 7.4 Hz, 1H), 4.52 (s, 1H), 3.84 (s, 6H), 3.76 (s, 3H), 3.70 (s, 3H), 2.52-2.21 (m, 3H), 2.17-1.84 (m, 1H) ppm. **^{13}C NMR** (101 MHz, $CDCl_3$) δ 160.4, 159.0, 152.2, 142.0, 120.1, 115.3, 114.8, 109.6, 91.0, 55.7, 55.7, 55.3, 48.8, 30.6, 14.8 ppm. **HRMS** (ESI^+, *m*/*z*) [$M+H^+$] calcd. for $C_{20}H_{24}N_2O_4$ 357.1809, found 357.1797.

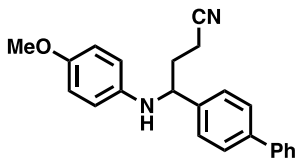

4-([1,1'-Biphenyl]-4-yl)-4-((4-methoxyphenyl)amino)butanenitrile ***5t***

Following procedure **3.5.5.2** with *p*-anisidine (0.2 mmol, 24.6 mg), 4-phenylbenzaldehyde (0.2 mmol, 36.4 mg), and acrylonitrile (0.4 mmol, 26 μL). The crude product was purified using flash column chromatography in a EtOAc/heptane eluent system. **Yield:** 57%. **^{1}H NMR** (400 MHz, $CDCl_3$) δ 7.60-7.52 (m, 4H), 7.38 (qd, *J* = 14.9, 7.3 Hz, 5H), 6.78-6.66 (m, 2H), 6.61-6.49 (m, 2H), 4.47 (t, *J* = 7.0 Hz, 1H), 3.74 (s, 1H), 3.70 (s, 3H), 2.56-2.33 (m, 2H), 2.16 (dtd, *J* = 20.9, 14.0, 6.9 Hz, 2H) ppm. **^{13}C NMR** (101 MHz, $CDCl_3$) δ 152.7, 140.9, 140.7, 140.6, 140.5, 128.8, 127.7, 127.4, 127.0, 126.8, 119.4, 115.3, 114.9, 57.6, 55.7, 33.6, 14.6 ppm. **HRMS** (ESI^+, *m*/*z*) [$M+H^+$] calcd. for $C_{23}H_{22}N_2O_1$ 343.1805, found 343.1789.

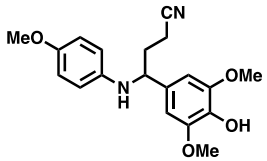

4-(4-Hydroxy-3,5-dimethoxyphenyl)-4-((4-methoxyphenyl)amino)butanenitrile ***5u***

Following procedure **3.5.5.2** with *p*-anisidine (0.2 mmol, 24.6 mg), syringaldehyde (0.2 mmol, 36.4 mg), and acrylonitrile (0.4 mmol, 26 μL). The crude product was purified using flash column chromatography in a EtOAc/heptane eluent system. **Yield:** 77%. **^{1}H NMR** (400 MHz, $CDCl_3$) δ 6.72 (d, *J* = 8.9 Hz, 2H), 6.55 (t, *J* = 4.4 Hz, 4H), 5.45 (s, 1H), 4.32 (t, *J* = 7.0 Hz, 1H), 3.87 (s, 6H), 3.71 (s, 3H), 2.64-2.25 (m, 2H), 2.25-1.91 (m, 2H) ppm. **^{13}C NMR** (101 MHz, $CDCl_3$) δ 152.7, 147.5, 140.8, 134.2, 133.1, 119.4, 115.4,

114.9, 103.0, 58.4, 56.4, 55.7, 33.7, 14.5 ppm. **HRMS** (ESI$^+$, *m*/*z*) [M+H$^+$] calcd. for $C_{19}H_{22}N_2O_4$ 343.1652, found 343.1644.

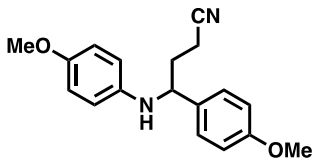

4-(4-Methoxyphenyl)-4-((4-methoxyphenyl)amino)butanenitrile ***5v***

Following procedure **3.5.5.2** with *p*-anisidine (0.2 mmol, 24.6 mg), 4-methoxybenzaldehyde (0.2 mmol, 24 µL), and acrylonitrile (0.4 mmol, 26 µL). The crude product was purified using flash column chromatography in a EtOAc/heptane eluent system. For isolation, **4b** (0.3 mmol, 94.0 mg) was used as the photoreductant. **Yield:** 65%. **^{1}H NMR** (400 MHz, $CDCl_3$) δ 7.23 (d, *J* = 8.6 Hz, 2H), 6.92-6.81 (m, 2H), 6.76-6.66 (m, 2H), 6.54 (d, *J* = 8.9 Hz, 2H), 4.37 (t, *J* = 7.0 Hz, 1H), 3.78 (s, 3H), 3.70 (s, 3H), 2.51-2.24 (m, 2H), 2.24-1.98 (m, 2H) ppm. **^{13}C NMR** (101 MHz, $CDCl_3$) δ 159.1, 152.6, 140.8, 133.8, 127.4, 119.4, 115.3, 114.9, 114.4, 57.4, 55.7, 55.3, 33.6, 14.5 ppm.

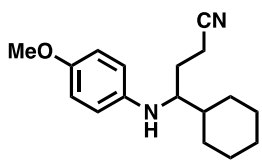

4-Cyclohexyl-4-((4-methoxyphenyl)amino)butanenitrile ***5w***

Following procedure **3.5.5.2** with *p*-anisidine (0.2 mmol, 24.6 mg), cyclohexanecarbaldehyde (0.4 mmol, 48 μL), acrylonitrile (0.4 mmol, 26 μL) and additional acetic acid (0.02 mmol, 1.1 μL). The crude product was purified using flash column chromatography in a EtOAc/heptane eluent system. **Yield:** 42%. **^{1}H NMR** (400 MHz, $CDCl_3$) δ 6.76 (d, *J* = 8.9 Hz, 2H), 6.56 (d, *J* = 8.9 Hz, 2H), 3.74 (s, 3H), 3.31-3.17 (m, 1H), 2.52-2.39 (m, 2H), 2.09-1.91 (m, 1H), 1.74 (s, 3H), 1.66 (dd, *J* = 12.5, 5.1 Hz, 2H), 1.51 (ddd, *J* = 11.7, 8.3, 4.6 Hz, 1H), 1.24-0.99 (m, 5H) ppm. **^{13}C NMR** (101 MHz, $CDCl_3$) δ 152.1, 142.2, 120.1, 115.1, 114.6, 58.1, 55.8, 42.1, 29.3, 29.0, 28.5, 26.5, 26.3, 26.3, 14.6 ppm.

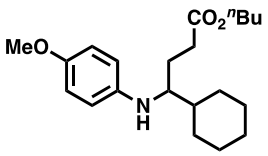

Butyl 4-cyclohexyl-4-((4-methoxyphenyl)amino)butanoate ***5x***

Following procedure **3.5.5.2** with *p*-anisidine (0.2 mmol, 24.6 mg), cyclohexanecarbaldehyde (0.4 mmol, 48 μL), *n*-butyl acrylate (0.4 mmol, 29 μL) and additional acetic acid (0.02 mmol, 1.1 μL). The crude product was purified using flash column chromatography in a EtOAc/heptane eluent system. **Yield:** 25 %. **^{1}H NMR** (400 MHz, $CDCl_3$) δ 6.73 (d, *J* = 8.8 Hz, 2H), 6.50 (d, *J* = 8.7 Hz, 2H), 4.03 (t, *J* = 6.3 Hz, 2H), 3.73 (s, 3H), 3.19-3.08 (m, 1H), 2.48-2.29 (m, 2H), 2.00-1.86 (m, 1H), 1.74 (d, *J* = 9.5 Hz, 3H), 1.65 (d, *J* = 5.8 Hz, 2H), 1.58-1.46 (m, 4H), 1.32 (dt, *J* = 14.8, 7.5 Hz, 2H), 1.11 (ddd, *J* = 35.8, 16.7, 7.4 Hz, 5H), 0.90 (t, *J* = 7.4 Hz, 3H) ppm. **^{13}C NMR**

(101 MHz, $CDCl_3$) δ 174.2, 151.5, 142.8, 115.0, 114.0, 64.3, 58.5, 55.9, 42.1, 31.7, 30.7, 29.2, 29.0, 27.4, 26.6, 26.5, 26.4, 19.1, 13.7 ppm.

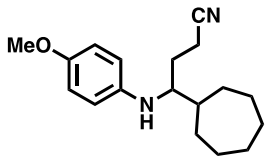

4-Cycloheptyl-4-((4-methoxyphenyl)amino)butanenitrile ***5y***

Following procedure **3.5.5.2** with *p*-anisidine (0.2 mmol, 24.6 mg), cycloheptanecarbaldehyde (0.4 mmol, 52 μL), acrylonitrile (0.4 mmol, 26 μL) and additional acetic acid (0.02 mmol, 1.1 μL). The crude product was purified using flash column chromatography in a EtOAc/heptane eluent system. **Yield:** 34 %. **^{1}H NMR** (400 MHz, $CDCl_3$) δ 6.77 (d, *J* = 8.9 Hz, 2H), 6.57 (d, *J* = 8.9 Hz, 2H), 3.75 (s, 3H), 3.29 (dt, *J* = 10.2, 3.6 Hz, 1H), 2.53-2.41 (m, 2H), 2.00-1.86 (m, 1H), 1.77-1.61 (m, 6H), 1.58-1.44 (m, 6H), 1.34 (ddd, *J* = 19.4, 12.2, 5.6 Hz, 2H) ppm. **^{13}C NMR** (101 MHz, $CDCl_3$) δ 152.2, 141.8, 120.1, 115.1, 114.8, 59.0, 55.8, 42.3, 30.8, 29.6, 28.3, 28.1, 27.9, 27.1, 26.4, 14.9 ppm. **HRMS** (ESI^+, *m*/*z*) [$M+H^+$] calcd. for $C_{18}H_{26}N_2O$ 287.2118, found 287.2132.

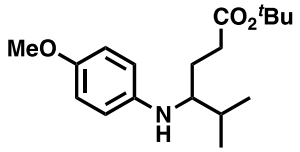

t-Butyl 4-((4-methoxyphenyl)amino)-5-methylhexanoate ***5z***

Following procedure **3.5.5.2** with *p*-anisidine (0.2 mmol, 24.6 mg), 2-methylpropanal (0.4 mmol, 36 μL), *t*-butyl acrylate (0.4 mmol, 29 μL) and additional acetic acid (0.02 mmol, 1.1 μL). The crude product was

purified using flash column chromatography in a EtOAc/heptane eluent system. **Yield:** 12 %. **^{1}H NMR** (400 MHz, $CDCl_3$) δ 6.74 (d, *J* = 8.9 Hz, 2H), 6.51 (d, *J* = 8.9 Hz, 2H), 3.73 (s, 3H), 3.23-3.06 (m, 1H), 2.40-2.23 (m, 2H), 1.95-1.77 (m, 2H), 1.61 (m, 1H), 1.42 (s, 9H), 0.93 (d, *J* = 6.9 Hz, 2H), 0.89 (d, *J* = 6.8 Hz, 2H) ppm. **^{13}C NMR** (101 MHz, $CDCl_3$) δ 173.4, 151.5, 142.8, 115.0, 114.1, 80.2, 58.9, 55.9, 53.4, 32.8, 31.3, 28.1, 18.6, 18.0 ppm.

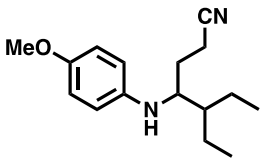

5-Ethyl-4-((4-methoxyphenyl)amino)heptanenitrile ***5aa***

Following procedure **3.5.5.2** with *p*-anisidine (0.2 mmol, 24.6 mg), 2-ethylbutanal (0.4 mmol, 50 μL), acrylonitrile (0.4 mmol, 26 μL) and additional acetic acid (0.02 mmol, 1.1 μL). The crude product was purified using flash column chromatography in a EtOAc/heptane eluent system. **Yield:** 17 %. **^{1}H NMR** (400 MHz, $CDCl_3$) δ 6.77 (d, *J* = 8.7 Hz, 2H), 6.57 (s, 2H), 3.74 (s, 3H), 3.46 (s, 1H), 2.51-2.43 (m, 2H), 1.90 (m, 1H), 1.61 (ddd, *J* = 16.1, 13.6, 6.5 Hz, 1H), 1.40 (dd, *J* = 13.7, 6.4 Hz, 3H), 1.29-1.16 (m, 3H), 0.96 (t, *J* = 7.1 Hz, 3H), 0.89 (t, *J* = 7.2 Hz, 3H) ppm. **^{13}C NMR** (101 MHz, $CDCl_3$) δ 152.2, 141.9, 120.0, 115.1, 114.7, 55.8, 44.5, 29.7, 27.9, 22.5, 22.0, 14.8, 12.1, 12.1 ppm. **HRMS** (ESI^+, *m*/*z*) [$M+H^+$] calcd. for $C_{16}H_{24}N_2O$ 261.1961, found 261.1953.

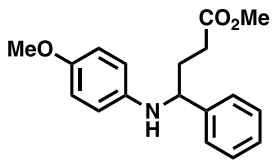

Methyl 4-((4-methoxyphenyl)amino-4-phenylbutanoate ***5ab***

Following procedure **3.5.5.2** with *p*-anisidine (0.2 mmol, 24.6 mg), benzaldehyde (0.2 mmol, 20 μL), and methyl acrylate (0.4 mmol, 36 μL). The crude product was purified using flash column chromatography in a EtOAc/heptane eluent system. For isolation, **4b** (0.3 mmol, 94.0 mg) was used as the photoreductant. **Yield:** 90%. **^{1}H NMR** (400 MHz, $CDCl_3$) δ 7.35-7.27 (m, 4H), 7.23-7.17 (m, 1H), 6.74-6.62 (m, 2H), 6.48 (m, , 2H), 4.30 (t, *J* = 6.8 Hz, 1H), 3.95 (s, 1H), 3.68 (s, 3H), 3.60 (s, 3H), 2.40 (t, *J* = 7.2 Hz, 2H), 2.26-1.87 (m, 2H) ppm. **^{13}C NMR** (101 MHz, $CDCl_3$) δ 174.0, 152.0, 143.3, 141.4, 128.7, 127.2, 126.4, 114.8, 114.6, 58.6, 55.8, 51.7, 33.3, 31.0 ppm.

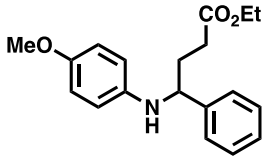

Ethyl 4-((4-methoxyphenyl)amino-4-phenylbutanoate ***5ac***

Following procedure **3.5.5.2** with *p*-anisidine (0.2 mmol, 24.6 mg), benzaldehyde (0.2 mmol, 20 μL), and ethyl acrylate (0.4 mmol, 43 μL). The crude product was purified using flash column chromatography in a EtOAc/heptane eluent system. For isolation, **4b** (0.3 mmol, 94.0 mg) was used as the photoreductant. **Yield:** 86%. **^{1}H NMR** (400 MHz, $CDCl_3$) δ 7.32-7.26 (m, 4H), 7.24-7.22 (m, 1H), 6.70-6.64 (m, 2H), 6.55-6.42 (m, 2H), 4.32-4.28 (t, *J* = 6.9 Hz 1H), 4.12 (q, *J* = 7.1 Hz, 2H), 3.97 (s, 1H), 3.68 (s, 3H), 2.39 (t, *J* = 7.2 Hz, 2H), 2.21-1.94 (m, 2H), 1.24 (t, *J* = 7.1 Hz, 3H) ppm. **^{13}C NMR** (101 MHz, $CDCl_3$) δ 173.6, 152.0, 143.4, 141.5, 128.7, 127.2, 126.5, 114.8, 114.6, 60.5, 58.6, 55.8, 33.3, 31.3, 14.2 ppm.

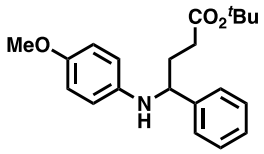

t-Butyl 4-((4-methoxyphenyl)amino-4-phenylbutanoate ***5ad***

Following procedure **3.5.5.2** with *p*-anisidine (0.2 mmol, 24.6 mg), benzaldehyde (0.2 mmol, 20 μL), and *t*-butyl acrylate (0.4 mmol, 29 μL). The crude product was purified using flash column chromatography in a EtOAc/heptane eluent system. For isolation, **4b** (0.3 mmol, 94.0 mg) was used as the photoreductant. **Yield:** 64 %. **^{1}H NMR** (400 MHz, $CDCl_3$) δ 7.33-7.27 (m, 4H), 7.21 (ddd, *J* = 8.5, 5.5, 2.4 Hz, 1H), 6.73-6.60 (m, 2H), 6.53-6.29 (m, 2H), 4.28 (dd, *J* = 7.4, 6.2 Hz, 1H), 4.04 (s, 1H), 3.68 (s, 3H), 2.31 (dd, *J* = 10.7, 4.2 Hz, 2H), 2.18-1.94 (m, 2H), 1.44 (s, 9H) ppm. **^{13}C NMR** (101 MHz, $CDCl_3$) δ 173.0, 151.9, 143.6, 141.6, 128.6, 127.1, 126.5, 114.8, 114.5, 80.5, 58.7, 55.8, 33.4, 32.5, 28.1 ppm.

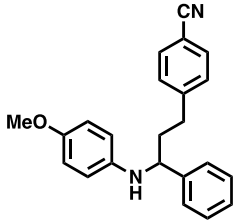

4-(3-((4-methoxyphenyl)amino)-3-phenylpropyl)benzonitrile ***5ae***

Following procedure **3.5.5.2** with *p*-anisidine (0.2 mmol, 24.6 mg), benzaldehyde (0.2 mmol, 20 μL), and 4-vinylbenzonitrile (0.4 mmol,

48 μL). The crude product was purified using flash column chromatography in a EtOAc/heptane eluent system. **Yield:** 36 %. **^{1}H NMR** (400 MHz, $CDCl_3$) δ 7.56 (d, *J* = 8.2 Hz, 2H), 7.38-7.28 (m, 5H), 7.23 (d, *J* = 9.1 Hz, 2H), 6.73-6.58 (m, 2H), 6.45 (dd, *J* = 9.6, 2.8 Hz, 2H), 4.24 (t, *J* = 6.8 Hz, 1H), 3.84 (s, 1H), 3.69 (s, 3H), 2.86-2.58 (m, 2H), 2.26-1.74 (m, 2H) ppm. **^{13}C NMR** (101 MHz, $CDCl_3$) δ 152.2, 147.3, 143.5, 141.2, 132.3, 129.2, 128.7, 127.3, 126.4, 119.0, 114.9, 114.7, 110.0, 58.3, 55.7, 39.6, 32.8 ppm.

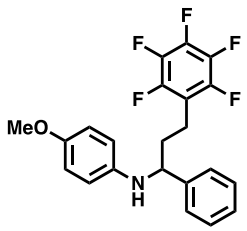

4-Methoxy-N-(3-(perfluorophenyl)-1-phenylpropyl)aniline ***5af***

Following procedure **3.5.5.2** with *p*-anisidine (0.2 mmol, 24.6 mg), benzaldehyde (0.2 mmol, 20 μL), and 2,3,4,5,6-pentafluorostyrene (0.4 mmol, 55 μL). The crude product was purified using flash column chromatography in a EtOAc/heptane eluent system. **Yield:** 48 %. **^{1}H NMR** (400 MHz, $CDCl_3$) δ 7.32 (d, *J* = 4.3 Hz, 4H), 7.23 (m, 1H), 6.70 (d, *J* = 8.8 Hz, 2H), 6.50 (d, *J* = 8.7 Hz, 2H), 4.32 (t, *J* = 6.7 Hz, 1H), 3.69 (s, 3H), 2.85 (dt, *J* = 15.2, 7.7 Hz, 1H), 2.78-2.64 (m, 1H), 2.06 (dd, *J* = 15.1, 7.6 Hz, 2H) ppm. **^{19}F NMR** (376 MHz, $CDCl_3$) δ -144.22, -157.60, -162.71 ppm. **^{13}C NMR** (101 MHz, $CDCl_3$) δ 152.3, 143.0, 141.2, 128.8, 127.4, 126.4, 114.9, 58.9, 55.7, 37.7, 19.7 ppm. **HRMS** (ESI^+, *m*/*z*) [$M+H^+$] calcd. for $C_{22}H_{18}NOF_5$ 408.1381, found 408.1388.

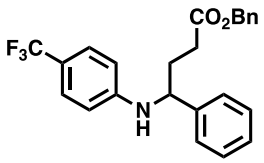

Benzyl 4-phenyl-4-((4-(trifluoromethyl)phenyl)amino)butanoate ***5ag***

Following procedure **3.5.5.5** with (*E*)-N-(4-(trifluoromethyl)phenyl)-1-phenylmethanimine (0.2 mmol, 49.8 mg) and benzyl acrylate (0.4 mmol, 59 µL). The crude product was purified using flash column chromatography in a EtOAc/heptane eluent system. For isolation, **4b** (0.3 mmol, 94.0 mg) was used as the photoreductant. **Yield:** 69 %. **^{1}H NMR** (400 MHz, $CDCl_3$) δ 7.36-7.21 (m, 12H), 6.47 (d, *J* = 8.5 Hz, 2H), 5.12 (s, 2H), 4.68 (s, 1H), 4.40 (t, *J* = 6.8 Hz, 1H), 2.55-2.38 (m, 2H), 2.30-2.03 (m, 2H) ppm. **^{19}F NMR** (376 MHz, $CDCl_3$) δ -61.11 ppm. **^{13}C NMR** (101 MHz, $CDCl_3$) δ 173.4, 149.6, 142.2, 135.7, 128.9, 128.6, 128.4, 128.4, 128.2, 127.6, 126.5, 126.5, 126.2, 112.5, 66.6, 57.6, 32.9, 31.2 ppm.

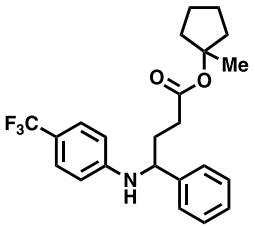

1-Methylcyclopentyl 4-phenyl-4-((4-(trifluoromethyl)phenyl)amino)butanoate ***5ah***

Following procedure **3.5.5.5** with (*E*)-*N*-(4-(trifluoromethyl)phenyl)-1-phenylmethanimine (0.2 mmol, 49.8 mg) and 1-methylcyclopentyl acrylate (0.4 mmol, 62 µL). The crude product was purified using flash column chromatography in a EtOAc/heptane eluent system. For isolation, **4b** (0.3 mmol, 94.0 mg) was used as the photoreductant. **Yield:** 67 %. **^{1}H NMR** (400 MHz, $CDCl_3$) δ 7.36-7.26 (m, 6H), 7.24-7.22 (m, 1H), 6.50 (d, *J* = 8.5 Hz, 2H), 4.84 (s, 1H), 4.39 (dd, *J* = 7.8, 5.9 Hz, 1H), 2.40-2.27 (m, 2H),

2.09 (pd, *J* = 14.2, 7.1 Hz, 4H), 1.76-1.59 (m, 6H), 1.55 (s, 3H) ppm. **^{19}F NMR** (376 MHz, $CDCl_3$) δ -61.09 ppm. **^{13}C NMR** (101 MHz, $CDCl_3$) δ 173.2, 149.7, 142.5, 128.9, 127.4, 126.5, 126.4, 126.3, 119.0-118.7 (d, CF_3), 112.4, 90.4, 57.9, 39.2, 39.2, 33.0, 32.3, 24.4, 23.8 ppm.

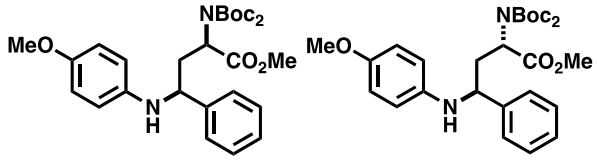

Methyl 2-(bis(t-butoxycarbonyl)amino)-4-((4-methoxyphenyl)amino)-4-phenylbutanoate ***5ai***

Following procedure **3.5.5.2** with *p*-anisidine (0.2 mmol, 24.6 mg), benzaldehyde (0.2 mmol, 20 μL), and methyl 2-(bis(*t*-butoxycarbonyl)amino)but-3-enoate (0.4 mmol, 120 mg). The crude product was purified using flash column chromatography in a EtOAc/heptane eluent system. **Yield:** 29 %. **^{1}H NMR** (400 MHz, $CDCl_3$) δ 7.39 (d, *J* = 7.4 Hz, 2H), 7.30 (t, *J* = 7.5 Hz, 2H), 7.24-7.17 (m, 1H), 6.67 (d, *J* = 8.8 Hz, 2H), 6.47 (d, *J* = 8.8 Hz, 2H), 5.05-4.96 (m, 1H), 4.50 (dd, *J* = 8.9, 4.6 Hz, 1H), 3.72 (s, 3H), 3.68 (s, 3H), 2.86-2.73 (m, 1H), 2.05 (ddd, *J* = 14.5, 9.0, 5.4 Hz, 1H), 1.47 (s, 18H) ppm. **^{13}C NMR** (101 MHz, $CDCl_3$) δ 171.2, 152.2, 151.9, 143.7, 141.7, 128.7, 127.1, 126.4, 114.8, 114.6, 83.4, 56.8, 56.0, 55.8, 52.3, 40.6, 28.0 ppm. **HRMS** (ESI^+, *m*/*z*) [M+H^+] calcd. for $C_{28}H_{38}N_2O_7$ 515.2752, found 515.2751.

Following procedure 1.6.2 with *p*-anisidine (0.2 mmol, 24.6 mg), benzaldehyde (0.2 mmol, 20 μL), and 2-(bis(*t*-butoxycarbonyl)amino)but-3-enoate (0.4 mmol, 120 mg). The crude product was purified using flash column chromatography in a EtOAc/heptane eluent system. **Yield:** 22 %. **^{1}H NMR** (400 MHz, $CDCl_3$) δ 7.33-7.28 (m, 4H), 7.21-7.16 (m, 1H), 6.68-6.62 (m, 2H), 6.47 (d, *J* = 6.1 Hz, 2H), 5.16 (dd, *J* = 7.7, 5.4 Hz, 1H), 4.38 (dd, *J* = 10.3, 3.9 Hz, 1H), 3.73 (s,

3H), 3.67 (s, 3H), 2.60 (ddd, *J* = 15.4, 10.3, 5.3 Hz, 1H), 2.28 (ddd, *J* = 14.9, 7.8, 4.0 Hz, 1H), 1.42 (s, 18H) ppm. **^{13}C NMR** (101 MHz, $CDCl_3$) δ 171.8, 152.0, 151.9, 143.7, 141.3, 128.7, 127.1, 126.2, 114.8, 114.8, 83.3, 56.5, 56.2, 55.8, 52.4, 39.9, 27.9 ppm. **HRMS** (ESI$^+$, *m*/*z*) [M+H$^+$] calcd. for $C_{28}H_{38}N_2O_7$ 515.2752, found 515.2751.

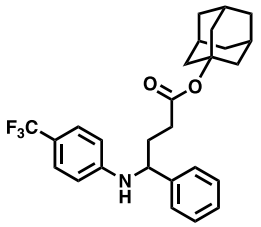

Admantan-1-yl 4-phenyl-4-((4-(trifluoromethyl)phenyl)amino)butanoate ***5aj***

Following procedure **3.5.5.5** with (*E*)-*N*-(4-(trifluoromethyl)phenyl)-1-phenylmethanimine (0.2 mmol, 49.8 mg) and adamantan-1-yl acrylate (0.4 mmol, 76 μL). The crude product was purified using flash column chromatography in a EtOAc/heptane eluent system. For isolation, **4b** (0.3 mmol, 94.0 mg) was used as the photoreductant. **Yield:** 70 %. **^{1}H NMR** (400 MHz, $CDCl_3$) δ 7.31 (h, *J* = 7.7 Hz, 6H), 7.23 (dd, *J* = 5.7, 2.8 Hz, 1H), 6.50 (d, *J* = 8.5 Hz, 2H), 4.84 (s, 1H), 4.39 (t, *J* = 6.7 Hz, 1H), 2.49-2.20 (m, 2H), 2.17 (s, 3H), 2.11-2.00 (m, 8H), 1.67 (s, 6H) ppm. **^{19}F NMR** (376 MHz, $CDCl_3$) δ -61.1 ppm. **^{13}C NMR** (101 MHz, $CDCl_3$) δ 172.8, 149.8, 142.6, 128.8, 127.4, 126.5, 126.4, 126.2, 118.9-118.6 (d, CF_3), 112.4, 81.1, 57.9, 41.4, 36.2, 33.0, 32.6, 30.9 ppm.

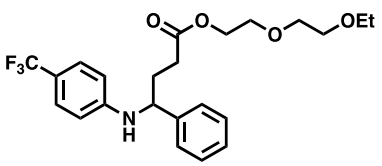

2-(2-Ethoxyethoxy)ethyl 4-phenyl-4-((4-(trifluoromethyl)phenyl)amino)butanoate ***5ak***

Following procedure **3.5.5.2** with 4-(trifluoromethyl)aniline (0.2 mmol, 25 μL), benzaldehyde (0.2 mmol, 20 μL), and 2-(2-ethoxyethoxy)ethyl acrylate (0.4 mmol, 74 μL). The crude product was purified using flash column chromatography in a EtOAc/heptane eluent system. **Yield:** 34 %. **^{1}H NMR** (400 MHz, $CDCl_3$) δ 7.37-7.26 (m, 7H), 6.52 (d, *J* = 8.5 Hz, 2H), 4.75 (d, *J* = 5.2 Hz, 1H), 4.42 (dd, *J* = 13.0, 6.0 Hz, 1H), 4.30-4.19 (m, 2H), 3.71-3.67 (m, 2H), 3.65-3.60 (m, 2H), 3.58-3.54 (m, 2H), 3.50 (q, *J* = 7.0 Hz, 2H), 2.53-2.38 (m, 2H), 2.26-2.04 (m, 2H), 1.19 (t, *J* = 7.0 Hz, 3H) ppm. **^{19}F NMR** (376 MHz, $CDCl_3$) δ -61.1 ppm. **^{13}C NMR** (101 MHz, $CDCl_3$) δ 173.5, 149.7, 142.3, 128.9, 127.5, 126.5, 126.5, 126.3, 119.0-118.8 (d, CF_3), 112.5, 70.7, 69.8, 69.1, 66.7, 63.9, 57.7, 33.0, 31.2, 15.1 ppm. **HRMS** (ESI^+, *m*/*z*) [$M+H^+$] calcd. for $C_{23}H_{28}NO_4F_3$ 440.2043, found 440.2033.

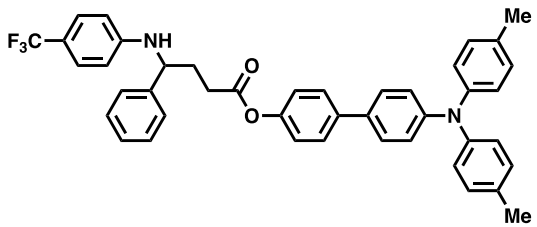

4'-(di-p-tolylamino)-[1,1'-biphenyl]-4-yl 4-phenyl-4-((4-(trifluoromethyl)phenyl)amino)butanoate ***5al***

Following procedure **3.5.5.2** with 4-(trifluoromethyl)aniline (0.2 mmol, 25 μL), benzaldehyde (0.2 mmol, 20 μL), and 4'-(di-p-tolylamino)-[1,1'-biphenyl]-4-yl acrylate (0.4 mmol, 167.8 mg). The crude product was purified using flash column chromatography in a EtOAc/heptane eluent system. **Yield:** 43 %. **^{1}H NMR** (400 MHz, $CDCl_3$) δ 7.53 (d, *J* = 8.6 Hz, 2H), 7.38 (d, *J* = 8.6 Hz, 2H), 7.35 (d, *J* = 3.9 Hz, 3H), 7.31 (d, *J* = 8.5 Hz, 2H), 7.05 (ddd, *J* = 21.3, 10.6, 6.3 Hz, 14H), 6.55 (d, *J* = 8.5 Hz, 2H), 4.69 (s, 1H), 4.52 (t, *J* = 6.6 Hz, 1H), 2.69 (td, *J* = 6.9, 2.7 Hz, 2H), 2.31 (s, 6H), 2.30 – 2.17 (m,

2H) ppm. **^{19}F NMR** (376 MHz, $CDCl_3$) δ -61.1 ppm. **^{13}C NMR** (101 MHz, $CDCl_3$) δ 172.3, 149.6, 149.4, 147.8, 145.2, 142.1, 138.8, 133.1, 132.7, 130.0, 129.9, 129.0, 127.7, 127.6, 126.6, 126.5, 126.3, 124.8, 124.6, 122.5, 121.6, 112.6, 57.6, 35.5, 32.8, 31.3, 20.8 ppm.

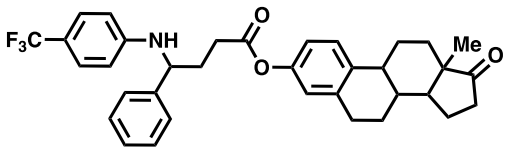

13-Methyl-17-oxo-7,8,9,11,12,13,14,15,16,17-decahydro-6H-cyclopenta[a] phenantren-2-yl 4-phenyl-4-((4-(trifluoromethyl)phenyl)amino)butanoate ***5am***

Following procedure **3.5.5.2** with 4-(trifluoromethyl)aniline (0.2 mmol, 25 μL), benzaldehyde (0.2 mmol, 20 μL), and estrone acrylate (**0.24** mmol, 77.9 mg). The crude product was purified using flash column chromatography in a EtOAc/heptane eluent system. **Yield:** 50 %. **^{1}H NMR** (400 MHz, $CDCl_3$) δ 7.36 (t, *J* = 5.0 Hz, 2H), 7.33-7.22 (m, 5H), 6.81 (dd, *J* = 8.5, 2.4 Hz, 1H), 6.74 (d, *J* = 1.8 Hz, 1H), 6.54 (d, *J* = 8.6 Hz, 2H), 4.70 (d, *J* = 5.4 Hz, 1H), 4.51 (dd, *J* = 12.8, 6.1 Hz, 1H), 3.02-2.79 (m, 2H), 2.66 (tt, *J* = 11.1, 5.7 Hz, 2H), 2.51 (dd, *J* = 18.8, 8.6 Hz, 1H), 2.44-2.35 (m, 1H), 2.34-1.97 (m, 7H), 1.69-1.41 (m, 7H), 0.91 (s, 3H) ppm. **^{19}F NMR** (376 MHz, $CDCl_3$) δ -61.08 ppm. **^{13}C NMR** (101 MHz, $CDCl_3$) δ 172.5, 149.6, 148.4, 142.1, 138.2, 137.6, 129.2, 129.0, 127.7, 126.6, 126.5, 126.5, 126.3, 125.7, 121.5, 121.2, 119.3, 118.9, 118.6, 112.6, 57.6, 50.5, 47.9, 44.2, 38.0, 35.9, 32.8, 31.6, 31.3, 29.4, 26.3, 25.8, 21.6, 13.8 ppm.

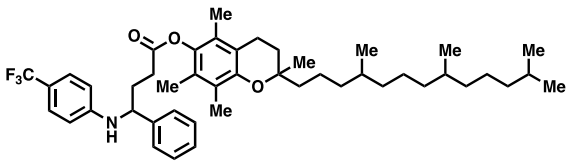

2,5,7,8-Tetramethyl-2-(4,8,12-trimethyltridecyl)chroman-6-yl 4-phenyl-4-((4-(trifluoromethyl)phenyl)amino)butanoate ***5an***

Following procedure **3.5.5.2** with 4-(trifluoromethyl)aniline (0.2 mmol, 25 μL), benzaldehyde (0.2 mmol, 20 μL), and α-tocopherol acrylate (**0.24** mmol, 116.4 mg). The crude product was purified using flash column chromatography in a EtOAc/heptane eluent system. **Yield:** 37 %. **^{1}H NMR** (400 MHz, $CDCl_3$) δ 7.37-7.33 (m, 4H), 7.29 (dd, *J* = 10.0, 6.4 Hz, 3H), 6.54 (d, *J* = 8.5 Hz, 2H), 4.82 (d, *J* = 6.1 Hz, 1H), 4.54 (dd, *J* = 13.0, 6.3 Hz, 1H), 2.81-2.65 (m, 2H), 2.58 (t, *J* = 6.7 Hz, 2H), 2.38-2.18 (m, 2H), 2.09 (s, 3H), 1.97 (s, 3H), 1.93 (s, 3H), 1.78 (ddq, *J* = 19.8, 13.2, 6.7 Hz, 2H), 1.59-1.46 (m, 2H), 1.38 (d, *J* = 4.8 Hz, 3H), 1.26 (t, *J* = 8.7 Hz, 12H), 1.18-1.06 (m, 7H), 0.89-0.84 (m, 12H) ppm. **^{19}F NMR** (376 MHz, $CDCl_3$) δ -61.12 ppm. **^{13}C NMR** (101 MHz, $CDCl_3$) δ 172.6, 149.6, 142.2, 140.4, 129.0, 127.6, 126.5, 126.5, 126.3, 124.8, 123.2, 117.5, 112.6, 75.2, 57.7, 39.4, 37.4, 37.3, 32.8, 30.8, 29.7, 28.0, 24.8, 24.5, 22.7, 22.6, 21.1, 20.6, 19.8, 19.7, 13.0, 12.2, 11.9 ppm. **HRMS** (ESI$^+$, *m*/*z*) [M+H$^+$] calcd. for $C_{46}H_{64}N_1O_3F_3$ 736.4911, found 736.4942.

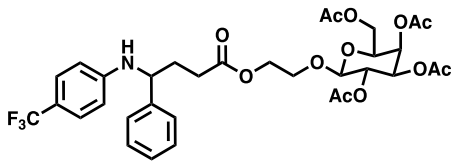

(2S,3R,4R,5S,6S)-2-(Acetoxymethyl)-6-(2-((4-phenyl-4-((4-(trifluoromethyl)phenyl)amino)butanoyl)oxy)ethoxy)tetrahydro-2H-pyran-3,4,5-triyl triacetate ***5ao***

Following procedure **3.5.5.2** with 4-(trifluoromethyl)aniline (0.2 mmol, 25 μL), benzaldehyde (0.2 mmol, 20 μL), and β-D-galactose pentaacetate acrylate (**0.24** mmol, 107.1 mg). The crude product was purified using flash column chromatography in a EtOAc/heptane eluent system. **Yield:** 80 %. **^{1}H NMR** (400 MHz, $CDCl_3$) δ 7.37-7.29 (m, 6H), 7.24 (d, *J* = 2.9 Hz,

1H), 6.53 (d, *J* = 8.5 Hz, 2H), 5.40-5.33 (m, 1H), 5.19 (dd, *J* = 13.2, 5.1 Hz, 1H), 5.01 (ddd, *J* = 10.5, 3.4, 1.8 Hz, 1H), 4.78 (s, 1H), 4.49 (dd, *J* = 7.9, 3.2 Hz, 1H), 4.42 (t, *J* = 6.6 Hz, 1H), 4.28-4.20 (m, 2H), 4.18-4.07 (m, 2H), 4.02-3.96 (m, 1H), 3.91-3.84 (m, 1H), 3.79-3.69 (m, 1H), 2.43 (t, *J* = 7.0 Hz, 2H), 2.25-2.09 (m, 5H), 2.04 (s, 3H), 2.01-1.94 (m, 6H) ppm. **^{19}F NMR** (376 MHz, $CDCl_3$) δ -61.1 ppm. **^{13}C NMR** (101 MHz, $CDCl_3$) δ 173.3, 173.2, 170.4, 170.2, 170.1, 169.4, 149.7, 142.2, 142.2, 128.9, 127.6, 126.5, 126.5, 126.3, 112.5, 101.3, 70.8, 68.7, 67.3, 67.0, 63.5, 61.2, 57.6, 57.5, 32.9, 31.1, 31.1, 20.7, 20.7, 20.6, 20.6 ppm. **HRMS** (ESI^+, *m*/*z*) [$M+H^+$] calcd. for $C_{33}H_{38}NO_{12}F_3$ 698.2419, found 698.2387.

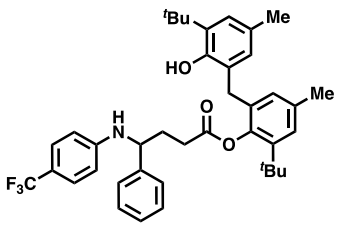

2-(t-Butyl)-6-(3-(t-butyl)-2-hydroxy-5-methylbenzyl)-4-methylphenyl 4-phenyl-4-((4-(trifluoromethyl)phenyl)amino)butanoate ***5ap***

Following procedure **3.5.5.2** with 4-(trifluoromethyl)aniline (0.2 mmol, 25 μL), benzaldehyde (0.2 mmol, 20 μL), and Irganox @3052 acrylate (**0.24** mmol, 94.7 mg). The crude product was purified using flash column chromatography in a EtOAc/heptane eluent system. **Yield:** 58 %. **^{1}H NMR** (400 MHz, $CDCl_3$) δ 7.31 (t, *J* = 6.2 Hz, 4H), 7.27-7.24 (m, 1H), 7.20 (d, *J* = 8.4 Hz, 2H), 7.08 (s, 1H), 7.04 (s, 1H), 6.74 (d, *J* = 1.2 Hz, 1H), 6.66 (s, 1H), 6.49 (d, *J* = 8.5 Hz, 2H), 5.11 (s, 1H), 4.74 (d, *J* = 25.3 Hz, 1H), 4.55 (s, 1H), 3.56 (d, *J* = 14.2 Hz, 2H), 2.78 (s, 2H), 2.27 (m, 5H), 2.20 (s, 3H), 1.38 (s, 9H), 1.30 (s, 9H) ppm. **^{19}F NMR** (376 MHz, $CDCl_3$) δ -61.1 ppm. **^{13}C NMR** (101 MHz, $CDCl_3$) δ 173.6, 151.0, 149.5, 145.2, 142.0, 141.1, 136.7, 135.9, 131.6, 130.0, 129.0, 128.6, 127.9, 127.6, 127.1, 126.6, 126.5, 126.4, 126.4, 126.3, 126.2, 124.4, 123.6, 119.2, 118.9, 112.6, 57.6, 35.5, 34.7, 34.6, 32.7, 32.4,

31.9, 30.6, 29.8, 29.0, 26.5, 26.4, 22.9, 22.7, 21.2, 20.8, 14.1 ppm. **HRMS** (ESI^+, *m*/*z*) [M+H^+] calcd. for $C_{40}H_{46}NO_3F_3$ 646.3503, found 646.3517.

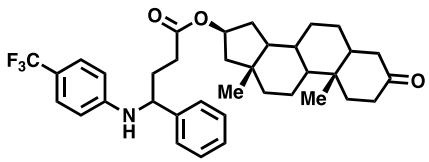

(10S,13R,16S)-10,13-dimethyl-3-oxohexadecahydro-1H-cyclopenta[a]phenanthren-16-yl 4-phenyl-4-((4-(trifluoromethyl)phenyl)amino)butanoate ***5aq***

Following procedure **3.5.5.2** with 4-(trifluoromethyl)aniline (0.2 mmol, 25 μL), benzaldehyde (0.2 mmol, 20 μL), and stanolone acrylate (**0.24** mmol, 82.7 mg). The crude product was purified using flash column chromatography in a EtOAc/heptane eluent system. **Yield:** 47 %. **^{1}H NMR** (400 MHz, $CDCl_3$) δ 7.41-7.29 (m, 7H), 6.53 (d, *J* = 8.2 Hz, 2H), 4.78 (d, *J* = 5.4 Hz, 1H), 4.65 (dd, *J* = 12.2, 4.7 Hz, 1H), 4.44 (dd, *J* = 12.8, 6.2 Hz, 1H), 2.49-1.98 (m, 10H), 1.78-1.64 (m, 4H), 1.51-1.31 (m, 7H), 1.24-1.14 (m, 3H), 1.03 (s, 3H), 0.97-0.85 (m, 3H), 0.77 (d, *J* = 13.0 Hz, 2H) ppm. **^{19}F NMR** (376 MHz, $CDCl_3$) δ -61.1 ppm. **^{13}C NMR** (101 MHz, $CDCl_3$) δ 211.8, 173.7, 158.8, 149.7, 142.4, 128.9, 127.5, 126.5, 126.3, 119.0-118.8 (d, CF_3), 112.5, 83.2, 57.8, 57.7, 53.8, 50.6, 46.7, 44.7, 42.8, 38.5, 38.1, 36.9, 35.7, 35.2, 33.0, 31.4, 31.2, 28.8, 27.6, 23.5, 20.9, 12.2, 11.5 ppm.

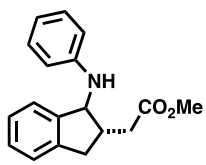

Methyl 2-((2S)-1-(phenylamino)-2,3-dihydro-1H-inden-2-yl)acetate ***7a***

Following procedure **3.5.5.3** with aniline (0.2 mmol, 18 μL) and methyl (*E*)-4-(2-formylphenyl)but-2-enoate (0.2 mmol, 40.8 mg). The crude product was purified using flash column chromatography in a EtOAc/heptane eluent system. **Yield:** 61 %. **^{1}H NMR** (400 MHz, $CDCl_3$) δ 7.29 (d, *J* = 7.4 Hz, 1H), 7.19 (ddd, *J* = 12.1, 11.6, 4.2 Hz, 5H), 6.74 (t, *J* = 7.8 Hz, 3H), 4.74 (d, *J* = 7.3 Hz, 1H), 3.91 (s, 1H), 3.66 (s, 3H), 3.22 (dd, *J* = 18.9, 10.7 Hz, 1H), 2.79 (dd, *J* = 14.8, 4.8 Hz, 1H), 2.72-2.63 (m, 2H), 2.56 (dd, *J* = 14.8, 7.9 Hz, 1H) ppm. **^{13}C NMR** (101 MHz, $CDCl_3$) δ 173.2, 148.0, 144.4, 141.5, 129.4, 127.9, 126.8, 124.9, 124.2, 117.6, 113.0, 63.4, 51.6, 45.2, 37.7, 36.3 ppm.

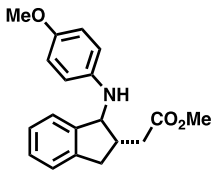

Methyl 2-((2S)-1-((4-methoxyphenyl)amino)-2,3-dihydro-1H-inden-2-yl)acetate ***7b***

Following procedure **3.5.5.3** with *p*-anisidine (0.2 mmol, 24.6 mg) and methyl (*E*)-4-(2-formylphenyl)but-2-enoate (0.2 mmol, 40.8 mg). The crude product was purified using flash column chromatography in a EtOAc/heptane eluent system. **Yield:** 67 %. **^{1}H NMR** (400 MHz, $CDCl_3$) δ 7.27 (s, 1H), 7.21 (d, *J* = 4.0 Hz, 2H), 7.15 (td, *J* = 8.0, 4.1 Hz, 1H), 6.79 (d, *J* = 8.9 Hz, 2H), 6.68 (d, *J* = 8.8 Hz, 2H), 4.63 (d, *J* = 7.2 Hz, 1H), 3.76 (s, 3H), 3.64 (s, 3H), 3.20 (dd, *J* = 18.8, 10.6 Hz, 1H), 2.76 (dd, *J* = 14.8, 4.7 Hz, 1H), 2.68-2.60 (m, 2H), 2.52 (dd, *J* = 14.8, 7.9 Hz, 1H) ppm. **^{13}C NMR** (101 MHz, $CDCl_3$) δ 173.2, 152.3, 144.7, 142.2, 141.5, 127.8, 126.8, 124.8, 124.2, 115.1, 114.5, 64.4, 55.8, 51.6, 45.0, 37.8, 36.2 ppm. **HRMS** (ESI^+, *m*/*z*) [$M+H^+$] calcd. for $C_{19}H_{21}NO_3$ 312.1594, found 312.1580.

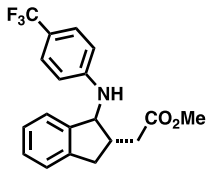

Methyl 2-((2S)-1-((4-(trifluoromethyl)phenyl)amino)-2,3-dihydro-1H-inden-2-yl)acetate ***7c***

Following procedure **3.5.5.3** with 4-(trifluoromethyl)aniline (0.2 mmol, 25 μL) and methyl (*E*)-4-(2-formylphenyl)but-2-enoate (0.2 mmol, 40.8 mg). The crude product was purified using flash column chromatography in a EtOAc/heptane eluent system. **Yield:** 51 %. **^{1}H NMR** (400 MHz, $CDCl_3$) δ 7.44 (d, *J* = 8.5 Hz, 2H), 7.28 (d, *J* = 1.2 Hz, 2H), 7.23-7.16 (m, 1H), 6.75 (d, *J* = 8.5 Hz, 2H), 4.80 (d, *J* = 6.2 Hz, 1H), 4.30 (s, 1H), 3.66 (s, 3H), 3.25 (q, *J* = 10.3 Hz, 1H), 2.79-2.66 (m, 3H), 2.65-2.56 (m, 1H) ppm. **^{19}F NMR** (376 MHz, $CDCl_3$) δ -61.1 ppm. ^{13}C NMR (101 MHz, $CDCl_3$) δ 173.0, 150.5, 143.4, 141.4, 128.2, 127.0, 126.9, 126.8, 126.8, 126.8, 126.3, 125.0, 124.0, 123.6, 119.3, 119.0, 112.1, 63.0, 51.7, 45.0, 37.6, 36.2 ppm.

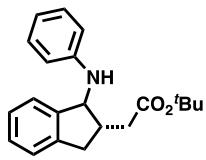

t-Butyl 2-((2S)-1-(phenylamino)-2,3-dihydro-1H-inden-2-yl)acetate ***7d***

Following procedure **3.5.5.3** with aniline (0.2 mmol, 18 μL) and *t*-butyl (*E*)-4-(2-formylphenyl)but-2-enoate (0.2 mmol, 49.3 mg). The crude product was purified using flash column chromatography in a

EtOAc/heptane eluent system. **Yield:** 55 %. **^{1}H NMR** (400 MHz, $CDCl_3$) δ 7.29 (d, *J* = 7.4 Hz, 1H), 7.25-7.12 (m, 5H), 6.79-6.68 (m, 3H), 4.73 (d, *J* = 7.6 Hz, 1H), 3.96 (s, 1H), 3.21 (dd, *J* = 14.5, 6.4 Hz, 1H), 2.78-2.57 (m, 3H), 2.52-2.39 (m, 1H), 1.46 (s, 9H) ppm. **^{13}C NMR** (101 MHz, $CDCl_3$) δ 172.0, 148.1, 144.6, 141.7, 129.4, 127.8, 126.7, 124.8, 124.1, 117.5, 113.0, 80.6, 63.4, 45.4, 39.2, 36.1, 28.1 ppm. **HRMS** (ESI^+, *m*/*z*) [$M+H^+$] calcd. for $C_{21}H_{25}NO_2$ 324.1958, found 324.1967.

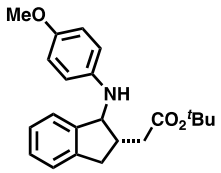

t-Butyl 2-((2S)-1-((4-methoxyphenyl)amino)-2,3-dihydro-1H-inden-2-yl)acetate ***7e***

Following procedure **3.5.5.3** with *p*-anisidine (0.2 mmol, 24.6 mg) and *t*-butyl (*E*)-4-(2-formylphenyl)but-2-enoate (0.2 mmol, 49.3 mg). The crude product was purified using flash column chromatography in a EtOAc/heptane eluent system. **Yield:** 46 %. **^{1}H NMR** (400 MHz, $CDCl_3$) δ 7.29 (s, 1H), 7.22 (d, *J* = 4.1 Hz, 2H), 7.18-7.11 (m, 1H), 6.81 (d, *J* = 8.9 Hz, 2H), 6.70 (d, *J* = 8.9 Hz, 2H), 4.63 (d, *J* = 7.6 Hz, 1H), 3.77 (s, 3H), 3.20 (dd, *J* = 14.6, 6.4 Hz, 1H), 2.66 (ddt, *J* = 16.0, 13.6, 6.5 Hz, 3H), 2.44 (dd, *J* = 14.8, 8.4 Hz, 1H), 1.45 (s, 9H) ppm. **^{13}C NMR** (101 MHz, $CDCl_3$) δ 172.1, 152.2, 144.9, 142.4, 141.7, 127.7, 126.7, 124.8, 124.1, 115.1, 114.5, 80.5, 64.5, 55.8, 45.3, 39.3, 36.1, 28.1 ppm. **HRMS** (ESI^+, *m*/*z*) [$M+H^+$] calcd. for $C_{22}H_{27}NO_3$ 354.2064, found 354.2080.

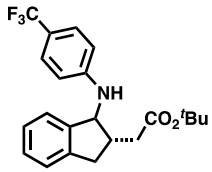

t-Butyl 2-((2S)-1-((4-(trifluoromethyl)phenyl)amino)-2,3-dihydro-1H-inden-2-yl)acetate ***7f***

Following procedure **3.5.5.3** with 4-(trifluoromethyl)aniline (0.2 mmol, 25 μL) and *t*-butyl (*E*)-4-(2-formylphenyl)but-2-enoate (0.2 mmol, 49.3 mg). The crude product was purified using flash column chromatography in a EtOAc/heptane eluent system. **Yield:** 61 %. **^{1}H NMR** (400 MHz, $CDCl_3$) δ 7.42 (d, *J* = 8.5 Hz, 2H), 7.27-7.20 (m, 3H), 7.22-7.09 (m, 1H), 6.74 (d, *J* = 8.5 Hz, 2H), 4.77 (t, *J* = 7.6 Hz, 1H), 4.32 (d, *J* = 8.4 Hz, 1H), 3.30-3.08 (m, 1H), 2.81-2.57 (m, 3H), 2.55-2.40 (m, 1H), 1.44 (s, 9H) ppm. **^{19}F NMR** (376 MHz, $CDCl_3$) δ -61.0 ppm. **^{13}C NMR** (101 MHz, $CDCl_3$) δ 171.8, 150.6, 143.7, 141.6, 128.1, 126.9, 126.9, 126.8, 126.8, 126.7, 126.3, 125.0, 124.0, 123.6, 119.2, 118.9, 112.1, 80.8, 63.1, 45.1, 39.1, 36.1, 28.1 ppm.

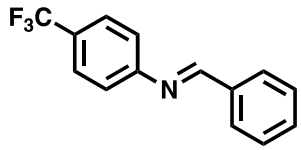

(E)-N-(4-(Trifluoromethyl)phenyl)-1-phenylmethanimine

Following procedure **3.5.5.6** with 4-(trifluoromethyl)aniline (2.0 mmol, 0.25 mL) and benzaldehyde (2.0 mmol, 0.20 mL). **^{1}H NMR** (400 MHz, $CDCl_3$) δ 8.42 (s, 1H), 7.93-7.87 (m, 2H), 7.64 (d, *J* = 8.3 Hz, 2H), 7.55-7.40 (m, 3H), 7.25 (t, *J* = 4.0 Hz, 2H).

3.6 References

1. a) Hobza, P.; Řezáč, J.; *Chem. Rev.* **2016**, *116*, 4911–4912; b) Hunter, C. A. *Angew. Chem. Int. Ed.* **2004**, *43*, 5310–5324; c) Mahadevi, A. S.; Sastry, G. N.; *Chem. Rev.* **2016**, *116*, 2775–2825; d) Mahmudov, K. T.; Kopylovich, M. N.; Guedes da Silva, M. F. C.; Pombeiro, A. J. L. *Coord. Chem. Rev.* **2017**, *345*, 54–72; e) Loh, C. C. J. *Nat. Rev. Chem.* **2021**, *5*, 792–815.

2. a) Neel, A. J.; Hilton, M. J.; Sigman, M. S.; Toste, F. D. *Nature* **2017**, *543*, 637−646; b) Proctor, R. S. J.; Colgan, A. C.; Phipps, R. J. *Nat. Chem.* **2020**, *12*, 990–1004; c) Fanourakis, A.; Docherty, P. J.; Chuentragool, P.; Phipps, R. J. *ACS Catal.* **2020**, *10*, 10672−10714; d) Jin, M. Y.; Zhen, Q.; Xiao, D.; Tao, G.; Xing, X.; Yu, P.; Xu, C. *Nat. Commun.* **2022**, *13*, 3276.

3. a) Kirby, A. J. *Angew. Chem., Int. Ed.* **1996**, *35*, 706−724; b) Benkovic, S. J.; Hammes-Schiffer, S. *Science* **2003**, *301*, 1196–1202; c) Biedermann, F.; Schneider, H.-J. *Chem. Rev.* **2016**, *116*, 5216–5300.

4. a) Mader, M. M.; Bartlett, P. A. *Chem. Rev.* **1997**, *97*, 1281–1302; b) Moulton, B.; Zaworotko, M. J.; *Chem. Rev.* **2001**, *101*, 1629–1658; c) Schreiner, P. R. *Chem. Soc. Rev.* **2003**, *32*, 289−296.

5. a) Taylor, M. S.; Jacobsen, E. N. *Angew. Chem., Int. Ed.* **2006**, *45*, 1520−1543; b) Doyle, A. G.; Jacobsen, E. N. *Chem. Rev.* **2007**, *107*, 5713−5743; c) Knowles, R. R.; Jacobsen, E. N. *Proc. Natl. Acad. Sci.* **2010**, *107*, 20678–20685; d) Davis, H. J.; Phipps, R. J. *Chem. Sci.* **2017**, *8*, 864–877; e) Silvi, M.; Melchiorre, P. *Nature* **2018**, *554*, 41–49.

6. a) Russell, G. A.; Wang, K. *J. Org. Chem.* **1991**, *56*, 3475−3479; b) Wade, P. A.; Morrison, H. A.; Kornblum, N. *J. Org. Chem.* **1987**, *52*, 3102−3107; c) Tobisu, M.; Furukawa, T.; Chatani, N. *Chem. Lett.* **2013**, *42*, 1203−1205; d) Kandukuri, S. R.; Bahamonde, A.; Chatterjee, I.; Jurberg, I. D.; Escudero-Adán, E. C.; Melchiorre, P. *Angew. Chem. Int. Ed.* **2015**, *54*, 1485−1489. e) Fu, M.-C.; Shang, R.; Zhao, B.; Wang, B.; Fu, Y. *Science* **2019**, *363*, 1429−1434.

7. a) Davies, J.; Booth, S. G.; Essafi, S.; Dryfe, R. A. W.; Leonori, D. *Angew. Chem., Int. Ed.* **2015**, *54*, 14017−14021; b) Liu, B.; Lim, C.-H.; Miyake, G. M. *J. Am. Chem. Soc.* **2017**, *139*, 13616−13619; c) Zhang, J.; Li, Y.; Xu, R.; Chen, Y. *Angew. Chem., Int. Ed.* **2017**, *56*, 12619−12623; d) Sandfort, F.; Strieth-Kalthoff, F.; Klauck, F. J. R.; James, M. J.; Glorius, F. *Chem. Eur. J.* **2018**, *24*, 17210−17214; e) Morack, T.; Mück-Lichtenfeld, C.; Gilmour, R. *Angew. Chem., Int. Ed.* **2019**, *58*, 1208−1212.

8. Skubi, K. L.; Kidd, Jung, J. B.; H.; Guzei, I. A.; Baik, M.-H.; Yoon, T. P. *J. Am. Chem. Soc.* **2017**, *139*, 17186−17192.

9. a) Arceo, E.; Jurberg, I. D.; Álvarez-Fernández, A.; Melchiorre, P. *Nat. Chem.* **2013**, *5*, 750−756; b) Emmanuel, M. A.; Greenberg, N. R.; Oblinsky, D. G.; Hyster, T. K. *Nature* **2016**, *540*, 414−417; c) Cao, Z.-Y.; Ghosh, T.; Melchiorre, P. *Nat. Commun.* **2018**, *9*, 3274; d) Biegasiewicz, K. F.; Cooper, S. J.; Gao, X.; Oblinsky, D. G.; Kim, J. H.; Garfinkle, S. E.; Joyce, L. A.; Sandoval, B. A.; Scholes, G. D.; Hyster, T. K. *Science* **2019**, *364*, 1166−1169.

10. a) Fawcett, A.; Pradeilles, J.; Wang, Y.; Mutsuga, T.; Myers, E. L.; Aggarwal, V. K. *Science* **2017**, *357*, 283−286; b) Wu, J.; He, L.; Noble, A.; Aggarwal, V. K. *J. Am. Chem. Soc.* **2018**, *140*, 10700−10704; c) Wu, J.; Bär, R. M.; Guo, L.; Noble, A.; Aggarwal, V. K. *Angew. Chem. Int. Ed.* **2019**, *58*, 18830−18834; d) Wu, J.; Grant, P. S.; Li, X.; Noble, A.; Aggarwal, V. K. *Angew. Chem., Int. Ed.* **2019**, *58*, 5697−5701.

11. a) Kohara, K.; Trowbridge, A.; Smith, M. A.; Gaunt, M. J. *J. Am. Chem. Soc.* **2021**, *143*, 19268–19274; b) Konev, M. O.; Cardinale, L.; von Wangelin, A. J. *Org. Lett.* **2020**, *22*, 1316–1320.

12. Bosque, I.; Bach, T. *ACS Catal.* **2019**, *9*, 9103−9109.

13. a) Crisenza, G. E. M.; Mazzarella, D.; Melchiorre, P. *J. Am. Chem. Soc.* **2020**, *142*, 5461–5476; b) Saux, E. L.; Zanini, M.; Melchiorre, P. *J. Am. Chem. Soc.* **2022**, *144*, *3*, 1113–1118; c) Zhou, W.; Wu, S.; Melchiorre, P. *J. Am. Chem. Soc.* **2022**, *144*, 20, 8914–8919; d) Rosso, C.; Cuadros, S.; Barison, G.; Costa, P.; Bonchio, M.; Prato, M.; Amico, L. D.; Filippini,

G. *ACS Catal.* **2022**, *12*, 4290−4295; e) Hsu, C.-W.; Sundén, H. *Org. Lett.* **2018**, *20*, 2051−2054; f) Peng, X.; Xu, K.; Zhang, Q.; Liu, L.; Tan, J. *Trends in Chemistry* **2022**, *4*, 643–657.

14. a) Beatty, J. W.; Stephenson, C. R. J. *Acc. Chem. Res.* **2015**, *48*,1474−1484; b) Nakajima, K.; Miyake, Y.; Nishibayashi, Y. *Acc. Chem. Res.* **2016**, *49*, 1946−1956; c) Chattopadhyay, A. K.; Hanessian, S. *Chem. Rev.* **2017**, *117*, 4104−4146; d) Proctor, R. S. J.; Davis, H. J.; Phipps, R. J. *Science* **2018**, *360*, 419.

15. a) Leitch, J. A.; Rossolini, T.; Rogova, T.; Maitland, J. A. P.; Dixon, D. J. *ACS Catal.* **2020**, *10*, 2009–2025; b) Trowbridge, A.; Walton, S. M.; Gaunt, M. J. *Chem. Rev.* **2020**, *120*, 2613–2692; c) Constantin, T.; Zanini, M.; Regni, A.; Sheikh, N. S.; Juliá, F.; Leonori, D. *Science* **2020**, *367*, 1021; d) Troyano, F. J. A.; Merkens, K.; Anwar, K.; Gómez-Suárez, A. *Angew. Chem. Int. Ed.* **2021**, *60*, 1098–1115.

16. Selected examples of amines synthesis via C–H bond functionalization: a) Bess, E. N.; DeLuca, R. J.; Tindall, D. J.; Oderinde, M. S.; Roizen, J. L.; Bois, J. D.; Sigman, M. S. *J. Am. Chem. Soc.* **2014**, *136*, 5783–5789; b) Clark, J. R.; Feng, K.; Sookezian, A.; White, M. C. *Nat. Chem.* **2018**, *10*, 583–591; c) Chen, S. –J.; Golden, D. L.; Krska, S. W.; Stahl, S. S. *J. Am. Chem. Soc.* **2021**, *143*, 14438–14444; d) Hou, Z.-W.; Liu, D.-J.; Xiong, P.; Lai, X.-L.; Song, J.; Xu, H.-C. *Angew. Chem.* **2021**, *133*, 2979–2983; e) Rivas, M.; Palchykov, V.; Jia, X.; Gevorgyan, V. *Nat. Rev. Chem.* **2022** (doi.org/10.1038/s41570-022-00403-8).

17. Selected examples of amines synthesis via reductive amination: a) Savile, C. K.; J. Janey, M.; Mundorff, E. C.; Moore, J. C.; Tam, S.; Jarvis, W. R.; Colbeck, J. C.; Krebber, A.; Fleitz, F. J.; Brands, J.; Devine, P. N.; Huisman, G. W.; Hughes, G. J. *Science* **2010**, *329*, 305−309; b) Wickens, Z. K.; Skakuj, K.; Morandi, B.; Grubbs, R. H. *J. Am. Chem. Soc.* **2014**, *136*, 890−893; c) Gusak, K. N.; Ignatovich, Z. V.; Koroleva, E. V. *Russ. Chem. Rev.* **2015**, *84*, 288−309; d) Jagadeesh, R. V.; Murugesan, K.; Alshammari, A. S.; Neumann, H.; Pohl, M.-M.; Radnik, J.; Beller, M.

Science **2017**, *358*, 326−332; e) Afanasyev, O. I.; Kuchuk, E.; Usanov, D. L.; Chusov, D. *Chem. Rev.* **2019**, *119*, 11857–11911.

18. a) Yoon, U. C.; Mariano, P. S. *Acc. Chem. Res.* **1992**, *25*, 233−240; b) Kobayashi, S.; Ishitani, H. *Chem. Rev.* **1999**, *99*, 1069–1094; c) Denmark, S. E.; Fu, J. *Chem. Rev.* **2003**, *103*, 2763–2793; d) Huynh, M. H. V.; Meyer, T. J. *Chem. Rev.* **2007**, *107*, 5004–5064; e) Fagnoni, M.; Dondi, D.; Ravelli, D.; Albini, A. *Chem. Rev.* **2007**, *107*, 2725−2756; f) Hoffmann, N. *Chem. Rev.* **2008**, *108*, 1052−1103; g) Condie, A. G.; González-Gómez, J. C.; Stephenson, C. R. J. *J. Am. Chem. Soc.* **2010**, *132*, 1464−1465; h) Kobayashi, S.; Mori, Y.; Fossey, J. S.; Salter, M. M. *Chem. Rev.* **2011**, *111*,2626–2704; i) McNally, A.; Prier, C. K.; MacMillan, D. W. C. *Science* **2011**, *334*, 1114−1117.

19. a) Weinberg, D. R.; Gagliardi, C. J.; Hull, J. F.; Murphy, C. F.; Kent, C. A.; Westlake, B. C.; Paul, A.; Ess, D. H.; McCafferty, D. G.; Meyer, T. J. *Chem. Rev.* **2012**, *112*, 4016–4093; b) Gentry, E. C.; Knowles, R. R. *Acc. Chem. Res.* **2016**, *49*, 1546–1556.

20. a) Thullen, S. M.; Rovis, T. *J. Am. Chem. Soc.* **2017**, *139*, 15504−15508. b) McManus, J. B.; Onuska, N. P. R.; Nicewicz, D. A. *J. Am. Chem. Soc.* **2018**, *140*, 9056−9060; c) Murray, P. R. D.; Cox, J. H.; Chiappini, N. D.; Roos, C. B.; McLoughlin, E. A.; Hejna, B. G.; Nguyen, S. T.; Ripberger, H. H.; Ganley, J. M.; Tsui, E.; Shin, N. Y.; Koronkiewicz, B.; Qiu, G.; Knowles, R. R. *Chem. Rev.* **2021**, doi.org/10.1021/acs.chemrev.1c00374.

21. a) Miyake, Y.; Nakajima, K.; Nishibayashi, Y. *J. Am. Chem. Soc.* **2012**, 134, *3338*–3341; b) Kohls, P.; Jadhav, D.; Pandey, G.; Reiser, O. *Org. Lett.* **2012**, *14*, 672–675; c) Ju, X.; Li, D.; Li, W.; Yu, W.; Bian, F. *Adv. Synth. Catal.* **2012**, *354*, 3561–3567; d) Prier, C. K.; Rankic, D. A.; MacMillan, D. W. C. *Chem. Rev.* **2013**, *113*, 5322−5363.

22. a) Zhu, S.; Das, A.; Bui, L.; Zhou, H.; Curran, D. P.; Rueping, M. *J. Am. Chem. Soc.* **2013**, *135*, 1823–1829; b) Ruiz Espelt, L.; Wiensch, E. M.; Yoon, T. P. *J. Org. Chem.* **2013**, *78*, 4107–4114; c) Chen, L.; Chao, C. S.;

Pan, Y.; Dong, S.; Teo, Y. C.; Wang, J.; Tan, C.-H. *Org. Biomol. Chem.* **2013**, *11*, 5922–5925.

23. a) Liang, Z.; Xu, S.; Tian, W.; Zhang, R. *Beilstein J. Org. Chem.* **2015**, *11*, 425–430; b) Ruiz Espelt, L.; McPherson, I. S.; Wiensch, E. M.; Yoon, T. P. *J. Am. Chem. Soc.* **2015**, *137*, 2452–2455; c) McManus, J. B.; Onuska, N. P. R.; Nicewicz, D. A. *J. Am. Chem. Soc.* **2018**, *140*, 9056–9060; d) McManus, J. B.; Onuska, N. P. R.; Jeffreys, M. S.; Goodwin, N. C.; Nicewicz, D. A. *Org. Lett.* **2020**, *22*, 679–683.

24. a) Noble, A.; D. W. C. MacMillan, *J. Am. Chem. Soc.* **2014**, *136*, 11602–11605; b) Nakajima, K.; Kitagawa, M.; Ashida, Y.; Miyake, Y.; Nishibayashi, Y. *Chem. Commun.* **2014**, *50*, 8900–8903; c) Chu, L.; Ohta, C.; Zuo, Z.; MacMillan, D. W. C. *J. Am. Chem. Soc.* **2014**, *136*, 10886–10889; d) Miyazawa, K.; Koike, T.; Akita, M. *Adv. Synth. Catal.* **2014**, *356*, 2749–2755.

25. a) Shaw, M. H.; Shurtleff, V. W.; Terrett, J. A.; Cuthbertson, J. D.; MacMillan, D. W. C. *Science* **2016**, *352*, 1304–1308; b) Ye, J.; Kalvet, I. Schoenebeck, F.; Rovis, T. *Nat. Chem.* **2018**, *10*, 1037–1041; c) A. Ryder, S. H.; Cunningham, W. B.; Ballantyne, G.; Mules, T.; Kinsella, A. G.; Turner-Dore, J.; Alder, C. M.; Edwards, L. J.; McKay, B. S. J.; Grayson, M. N.; Cresswell, A. J. *Angew. Chem. Int. Ed.* **2020**, *59*, 14986–14991; d) Aycock, R. A.; Pratt, C. J.; Jui, N. T. *ACS Catal.* **2018**, *8*, 9115–9119.

26. a) Hager, D.; MacMillan, D. W. C. *J. Am. Chem. Soc.* **2014**, *136*, 16986–16989; b) Nakajima, M.; Fava, E.; Loescher, S.; Jiang, Z.; Rueping, M. *Angew. Chem. Int. Ed.* **2015**, *54*, 8828–8832; c) Miller, D. C.; Choi, G. J.; Orbe, H. S.; Knowles, R. R. *J. Am. Chem. Soc.* **2015**, *137*, 13492–13495; d) Uraguchi, D.; Kinoshita, N.; Kizu, T.; Ooi, T. *J. Am. Chem. Soc.* **2015**, *137*, 13768–13771.

27. a) Fava, E.; Millet, A.; Nakajima, M.; Loescher, S.; Rueping, M. *Angew. Chem. Int. Ed.* **2016**, *55*, 6776–6779; b) Qi, L.; Chen, Y. *Angew. Chem. Int. Ed.* **2016**, *55*, 13312–13315; c) Fuentes de Arriba, A. L.; Urbitsch, F.;

Dixon, D. J. *Chem. Commun.* **2016**, *52*, 14434–14437; d) Lee, K. N.; Lei, Z.; Ngai, M.-Y. *J. Am. Chem. Soc.* **2017**, *139*, 5003–5006.

28. a) Rogova, T.; Gabriel, P.; Zavitsanou, S.; Leitch, J. A.; Duarte, F.; Dixon, D. J. *ACS Catal.* **2020**, *10*, 11438–11447; b) Guo, X.; Wenger, O. S. *Angew. Chem., Int. Ed.* **2018**, *57*, 2469−2473; c) Trowbridge, A.; Reich, D.; Gaunt, M. J. *Nature* **2018**, *561*, 522−527; d) Flodén, N. J.; Trowbridge, A.; Willcox, D.; Walton, S. M.; Kim, Y.; Gaunt, M. J. *J. Am. Chem. Soc.* **2019**, *141*, 8426−8430.

29. a) Lefebvre, Q.; Porta, R.; Millet, A.; Jia, J.; Rueping, M. *Chem. Eur. J.* **2020**, *26*, 1363–1367; b) Reich, D.; Trowbridge, A.; Gaunt, M. J. *Angew. Chem., Int. Ed.* **2020**, *59*, 2256−2261; c) Blackwell, J. H.; Harris, G. R.; Smith, M. A.; Gaunt, M. J. *J. Am. Chem. Soc.* **2021**, *143*, 15946−15959; d) Maitland, J. A. P.; Leitch, J. A.; Yamazaki, K.; Christensen, K. E.; Cassar, D. J.; Hamlin, T. A.; Dixon, D. J. *Angew. Chem., Int. Ed.* **2021**, *60*, 24116−24123; e) Garrido-Castro, A. F.; Maestro, M. C.; Alemán, J. *Catalysts* **2020**, *10*, 562−583.

30. a) Zhang, Y.; Riemer, D.; Schilling, W.; Kollmann, J.; Das, S. *ACS Catal.* **2018,** *8*, 6659−6664; b) Ye, J.; Kalvet, I.; Schoenebeck, F.; Rovis, T. *Nat. Chem.* **2018,** *10*, 1037−1041; c) Zuo, Z.; Cong, H.; Li, W.; Choi, J.; Fu, G. C.; MacMillan, D. W. C. *J. Am. Chem. Soc.* **2016,** *138*, 1832−1835.

31. a) Wang, P.-Z.; Chen, J.-R.; Xiao, W.-J. *Org. Biomol. Chem.* **2019**, *17*, 6936−6951; b) Zhu, D.-L.; Wu, Q.; Li, H.-Y.; Li, H.-X.; Lang, J.-P. *Chem. Eur. J.* **2020**, *26*,3484 –3488; c) Schuster, T.; Kurz, M.; Göbel, M. W. *J. Org. Chem.* **2000**, *65*, 1697−1701; d) Chen, W.; Tao, H.; Huang, W.; Wang, G.; Li, S.; Cheng, X.; Li, G. *Chem. Eur. J.* **2016**, *22*, 9546–9550; e) Jung, J.; Kim, J.; Park, G.; You, Y.; Cho, E. J. *Adv. Synth. Catal.* **2016**, *358*, 74–80.

32. a) Dinnocenzo, J. P.; Banach, T. E. *J. Am. Chem. Soc.* **1989**, *111*, 8646–8653; b) Zhao, H.; Leonori, D. *Angew. Chem. Int. Ed.* **2021**, 60, 7669–7674.

33. Heredia, M. D.; Guerra, W. D.; Barolo, S. M.; Fornasier, S. J.; Rossi, R. A.; Budén, M. E. *J. Org. Chem.* **2020**, *85*, 13481–13494.

34. a) Sinnokrot, M. O.; Sherrill, C. D. *J. Am. Chem. Soc.* **2004**, *126*, 7690–7697; b) Bloom, J. W. G.; Wheeler, S. E. *Angew. Chem. Int. Ed.* **2011**, *50*, 7847–7849; c) Wheeler, S. E.; Houk, K. N. *J. Am. Chem. Soc.* **2008**, *130*, 10854–10855; d) Wheeler, S. E.; Houk, K. N. *Mol. Phys.* **2009**, *107*, 749–760; e) Wheeler, S. E. *J. Am. Chem. Soc.* **2011**, *133*, 10262–10274.

35. Yeh, C.-H.; Korivi, R. P.; Cheng, C.-H. *Angew. Chem. Int. Ed.* **2008**,*47*,4892–4895.

36. Kumar, R.; Flodén, N. J.; Whitehurst, W. G.; Gaunt, M. J. *Nature* **2020**, *581*, 415–420.

37. Allgäuer, D. S.; Jangra, H.; Asahara, H.; Li, Z.; Chen, Q.; Zipse, H.; Ofial, A. R.; Mayr, H. *J. Am. Chem. Soc.* **2017**, *139*, 13318–13329.

38. Zhang, T.; Schilling, W.; Khan, S. U.; Ching, H. Y. V.; Lu, C.; Chen, J.; Jaworski, A.; Barcaro, G.; Monti, S.; De Wael, K.; Slabon, A.; Das, S. *ACS Catal.* **2021**, 11, 14087–14101.

39. Simmons, E. M.; Hartwig, J. F. *Angew. Chem. Int. Ed.* **2012**, *51*, 3066–3072.

40. Roth, H. G.; Romero, N. A.; Nicewicz, D. A. *Synlett* **2016**, *27*, 714–723.

41. Vainio, M. J.; Johnson, M. S. *J. Chem. Inf. Model.* **2007**, *47*, 2462–2474.

42. Loco, D.; Gelfand, N.; Jurinovich, S.; Protti, S.; Mezzetti, A.; Mennucci, B. *J. Phys. Chem. A* **2018**, *122*, 390–397.

43. Zhou, Q. Q.; Guo, W.; Ding, W.; Wu, X.; Chen, X.; Lu, L. Q.; Xiao, W. J. *Angew. Chem. Int. Ed.* **2015**, *54*, 11196–11199.

44. Sheppard, D.; Terrell, R.; Henkelman, G. *J. Chem. Phys.* **2008**, *128*, 134106.

45. Giannozzi, P.; Baroni, S.; Bonini, N.; Calandra, M.; Car, R.; Cavazzoni, C.; Ceresoli, D.; Chiarotti, G.; Cococcioni, M.; Dabo, I. et al. *J. Phys.: Condens. Matter* **2009**, *21*, 395502.

46. Das, M.; Vu, M. D.; Zhang, Q.; Liu, X.-W. *Chem. Sci.*, **2019**, *10*, 1687–1691.

47. Tatunashvili, E.; Chan, B.; Nashara, P. E.; McErlean, C. S. P. *Org. Biomol. Chem.* **2020**, *18*, 1812–1819.

48. Leitch, J. A.; Rossolini, T.; Rogova, T.; Dixon, D. J. *ACS Catal.* **2020**, 10, 11430–11437.

Chapter 4

Red light-mediated sulfonyltrifluoromethylation of alkenes

ABSTRACT: In this study, we successfully designed an efficient and selective method for the sulfonyltrifluoromethylation of olefins under the irradiation of red-light. The key elements of this strategy encompass an osmium photocatalyst, sodium sulfinate salts, and an electrophilic CF_3 source, trifluoromethyl thianthrenium triflate. Through this approach, we achieved the synthesis of sulfonyltrifluoromethylated products with high yields, while manifesting exceptional tolerance towards diverse functional groups. Mechanistic investigations elucidated a sequential process, involving radical generation, followed by Cu-catalyzed cross-coupling reactions.

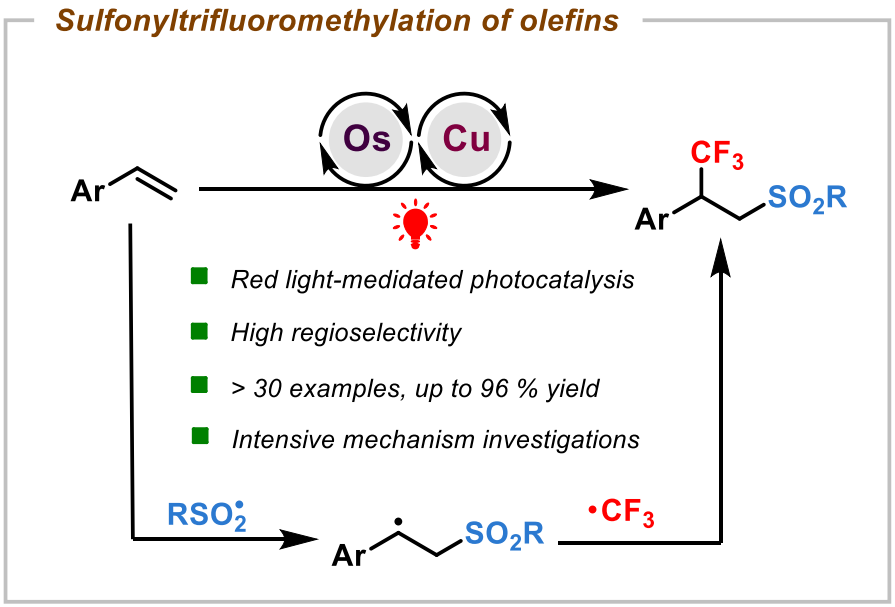

4.1 Introduction

4.1.1 Importance of trifluoromethyl and sulfonyl functional group

The facile incorporation of functional groups remains an ongoing interest in organic synthesis.[1] Among various functional groups, the incorporation of the trifluoromethyl group (CF_3) and the sulfonyl fragment (SO_2R) presents significant challenges and therefore, holds high demand.[2-7] These functional groups, CF_3 and SO_2R, find widespread utility in pharmaceutical compounds, as exemplified by CJ-17493, an NK-1 receptor antagonist, and eletriptan, a medication for migraine headaches, etc. (**Figure 4.1**).[8] The favourable attributes of these groups include stability, membrane permeability, and metabolism characteristics.[9] To date, no reported reaction systems can simultaneously introduce both the CF_3 and SO_2R functional groups in a single step. However, the difunctionalization of olefins offers a highly atom-economical approach to achieve this objective.[10]

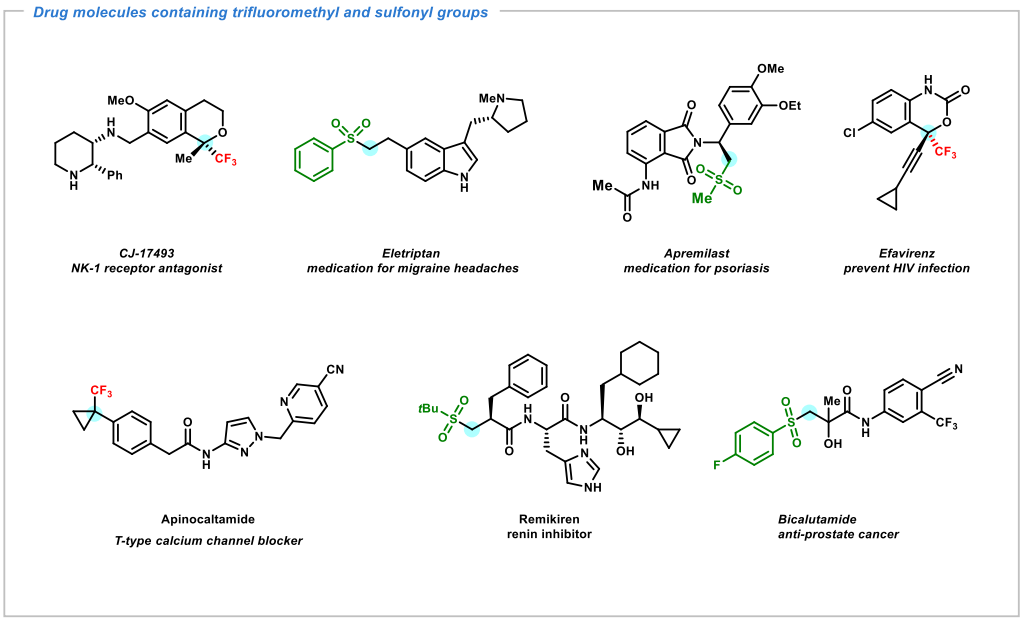

Figure 4.1. Representative -CF_3/-SO_2R-containing drugs and bioactive compounds.

4.1.2 Literature for the β-CF_3-difunctionalized olefins

In the domain of difunctionalization of olefins, a significant focus lies in introducing a CF_3 group. Frequently, this CF_3 group is utilized as an initiator, adding to the terminal (β) position of the olefin. Subsequently, coupling with other functional groups, such as chloro, chlorosulfonyl, trifluoromethyl, cyano, or carboxylic groups, are performed to achieve the desired products (**Figure 4.2**).[11]

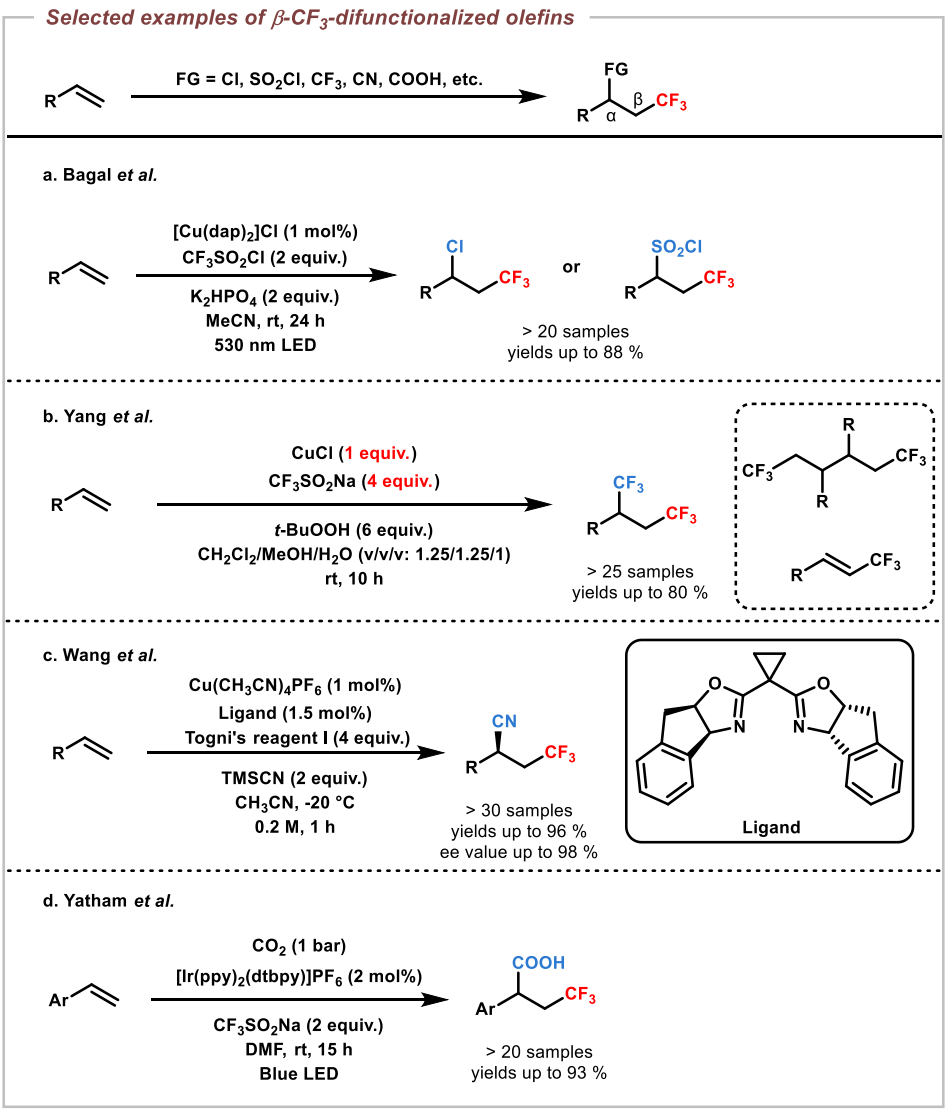

Figure 4.2. Selected examples β-CF_3-difunctionalized olefins

In 2015, Reiser *et al.* developed a visible-light-mediated photocatalytic system for the trifluoromethylchlorosulfonylation of unactivated alkenes with triflyl chloride (CF_3SO_2Cl) (**Figure 4.2a**).[11a] In this reaction, $[Cu(dap)_2]Cl$ was chosen as the unique photocatalyst and its photoexcited state $[Cu(dap)_2]Cl^*$ can efficiently reduce the CF_3SO_2Cl to generate CF_3 radical, followed by the addition reaction to the olefins. The remaining SO_2Cl anion species would be coordinated with Cu center, preventing the extrusion of SO_2, which cannot be realized by [Ru]- or [Ir]-based photocatalysts. Therefore, this approach provide the opportunity to incorprate both CF_3 and SO_2Cl functional groups to olefins, where CF_3 radical was utilized as an initiator.

In the same year, Yang *et al.* reported a copper-mediated approach for 1,2-bis(trifluoromethylation) of alkenes (**Figure 4.2b**).[11b] The sodium trifluoromethanesulfinate (CF_3SO_2Na) was selected as the CF_3 radical precursor, which would activated the alkenes to generate the carbon-centered radical *via* the radical addition reaction. To promote the followed radical cross-coupling, the stoichiometric amount of CuCl (1 equiv.) was used to suppress undesired competitive reactions such as dimerization or elimination (side products in dashed box). It also should be noted that the amount of CF_3SO_2Na was also excess, as the chemoselectivities observed in radical trifluoromethylation were markedly influenced by the concentration of the initiator.

In 2016, Wang *et al.* developed a Cu-mediated catalytic strategy for enantioselective cyanotrifluoromethylation of alkenes (**Figure 4.2c**).[11c] In this method, Togni's reagent I was chosen as the CF_3 radical precursor, which was initially activated by $Cu(CH_3CN)_4PF_6$ *via* SET process to give the CF_3 radical. The released CF_3 radical readily added to styrene, leading to the formation of a benzylic radical. Subsequently, this benzylic radical was trapped by a chiral Cu(II) cyanide species, provideing the targeted alkylnitriles with good enantioselectivity.

In 2017, Yatham *et al.* reported a photocatalytic system for dicarbofunctionalization of styrenes with CO_2 and various radical precursors involving CF_3 functional group (**Figure 4.2d**).[11d] The candidates of radical precursors such as sulfinates, trifluoroborates and oxalates were required to generate the radical *via* an oxidation process, which can provide not only the radical initiators and also the reduced photocatalyst $PC^{\bullet-}$. Upon the initiators adding to styrene, the resulting benzylic radical would be reduced by $PC^{\bullet-}$ to the benzylic anion, followed by trapping CO_2 to the desired carboxylated product.

4.1.3 Literature for the α-CF_3-difunctionalized olefins

Conversely, the synthetic approach for α-CF_3-difunctionalized olefins remains relatively scarce. From the discussion of the aforementioned literatures, to install the -CF_3 functional group at α position of olefins, CF_3 radical cannot be the initiator, as it would easily add to the olefins and provide the resulting β-CF_3-difunctionalized olefins. Therefore, the -CF_3 source and the radical initiator need to be carefully selected to realize the desired α-CF_3-difunctionalized olefins. In 2019, the Li group introduced an elegant catalytic approach which involved Copper/N-fluorobenzenesulfonimide (NFSI) for the synthesis of aminotrifluoromethylated olefins. In this approach, the N-centered radical derived from the electrophilic NFSI served as the initiator, facilitating addition to the β position of the olefin substrate. The $(bpy)Zn(CF_3)_2$ complex was employed as a nucleophilic CF_3 reagent, leading to the formation of the desired α-CF_3-difunctionalized olefin product (**Figure 4.3**).[3d]

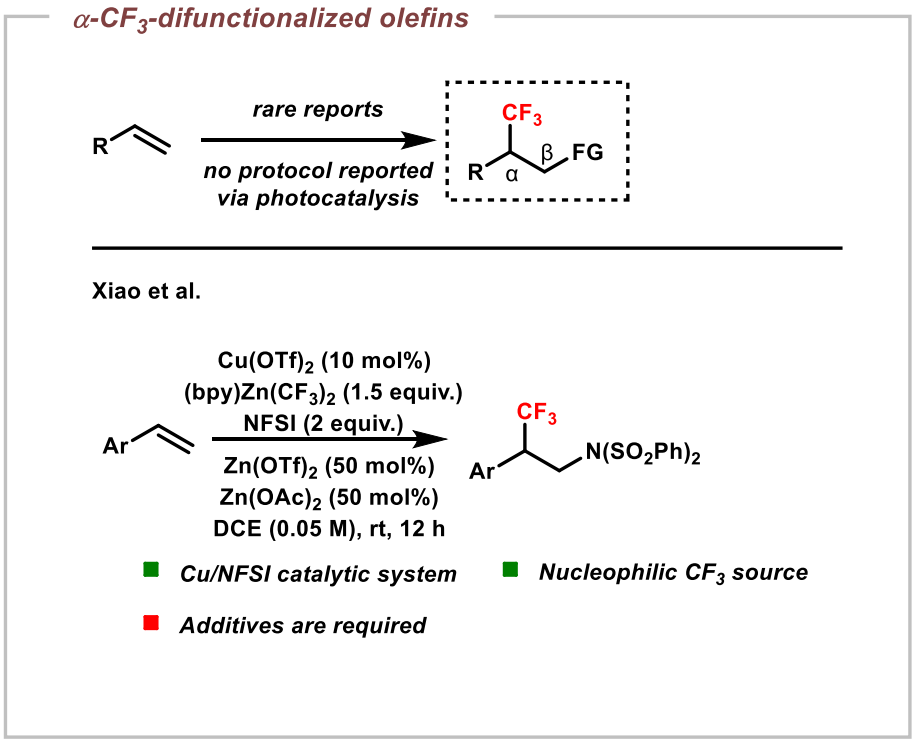

Figure 4.3. Copper/NFSI catalytic system for the synthesis of aminotrifluoromethylated olefins.

4.1.4 Obstacle and solution for photocatalyzed sulfonyltrifluoromethylation of alkenes

Recently, photocatalysis has emerged as a powerful technique for introducing CF_3 groups in organic synthesis.[2,4b] To the best of our knoweldge, there are currently no documented protocols by utilizing photocatalysis for the synthesis of α-CF_3-difunctionalized olefins. Our objective is to address this research gap and make significant contributions in this field.

In photocatalysis, a major challenge arises concerning site selectivity when dealing with the coupling of two functional groups. The reaction system proposed by Li group, involving a single radical, obviated the requirement to consider selectivity issues. However, while introducing two radicals simultaneously as coupling partners, it became crucial to

address regioselectivity concerns. Specifically, when both CF_3 and SO_2R radicals coexist, the CF_3 radical exhibits a higher preference for adding to the olefins first. This preference for CF_3 group addition accounts for its frequent use as an initiator. To overcome this obstacle, it is essential to ensure two main conditions: 1) the formation of the CF_3 radical occurs subsequent to that of the SO_2R radical, which can readily initiate the addition to olefins; 2) to utilize copper to capture the free CF_3 radical, as copper can simultaneously facilitate cross-coupling reactions involving the CF_3 radical.[2d,2e]

To fulfill the aforementioned requirements, the photocatalyst **PC**, along with sulfinate salts (**I**) and electrophilic CF_3 source (**IV**), is required to undergo the chemical transformation through pathway **B**, as illustrated in **Figure 4.4**.[12] The formed sulfonyl radical (**II**) participates in an addition reaction with the alkene, generating a carbon-centered radical (**III**). Simultaneously, CF_3 radical (**V**) is formed through the reduction of **IV** by the $\mathbf{PC}^{\bullet-}$ species. The desired product (**VI**) can be obtained by subjecting radical (**III**) and radical **V** to a Cu-catalyzed cross-coupling reaction, where the Cu catalyst could lower the energy barrier of cross-coupling reaction.

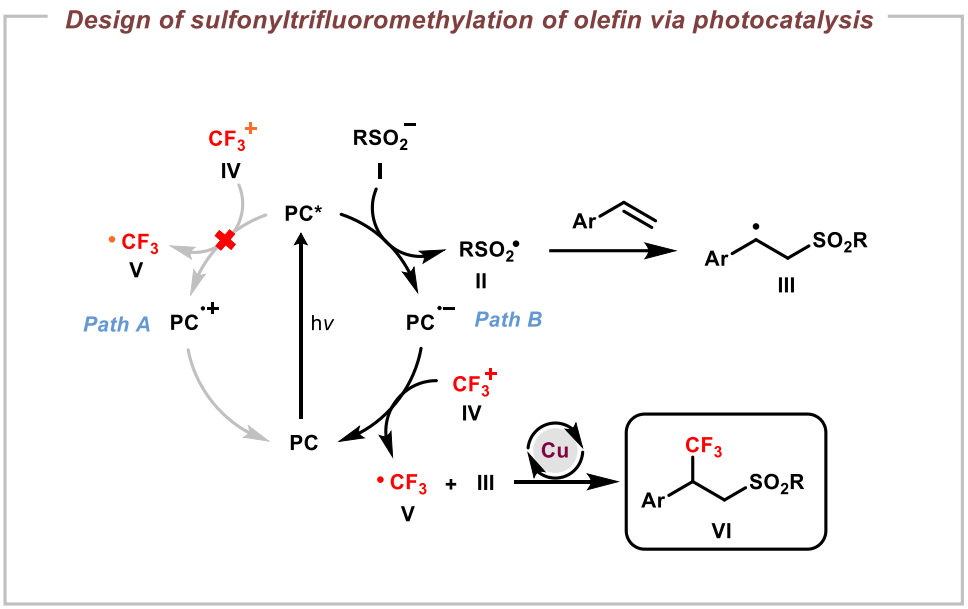

Figure 4.4. Design of sulfonyltrifluoromethylation of olefins *via* photocatalysis.

In our preliminary investigations, we employed conventional photocatalysts, commercially available -CF_3 reagents, and sulfinate salts under the irradiation of blue light to achieve the desired product. However, this photocatalytic process led to the formation of not only the desired product but also additional trifluoromethylated byproducts. Despite extensive optimizations, the yield of the desired product could only be enhanced to 42 % (details are in **4.3.1**).

4.1.5 Literature for the red light-mediated organic synthesis

Inspired by the excellent work of the Rovis group,[13] our focus shifted towards exploring a novel 'red light system' for promoting reactions in organic synthesis. It is important to highlight that red light-mediated organic synthesis in this context are still in their early stages of development.[14]

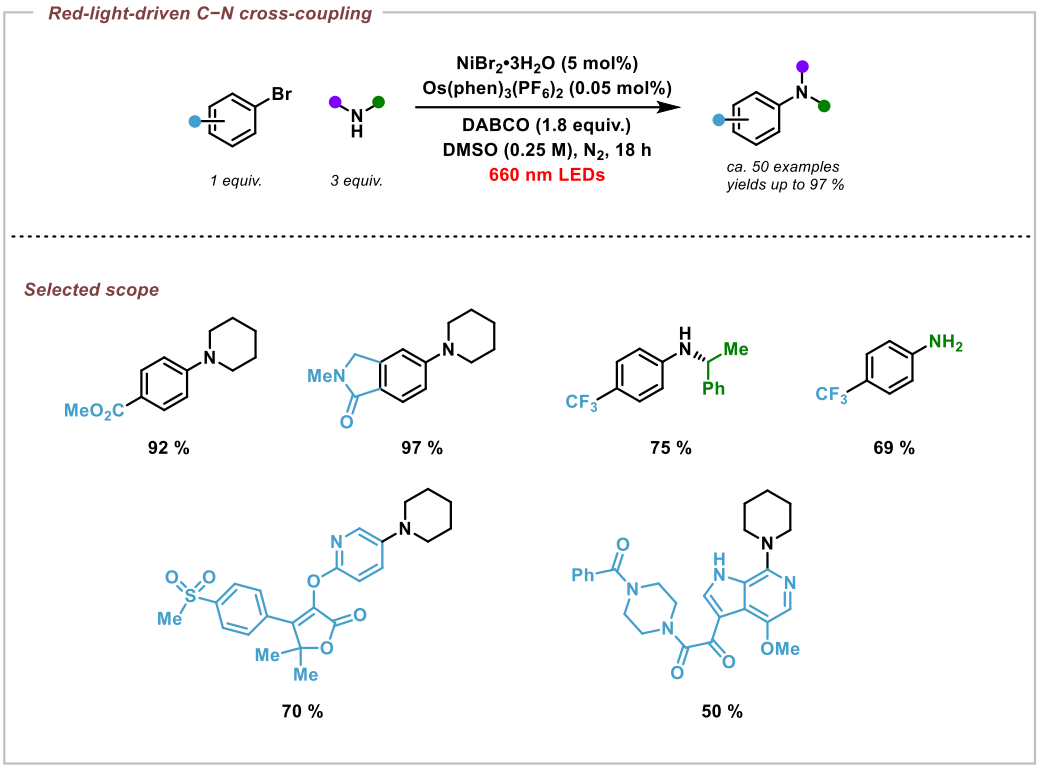

Figure 4.5. Dual nickel/photoredox catalyzed C–N cross-coupling reaction.

In 2022, Rovis *et al.* has developed a nickel/photoredox catalytic system for facilitating C–N cross-coupling reactions with red light (**Figure 4.5**).[13d] The use of red light provided the deeper penetration of light into the reaction media compared to blue light, facilitating the upscaling reaction in batch. Furthermore, the mild conditions of red light extended the substrate scope, as the photosensitive functional groups were tolerant under the conditions. This approach has demonstrated the promise of employing low-energy light coupled with metal catalysts in organic synthesis.

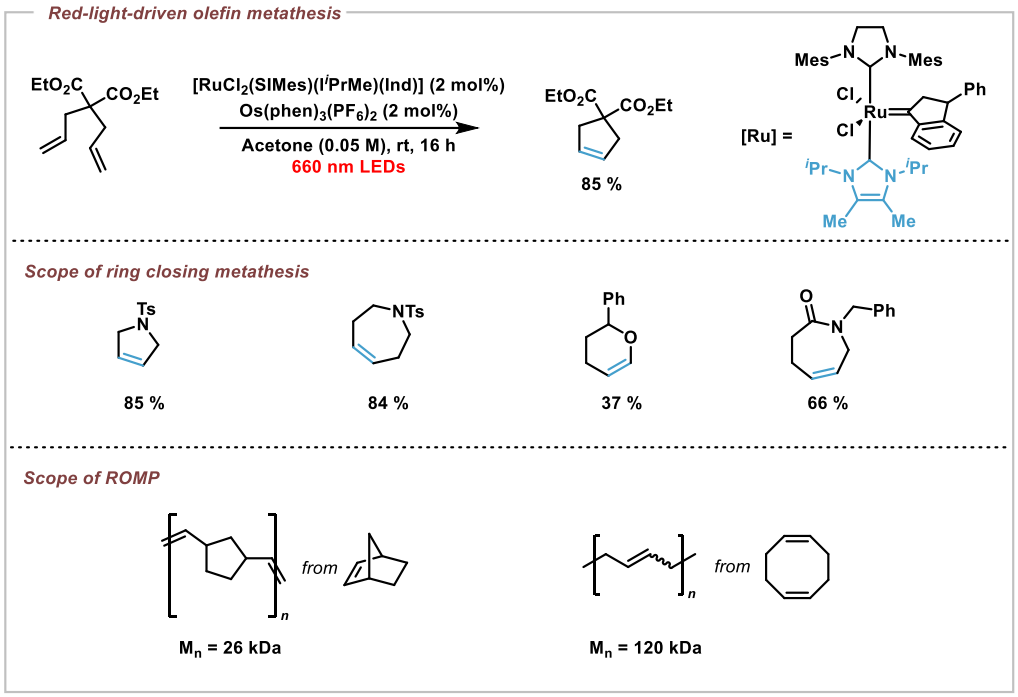

Figure 4.6. Red light-mediated ruthenium-catalyzed olefin metathesis.

Recently, group of Rovis has developed a red light-mediated ruthenium (Ru)-catalyzed olefin metathesis with $Os(phen)_3(PF_6)_2$, which was directly activated from its ground state to its triplet state *via* spin-forbidden excitation (**Figure 4.6**).[13e] This strategy provided not only the spatiotemporal control for the metathesis, but also the advantages of red light photocatalysis, namely good functional tolerance and efficient scale-up reaction in batch. It should be noted that this approach can be used for ring-opening metathesis polymerization (ROMP), which is highly robust and offers mechanically strong polymers. The method has paved new directions for metathesis and polymerization *via* low-energy-light-mediated photoredox.

4.2 Objective

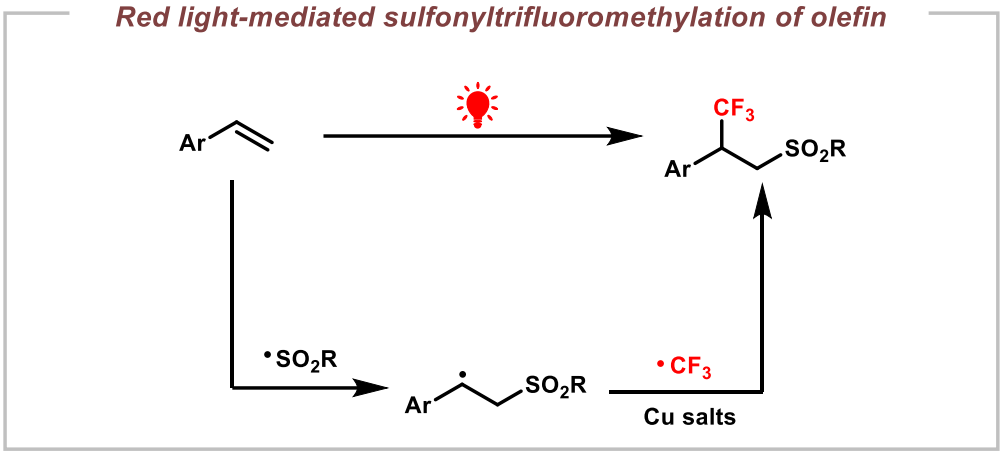

Figure 4.7. Concept of red light-mediated sulfonyltrifluoromethylation of alkenes.

Inspired by the inherent advantages of red light-mediated photocatalysis, we were drawn to this field since this offers a narrower redox window, enabling better reaction control and leading to enhanced selectivity. Motivated by these promising features of the 'red light system', we aimed to meticulously designed a red light-mediated photocatalytic system that exhibited remarkable regioselectivity for the sulfonyltrifluoromethylation of alkenes (**Figure 4.7**).[15] As aforementioned concept, appropriate photocatalysts, sulfinates and electrophilic CF_3 reagent would be selected. After the optimization of reaction conditions, substrate scope and the application of this strategy will be evaluated. Finally, the mechanism of this approach will also be analyzed.

4.3 Results and Discussion

4.3.1 Optimization of reaction conditions with blue light

4.3.1.1 Screening of the photocatalyst

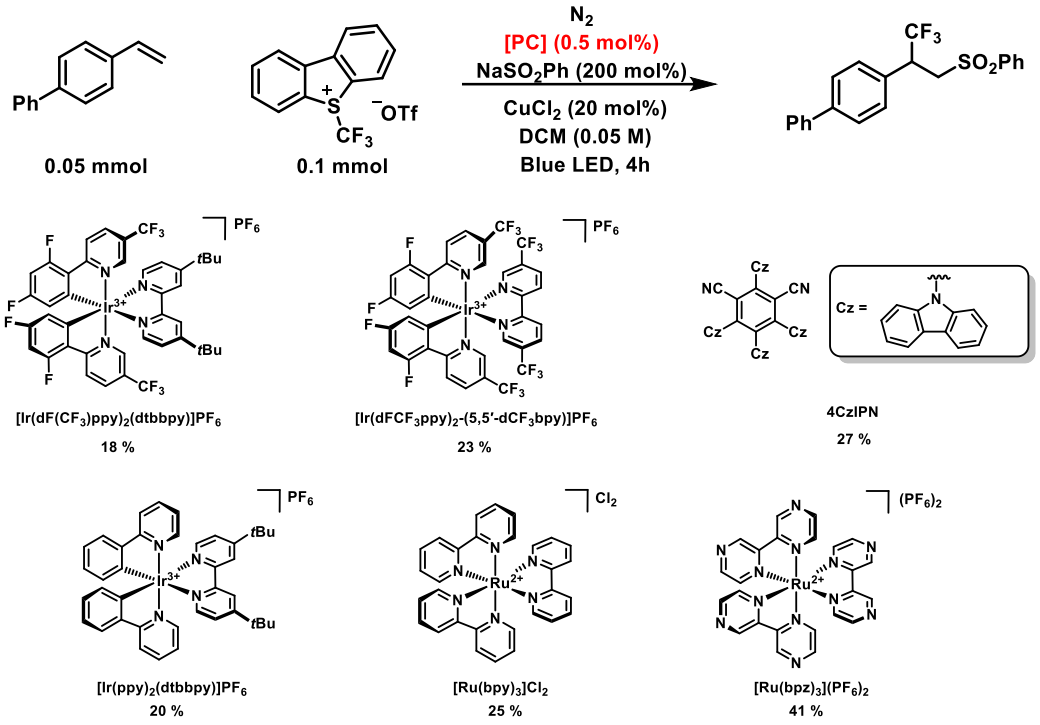

To firstly evaluate the concept of the reaction, 4-vinyl-1,1'-biphenyl, Umemoto's reagent and sodium benzenesulfinate ($NaSO_2Ph$) were initially chosen based on their redox potentials as the model substrate, electrophilic CF_3 source and sulfinate, respectively. Several commercially available Ru- and Ir-based photocatalysts and organic dye, 4-CzIPN, were investigated and all of them offered the desired product in 18-41% yield.

4.3.1.2 Screening of CF_3-sources

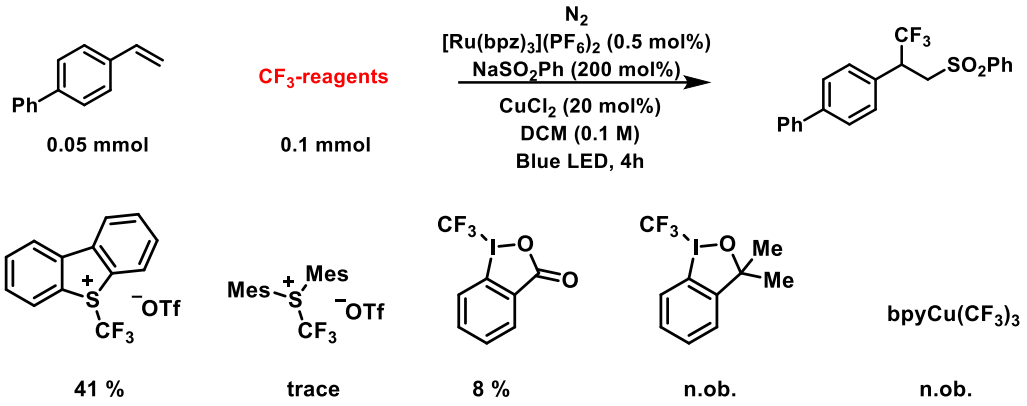

41 % | trace | 8 % | n.ob. | n.ob.

Since the $[Ru(bpz)_3](PF_6)_2$ has provided the best result, we continuously used it as the photocatalyst and further examined the CF_3 source. Various electrophilic CF_3 sources such as Mes-Umemoto's reagent, Togni reagent I/II and $Cu(CF_3)_3bpy$ were utilized under the conditions, however, none of them offered the better yield. The Mes-Umemoto's reagent has more negative reduction potential compared to that of Umemoto's reagent, therefore, the reduction process of CF_3 source was probably not efficient by $[Ru(bpz)_3](PF_6)_2$. It is worth noting that both Togni's reagents are able to react with Cu-salts (here was $CuCl_2$) to form the Cu–CF_3 complexes, which can directly proceed the addition reaction with olefins. Therefore, main side-products were β-CF_3-difunctionalized products. The use of complex $bpyCu(CF_3)_3$ did not show any conversion of the substrate under this conditions.

4.3.1.3 Screening of co-catalysts

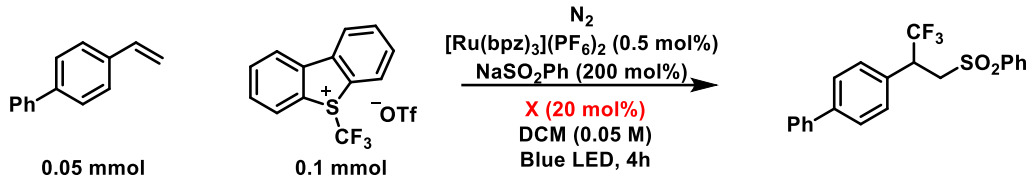

X	Yield (%)
$CuCl_2$	41
CuCl	30
$Cu(CH_3CN)PF_6$	0
$Cu(OTf)_2$	0
CuCN	31
$FeCl_2$	0
$MnCl_2$	0

Based on previous work of CF_3-functionalizations, Cu-salts also played the crucial role since it can capture the CF_3 free radical and further facilitate the cross-coupling reactions involving the CF_3 radical. Therefore, various Cu-salts with different counter anions were examined under the conditions. The results showed that only $CuCl_x$ (X = 1, 2) and CuCN provided the product in 31-41 % yield. Other Cu salts such as $Cu(CH_3CN)PF_6$ and $Cu(OTf)_2$ offered no desired product. To investigate the potential of alternative metal catalysts in promoting the reaction, iron or manganese chloride were also evaluated under conditions, however, both were not efficient in this reaction.

4.3.1.4 Screening of solvents

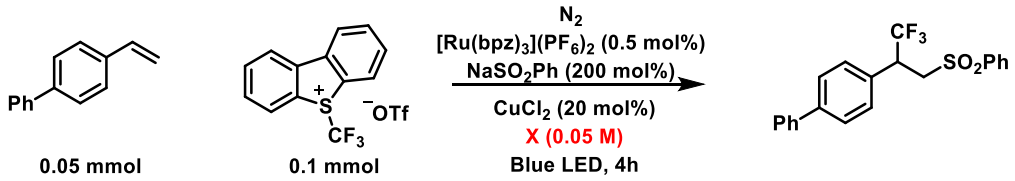

X	Yield (%)
MeCN	34
DMSO	trace
DCM	41
1,2-DCE	28
DMF	0
Acetone	trace
EtOAc	27
DCM (0.1 M)	42

The solvent is sometimes an elusive component in the reaction. We have evaluated several solvents, which were reported in literatures related to CF_3 functionalization. We firstly evaluated the most common solvents used in photochemical reactions, namely acetonitrile (MeCN), dimethyl sulfoxide (DMSO) and dichloromethane (DCM). To our delight, both MeCN and DCM showed acceptable yields of the desired product. Since 1,2-dichloroethene (1,2-DCE) as one of the organochlorine compounds is similar to DCM, we also carried out the reaction with 1,2-DCE, which provided slightly lower yield of the product compared to DCM. Dimethylformamide (DMF) and acetone classified as dipolar aprotic solvent were also tested under the conditions, however, none of them provided the product. Ethyl acetate (EtOAc) as one of the candidates

was evaluated and it gave the product in 27 % yield, albeit lower than the yield of reaction with DCM. At last, the reaction was carried out in the concentrated reaction mixture, the yield of product was slightly increased from 41% to 42%. After comparing all these solvents, DCM (0.1 M) was chosen as the optimized solvent for this reaction.

4.3.2 Optimization of reaction conditions with red light

4.3.2.1 Comparison of 'blue light' and 'red light' system

After intensive optimizations of the reaction conditions under the irradiation of blue light, the highest yield of the desired product only reached to 42% and this low yield could be attributed to the formation of various trifluoromethylated side-products. To increase the selectivity and efficiency of this reaction, we carried out the reaction with an Os-photocatalyst under the irradiation of red light. Since the redox potentials of the catalyst, CF_3 reagent and the sulfinate source should be matched well according to the aforementioned requirements (**Figure 4.4**), we have chosen the combination of $Os(bptpy)_2(PF_6)_2$, S-(trifluoromethyl)thianthrenium triflate ($TT\text{-}CF_3^+OTF^-$) and $NaSO_2Ph$ as the photocatalyst, the CF_3 reagent and sulfiante salts, respectively. As expected, the performance of our 'red light system' was excellent, demonstrating negligible generation of trifluoromethylated side products and significantly higher yields of the desired product (**Figure 4.8**).

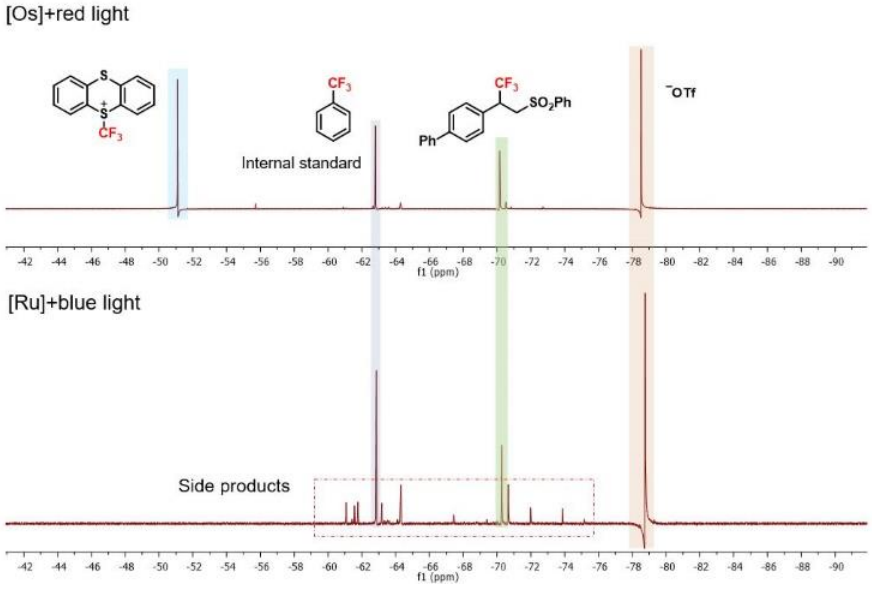

Figure 4.8. Comparison in ^{19}F NMR spectra for initial investigation of the reactions under blue and red light with respective photocatalysts.

4.3.2.2 Screening of the amount of components

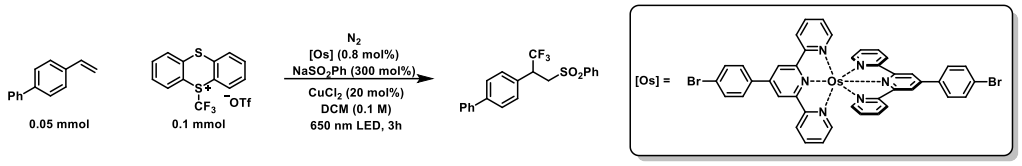

Entry	Variations	Yield (%)[a]
1	none	76(73[b])
2	1.5 equiv. CF_3-reagent	66
3	2 equiv. $NaSO_2Ph$	50
4	DCM (0.05 M)	43
5	30 mol% bpy ligand	0
6	30 mol% 1,10-phen ligand	0

[a]Yield was determined by ^{19}F NMR with trifluorotoluene as internal standard. [b]Isolated yields.

Later, we conducted an exhaustive screening of various reaction conditions based on the 'red light' system. The amount of each of the component was evaluated: Lower concentration or equivalent of CF_3 reagent and sulfinate salts provided comparably lower yield of product, which can be attributed to the kinetic effect. In general, the reactions involving the installation of CF_3 functional groups required excess amount of CF_3 reagents to accelerate the reaction rate.[2b] In this reaction, it is also necessary to use the excess amount of sulfinate salts, ensuring the fast oxidation process of sulfinate salts to the $-SO_2R$ radical. In addition, due to the low solubility in DCM, the use of the excess amount of sulfinate salts could also accelerate the reaction rate. Compared to the reaction mediated by the blue light, the concentrated reaction mixture dramatically improved the yield of product around 30%. Since the presence of Cu salts, common used ligands such as 2,2 ' -bipyridine (bpy) and 1,10-phenanthroline (1,10-phen) were added in the reactions, however, both ligands provided no products. Therefore, it is of significance to underscore that an excess of ligands exerted deleterious effects on the reaction. We assumed that the presence of ligands occupied the coordination sites for CF_3 radical or hindered the binding of CF_3 radical to Cu center due to the steric effect.

4.3.2.3 Screening of CF_3-sources

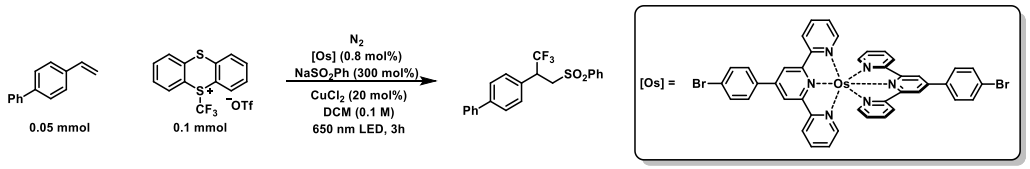

Entry	Variations	Yield (%)[a]
1	2.0 equiv. Togni I	trace
2	2.0 equiv. Togni II	8
3	2.0 equiv. Umemoto reagent	20
4	2.0 equiv. Mes-Umemoto reagent	trace
5	2.0 equiv. bpyCu(CF_3)$_3$	0

[a]Yield was determined by ^{19}F NMR with trifluorotoluene as internal standard. [b]Isolated yields.

Our rationale for selecting CF_3 sources based on the redox potentials. When exploring alternative electrophilic CF_3 sources such as Togni reagents, Umemoto reagents, and Cu(CF_3)$_3$bpy, we observed substantially lower or negligible yields of the desired product. For Togni reagents, Cu-salts would directly react with them to form the Cu−CF_3 complexes, which cause the low selectivity and activity of the reaction. When using Umemoto reagent as the CF_3 source, the Os catalyst at excited state could directly reduce it to the corresponding CF_3 radical, which generated the free CF_3 radical in advance and caused the formation of side products, β-trifluoromethylated products. Compared to Umemoto reagent, Mes-Umemoto reagent is more difficult to be reduced by the Os catalyst. Therefore, only trace product can be detected. At last, Cu(CF_3)$_3$bpy was also tested and no product can be obtained. From the ^{19}F NMR spectra, Cu(CF_3)$_3$bpy was intact under this reaction conditions.

4.3.2.4 Screening of Cu-salts and solvents

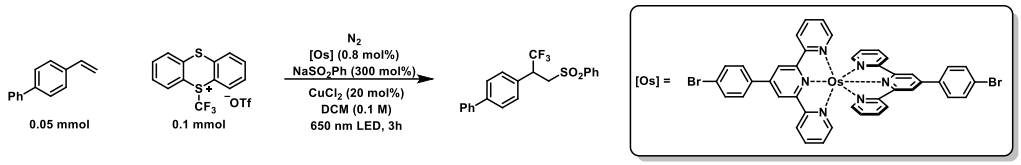

Entry	Variations	Yield (%)[a]
1	20 mol% CuCl	51
2	20 mol% Cu powder	0
3	MeCN (0.1 M)	26
4	EtOAc (0.1 M)	30
5	6 h	61

[a]Yield was determined by ^{19}F NMR with trifluorotoluene as internal standard. [b]Isolated yields.

Furthermore, an investigation was conducted to find out whether variations in the Cu valence state, specifically involving Cu^{I} salts (such as CuCl) and Cu^{0} in the form of fresh copper powder, have an influence on the reaction. The results indicated that the presence of CuCl promoted the reaction to obtain the product, albeit resulting in a slightly reduced yield of approximately 20%. We assumed that the concentration of chloride is also crucial for achieving high photocatalytic activity (More details could be found in **4.3.5.2**). However, Cu powder was not efficient under this conditions, giving no product. Additionally, two of the best solvent for the reaction mediated by blue light, namely MeCN and EtOAc, were also evaluated, however, no improvement was found. At last, to further increase the yield of product, we prolonged the reaction time to 6 hours, however, it revealed that extending the reaction time resulted in a marginal reduction in yield.

4.3.2.5 Control experiments

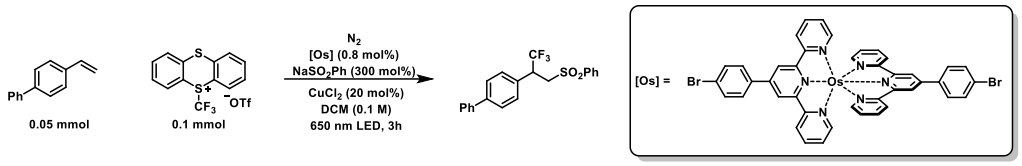

Entry	Variations	Yield (%)[a]
1	No $CuCl_2$	0
2	No [Os]	0
3	No light	0
4	40 W NIR Kessil lamp (740 nm)	24

[a]Yield was determined by ^{19}F NMR with trifluorotoluene as internal standard. [b]Isolated yields.

To assess the necessity of the photocatalyst, Cu salts, and light, a series of control experiments were meticulously conducted, elucidating their necessity in propelling the reaction. In addition, to verify the significance of the light wavelength, one 40 W NIR Kessil lamp (740 nm, near infrared) instead of 650 nm red LED light was utilized. This substitution resulted in a diminished product yield.

4.3.3 Substrate scope evaluation

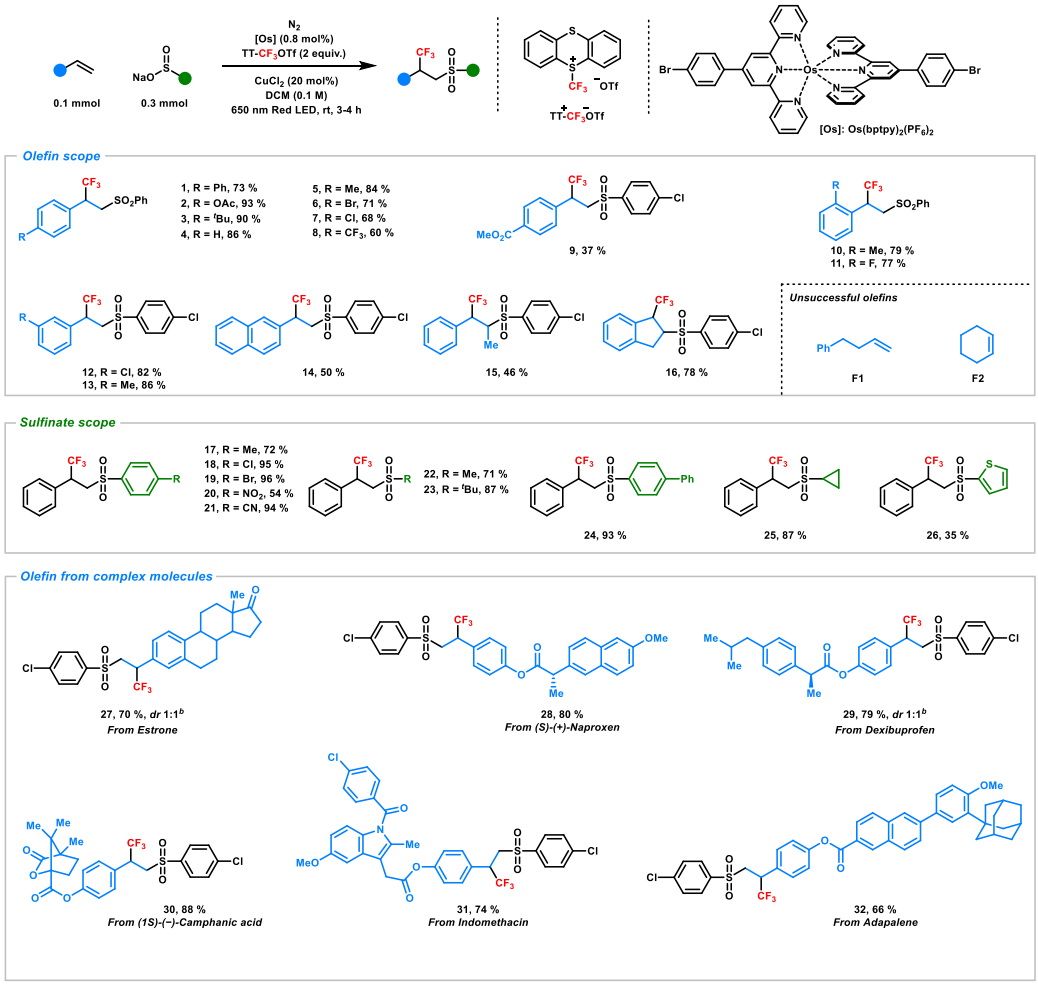

Figure 4.9. Scope of the sulfonyltrifluoromethylation of olefins[a].

With the optimized reaction conditions in hand, we focused on the scope of the sulfonyltrifluoromethylation of alkenes. As depicted in **Figure 4.9**, a diverse array of *para*-substituted styrenes, containing both electron-donating (EDGs) and electron-withdrawing groups (EWGs), furnished the corresponding sulfonyltrifluoromethylated products with moderate to excellent yields (**Figure 4.9**, **1-8**). Notably, 4-bromostyrene and 4-chlorostyrene exhibited tolerance under the reaction conditions, affording the desired products (**6** and **7**), indicating the potential for subsequent functionalization. Moreover, the reaction displayed

compatibility with 2- and 3-substituted styrenes (**10-13**), yielding products satisfactorily, regardless of the presence of -EDGs or -EWGs. In contrast, electron-deficient alkenes (**9** and **14**) exhibited reduced efficiency, however, the use of *p*-chlorophenyl sulfinate improved the reaction. Ordinarily, β-substituted styrenes pose challenges for difunctionalization due to steric effects.[3d] Nonetheless, we were pleased to observe that (*E*)-β-methylstyrene (**15**) and indene (**16**) substrates were also applicable to our system, yielding products with satisfactory yields. Unfortunately, the unactivated olefins do not work under this reaction conditions. Aliphatic olefins such as 4-phenyl-1-butene (**F1**) and cycloalkenes such as cyclohexene (**F2**) could not provide the desired sulfonyltrifluoromethylated products but β-trifluoromethylated side products.

Subsequently, the efficacy of sulfinate salts was evaluated within the framework of a model reaction. Diverse *p*-substituted phenyl sulfinate compounds, containing methyl, chloro, bromo, nitro, and cyano substituents (**17-21**), were found to be well-tolerated, yielding the desired products in notable yields. Moreover, aliphatic sulfinates (**22** and **23**) demonstrated compatibility under the conditions. Notably, sulfinates containing biphenyl, cyclopropane, and thiophene groups exhibited smooth reactivity under red light irradiation, resulting in product yields ranging from 35 - 93% (**24-26**). To investigate the applicability of this methodology to complex molecules, several existing pharmaceuticals and derivatives of natural products were employed as candidates (**27-32**). Remarkably, these reactions yielded the desired products in 66 - 88% yields, indicating the method's high efficiency and potential for constructing more intricate sulfonyltrifluoromethylated molecules.

4.3.4 Industrial applications

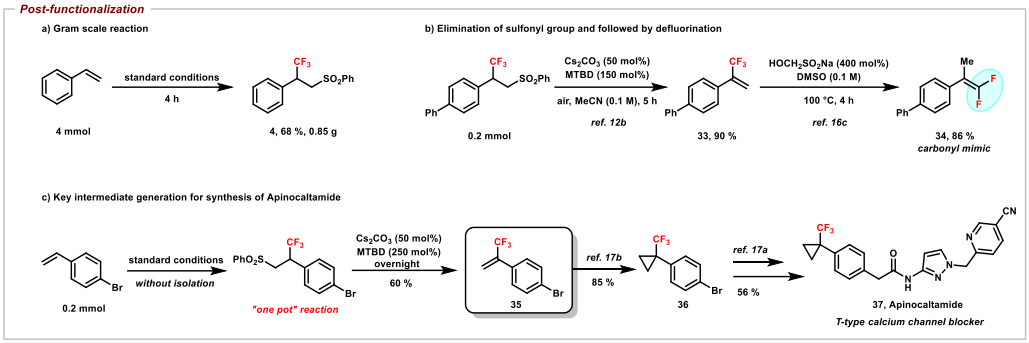

Figure 4.10. Post-functionalization of the sulfonyltrifluoromethylated product.

To further explore the potential industrial applications, a gram-scale reaction was conducted, which proceeded smoothly within 4 hours and yielded approximately 0.85 grams of the product (**Figure 4.10a**). The synthetic utility of these sulfonyltrifluoromethylated alkenes was demonstrated by achieving the elimination of the -sulfonyl group through a straightforward strategy, resulting in the production of α-trifluoromethyl styrene (**33)** with a promising yield of 90% (**Figure 4.10b**).[12b] Moreover, the obtained α-trifluoromethyl styrenes, as valuable compounds, exhibited the potential to undergo further transformations into gem-difluoroalkenes, **34**, with a high yield of 86%. These fluorinated compounds hold promise as ketone mimics in pharmaceutical agents.[16] Furthermore, our methodology offered a pathway to generate a key intermediate, **35**, which enabled the synthesis of apinocaltamide (**37)**, a T-type calcium channel blocker, from a simple starting material, 4-bromostyrene (**Figure 4.10c**).[17]

4.3.5 Mechanistic studies

4.3.5.1 Quenching and radical probe experiments

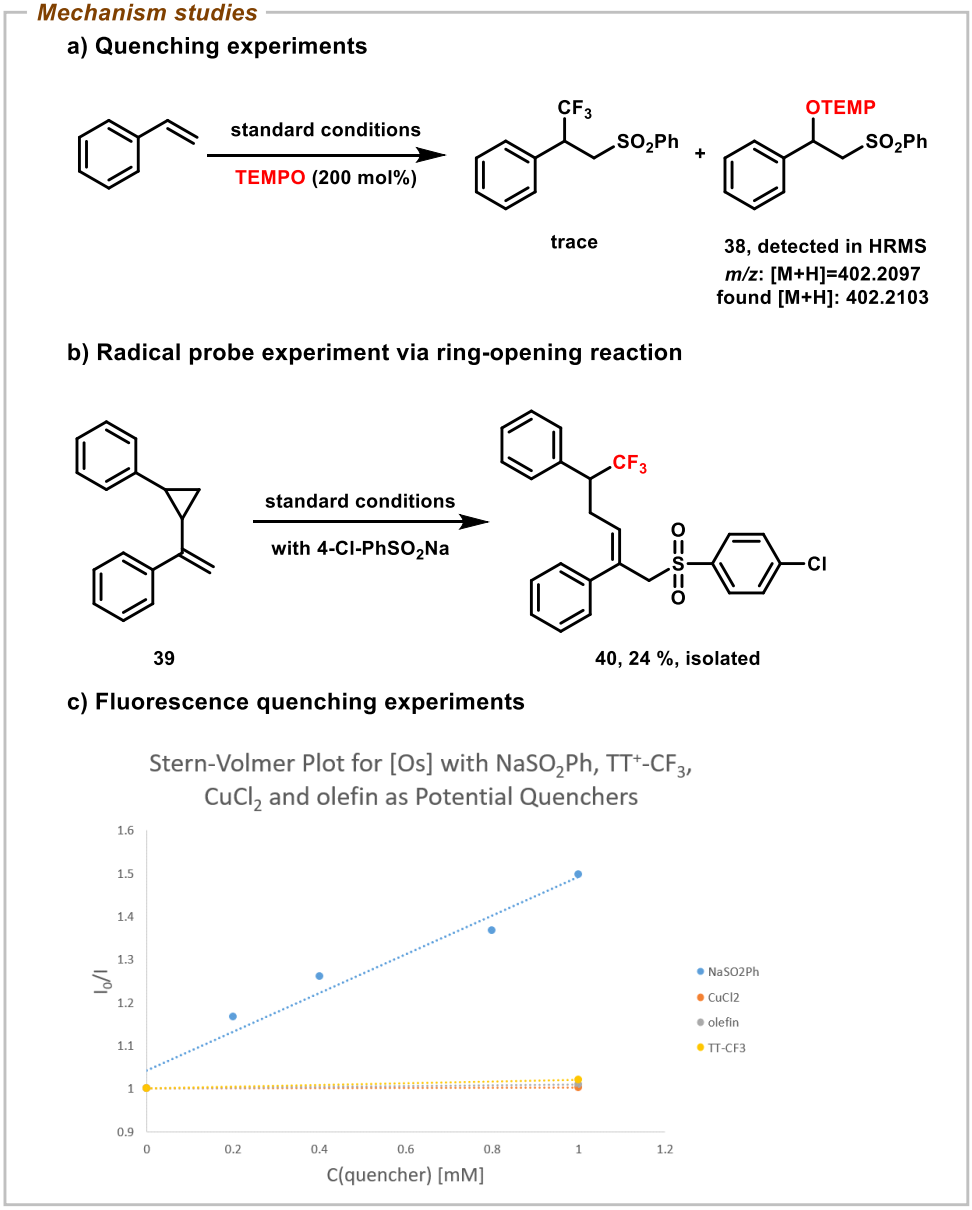

Figure 4.11. Mechanism studies of the sulfonyltrifluoromethylation.

To validate the proposed mechanism, a series of experiments were performed. Initially, (2,2,6,6-Tetramethylpiperidin-1-yl)oxyl (TEMPO)

was utilized as a radical quenching reagent under model reaction conditions. As expected, only a negligible product was obtained, and carbon-centered radical (**III**) was captured by TEMPO and identified using high-resolution mass spectrometry (HRMS) (**Figure 4.11a**). To further prove the involvement of radicals in the sulfonyl radical addition reaction, a radical probe experiment was conducted under model reaction conditions, wherein styrene (**39**) yielded the ring-opening product, **40** (**Figure 4.11b**). Additionally, fluorescence quenching experiments were conducted, revealing that the sodium sulfinate salt exhibited the highest potential as a quencher for the excited state of the Os-photocatalyst which was also supported by the electrochemical measurements for redox potentials (**Figure 4.11c**, SI section **4.5.4.1**).[13a] This finding provided evidence for our designed approach where the generation of the sulfonyl radical preceded the formation of the CF_3 radical.

4.3.5.2 Investigation of Cu-CF_3 active species

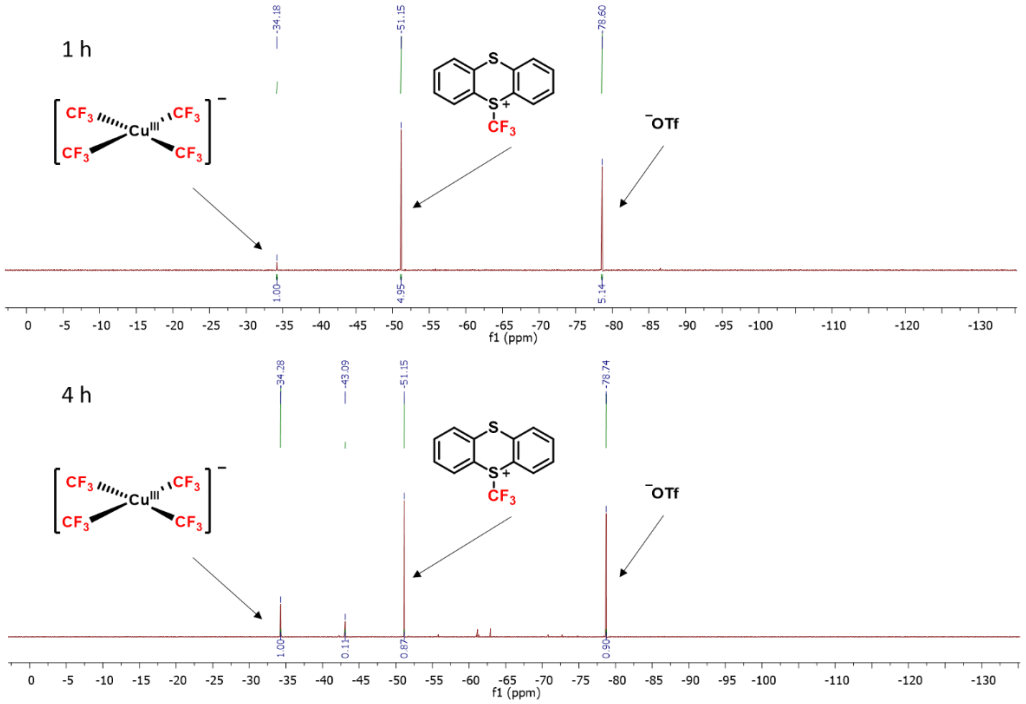

Figure 4.12. ^{19}F NMR analysis of the reaction in the absence of styrene in 1 and 4 hours.

We also investigated the form of the Cu-CF_3 active species. Initially, we attempted to detect the active species in the absence of any styrenes. While no new peak corresponding to Cu^{II}-CF_3 was observed, we did observe the presence of the $Cu^{III}(CF_3)_4$ anion peak (**Figure 4.12** and **4.17b**).

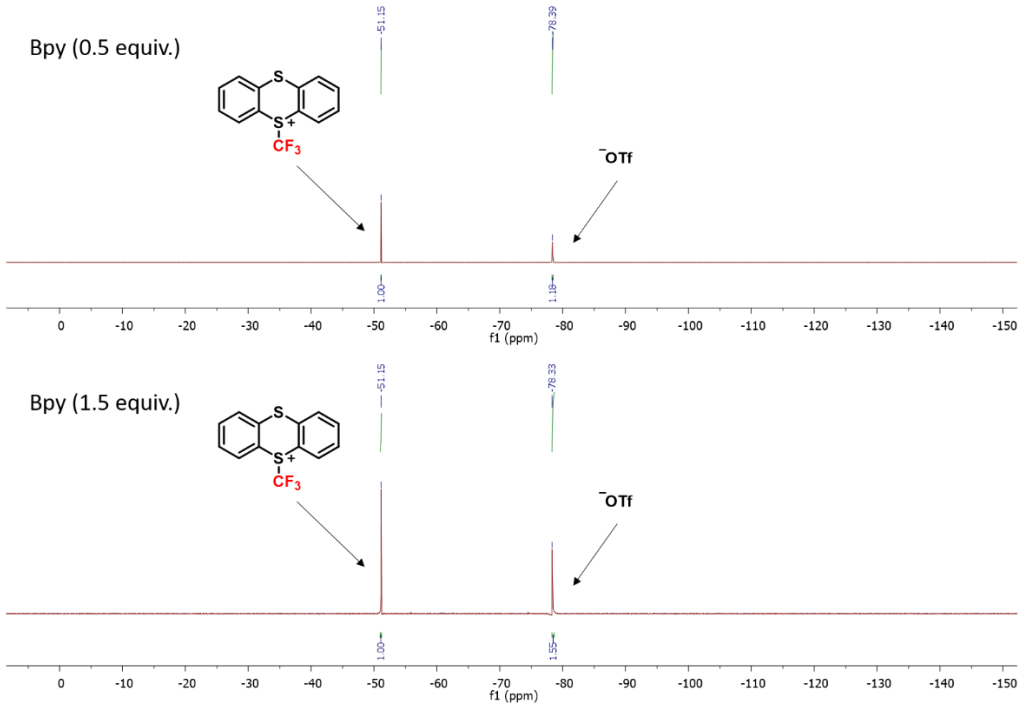

Figure 4.13. ^{19}F NMR analysis of the reaction in the absence of styrene and adding 2,2'-bipyridine (bpy) ligand.

To capture the active species, the 2,2'-bipyridine (bpy) ligand was added into the system. Unfortunately, only peak of $TTCF_3^+OTF^-$ was observed in ^{19}F NMR (**Figure 4.13** and **4.17c**). Therefore, it was necessary to examine whether the $Cu^{III}(CF_3)_4$ anion complex is the active species.

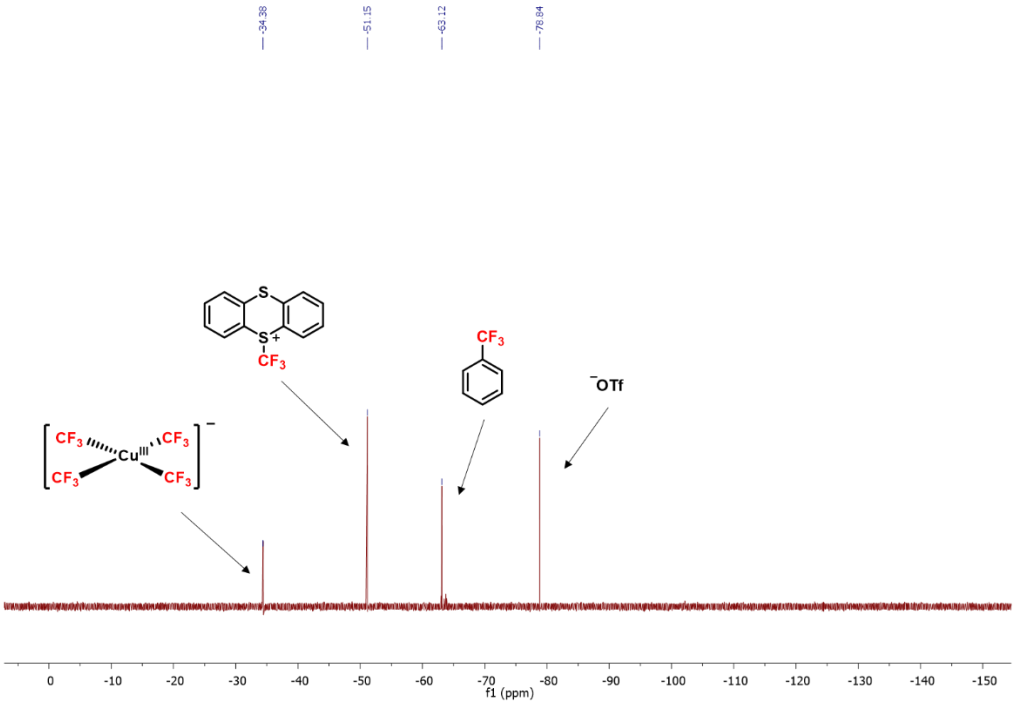

Figure 4.14. ^{19}F NMR analysis of the reaction with $Me_4NCu^{III}(CF_3)_4$ complex instead of $CuCl_2$.

The styrene was added to system after the formation of $Cu^{III}(CF_3)_4$ anion complex, however, no desired sulfonyltrifluoromethylated product was obtained. To further examine the $Cu^{III}(CF_3)_4$ anion complex, we synthesized one stable $Me_4NCu^{III}(CF_3)_4$ complex according to the reference.[18] As expected, no product was obtained by using $Me_4NCu^{III}(CF_3)_4$ complex instead of $CuCl_2$ (**Figure 4.14** and **4.17d**).

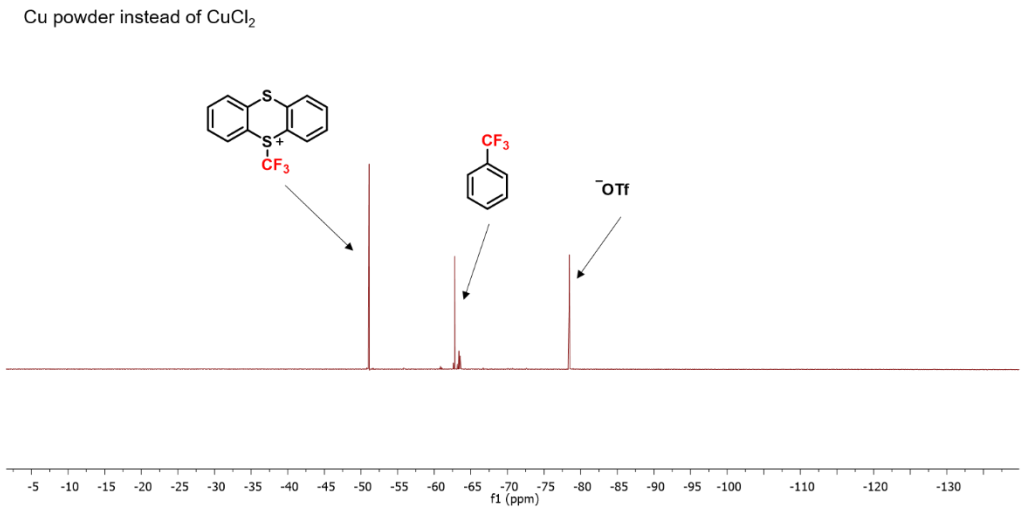

Figure 4.15. ^{19}F NMR analysis of the reaction with fresh Cu^0 powder instead of $CuCl_2$.

Fresh Cu^0 powder was also used as catalyst instead of $CuCl_2$, and no product could be found in the system (**Figure 4.15** and **4.17e**).

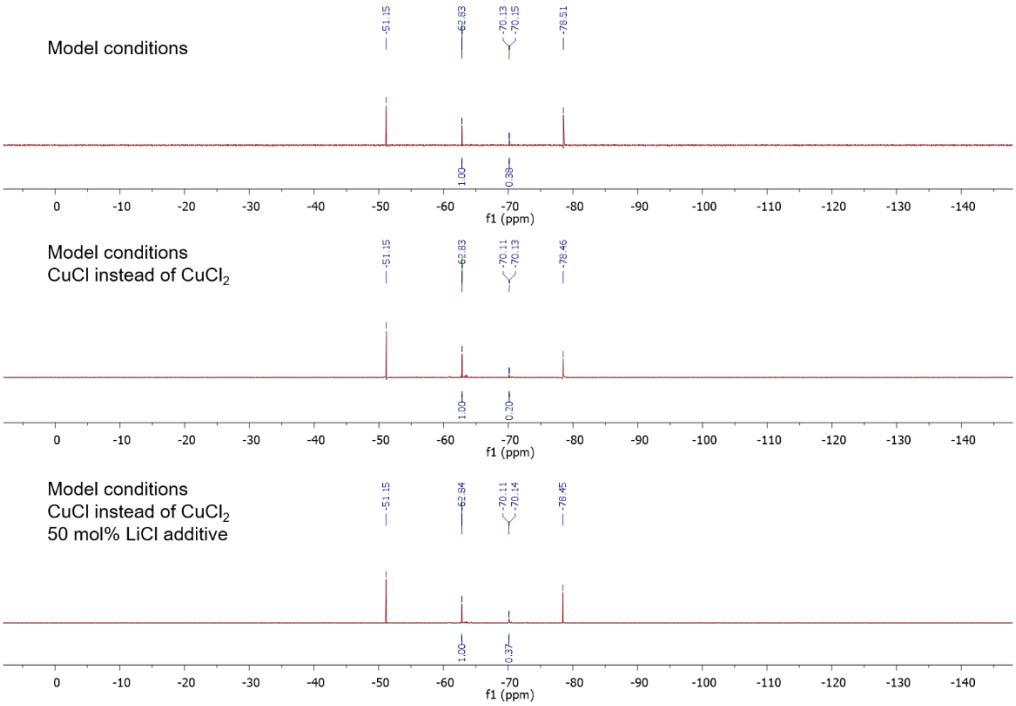

Figure 4.16. Top: ^{19}F NMR analysis of the model reaction. Middle: ^{19}F NMR analysis of the reaction with CuCl instead of $CuCl_2$. Bottom: ^{19}F NMR analysis of the reaction with CuCl with 50 mol% LiCl instead of $CuCl_2$.

As elucidated in the optimization table, the introduction of CuCl instead of $CuCl_2$ resulted in a decrease in yield by approximately 20%. As expected, if Cu^{I} effectively captured the CF_3 radical to form the active species, the yield should have been comparable to that obtained with Cu^{II} salts, which can generate Cu^{I} in situ. We hypothesized that the concentration of chloride anion(Cl^-) might also play a crucial role in the reaction, as reported in the literature.[2e]

Consequently, the addition of 50 mol% of LiCl was incorporated as an additive to the system, resulting in an increased yield comparable to that of the model reaction.

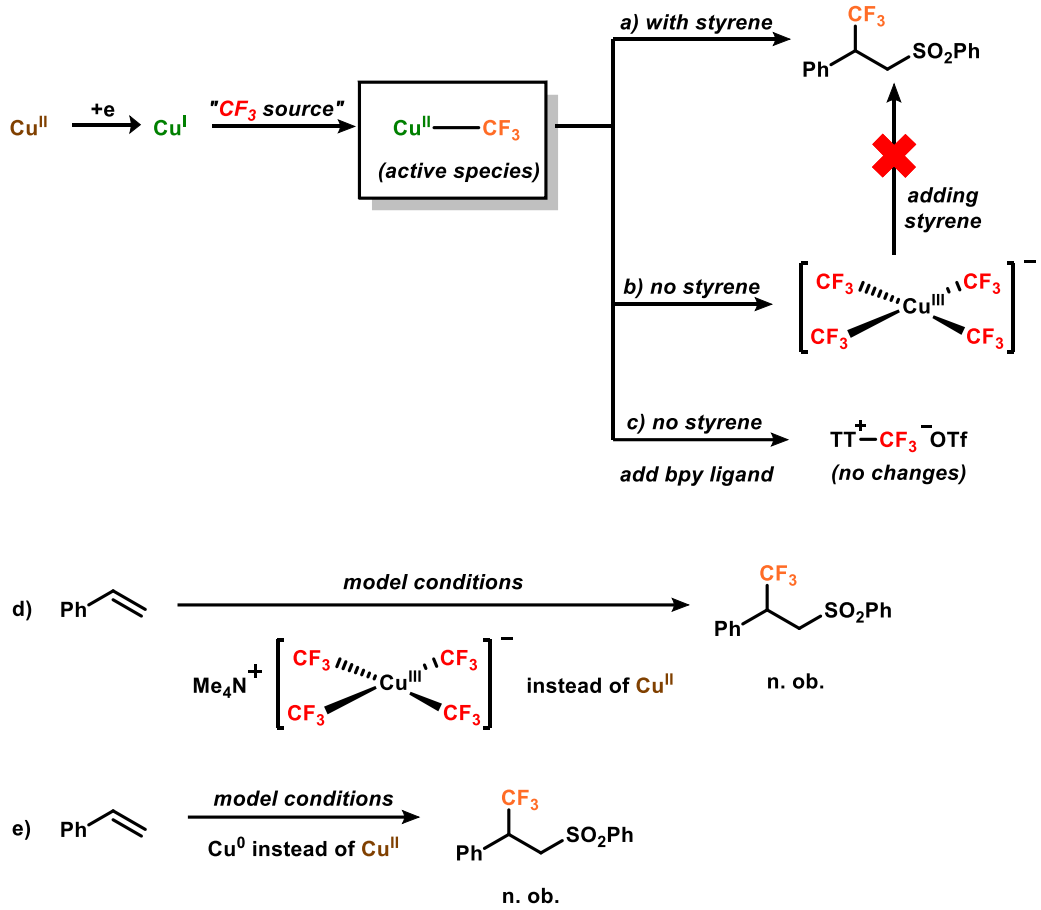

Figure 4.17. The comprehensive analysis of Cu-CF_3 complexes.

Based on these analysis, we can conclude that Cu^{II}-CF_3 (**VI**) was the possible active species for conducting the desired product *via* cross-coupling with **III**.

Combining all these experimental observation, the proposed reaction mechanism is illustrated. The excited state of the photocatalyst [Os^{II}]* underwent exclusive reduction by **I** to form the sulfonyl radical (**II**, *Path A*) rather than oxidation by **IV** to generate the CF_3 radical (**V**, *Path B*). The formed sulfonyl radical (**II**) was then added to the alkene to generate carbon-centered radical (**III**). The Cu^{I} effectively captured the CF_3 radical (**V**), which was generated by the reduction of **IV** by using [Os^{I}] as a reactant. This interaction led to the formation of the Cu^{II}–CF_3 complex **VI**. At last, the cross-coupling reaction between **III** and **VI** facilitated the delivery of the final product **VII**.

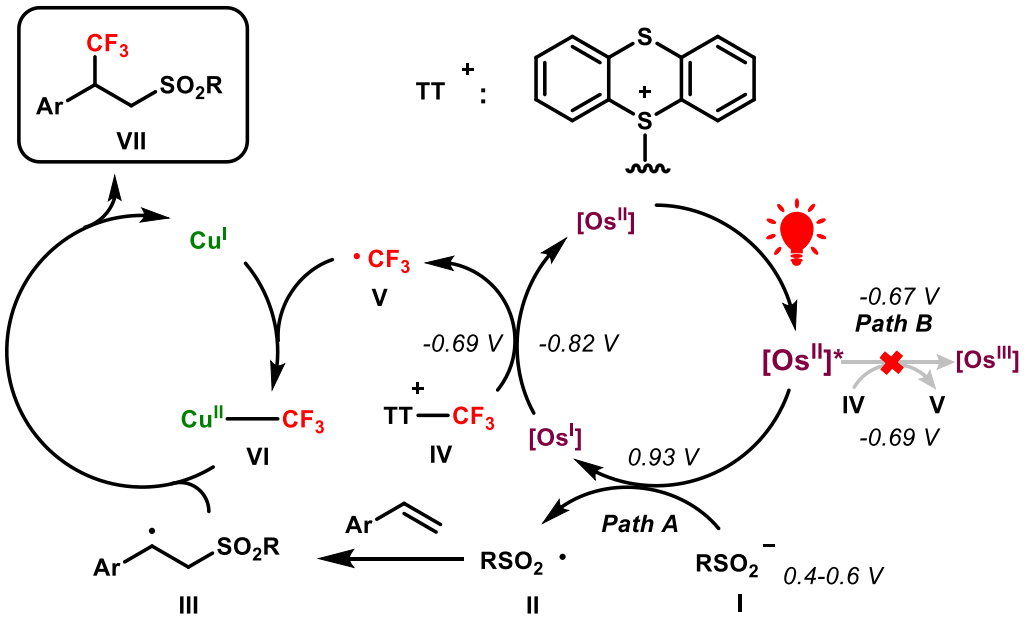

The obtained value was referenced to Ag/AgCl (3 M KCl) in DCM.

4.4 Conclusion

In summary, we have successfully developed a groundbreaking protocol by utilizing red light-mediated photocatalysis for the sulfonyltrifluoromethylation of olefins. The thoughtfully designed reaction system has effectively surmounted challenges related to radical regioselectivity. The impressive breadth of substrate compatibility and

outstanding performance on intricate molecules underscore the high efficiency and excellent functional group tolerance of these reactions. Post-functionalization studies further emphasize the substantial industrial potential of the sulfonyltrifluoromethylated product, thus validating the significance of our reaction system. Through comprehensive mechanistic investigations, we have elucidated a sequential process involving radical generation followed by Cu-catalyzed cross-coupling reactions. We firmly believe that our innovative strategy will advance regioselective functionalization through red light-mediated photocatalysis, thereby catalyzing the development of additional methods in this field.

4.5 Supporting Information

4.5.1. Chemicals and solvents

All reagents and solvents were purchased from certified chemical vendors and used without prior purification. Demineralized water was obtained through deionization of tap water using a EUROTEC L4 reverse osmosis installation. This instrument filters out salts by means of a semi-permeable membrane. Water that was used never exceeded a conductivity of 0.5 μS/cm. Gases were purchased in high-pressured cylinders (200 bar) and converted to the desired pressure by means of a pressure regulator.

4.5.2. Analysis

4.5.2.1. Nuclear magnetic resonance

^{1}H NMR (400 MHz) and ^{13}C NMR (101 MHz) spectra were recorded using a Bruker Avance III Fourier Transform NMR spectrometer at 300 K unless explicitly stated otherwise, using deuterated solvents as internal standard (^{1}H: δ 7.26 ppm and ^{13}C {^{1}H}: δ 77.2 ppm in $CDCl_3$; ^{1}H: δ 2.50 ppm and 13C {^{1}H}: δ 39.52 in DMSO-d6). Chemical shifts (δ) were expressed in ppm and coupling constants (*J*) in Hertz (Hz). Splitting patterns are reported as: s (singlet), d (doublet), t (triplet), q (quadruplet), p (pentuplet), m (multiplet) or combinations thereof. Integration of the signals is presented as the number of hydrogen atoms.

4.5.2.2. Chromatography

Thin-layer chromatography was performed using a heptane/ethyl acetate (EtOAc) solvent system as mobile phase and a 0.20 mm silica gel on an aluminium plate (Machery-Nagel Precoated TLC sheets Alugram® SIL G/UV254) as stationary phase. Visualization of the 'spots' was enhanced by illumination with UV-light (254 nm).

Flash chromatography was performed using an automatic chromatographic system (Biotage® or Combiflash®) with on-line UV-

detection (254 nm and 280 nm unless explicitly stated otherwise). A heptane/EtOAc solvent system was used as mobile phase and commercial silica cartridges (12-80 g, Grace®) as stationary phase.

4.5.3. General procedure and optimizations

A dried 8 mL reaction vial with magnetic stirring bar was charged with photocatalyst, CF_3-source, co-catalyst, sodium sulfinate salts (RSO_2Na) and 4-vinylbiphenyl (0.05 mmol, 1 equiv.) after which the vessel was evacuated using Schlenk techniques and flushed with N_2 three times. Dry DCM were added using a syringe flushed with inert gas. The resulting mixture was stirred for 3-4 h under irradiation of blue LED (40 W, 456 nm) or red light (EvoluChem™ LED 650PF, 650 nm, 20 mW/cm^2) with the EvoluChem PhotoRedOx Box at room temperature. After 3-4 h, trifluorotoluene (prepared in stock solution) was added as internal standard. After shaking the vial, the mixture was filtered by celite and submit to the NMR to determine the yield through ^{19}F NMR.

4.5.4. Mechanism investigation

4.5.4.1. Electrochemical measurements

The electrochemical redox potentials were obtained using a Metrohm Autolab potentiostat-galvanostat PGSTAT204 fitted with a glassy carbon (GC) working electrode (diameter = 3 mm), an Ag/AgCl (3 M KCl) reference electrode and a Pt-foil counter electrode, attached to a PC using Nova v2.1.5 software. 0.1 mmol samples were dissolved in 15 mL 0.1 M tetra-*n*-butylammonium hexafluorophosphate ($^nBu_4NPF_6$) in dry, degassed DCM. Reductions were measured by scanning potentials in the negative direction and oxidations in the positive direction. The obtained value was referenced to Ag/AgCl (3 M KCl).

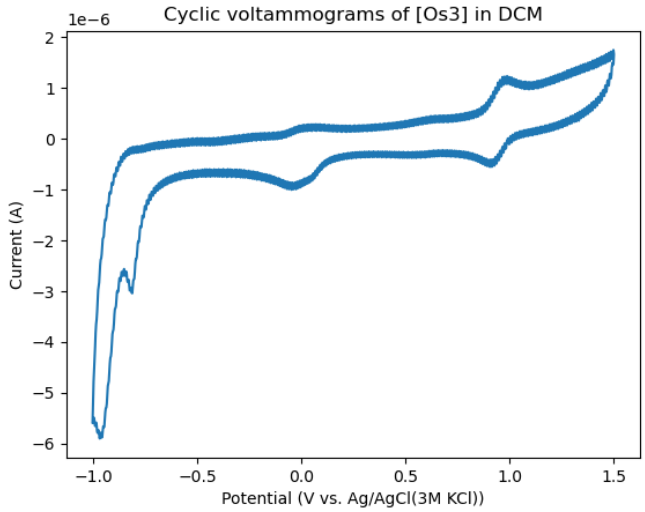

Figure 4.10. Redox potential analysis of [Os] catalyst via cyclic voltammetry.

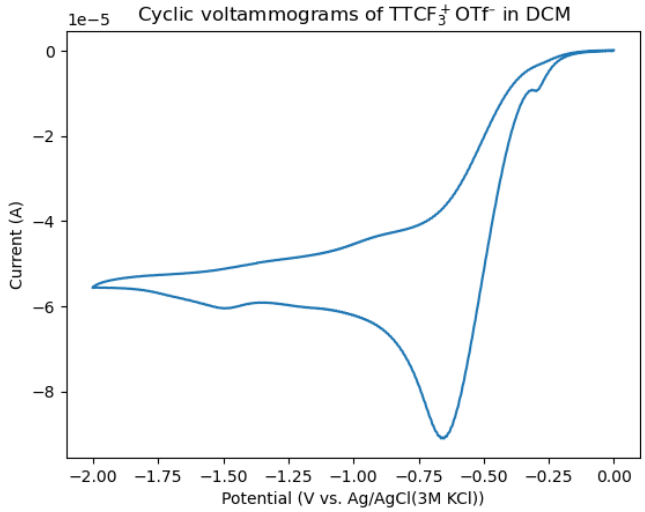

Figure 4.11. Redox potential analysis of TT-$CF_3^+OTf^-$ catalyst via cyclic voltammetry.

The redox potentials of Os photocatalyst and $TTCF_3^+OTF^-$ were measured in DCM (0.1 M). The E_{ox} and E_{red} of [Os] are 1.05 V and -0.82 V vs. Ag/AgCl (3 M KCl), respectively. Although the solvent is different from the refenrece, those values are consistent with the reference.[13a]

Therefore, the redox potential of excited state would be estimated same as the reference. The reduction potential of $TTCF_3^+OTF^-$ is ca. -0.69 V vs. Ag/AgCl (3 M KCl).

According to these redox potentials, we can demonstrate that the excited state of catalyst $[Os^{II}]^*$ can exclusively undergo reduction by **I** to form the sulfonyl radical **II** (*Path A*) rather than oxidation by **IV** to generate the free CF_3 radical **V** (*Path B*). *We highlight the aspect of mechanism we have verified in this part.*

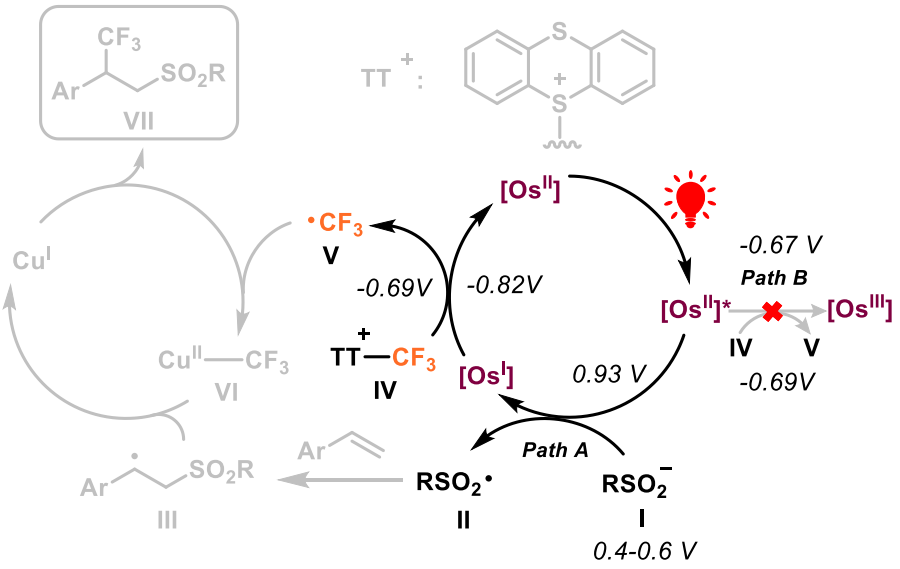

The obtained value was referenced to Ag/AgCl (3 M KCl).

4.5.4.2. Quenching experiment and radical probe experiment

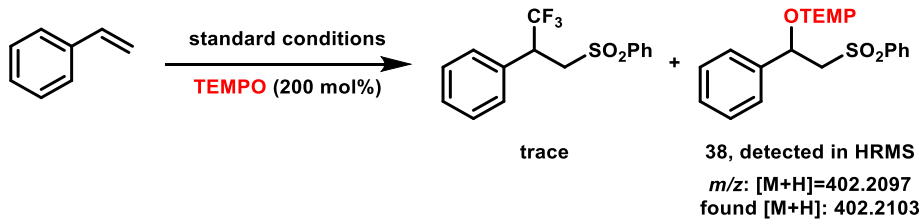

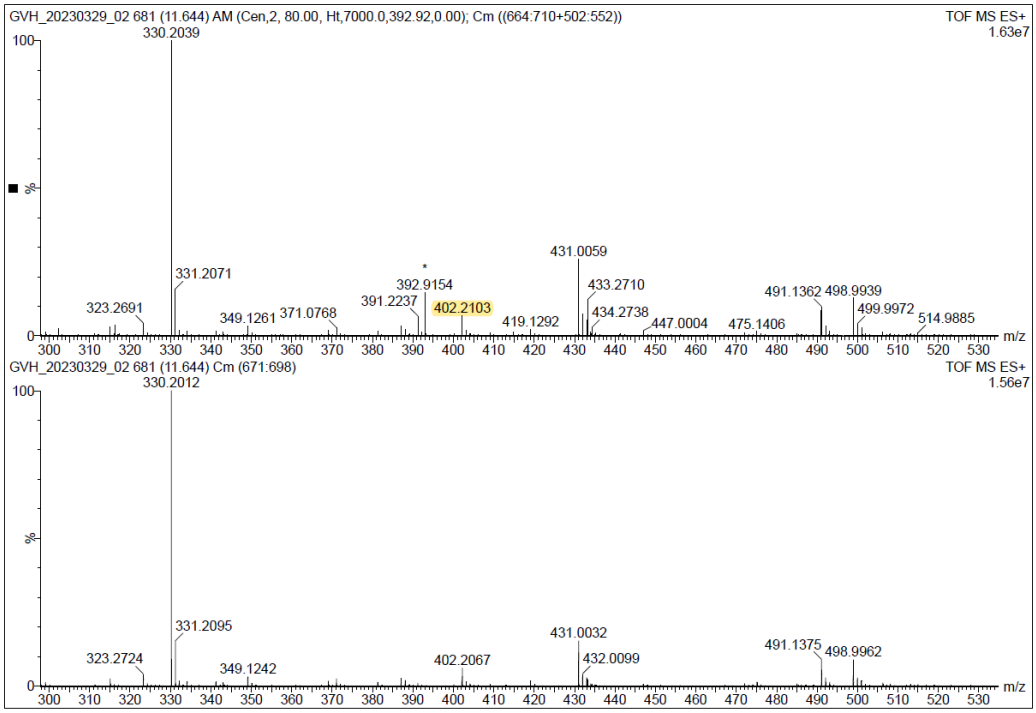

Figure 4.12. HRMS analysis of carbon-centered radical **III** trapped by TEMPO.

The quenching experiment was carried out with 2 equiv. TEMPO and the carbon-centered radical **III** was captured by TEMPO, which was detected in HRMS.

Radical probe experiment via ring-opening reaction

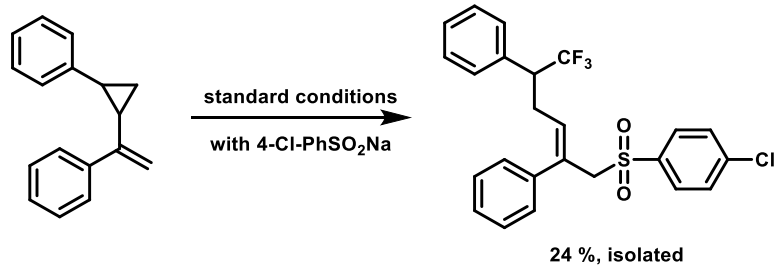

24 %, isolated

Fluorescence quenching experiments

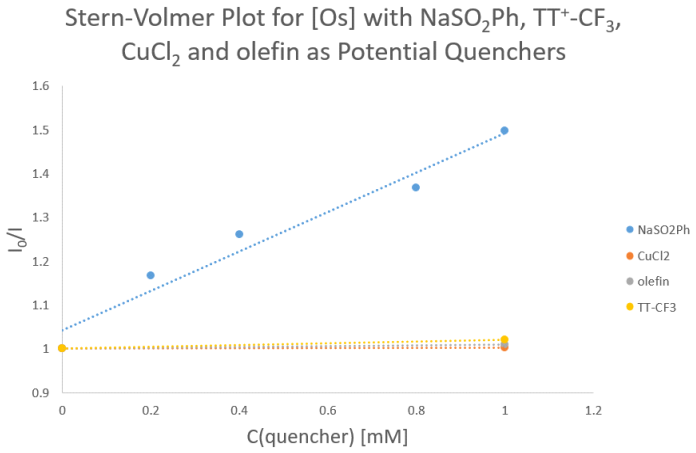

The radical probe experiment and Stern-Volmer analysis were also carried out. These results verified the the excited state of catalyst [Os^{II}]* was quenched by sulfinate anion and the following steps involved radical process. *We highlight the aspect of mechanism we have verified in this part.*

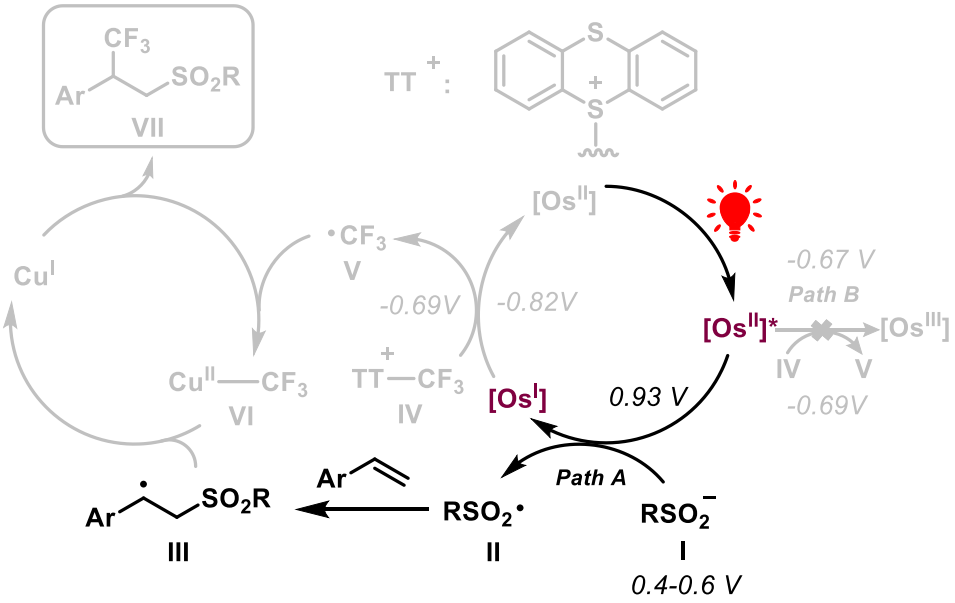

The obtained value was referenced to Ag/AgCl (3 M KCl).

4.5.5. Experiments

4.5.5.1. Photocatalytic reaction setup

The reaction was carried out with the red LED light (EvoluChem™ LED 650PF HCK1012-XX-014 650 nm 20 mW/cm²) in the EvoluChem PhotoRedOx Box. In the box, it contains an electric fan to cool down the reaction. The reaction holder could support 8 reaction vials at the same time. The reaction mixture was stirred using a magnetic stirring plate and stirring bar at 800 rpm on average.

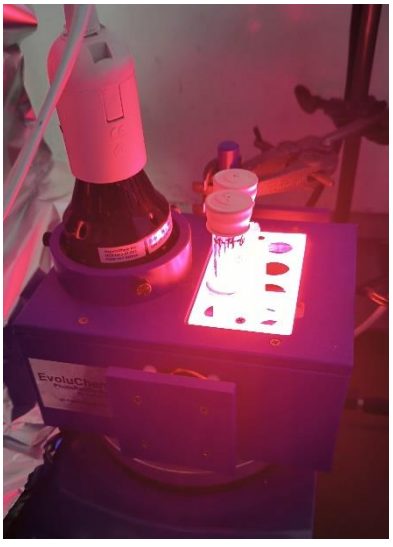

4.5.5.2. Procedure for synthesis of TT-$CF_3^+OTF^-$

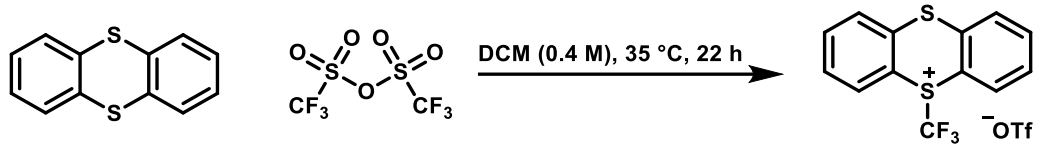

The S-(trifluoromethyl)thianthrenium triflate was prepared according to the literature.[15] A dried 250 mL round-bottom flask with magnetic stirring bar was charged with thianthrene (40 mmol, 1 equiv.) and DCM (100 mL, 0.4 M) under an ambient atmosphere. Subsequently, triflic anhydride (44 mmol, 1.1 equiv.) was added in one portion. The reaction mixture was stirred at 35 °C for 22 h. Subsequently, a saturated aqueous $NaHCO_3$ solution (50 mL) was added carefully. The organic layer was separated and concentrated in vacuo. Et_2O (50 mL) was added to the residue and the suspension was stirred vigorously at room temperature for 30 min. The mixture was allowed to stand for 5 minutes, and the solvent was decanted carefully. The resulting yellow slurry was concentrated to dryness in vacuo and TT-$CF_3^+OTF^-$ salts can be used without further purification.

4.5.5.3. Procedure for synthesis of $Os(bptpy)_2(PF_6)_2$

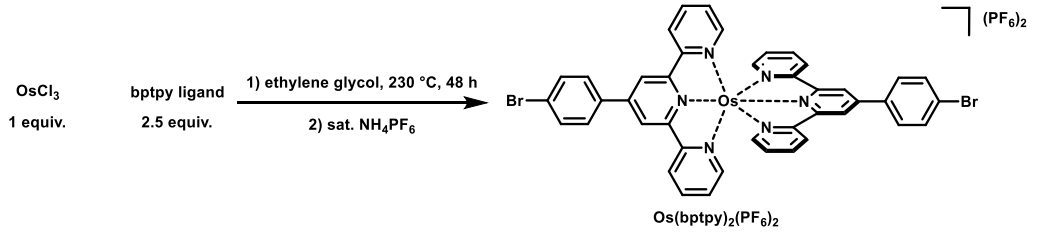

A dried 50 mL pressure tube with magnetic stirring bar was charged with $OsCl_3$ (1 equiv.) and bptpy ligand (2.5 equiv.), followed by addition of anhydrous ethylene glycol (0.075 M) in glovebox. The tube was sealed and heated at 230 °C in a sand bath. (*Caution*: a blast shield is required for all sealed tube reactions since pressure develops in the tube.) After 48 h,

the reaction was allowed to cool to 60 °C. Then, NH_4PF_6 (10 equiv.) was added to the flask under an ambient atmosphere, followed by adding equal volume of distilled water. After 45 minutes, a dark precipitate collected on filter paper was washed with water, methanol, DCM and Et_2O to obtain pure catalyst. The catalyst was dried under vacuum and can be used without further purification.[13a]

4.5.5.4. Procedure for synthesis of olefins from phenols

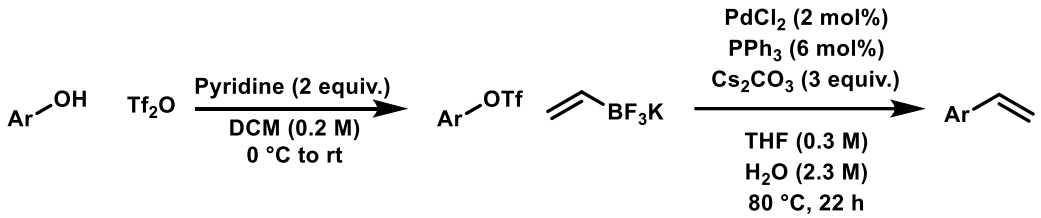

The olefin substrates were synthesized according to a reported procedure.[19] A dried Schlenk flask with magnetic stirring bar was charged with phenol (1.0 mmol, 1.0 equiv), after which the vessel was evacuated using Schlenk techniques and flushed with N_2 three times. Under nitrogen atmosphere, DCM (5.0 mL, 0.20 M) and pyridine (2.0 mmol, 2.0 equiv) was added. The resulting mixture was cooled to 0 °C. Subsequently, Tf_2O (1.5 mmol, 1.5 equiv) was added dropwise over 5 minutes. The reaction mixture was warmed to room temperature and stirred for 5 hours. After 5 h, the reaction mixture was quenched by adding distilled water (15 mL). The organic phase was extracted by DCM (3 × 20 mL) and concentrated in vacuo. Purification proceeded to obtain *triflate substrate* via flash column chromatography.

A dried two-necked flask with stirring bar was charged with *triflate substrate* (0.5 mmol, 1.00 equiv) from previous step, potassium vinyltrifluoroborate (0.6 mmol, 1.2 equiv), $PdCl_2$ (0.01 mmol, 2.00 mol%), PPh_3 (0.03 mmol, 6.00 mol%) and Cs_2CO_3 (1.5 mmol, 3.00 equiv), after which the vessel was evacuated using Schlenk techniques and flushed

with N_2 three times. Distilled THF (2.00 mL) and degassed distilled water (0.25 mL) were added. After stirring at 80 °C for 22 h, the reaction mixture was quenched by adding DCM (15.0 mL) and water (20.0 mL). The layers were separated, and the aqueous layer was extracted with DCM (3 × 15 mL). The organic phase was extracted and concentrated in vacuo. The residue was purified by flash column chromatography.

4.5.5.5. Procedure for synthesis of olefins from acids

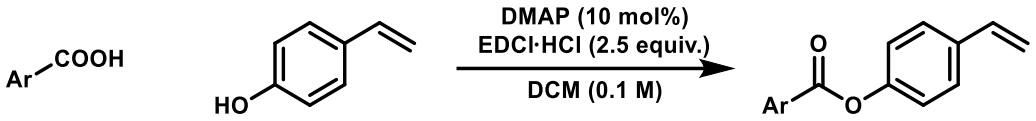

These olefins were prepared following reported literature procedure.[20] A dried two-necked flask with stirring bar was charged with acid (2 mmol, 1 equiv.), DMAP (0.2 mmol, 10 mol%) and EDCI•HCl (5 mmol, 2.5 equiv.), after which the vessel was evacuated using Schlenk techniques and flushed with N_2 three times. Under nitrogen gas flow, 4-vinylphenol (2 mmol, 1 equiv.) and DCM (0.1 M) were added using a syringe flushed with inert gas. The mixture was stirred at room temperature under N_2 until the reaction was complete by TLC monitoring. The mixture was diluted with water and the organic layer was separated, dried over anhydrous Na_2SO_4 and concentrated. Purification proceeded via flash column chromatography.

4.5.5.6. Procedure for sulfonyltrifluoromethylation of olefins

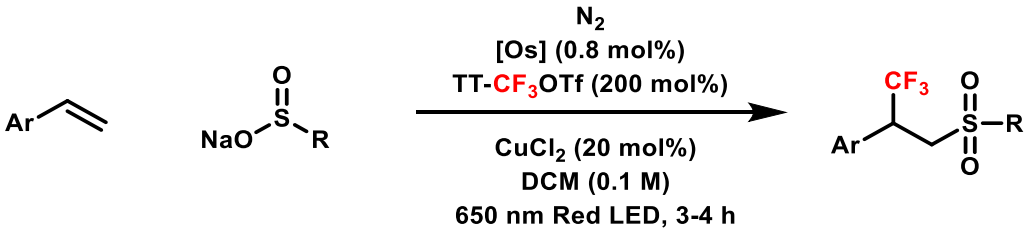

A dried reaction vial with magnetic stirring bar was charged with $Os(bptpy)_2(PF_6)_2$ (0.0008 mmol, 0.8 mol%), $CuCl_2$ (0.02 mmol, 20 mol%), TT-$CF_3^+OTF^-$ (0.2 mmol, 2 equiv.) and sadium sulfinate (0.3 mmol, 3 equiv.), after which the vessel was evacuated using Schlenk techniques and flushed with N_2 three times. Under nitrogen gas flow, olefin (0.1 mmol, 1 equiv.) (if liquid, otherwise added before flushing cycle) and dry DCM (0.1 M) were added using a syringe flushed with inert gas. The resulting mixture was stirred for 3-4 h under irradiation of red LED light (EvoluChem™ LED 650PF HCK1012-XX-014 650 nm 20 mW/cm²) in the EvoluChem PhotoRedOx Box. After completion of reaction, the reaction mixture was quenched by adding distilled water (2 mL). The organic phase was extracted and concentrated in vacuo. 1,1,1-Trifluorotoluene was added as internal standard to determine the NMR yield of the functionalised product through ^{19}F NMR. Purification proceeded via flash column chromatography.

4.5.6. Characterization

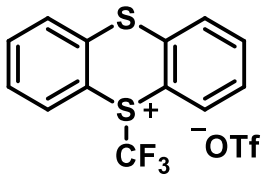

TT-$CF_3^+OTF^-$

^{1}H NMR (400 MHz, $CDCl_3$) δ 8.58 (dd, *J* = 8.1, 1.2 Hz, 1H), 7.93 – 7.87 (m, 1H), 7.82 (dd, *J* = 8.0, 1.3 Hz, 1H), 7.79 – 7.74 (m, 1H).

^{19}F NMR (376 MHz, $CDCl_3$) δ -51.11 (s), -78.39 (s).

^{13}C NMR (101 MHz, $CDCl_3$) δ 136.90, 136.81, 136.65, 130.33, 129.41, 124.43 (q, *J* = 337.2 Hz), 120.68 (q, *J* = 320.3 Hz), 108.95.

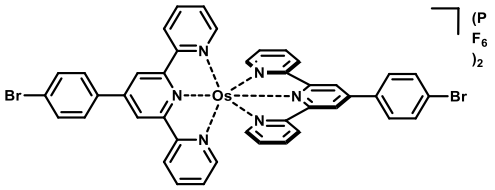

$Os(bptpy)_2(PF_6)_2$

^{1}H NMR (400 MHz, DMSO) δ 9.40 (s, 4H), 8.97 (d, *J* = 8.2 Hz, 4H), 8.27 (d, *J* = 8.5 Hz, 4H), 7.88 (d, *J* = 8.5 Hz, 4H), 7.81 (t, *J* = 7.8 Hz, 4H), 7.31 (d, *J* = 5.6 Hz, 4H), 7.09 (t, *J* = 6.5 Hz, 4H).

^{19}F NMR (376 MHz, DMSO) δ -70.18 (d, *J* = 711.2 Hz).

^{13}C NMR (101 MHz, DMSO) δ 160.12, 155.18, 152.96, 152.75, 138.30, 135.09, 132.58, 130.43, 128.47, 125.49, 124.64, 120.10.

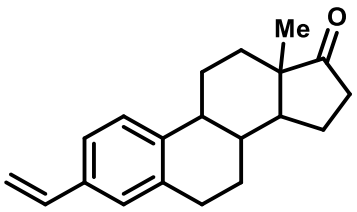

S1

^{1}H NMR (400 MHz, $CDCl_3$) δ 7.21 (dd, *J* = 17.6, 8.2 Hz, 2H), 7.12 (s, 1H), 6.68 – 6.55 (m, 1H), 5.69 (d, *J* = 17.6 Hz, 1H), 5.18 (d, *J* = 10.9 Hz, 1H), 2.90 (dd, *J* = 8.6, 3.9 Hz, 2H), 2.44 (ddd, *J* = 17.4, 16.0, 6.8 Hz, 2H), 2.25 (dd, *J* = 13.6, 7.1 Hz, 1H), 2.19 – 1.89 (m, 4H), 1.67 – 1.33 (m, 6H), 0.89 (s, 3H).

^{13}C NMR (101 MHz, $CDCl_3$) δ 220.9, 139.57, 136.64, 136.57, 135.24, 126.90, 125.55, 123.64, 113.16, 50.55, 47.98, 44.47, 38.20, 35.86, 31.65, 29.41, 26.53, 25.76, 21.62, 13.88.

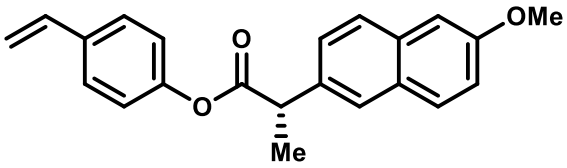

S2

^{1}H NMR (400 MHz, $CDCl_3$) δ 7.80 – 7.69 (m, 3H), 7.50 (dd, *J* = 8.5, 1.9 Hz, 1H), 7.40 – 7.31 (m, 2H), 7.16 (dt, *J* = 7.2, 2.4 Hz, 2H), 7.00 – 6.88 (m, 2H), 6.67 (dd, *J* = 17.6, 10.9 Hz, 1H), 5.67 (dd, *J* = 17.6, 0.8 Hz, 1H), 5.21 (dd, *J* = 10.9, 0.7 Hz, 1H), 4.09 (q, *J* = 7.1 Hz, 1H), 3.93 (s, 3H), 1.69 (d, *J* = 7.1 Hz, 3H).

^{13}C NMR (101 MHz, $CDCl_3$) δ 173.10, 157.80, 150.42, 135.91, 135.31, 135.14, 133.85, 129.33, 129.03, 127.38, 127.07, 126.15, 126.13, 121.45, 119.11, 113.93, 105.67, 55.34, 45.61, 18.52.

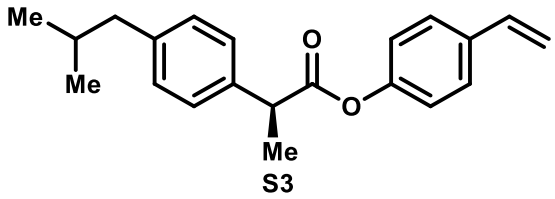

S3

^{1}H NMR (400 MHz, $CDCl_3$) δ 7.41 – 7.34 (m, 2H), 7.32 – 7.23 (m, 2H), 7.15 (d, *J* = 8.1 Hz, 2H), 6.99 – 6.93 (m, 2H), 6.68 (dd, *J* = 17.6, 10.9 Hz, 1H), 5.68 (dd, *J* = 17.6, 0.7 Hz, 1H), 5.22 (dd, *J* = 10.9, 0.6 Hz, 1H), 3.93 (q, *J* = 7.1 Hz, 1H), 2.48 (d, *J* = 7.2 Hz, 2H), 1.97 – 1.79 (m, 1H), 1.61 (d, *J* = 7.2 Hz, 3H), 0.92 (d, *J* = 6.6 Hz, 6H).

^{13}C NMR (101 MHz, $CDCl_3$) δ 173.16, 150.47, 140.83, 137.24, 135.94, 135.27, 129.51, 127.22, 127.07, 121.46, 113.90, 45.29, 45.07, 30.18, 22.39, 18.53.

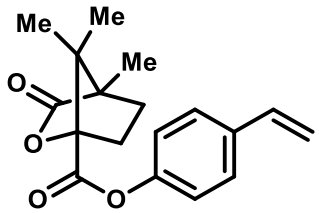

S4

^{1}H NMR (400 MHz, $CDCl_3$) δ 7.47 – 7.37 (m, 2H), 7.15 – 7.06 (m, 2H), 6.71 (dd, *J* = 17.6, 10.9 Hz, 1H), 5.72 (dd, *J* = 17.6, 0.5 Hz, 1H), 5.27 (d, *J* = 10.9 Hz, 1H), 2.57 (ddd, *J* = 13.5, 10.8, 4.3 Hz, 1H), 2.20 (ddd, *J* = 13.6, 9.3, 4.6 Hz, 1H), 1.99 (ddd, *J* = 13.2, 10.8, 4.6 Hz, 1H), 1.77 (ddd, *J* = 13.4, 9.4, 4.3 Hz, 1H), 1.16 (d, *J* = 7.6 Hz, 6H), 1.11 (s, 3H).

^{13}C NMR (101 MHz, $CDCl_3$) δ 177.79, 166.08, 149.49, 135.71, 127.31, 121.36, 114.49, 90.83, 54.91, 54.68, 30.78, 28.99, 16.89, 9.73.

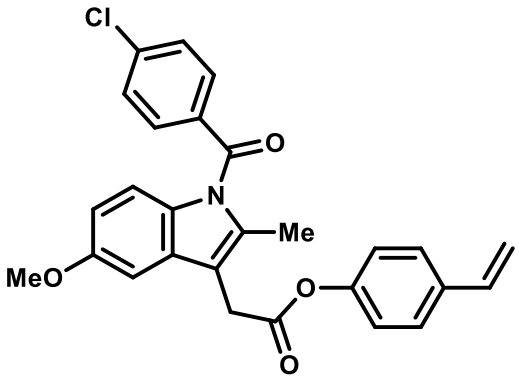

S5

^{1}H NMR (400 MHz, $CDCl_3$) δ 7.74 – 7.62 (m, 2H), 7.55 – 7.45 (m, 2H), 7.41 – 7.35 (m, 2H), 7.04 (ddd, *J* = 11.2, 6.9, 2.5 Hz, 3H), 6.91 (d, *J* = 9.0 Hz, 1H), 6.75 – 6.62 (m, 2H), 5.69 (dd, *J* = 17.6, 0.6 Hz, 1H), 5.24 (dd, *J* = 10.9, 0.5 Hz, 1H), 3.90 (s, 2H), 3.84 (s, 3H), 2.46 (s, 3H).

^{13}C NMR (101 MHz, $CDCl_3$) δ 169.24, 168.31, 156.18, 150.26, 139.37, 136.22, 135.83, 135.52, 133.88, 131.21, 130.90, 130.52, 129.16, 127.16, 121.44, 115.03, 114.15, 112.00, 111.85, 101.28, 55.75, 30.59, 13.42.

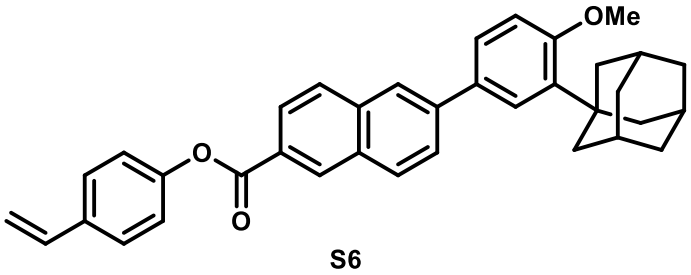

S6

^{1}H NMR (400 MHz, $CDCl_3$) δ 8.78 (s, 1H), 8.20 (d, *J* = 8.6 Hz, 1H), 8.01 (dd, *J* = 23.4, 9.1 Hz, 3H), 7.83 (d, *J* = 8.5 Hz, 1H), 7.62 (s, 1H), 7.57 (d, *J* = 8.4 Hz, 1H), 7.50 (d, *J* = 7.6 Hz, 1H), 7.24 (d, *J* = 8.4 Hz, 2H), 7.01 (d, *J* = 8.5 Hz, 1H), 6.75 (dd, *J* = 17.7, 10.8 Hz, 1H), 5.75 (d, *J* = 17.5 Hz, 1H), 5.28 (d, *J* = 10.8 Hz, 1H), 3.92 (d, *J* = 1.1 Hz, 3H), 2.20 (s, 6H), 2.11 (s, 3H), 1.81 (s, 6H).

^{13}C NMR (101 MHz, $CDCl_3$) δ 165.37, 159.05, 150.69, 141.83, 139.10, 136.31, 136.01, 135.45, 132.48, 131.72, 131.27, 129.84, 128.46, 127.29, 126.68, 126.23, 126.02, 125.82, 125.77, 124.78, 121.85, 114.03, 112.18, 55.19, 40.66, 37.26, 37.16, 29.15.

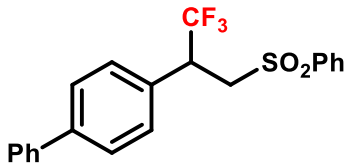

1

^{1}H NMR (400 MHz, $CDCl_3$) δ 7.61 – 7.57 (m, 2H), 7.52 – 7.42 (m, 5H), 7.40 – 7.35 (m, 3H), 7.34 – 7.28 (m, 2H), 7.17 (d, *J* = 8.2 Hz, 2H), 4.08 – 3.98 (m, 1H), 3.80 (qd, *J* = 14.7, 6.8 Hz, 2H).

^{19}F NMR (376 MHz, $CDCl_3$) δ -69.95 (d, *J* = 9.1 Hz).

^{13}C NMR (101 MHz, $CDCl_3$) δ 141.84, 140.18, 139.12, 133.47, 129.84, 129.56, 129.04, 128.88, 127.88, 127.72, 127.42, 127.02, 126.80, 55.48, 45.67 (q, *J* = 28.6 Hz).

HRMS (ESI$^+$, *m*/*z*) [M+H$^+$] calcd. for $C_{21}H_{17}SO_2F_3$ 391.0974, found 391.0976.

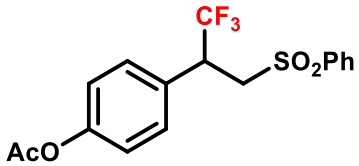

2

^{1}H NMR (400 MHz, $CDCl_3$) δ 7.62 – 7.48 (m, 3H), 7.43 – 7.30 (m, 2H), 7.11 (d, *J* = 8.5 Hz, 2H), 6.96 – 6.86 (m, 2H), 4.08 – 3.92 (m, 1H), 3.74 (m, 2H), 2.29 (s, 3H).

^{19}F NMR (376 MHz, $CDCl_3$) δ -70.06 (d, *J* = 9.0 Hz).

^{13}C NMR (101 MHz, $CDCl_3$) δ 168.81, 151.11, 138.91, 133.84, 130.16, 129.24, 128.49, 127.77, 126.66, 121.95, 55.50, 45.39 (q, *J* = 29.0 Hz), 21.10.

HRMS (ESI$^+$, *m*/*z*) [M+H$^+$] calcd. for $C_{17}H_{15}SO_4F_3$ 373.0716, found 373.0718.

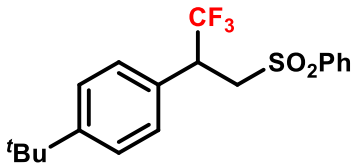

3

^{1}H NMR (400 MHz, $CDCl_3$) δ 7.59 – 7.52 (m, 2H), 7.48 – 7.39 (m, 1H), 7.33 – 7.22 (m, 2H), 7.20 – 7.08 (m, 2H), 6.99 (d, *J* = 8.3 Hz, 2H), 3.96 (pd, *J* = 9.2, 3.3 Hz, 1H), 3.85 – 3.68 (m, 2H), 1.27 (s, 9H).

^{19}F NMR (376 MHz, $CDCl_3$) δ -70.14 (d, *J* = 9.1 Hz).

^{13}C NMR (101 MHz, $CDCl_3$) δ 151.77, 139.13, 133.45, 128.92, 128.74, 127.87, 127.75, 126.86, 125.64, 55.38, 45.54 (q, *J* = 28.5 Hz), 34.49, 31.20.

HRMS (ESI$^+$, *m*/*z*) [M+H$^+$] calcd. for $C_{19}H_{21}SO_2F_3$ 371.1287, found 371.1292. [M+Na$^+$] 393.1107, found 393.1114.

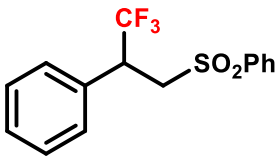

4

^{1}H NMR (400 MHz, $CDCl_3$) δ 7.62 – 7.58 (m, 2H), 7.50 (ddd, *J* = 8.7, 2.4, 1.2 Hz, 1H), 7.38 – 7.32 (m, 2H), 7.25 – 7.17 (m, 3H), 7.13 (d, *J* = 7.4 Hz, 2H), 3.98 (pd, *J* = 9.1, 3.9 Hz, 1H), 3.83 – 3.69 (m, 2H).

^{19}F NMR (376 MHz, $CDCl_3$) δ -70.02 (d, *J* = 9.1 Hz).

^{13}C NMR (101 MHz, $CDCl_3$) δ 139.07, 133.65, 131.10, 129.12, 129.08, 128.91, 128.77, 127.85, 126.80, 55.42, 45.86 (q, *J* = 28.7 Hz).

HRMS (ESI$^+$, *m*/*z*) [M+H$^+$] calcd. for $C_{15}H_{13}SO_2F_3$ 315.0661, found 315.0668.

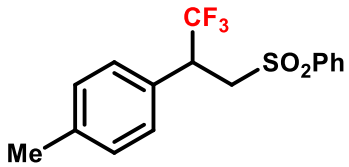

5

^{1}H NMR (400 MHz, $CDCl_3$) δ 7.65 – 7.58 (m, 1H), 7.57 – 7.46 (m, 1H), 7.41 – 7.29 (m, 1H), 7.03 – 6.98 (m, 2H), 3.93 (pt, *J* = 8.4, 4.1 Hz, 1H), 3.81 – 3.65 (m, 1H), 2.31 – 2.25 (m, 2H).

^{19}F NMR (376 MHz, $CDCl_3$) δ -70.16 (d, *J* = 9.1 Hz).

^{13}C NMR (101 MHz, $CDCl_3$) δ 139.16, 138.79, 133.45, 129.44, 129.01, 128.98, 128.06, 127.88, 124.07, 55.54, 45.44 (q, J = 28.6 Hz), 21.04.

HRMS (ESI$^+$, *m*/*z*) [M+H$^+$] calcd. for $C_{16}H_{15}SO_2F_3$ 329.0818, found 329.0827.

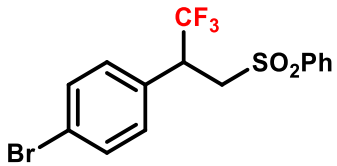

6

^{1}H NMR (400 MHz, $CDCl_3$) δ 7.62 – 7.52 (m, 3H), 7.45 – 7.36 (m, 2H), 7.35 – 7.29 (m, 2H), 7.00 (d, *J* = 8.4 Hz, 2H), 4.04 – 3.87 (m, 1H), 3.78 – 3.64 (m, 2H).

^{19}F NMR (376 MHz, $CDCl_3$) δ -70.04 (d, *J* = 9.0 Hz).

^{13}C NMR (101 MHz, $CDCl_3$) δ 138.99, 133.74, 131.97, 130.76, 130.03, 129.22, 127.81, 126.47, 123.34, 55.25, 45.40.

HRMS (ESI^+, *m/z*) [M+H^+] calcd. for $C_{15}H_{12}SO_2F_3Br$ 392.9766, found 392.9778. [M+Na^+] 414.9586, found 414.9603.

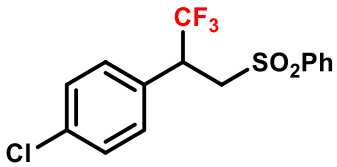

7

^{1}H NMR (400 MHz, $CDCl_3$) δ 7.67 – 7.50 (m, 1H), 7.45 – 7.33 (m, 1H), 7.22 – 7.13 (m, 1H), 7.07 (d, *J* = 8.4 Hz, 1H), 4.03 – 3.89 (m, 1H), 3.72 (d, *J* = 7.0 Hz, 1H).

^{19}F NMR (376 MHz, $CDCl_3$) δ -70.07 (d, *J* = 8.9 Hz).

^{13}C NMR (101 MHz, $CDCl_3$) δ 139.01, 135.17, 133.76, 130.47, 129.55, 129.20, 129.01, 127.82, 126.55, 55.31, 45.30.

HRMS (ESI^+, *m/z*) [M+H^+] calcd. for $C_{15}H_{12}SO_2F_3Cl$ 349.0271, found 349.0275. [M+Na^+] 371.0091, found 371.0099.

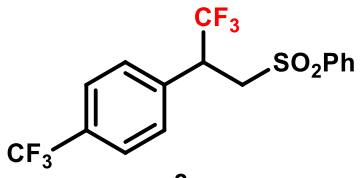

8

^{1}H NMR (400 MHz, $CDCl_3$) δ 7.60 – 7.55 (m, 2H), 7.55 – 7.49 (m, 1H), 7.45 (d, *J* = 8.2 Hz, 2H), 7.34 (dd, *J* = 10.8, 4.9 Hz, 2H), 7.27 (m, 2H), 4.07 (pd, *J* = 8.9, 4.9 Hz, 1H), 3.83 – 3.71 (m, 2H).

^{19}F NMR (376 MHz, $CDCl_3$) δ -63.05, -69.78 (d, *J* = 8.8 Hz).

^{13}C NMR (101 MHz, $CDCl_3$) δ 138.88, 134.96, 134.06, 133.91, 129.68, 129.22, 127.76, 125.73, 125.69, 123.65, 55.08, 45.75 (d, *J* = 28.8 Hz).

HRMS (ESI$^+$, *m*/*z*) [M+Na$^+$] calcd. for $C_{16}H_{12}SO_2F_6$ 405.0354, found 405.0351.

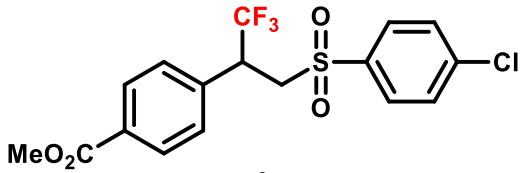

9

^{1}H NMR (400 MHz, $CDCl_3$) δ 7.93 – 7.86 (m, 2H), 7.56 – 7.48 (m, 2H), 7.35 – 7.29 (m, 2H), 7.22 (d, *J* = 8.2 Hz, 2H), 4.04 (pd, *J* = 8.8, 5.0 Hz, 1H), 3.93 (s, 3H), 3.80 – 3.69 (m, 2H).

^{19}F NMR (376 MHz, $CDCl_3$) δ -69.68 (d, *J* = 8.8 Hz).

^{13}C NMR (101 MHz, $CDCl_3$) δ 166.12, 140.90, 137.26, 135.70, 130.97, 130.01, 129.50, 129.32, 126.41, 126.13, 55.29, 52.32, 45.77 (d, *J* = 29.0 Hz).

HRMS (ESI$^+$, *m*/*z*) [M+H$^+$] calcd. for $C_{17}H_{14}SO_4F_3Cl$ 407.0326, found 407.0330.

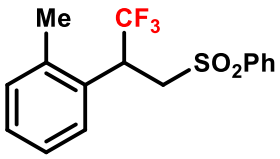

10

^{1}H NMR (400 MHz, $CDCl_3$) δ 7.60 – 7.52 (m, 2H), 7.51 – 7.44 (m, 1H), 7.36 – 7.28 (m, 2H), 7.11 (ddd, *J* = 11.3, 9.2, 4.5 Hz, 2H), 6.90 (dt, *J* = 7.9, 4.4 Hz, 2H), 4.40 (pd, *J* = 9.1, 3.5 Hz, 1H), 3.79 (qd, *J* = 14.7, 6.8 Hz, 2H), 2.45 (s, 3H).

^{19}F NMR (376 MHz, $CDCl_3$) δ -69.97 (d, *J* = 9.0 Hz).

^{13}C NMR (101 MHz, $CDCl_3$) δ 139.20, 138.15, 133.55, 130.82, 129.46, 129.00, 128.65, 127.54, 127.17, 127.05, 126.27, 55.69, 40.38 (d, *J* = 29.8 Hz), 19.84.

HRMS (ESI$^+$, *m*/*z*) [M+H$^+$] calcd. for $C_{16}H_{15}SO_2F_3$ 329.0818, found 329.0821.

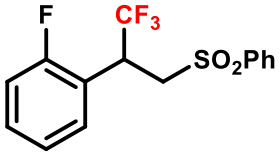

11

^{1}H NMR (400 MHz, $CDCl_3$) δ 7.68 (dt, *J* = 8.6, 1.6 Hz, 2H), 7.57 – 7.48 (m, 1H), 7.41 – 7.36 (m, 2H), 7.28 – 7.21 (m, 1H), 7.14 (t, *J* = 7.4 Hz, 1H), 7.04 – 6.98 (m, 1H), 6.97 – 6.88 (m, 1H), 4.36 – 4.25 (m, 1H), 3.87 (dd, *J* = 14.7, 10.9 Hz, 1H), 3.71 (dd, *J* = 14.7, 2.6 Hz, 1H).

^{19}F NMR (376 MHz, $CDCl_3$) δ -70.04 (dd, *J* = 8.9, 6.0 Hz), -115.26.

^{13}C NMR (101 MHz, $CDCl_3$) δ 162.31, 159.83, 138.56, 133.89, 130.91/130.83, 129.95, 129.18, 127.94, 124.49/ 124.45, 118.48/118.36, 116.13/115.91, 54.11, 39.19 (q, *J* = 30.0 Hz).

HRMS (ESI^+, *m*/*z*) [M+H^+] calcd. for $C_{15}H_{12}SO_2F_4$ 333.0567, found 333.0572.

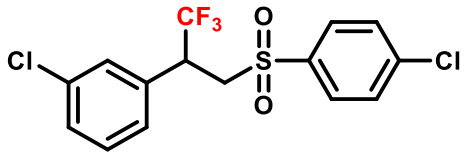

12

^{1}H NMR (400 MHz, $CDCl_3$) δ 7.54 – 7.46 (m, 2H), 7.38 – 7.31 (m, 2H), 7.26 (ddd, *J* = 8.0, 1.9, 1.1 Hz, 1H), 7.17 (t, *J* = 7.8 Hz, 2H), 7.09 – 6.97 (m, 2H), 4.00 – 3.87 (m, 1H), 3.80 – 3.66 (m, 2H).

^{19}F NMR (376 MHz, $CDCl_3$) δ -69.93 (d, *J* = 8.8 Hz).

^{13}C NMR (101 MHz, $CDCl_3$) δ 140.89, 137.21, 134.87, 132.62, 130.14, 129.43, 129.22, 127.59, 126.38, 123.59, 55.13, 45.67 (q, *J* = 29.0 Hz).

HRMS (ESI^+, *m*/*z*) [M+Na^+] calcd. for $C_{15}H_{11}SO_2F_3Cl_2$ 404.9701, found 404.9704.

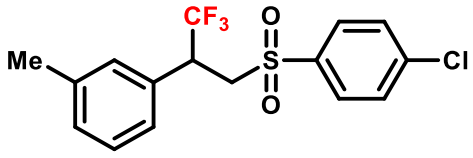

13

^{1}H NMR (400 MHz, $CDCl_3$) δ 7.49 – 7.38 (m, 2H), 7.25 (dt, *J* = 4.4, 1.9 Hz, 2H), 7.12 – 7.03 (m, 2H), 6.92 (d, *J* = 7.2 Hz, 1H), 6.76 (s, 1H), 3.98 – 3.84 (m, 1H), 3.82 – 3.70 (m, 2H), 2.21 (s, 3H).

^{19}F NMR (376 MHz, $CDCl_3$) δ -70.07 (d, *J* = 8.9 Hz).

^{13}C NMR (101 MHz, $CDCl_3$) δ 140.36, 138.57, 137.44, 130.47, 130.25, 129.66, 129.60, 129.26, 129.11, 128.76, 126.51, 55.38, 45.98 (dd, *J* = 57.6, 28.9 Hz), 21.10.

HRMS (ESI$^+$, *m*/*z*) [M+Na$^+$] calcd. for $C_{16}H_{14}SO_2F_3Cl$ 385.0247, found 385.0253.

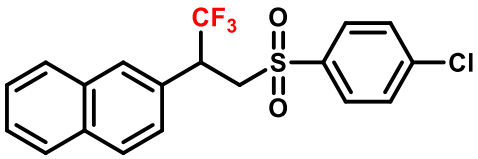

14

^{1}H NMR (400 MHz, $CDCl_3$) δ 7.82 – 7.76 (m, 1H), 7.67 (ddd, *J* = 19.1, 9.4, 6.0 Hz, 2H), 7.57 – 7.47 (m, 3H), 7.39 – 7.32 (m, 2H), 7.14 (d, *J* = 7.9 Hz, 1H), 7.00 – 6.89 (m, 2H), 4.20 – 4.05 (m, 1H), 3.86 (ddd, *J* = 17.9, 14.8, 6.9 Hz, 2H).

^{19}F NMR (376 MHz, $CDCl_3$) δ -69.75 (d, *J* = 8.9 Hz).

^{13}C NMR (101 MHz, $CDCl_3$) δ 140.35, 137.35, 133.18, 132.81, 129.69, 129.48, 129.19, 129.10, 128.95, 128.80, 127.71, 127.55, 127.09, 126.89, 125.51, 55.46, 46.24.

HRMS (ESI$^+$, *m*/*z*) [M+H$^+$] calcd. for $C_{19}H_{14}SO_2F_3Cl$ 399.0428, found 399.0427. [M+Na$^+$] 421.0247, found 421.0248.

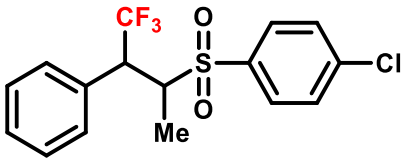

15

^{1}H NMR (400 MHz, $CDCl_3$) δ 7.35 – 7.30 (m, 2H), 7.18 (m, 6H), 4.19 (d, *J* = 9.8 Hz, 1H), 3.51 – 3.34 (m, 1H), 1.79 (d, *J* = 7.0 Hz, 3H).

^{19}F NMR (376 MHz, $CDCl_3$) δ -68.40 (d, *J* = 8.0 Hz).

^{13}C NMR (101 MHz, $CDCl_3$) δ 140.16, 136.74, 132.67, 130.08, 129.73, 129.02, 128.71, 128.61, 71.43, 40.82 (dd, *J* = 52.3, 26.1 Hz), 30.89, 12.84.

HRMS (ESI^+, *m*/*z*) [M+Na^+] calcd. for $C_{16}H_{14}SO_2F_3Cl$ 385.0247, found 385.0252.

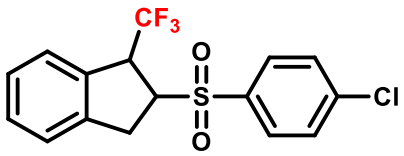

16

^{1}H NMR (400 MHz, $CDCl_3$) δ 7.84 – 7.80 (m, 2H), 7.54 – 7.48 (m, 2H), 7.35 – 7.17 (m, 4H), 4.32 (qd, *J* = 9.0, 2.4 Hz, 1H), 4.06 – 4.01 (m, 1H), 3.57 – 3.43 (m, 2H).

^{19}F NMR (376 MHz, $CDCl_3$) δ -70.74 (d, *J* = 9.1 Hz).

^{13}C NMR (101 MHz, $CDCl_3$) δ 141.19, 141.06, 135.24, 133.52, 130.29, 129.71, 129.56, 127.70, 125.84, 124.68, 63.55, 50.96 (q, *J* = 29.5 Hz), 33.20, 29.69.

HRMS (ESI^+, *m*/*z*) [M+H^+] calcd. for $C_{16}H_{12}SO_2F_3Cl$ 361.0271, found 361.0278.

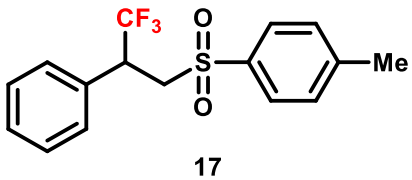

17

^{1}H NMR (400 MHz, $CDCl_3$) δ 7.53 – 7.43 (m, 2H), 7.29 – 7.18 (m, 3H), 7.13 (dd, *J* = 7.6, 4.2 Hz, 4H), 3.94 (pd, *J* = 9.1, 4.2 Hz, 1H), 3.80 – 3.65 (m, 2H), 2.37 (s, 3H).

^{19}F NMR (376 MHz, $CDCl_3$) δ -70.03 (d, *J* = 9.0 Hz).

^{13}C NMR (101 MHz, $CDCl_3$) δ 150.45, 144.76, 136.04, 131.31, 130.00, 129.70, 129.14, 128.71, 127.91, 55.48, 45.85, 21.53.

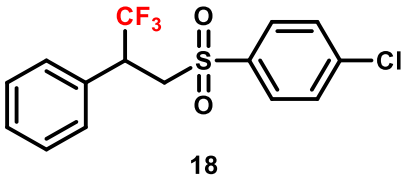

18

^{1}H NMR (400 MHz, $CDCl_3$) δ 7.52 – 7.42 (m, 2H), 7.32 – 7.24 (m, 3H), 7.20 (dd, *J* = 10.3, 4.8 Hz, 2H), 7.10 (d, *J* = 7.6 Hz, 2H), 3.96 (pd, *J* = 9.1, 4.5 Hz, 1H), 3.84 – 3.68 (m, 2H).

^{19}F NMR (376 MHz, $CDCl_3$) δ -70.05 (d, *J* = 9.1 Hz).

^{13}C NMR (101 MHz, $CDCl_3$) δ 140.50, 137.44, 130.81, 129.31, 129.16, 128.97, 128.85, 126.69, 123.90, 55.50, 45.98 (q, *J* = 28.6 Hz).

HRMS (ESI^{+}, *m*/*z*) [M+Na^{+}] calcd. for $C_{15}H_{12}SO_2F_3Cl$ 371.0091, found 371.0097.

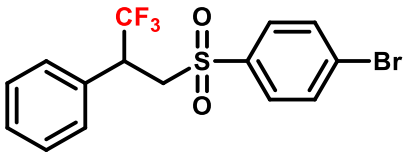

19

^{1}H NMR (400 MHz, $CDCl_3$) δ 7.46 – 7.36 (m, 4H), 7.31 – 7.26 (m, 1H), 7.23 – 7.17 (m, 2H), 7.09 (d, *J* = 7.6 Hz, 2H), 3.95 (pt, *J* = 8.0, 3.9 Hz, 1H), 3.82 – 3.68 (m, 2H).

^{19}F NMR (376 MHz, $CDCl_3$) δ -70.05 (d, *J* = 9.0 Hz).

^{13}C NMR (101 MHz, $CDCl_3$) δ 137.95, 132.32, 130.78, 129.34, 129.16, 129.10, 128.95, 128.87, 126.68, 55.49, 45.97 (q, *J* = 28.7 Hz).

HRMS (ESI^+, *m*/*z*) [$M+H^+$] calcd. for $C_{15}H_{12}SO_2F_3Br$ 392.9766, found 392.9759. [$M+Na^+$] 414.9586, found 414.9589.

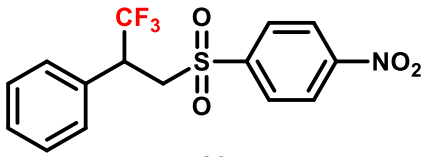

20

^{1}H NMR (400 MHz, $CDCl_3$) δ 8.12 – 8.07 (m, 2H), 7.71 – 7.66 (m, 2H), 7.24 (dt, *J* = 2.6, 1.7 Hz, 1H), 7.18 – 7.13 (m, 2H), 7.08 (d, *J* = 7.6 Hz, 2H), 4.07 – 3.94 (m, 1H), 3.90 – 3.77 (m, 2H).

^{19}F NMR (376 MHz, $CDCl_3$) δ -70.02 (d, *J* = 8.8 Hz).

^{13}C NMR (101 MHz, $CDCl_3$) δ 150.47, 144.52, 130.43, 130.41, 129.31, 129.26, 128.92, 126.52, 123.98, 55.56, 46.05 (q, *J* = 29.0 Hz).

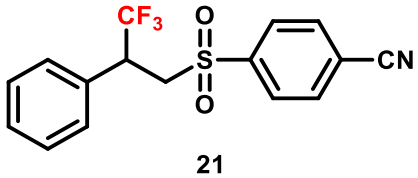

21

^{1}H NMR (400 MHz, $CDCl_3$) δ 7.65 – 7.52 (m, 4H), 7.30 – 7.23 (m, 1H), 7.21 – 7.14 (m, 2H), 7.07 (d, *J* = 7.6 Hz, 2H), 3.99 (pd, *J* = 8.9, 4.8 Hz, 1H), 3.89 – 3.75 (m, 2H).

^{19}F NMR (376 MHz, $CDCl_3$) δ -70.03 (d, *J* = 8.8 Hz).

^{13}C NMR (101 MHz, $CDCl_3$) δ 143.10, 132.59, 130.44, 129.24, 129.21, 128.93, 128.53, 126.54, 123.75, 117.30, 116.84, 55.45, 46.02 (q, *J* = 28.9 Hz).

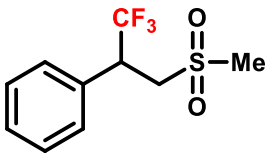

22

^{1}H NMR (400 MHz, $CDCl_3$) δ 7.47 – 7.38 (m, 5H), 4.13 – 3.93 (m, 1H), 3.69 – 3.53 (m, 2H), 2.36 (s, 3H).

^{19}F NMR (376 MHz, $CDCl_3$) δ -69.61 (d, *J* = 9.0 Hz).

^{13}C NMR (101 MHz, $CDCl_3$) δ 129.62, 129.49, 129.30, 129.20, 127.14, 54.94, 46.13 (d, *J* = 28.9 Hz), 42.27.

HRMS (ESI^+, *m*/*z*) [M+Na^+] calcd. for $C_{10}H_{11}SO_2F_3$ 275.0324, found 275.0326.

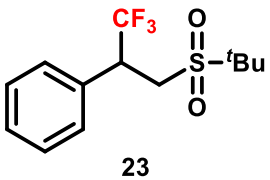

23

^{1}H NMR (400 MHz, $CDCl_3$) δ 7.43 – 7.34 (m, 5H), 4.12 (pd, *J* = 9.4, 3.1 Hz, 1H), 3.51 (qd, *J* = 13.6, 6.4 Hz, 2H), 1.38 (s, 9H).

^{19}F NMR (376 MHz, $CDCl_3$) δ -69.53 (d, *J* = 9.3 Hz).

^{13}C NMR (101 MHz, $CDCl_3$) δ 132.64, 129.08, 129.00, 128.91, 124.49, 60.03, 45.61, 44.14, 23.24.

HRMS (ESI^+, *m*/*z*) [M+Na^+] calcd. for $C_{13}H_{17}SO_2F_3$ 317.0794, found 317.0793.

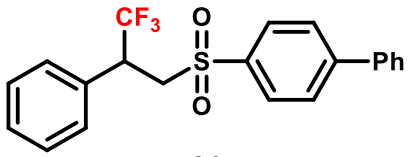

24

^{1}H NMR (400 MHz, $CDCl_3$) δ 7.66 – 7.62 (m, 2H), 7.58 – 7.45 (m, 7H), 7.27 – 7.13 (m, 5H), 4.02 (pd, *J* = 9.1, 3.4 Hz, 1H), 3.82 (qd, *J* = 14.7, 6.7 Hz, 2H).

^{19}F NMR (376 MHz, $CDCl_3$) δ -70.03 (d, *J* = 9.0 Hz).

^{13}C NMR (101 MHz, $CDCl_3$) δ 146.63, 139.09, 137.40, 131.09, 129.20, 129.11, 128.77, 128.75, 128.73, 128.38, 127.67, 127.31, 126.80, 55.48, 45.98 (q, *J* = 28.7 Hz).

HRMS (ESI^+, *m*/*z*) [M+H^+] calcd. for $C_{21}H_{17}SO_2F_3$ 391.0974, found 391.0980.

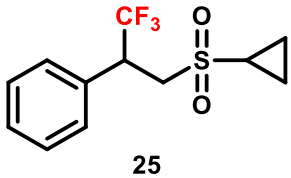

25

^{1}H NMR (400 MHz, $CDCl_3$) δ 7.45 – 7.36 (m, 5H), 4.12 – 3.95 (m, 1H), 3.65 (ddd, *J* = 17.6, 14.7, 6.8 Hz, 2H), 1.71 – 1.58 (m, 1H), 1.20 – 1.11 (m, 1H), 1.08 – 0.97 (m, 1H), 0.82 – 0.63 (m, 2H).

^{19}F NMR (376 MHz, $CDCl_3$) δ -69.77 (d, *J* = 9.0 Hz).

^{13}C NMR (101 MHz, $CDCl_3$) δ 132.16, 129.37, 129.32, 129.15, 126.95, 53.79, 45.79, 30.95, 5.51, 5.33.

HRMS (ESI^+, *m*/*z*) [M+H^+] calcd. for $C_{12}H_{13}SO_2F_3$ 301.0481, found 301.0485.

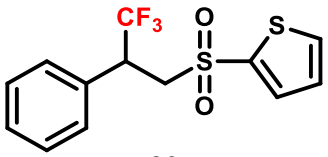

26

^{1}H NMR (400 MHz, $CDCl_3$) δ 7.57 (dd, *J* = 5.0, 1.3 Hz, 1H), 7.33 – 7.16 (m, 6H), 6.91 (dd, *J* = 4.9, 3.8 Hz, 1H), 4.08 – 3.93 (m, 1H), 3.93 – 3.79 (m, 2H).

^{19}F NMR (376 MHz, $CDCl_3$) δ -70.00 (d, *J* = 8.9 Hz).

^{13}C NMR (101 MHz, $CDCl_3$) δ 139.88, 134.71, 134.49, 131.22, 129.07, 128.97, 128.84, 127.78, 126.75, 56.8, 46.11 (q, *J* = 28.6 Hz).

HRMS (ESI$^+$, *m*/*z*) [M+H$^+$] calcd. for $C_{13}H_{11}S_2O_2F_3$ 321.0225, found 321.0231. [M+Na$^+$] 343.0045, found 343.0053.

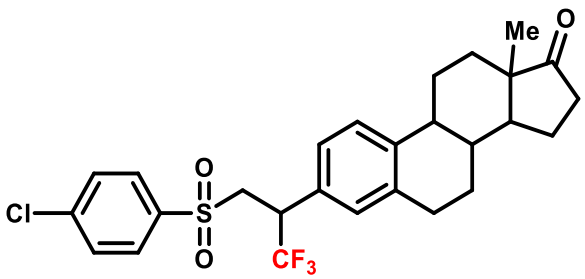

27

^{1}H NMR (400 MHz, $CDCl_3$) δ 7.44 – 7.37 (m, 2H), 7.23 – 7.18 (m, 2H), 7.09 (2d, *J* = 8.1 Hz, 1H), 6.88 (2d, *J* = 8.1 Hz, 1H), 6.62 (2s, 1H), 3.95 – 3.83 (m, 1H), 3.80 – 3.66 (m, 2H), 2.82 – 2.46 (m, 3H), 2.43 – 2.30 (m, 1H), 2.25 – 1.93 (m, 5H), 1.70 – 1.33 (m, 6H), 0.95 (2s, 3H).

^{19}F NMR (376 MHz, $CDCl_3$) δ -70.12 (d, *J* = 8.8 Hz), -70.17 (d, *J* = 8.8 Hz).

^{13}C NMR (101 MHz, $CDCl_3$) δ 220.38, 140.92/140.87, 139.96/139.90, 137.66/137.63, 136.91/136.89, 129.72, 129.31/129.29, 129.06, 128.86, 127.67/127.56, 127.21, 126.55, 125.83/125.81, 55.29/55.15, 53.40, 50.53/50.52,

47.94/47.89, 45.74 (q, *J* = 28.8 Hz), 44.30/44.24, 37.99/37.97, 35.80, 31.58/31.56, 29.20/29.18, 26.24, 25.74/25.58, 21.56, 14.01/13.90.

HRMS (ESI$^+$, *m*/*z*) [M+H$^+$] calcd. for $C_{27}H_{28}SO_4F_3Cl$ 525.1473, found 525.1482.

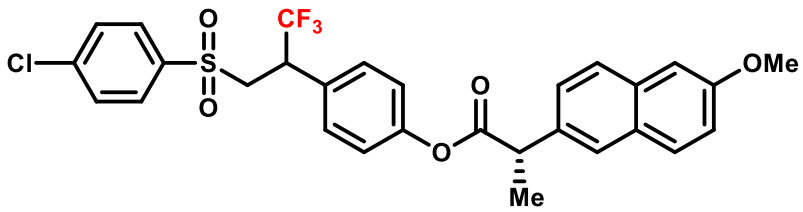

28

^{1}H NMR (400 MHz, $CDCl_3$) δ 7.81 – 7.69 (m, 3H), 7.49 (dt, *J* = 8.6, 1.6 Hz, 1H), 7.44 – 7.37 (m, 2H), 7.33 – 7.26 (m, 2H), 7.20 – 7.12 (m, 2H), 7.03 (d, *J* = 8.6 Hz, 2H), 6.87 – 6.79 (m, 2H), 4.16 – 4.04 (m, 1H), 4.00 – 3.86 (m, 4H), 3.76 – 3.61 (m, 2H), 1.71 (d, *J* = 7.1 Hz, 3H).

^{19}F NMR (376 MHz, $CDCl_3$) δ -70.13 (d, *J* = 8.8 Hz).

^{13}C NMR (101 MHz, $CDCl_3$) δ 172.59, 157.86, 151.40, 140.63, 137.34, 134.86, 134.81, 133.91, 130.09, 129.52, 129.32, 129.15, 129.02, 128.05, 127.43, 126.17, 126.06, 126.04, 121.87, 119.18, 105.68, 55.56, 55.35, 45.56, 18.36.

HRMS (ESI$^+$, *m*/*z*) [M+H$^+$] calcd. for $C_{29}H_{24}SO_5F_3Cl$ 577.1058, found 577.1053.

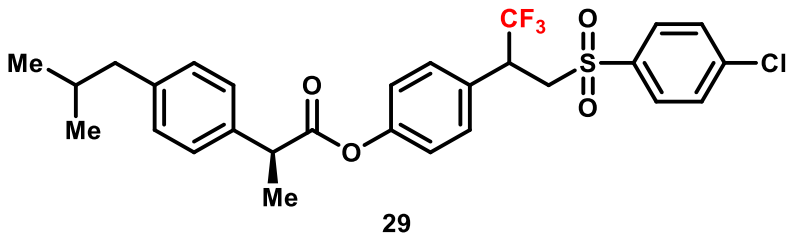

29

^{1}H NMR (400 MHz, $CDCl_3$) δ 7.48 – 7.38 (m, 2H), 7.30 (ddd, *J* = 6.9, 4.6, 1.7 Hz, 4H), 7.15 (d, *J* = 7.9 Hz, 2H), 7.04 (d, *J* = 8.5 Hz, 2H), 6.85 (d, *J* = 8.5 Hz, 2H), 4.02 – 3.87 (m, 2H), 3.76 – 3.65 (m, 2H), 2.48 (d, *J* = 7.2 Hz, 2H), 1.87 (dp, *J* = 13.5, 6.7 Hz, 1H), 1.62 (d, *J* = 7.2 Hz, 3H), 0.92 (d, *J* = 6.6 Hz, 6H).

^{19}F NMR (376 MHz, $CDCl_3$) δ -70.13 (dd, *J* = 8.9, 4.9 Hz).

^{13}C NMR (101 MHz, $CDCl_3$) δ 172.63, 151.44, 140.96, 140.64, 138.40, 137.37, 137.35, 136.97, 136.93, 130.08, 129.54, 129.15, 127.97, 127.20, 121.87, 55.59, 45.26, 45.06, 30.18, 22.38, 18.39.

HRMS (ESI$^+$, *m*/*z*) [M+H$^+$] calcd. for $C_{28}H_{28}SO_4F_3Cl$ 553.1422, found 553.1413.

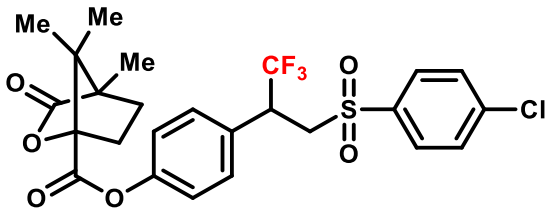

30

^{1}H NMR (400 MHz, $CDCl_3$) δ 7.47 (d, *J* = 8.7 Hz, 2H), 7.34 (dd, *J* = 8.5, 1.4 Hz, 2H), 7.14 (d, *J* = 8.5 Hz, 2H), 7.00 (d, *J* = 8.6 Hz, 2H), 4.07 – 3.92 (m, 1H), 3.75 (m, 2H), 2.63 – 2.50 (m, 1H), 2.20 (dddd, *J* = 13.6, 9.3, 4.5, 2.2 Hz, 1H), 2.06 – 1.94 (m, 1H), 1.78 (ddd, *J* = 13.4, 9.3, 4.2 Hz, 1H), 1.17 (d, *J* = 5.7 Hz, 6H), 1.11 (s, 3H).

^{19}F NMR (376 MHz, $CDCl_3$) δ -70.06 (d, *J* = 8.8 Hz).

^{13}C NMR (101 MHz, $CDCl_3$) δ 177.68, 165.67/165.64, 150.46, 140.65, 137.43, 137.40, 130.41, 129.58, 129.21, 128.93, 121.79, 90.70, 55.50, 54.92, 54.72, 45.89, 45.60, 45.31, 45.02, 30.82/30.78, 28.96, 16.89/16.86, 9.72.

HRMS (ESI$^+$, *m*/*z*) [M+H$^+$] calcd. for $C_{25}H_{24}SO_6F_3Cl$ 545.1007, found 545.1004.

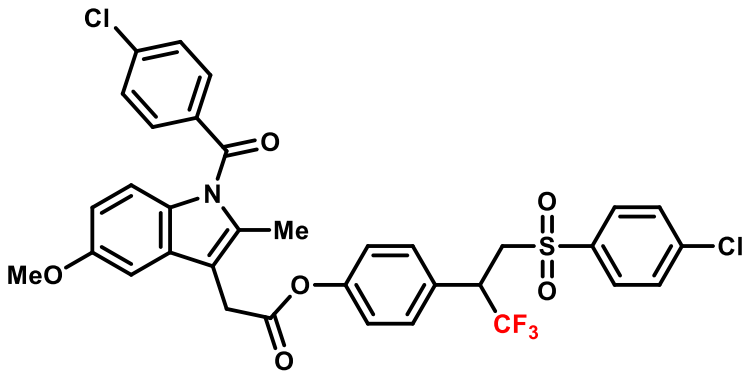

31

^{1}H NMR (400 MHz, $CDCl_3$) δ 7.73 – 7.65 (m, 2H), 7.51 – 7.41 (m, 4H), 7.33 – 7.28 (m, 2H), 7.07 (dd, *J* = 12.2, 5.5 Hz, 3H), 6.96 – 6.84 (m, 3H), 6.71 (dd, *J* = 9.0, 2.5 Hz, 1H), 3.96 (ddd, *J* = 15.8, 7.8, 4.5 Hz, 1H), 3.91 (s, 2H), 3.85 (s, 3H), 3.71 (m, 2H), 2.47 (s, 3H).

^{19}F NMR (376 MHz, $CDCl_3$) δ -70.08 (d, *J* = 8.9 Hz).

^{13}C NMR (101 MHz, $CDCl_3$) δ 168.67, 168.30, 156.19, 151.22, 140.64, 139.44, 137.38, 136.35, 133.81, 131.21, 130.91, 130.46, 130.20, 129.55, 129.19, 128.37, 121.89, 115.04, 111.72, 101.39, 55.78, 55.55, 45.40 (d, *J* = 29.0 Hz), 30.52, 13.38.

HRMS (ESI$^+$, *m*/*z*) [M+H$^+$] calcd. for $C_{34}H_{26}NSO_6F_3Cl_2$ 704.0883, found 704.0882.

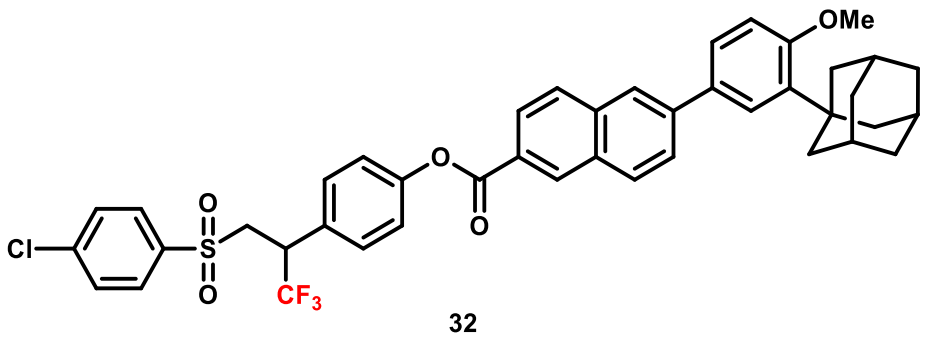

32

^{1}H NMR (400 MHz, $CDCl_3$) δ 8.79 (d, *J* = 10.8 Hz, 1H), 8.19 (dd, *J* = 8.6, 1.7 Hz, 1H), 8.02 (dd, *J* = 20.9, 9.2 Hz, 3H), 7.85 (dd, *J* = 8.5, 1.7 Hz, 1H), 7.63 (d, *J* = 2.3 Hz, 1H), 7.57 (dd, *J* = 8.4, 2.3 Hz, 1H), 7.53 – 7.49 (m, 2H), 7.43 – 7.38 (m, 2H), 7.21 – 7.13 (m, 4H), 7.02 (d, *J* = 8.5 Hz, 1H), 4.10 – 3.98 (m, 1H), 3.92 (s, 3H), 3.79 (d, *J* = 6.9 Hz, 2H), 2.20 (d, *J* = 2.4 Hz, 6H), 2.12 (s, 3H), 1.82 (s, 6H).

^{19}F NMR (376 MHz, $CDCl_3$) δ -70.01 (d, *J* = 8.9 Hz).

^{13}C NMR (101 MHz, $CDCl_3$) δ 164.80, 159.09, 152.14, 151.71, 141.99, 140.74, 139.13, 137.45, 136.39, 132.40, 131.83, 131.24, 130.31, 129.86, 129.63, 129.27, 128.57, 126.78, 126.01, 125.86, 125.78, 125.71, 124.78, 122.31, 112.19, 55.19, 40.66, 37.26, 37.15, 29.70, 29.14.

HRMS (ESI$^+$, *m*/*z*) [M+Na$^+$] calcd. for $C_{43}H_{38}SO_5F_3Cl$ 781.1973, found 781.1963.

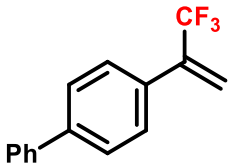

33

^{1}H NMR (400 MHz, $CDCl_3$) δ 7.61 – 7.55 (m, 4H), 7.52 (d, *J* = 8.2 Hz, 2H), 7.43 (t, *J* = 7.5 Hz, 2H), 7.34 (t, *J* = 7.3 Hz, 1H), 5.95 (d, *J* = 1.1 Hz, 1H), 5.79 (d, *J* = 1.6 Hz, 1H).

^{19}F NMR (376 MHz, $CDCl_3$) δ -64.78.

^{13}C NMR (101 MHz, $CDCl_3$) δ 141.90, 140.30, 138.67 (q, *J* = 30.0 Hz), 132.51, 128.91, 127.78, 127.73, 127.30, 127.11, 123.46 (q, *J* = 274.1 Hz), 120.20 (q, *J* = 5.8 Hz).

GCMS (EI, *m*/*z*) [M$^+$] calcd. for $C_{15}H_{11}F_3$ 248.0807, found 248.0804.

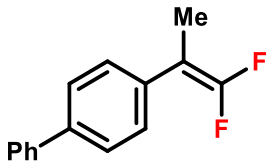

34

^{1}H NMR (400 MHz, $CDCl_3$) δ 7.64 – 7.57 (m, 4H), 7.48 – 7.40 (m, 4H), 7.40 – 7.30 (m, 1H), 2.02 (t, *J* = 3.4 Hz, 3H).

^{19}F NMR (376 MHz, $CDCl_3$) δ -89.82 (dq, *J* = 42.9, 3.3 Hz), 90.20 (dq, *J* = 42.8, 3.3 Hz).

^{13}C NMR (101 MHz, $CDCl_3$) δ 153.59 (dd, *J* = 290.7, 286.3 Hz), 140.60, 139.88, 133.84 (t, *J* = 4.2 Hz), 128.81, 127.83 (dd, *J* = 4.7, 3.4 Hz), 127.38, 127.04, 127.01, 87.23 (dd, *J* = 22.6, 14.1 Hz), 13.15 (t, *J* = 1.8 Hz).

GCMS (EI, *m*/*z*) [M^+] calcd. for $C_{15}H_{12}F_2$ 230.0902, found 230.0899.

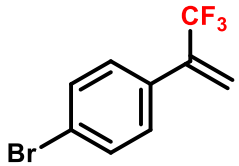

35

^{1}H NMR (400 MHz, $CDCl_3$) δ 7.56 – 7.50 (m, 2H), 7.32 (d, *J* = 8.4 Hz, 2H), 5.98 (q, *J* = 1.3 Hz, 1H), 5.78 (q, *J* = 1.6 Hz, 1H).

^{19}F NMR (376 MHz, $CDCl_3$) δ -64.95 (s).

^{13}C NMR (101 MHz, $CDCl_3$) δ 138.28 (q, *J* = 30.5 Hz), 132.67, 131.95, 129.16, 123.54, 122.04 (q, *J* = 273.9 Hz), 121.03 (q, *J* = 5.7 Hz).

GCMS (EI, *m*/*z*) [M^+] calcd. for $C_9H_6F_3Br$ 251.9579, found 251.9577.

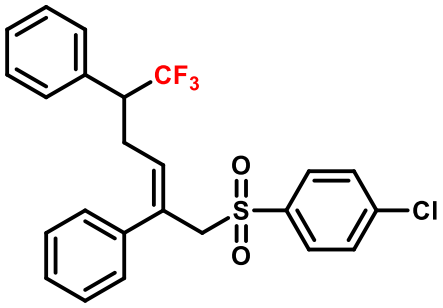

40

^{1}H NMR (400 MHz, $CDCl_3$) δ 7.59 (dd, *J* = 8.9, 2.1 Hz, 2H), 7.37 (m, 4H), 7.31 – 7.27 (m, 4H), 7.15 – 7.11 (m, 2H), 6.95 – 6.88 (m, 2H), 5.78 (t, *J* = 7.4 Hz, 1H), 4.26 (s, 2H), 3.49 – 3.37 (m, 1H), 2.98 – 2.88 (m, 1H), 2.84 – 2.73 (m, 1H).

^{19}F NMR (376 MHz, $CDCl_3$) δ -69.30 (d, *J* = 9.2 Hz).

^{13}C NMR (101 MHz, $CDCl_3$) δ 140.48, 140.17, 137.35, 133.53, 130.29, 129.85, 129.18, 128.98, 128.92, 128.86, 128.48, 128.36, 128.20, 127.55, 126.37, 57.90, 49.77, 29.23.

HRMS (ESI^+, *m*/*z*) [$M+H^+$] calcd. for $C_{24}H_{20}SO_2F_3Cl$ 465.0897, found 465.0911.

4.6 References

1. (a) Godula, K.; Sames, D. C—H Bond Functionalization in Complex Organic Synthesis. *Science*, **2006**, *312*, 67–72. (b) Davies, H. M. L.; Bois, J. D.; Yu, J.-Q. C–H Functionalization in organic synthesis. *Chem. Soc. Rev.* **2011**, *40*, 1855–1856. (c) Davies, H. M. L.; Morton, D. Recent Advances in C–H Functionalization. *J. Org. Chem.* **2016**, *81*, 343–350.
2. (a) Allen, A. E.; MacMillan, D. W. C. The Productive Merger of Iodonium Salts and Organocatalysis: A Non-photolytic Approach to the Enantioselective α-Trifluoromethylation of Aldehydes. *J. Am. Chem. Soc.* **2010**, *132*, 4986–4987. (b) Nagib, D. A.; MacMillan, D. W. C. Trifluoromethylation of arenes and heteroarenes by means of photoredox catalysis. *Nature* **2011**, *480*, 224–228. (c) Kautzky, J. A.; Wang, T.; Evans, R. W.; MacMillan, D. W. C. Decarboxylative Trifluoromethylation of Aliphatic Carboxylic Acids. *J. Am. Chem. Soc.* **2018**, *140*, 6522–6526. (d) Kornfilt, D. J. P.; MacMillan, D. W. C. Copper-Catalyzed Trifluoromethylation of Alkyl Bromides. *J. Am. Chem. Soc.* **2019**, *141*, 6853−6858. (e) Sarver, P. J.; Bacauanu, V.; Schultz, D. M.; DiRocco, D. A.; Lam, Y.-h.; Sherer, E. C.; MacMillan, D. W. C. The merger of decatungstate and copper catalysis to enable aliphatic C(sp^3)–H trifluoromethylation. *Nat. Chem.* **2020**, *12*, 459–467.
3. (a) Shen, H.; Liu, Z.; Zhang, P.; Tan, X.; Zhang, Z.; Li, C. Trifluoromethylation of Alkyl Radicals in Aqueous Solution. *J. Am. Chem. Soc.* **2017**, *139*, 9843–9846. (b) Tan, X.; Liu, Z.; Shen, H.; Zhang, P.; Zhang, Z.; Li, C. Silver-Catalyzed Decarboxylative Trifluoromethylation of Aliphatic Carboxylic Acids. *J. Am. Chem. Soc.* **2017**, *139*, 12430–12433. (c) Xiao, H.; Liu, Z.; Shen, H.; Zhang, B.; Zhu, L.; Li, C. Copper-Catalyzed Late-Stage Benzylic C(sp^3)–H Trifluoromethylation. *Chem* **2019**, *5*, 940–949. (d) Xiao, H.; Shen, H.; Zhu, L.; Li, C. Copper-Catalyzed Radical Aminotrifluoromethylation of Alkenes. *J. Am. Chem. Soc.* **2019**, *141*, 11440–11445. (e) Zhang, Z.; Zhu, L.; Li, C. Copper-Catalyzed Carbotrifluoromethylation of Unactivated Alkenes Driven by Trifluoromethylation of Alkyl Radicals. *Chin. J. Chem.* **2019**, *37*, 452–456. (f) Zhu, L.; Fang, Y.; Li, C. Trifluoromethylation of Alkyl Radicals: Breakthrough and Challenges. *Chin. J. Chem.* **2020**, *38*, 787–789.

4. (a) Jiang, C.; Wang, L.; Zhang, H.; Chen, P.; Guo, Y.-L. Liu, G. Enantioselective Copper-Catalyzed Trifluoromethylation of Benzylic Radicals via Ring Opening of Cyclopropanols. *Chem* **2020**, *6*, 2407–2419. (b) Xu, P.; Fan, W.; Chen, P.; Liu, G. Enantioselective Radical Trifluoromethylation of Benzylic C–H Bonds via Cooperative Photoredox and Copper Catalysis. *J. Am. Chem. Soc.* **2022**, *144*, 13468–13474. (c) Fu, L.; Chen, X.; Fan, W.; Chen, P.; Liu, G. Copper-Catalyzed Asymmetric Functionalization of Vinyl Radicals for the Access to Vinylarene Atropisomers. *J. Am. Chem. Soc.* **2023**, *145*, 13476–13483.
5. (a) Guo, S.; AbuSalim, D. I.; Cook, S. P. Aqueous Benzylic C–H Trifluoromethylation for Late-Stage Functionalization. *J. Am. Chem. Soc.* **2018**, *140*, 12378–12382. (b) Guo, S.; AbuSalim, D. I.; Cook, S. P. 1,2-(Bis)trifluoromethylation of Alkynes:A One-Step Reaction to Install an Underutilized Functional Group. *Angew. Chem. Int. Ed.* **2019**, *58*, 11704–11708. (c) Choi, G.; Lee, G. S.; Park, B.; Kim, D.; Hong, S. H. Direct C(sp^3)–H Trifluoromethylation of Unactivated Alkanes Enabled by Multifunctional Trifluoromethyl Copper Complexes. *Angew. Chem. Int. Ed.* **2021**, *60*, 5467–5474. (d) Li, X.; Shui, Y.; Shen, P.; Wang, Y.-P.; Zhang, C.; Feng, C. A novel type of radical-addition-induced b-fragmentation and ensuing remote functionalization. *Chem* **2022**, *8*, 2245–2259.
6. (a) Wang, Q.; Ni, C.; Hu, M.; Xie, Q.; Liu, Q.; Pan, S.; Hu, J. From C1 to C3: Copper-Catalyzed gem-Bis(trifluoromethyl)olefination of α-Diazo Esters with $TMSCF_3$. *Angew. Chem. Int. Ed.* **2020**, *59*, 8507—8511. (b) Wang, Q.; Tao, Q.; Dong, H.; Ni, C.; Xie, X.; Hu, J. Fluorination Triggers Fluoroalkylation: Nucleophilic Perfluoro-tertbutylation with 1,1-Dibromo-2,2-bis(trifluoromethyl)ethylene (DBBF) and CsF. *Angew. Chem. Int. Ed.* **2021**, *60*, 27318–27323. (c) Wei, Z.; Wen, L.; Zhu, K.; Wang, Q.; Zhao, Y.; Hu, J. Regioselective Aromatic Perfluoro-tert-butylation Using Perfluoro-tert-butyl Phenyl Sulfone and Arynes. *J. Am. Chem. Soc.* **2022**, *144*, 22281–22288.
7. (a) Meyer, A. U.; Straková, K.; Slanina, T.; König, B. Eosin Y (EY) Photoredox-Catalyzed Sulfonylation of Alkenes: Scopeand Mechanism. *Chem. Eur. J.* **2016**, *22*, 8694–8699. (b) He, J.; Chen, G.; Zhang, B.; Li, Y.; Chen, J.-R.; Xiao, W.-J.; Liu, F.; Li, C. Catalytic Decarboxylative Radical Sulfonylation. *Chem* **2020**, *6*, 1149–1159. (c)

Ueda, M.; Kamikawa, K.; Fukuyama, T.;Wang, Y.-T.; Wu, Y.-K.; Ryu, I. Site-Selective Alkenylation of Unactivated C(sp^3)−H Bonds Mediated by Compact Sulfate Radical. *Angew. Chem.* **2021**, *133*, 3587–3592. (d) Du, X.; Cheng-Sánchez, I.; Nevado, C. Dual Nickel/Photoredox-Catalyzed Asymmetric Carbosulfonylation of Alkenes. *J. Am. Chem. Soc*. **2023**, *145*, 12532–12540. (e) Lasso, J. D.; Castillo-Pazos, D. J.; Sim, M.; Flores, J. B.; Li, C.-J. EDA mediated S–N bond coupling of nitroarenes and sodium sulfinate salts. *Chem. Sci.* **2023**, *14*, 525–532. (f) Liu, X.; Chen, H.; Yang, D.; Hu, B.; Hu, Y.; Wang, S.; Lan, Y.; Lei, A.; Li, J. Anion-Tuning of Organozincs Steering Cobalt-Catalyzed Radical Relay Couplings. *ACS Catal.* **2023**, *13*, 9254–9263.

8. (a) Caron, S.; Do, N. M.; Sieser, J. E.; Arpin, P.; Vazquez, E. Process Research and Development of an NK-1 Receptor Antagonist. Enantioselective Trifluoromethyl Addition to a Ketone in the Preparation of a Chiral Isochroman. *Org. Process Res. Dev.* **2007**, *11*, 1015–1024. (b) Goadsby, P. J.; Ferrari, M. D.; Olesen, J.; Stovner, L. J.; Senard, J. M.; Jackson, N. C.; Poole, P. H. Eletriptan in acute migraine: A double-blind, placebo-controlled comparison to sumatriptan. *Neurology* **2000**, *54*, 156−163.
9. (a) Müller, K.; Faeh, C.; Diederich, F. Fluorine in Pharmaceuticals: Looking Beyond Intuition. *Science* **2007**, *317*, 1881–1886. (b) Purser, S.; Moore, P. R.; Swallow, S.; Gouverneur, V. Fluorine in medicinal chemistry. *Chem. Soc. Rev.* **2008**, *37*, 320–330. (c) Zhou, Y.; Wang, J.; Gu, Z.; Wang, S.; Zhu, W.; AceÇa, J. L.; Soloshonok, V. A.; Izawa, K.; Liu, H. Next Generation of Fluorine-Containing Pharmaceuticals, Compounds Currently in Phase II–III Clinical Trials of Major Pharmaceutical Companies: New Structural Trends and Therapeutic Areas. *Chem. Rev.* **2016**, *116*, 422–518.
10. (a) Koike, T.; Akita, M. A versatile strategy for difunctionalization of carbon−carbon multiple bonds by photoredox catalysis. *Org. Chem. Front.* **2016**, *3*, 1345–1349. (b) Cao, M.-Y.; Ren, X.; Lu, Z. Olefin difunctionalizations via visible light photocatalysis. *Tetrahedron Lett.* **2015**, *56*, 3732–3742. (c) Yan, M.; Lo, J. C.; Edwards, J. T.; Baran, P. S. Radicals: Reactive Intermediates with Translational Potential. *J. Am. Chem. Soc.* **2016**, *138*, 12692–12714. (d) Bian, K.-J.; Nemoto Jr., D.; Kao,

S.-C.; He, Y.; Li, Y.; Wang, X.-S.; West, J. G. Modular Difunctionalization of Unactivated Alkenes through Bio-Inspired Radical Ligand Transfer Catalysis. *J. Am. Chem. Soc.* **2022**, *144*, 11810–11821.

11. (a) Bagal, D. B., Kachkovskyi, G.; Knorn, M.; Rawner, T.; Bhanage, B. M.; Reiser, O. Trifluoromethylchlorosulfonylation of Alkenes: Evidence for an InnerSphere Mechanism by a Copper Phenanthroline Photoredox Catalyst. *Angew. Chem. Int. Ed.* **2015**, *54*, 6999–7002. (b) Yang, B.; Xu, X.-H.; Qing, F.-L. Copper-Mediated Radical 1,2-Bis(trifluoromethylation) of Alkenes with Sodium Trifluoromethanesulfinate. *Org. Lett.* **2015**, *17*, 1906–1909. (c) Wang, F.; Wang, D.; Wan, X.; Wu, L.; Chen, P.; Liu, G. Enantioselective Copper-Catalyzed Intermolecular Cyanotrifluoromethylation of Alkenes via Radical Process. *J. Am. Chem. Soc.* **2016**, *138*, 15547–15550. (d) Yatham, V. R.; Shen, Y.; Martin, R. Catalytic Intermolecular Dicarbofunctionalization of Styrenes with CO2 and Radical Precursors. *Angew. Chem. Int. Ed.* **2017**, *56*, 10915–10919. (e) Fu, L.; Zhou, S.; Wan, X.; Chen, P.; Liu, G. Enantioselective Trifluoromethylalkynylation of Alkenes via Copper-Catalyzed Radical Relay. *J. Am. Chem. Soc.* **2018**, *140*, 10965–10969. (f) Zhou, S.; Zhang, G.; Fu, L.; Chen, P.; Li, Y.; Liu, G. Copper-Catalyzed Asymmetric Cyanation of Alkenes via Carbonyl-Assisted Coupling of Alkyl-Substituted Carbon-Centered Radicals. *Org. Lett.* **2020**, *22*, 6299–6303.
12. (a) Zhu, S.; Qin, J.; Wang, F.; Li, H.; Chu, L. Photoredox-catalyzed branch-selective pyridylation of alkenes for the expedient synthesis of Triprolidine. *Nat. Commun.* **2019**, *10*, 749. (b) Liu, K.; Studer, A. Direct α-Acylation of Alkenes via N-Heterocyclic Carbene, Sulfinate, and Photoredox Cooperative Triple Catalysis. *J. Am. Chem. Soc.* **2021**, *143*, 4903–4909.
13. (a) Ravetz, B. D.; Tay, N. E. S.; Joe, C. L.; Sezen-Edmonds, M.; Schmidt, M. A.; Tan, Y.; Janey, J. M.; Eastgate, M. D.; Rovis, T. Development of a Platform for Near-Infrared Photoredox Catalysis. *ACS Cent. Sci.* **2020**, *6*, 2053–2059. (b) Goldschmid, S. L.; Bednářová, E.; Beck, L. R.; Xie, K.; Tay, N. E. S.; Ravetz, B. D.; Li, J.; Joe, C. L.; Rovis, T. Tuning the Electrochemical and Photophysical Properties of Osmium-Based

Photoredox Catalysts. *Synlett* **2022**, 33, 247–258. (c) Tay, N. E. S.; Ryu, K. A.; Weber, J. L.; Olow, A. K.; Cabanero, D. C.; Reichman, D. R.; Oslund, R. C.; Fadeyi, O. O.; Rovis, T. Targeted activation in localized protein environments via deep red photoredox catalysis. *Nat. Chem.* **2023**, *15*, 101–109. (d) Goldschmid, S. L.; Tay, N. E. S.; Joe, C. L.; Lainhart, B. C.; Sherwood, T. C.; Simmons, E. M.; Sezen-Edmonds, M.; Rovis, T. Overcoming Photochemical Limitations in Metallaphotoredox Catalysis: Red-Light-Driven C–N Cross-Coupling. *J. Am. Chem. Soc.* **2022**, *144*, 22409–22415. (e) Cabanero, D. C.; Nguyen, J. A.; Cazin, C. S. J.; Nolan, S. P.; Rovis, T. Deep Red to Near-Infrared Light-Controlled Ruthenium-Catalyzed Olefin Metathesis. *ACS Catal.* **2023**, *13*, 4384–4390.

14. Schade, A. H.; Mei, L. Applications of red light photoredox catalysis in organic synthesis. *Org. Biomol. Chem.* **2023**, *21*, 2472.
15. Jia, H.; Häring, A. P.; Berger, F.; Zhang, L.; Ritter, T. Trifluoromethyl Thianthrenium Triflate: A Readily Available Trifluoromethylating Reagent with Formal CF_3^+, $CF_3\bullet$, and CF_3^- Reactivity. *J. Am. Chem. Soc.* **2021**, *143*, 7623–7628.
16. (a) Lang, S. B.; Wiles, R. J.; Kelly, C. B.; Molander, G. A. Photoredox Generation of Carbon-Centered Radicals Enables the Construction of 1,1-Difluoroalkene Carbonyl Mimics. *Angew. Chem. Int. Ed.* **2017**, *56*, 15073–15077. (b) Zhang, J.; Yang, J.-D.; Cheng, J.-P. Chemoselective catalytic hydrodefluorination of trifluoromethylalkenes towards mono-/gem-di-fluoroalkenes under metal-free conditions. *Nat. Commun.* **2021**, *12*, 2835. (c) Chen, X.-L.; Yang, D.-S.; Tang, B.-C.; Wu, C.-Y.; Wang, H.-Y.; Ma, J.-T.; Zhuang, S.-Y.; Yu, Z.-C.; Wu, Y.-D.; Wu, A.-X. Direct Hydrodefluorination of CF_3-Alkenes via a Mild S_N2' Process Using Rongalite as a Masked Proton Reagent. *Org. Lett.* **2023**, *25*, 2294–2299.
17. (a) Bezençon, O.; Heidmann, B.; Siegrist, R.; Stamm, S.; Richard, S.; Pozzi, D.; Corminboeuf, O.; Roch, C.; Kessler, M.; Ertel, E. A.; Reymond, Is.; Pfeifer, T.; de Kanter, R.; Toeroek-Schafroth, M.; Moccia, L. G.; Mawet, J.; Moon, R.; Rey, M.; Capeleto, B.; Fournier, E. Discovery of a Potent, Selective T-type Calcium Channel Blocker as a Drug Candidate for the Treatment of Generalized Epilepsies. *J. Med. Chem.*

2017, *60*, 9769–9789. (b) Phelan, J. P.; Lang, S. B.; Compton, J. S.; Kelly, C. B.; Dykstra, R.; Gutierrez, O.; Molander, G. A. Redox-Neutral Photocatalytic Cyclopropanation via Radical/Polar Crossover. *J. Am. Chem. Soc*. **2018**, *140*, 8037–8047.

18. Romine, A. M.; Nebra, N.; Konovalov, A. I.; Martin, E.; Benet-Buchholz, J.; Grushin, V. V. Easy Access to the Copper(III) Anion $[Cu(CF_3)_4]^-$. *Angew. Chem. Int. Ed.* **2015**, *54*, 2745–2749.
19. Ratushnyy, M.; Kamenova, M.; Gevorgyan, V. A mild light-induced cleavage of the S–O bond of aryl sulfonate esters enables efficient sulfonylation of vinylarenes. *Chem. Sci.* **2018**, 9, 7193–7197.
20. Tan, G.; Das, M.; Kleinmans, R.; Katzenburg, F.; Daniliuc, C.; Glorius, F. Energy transfer-enabled unsymmetrical diamination using bifunctional nitrogen-radical precursors. *Nat. Catal.* **2022**, *5*, 1120–1130.

Chapter 5

Visible light-mediated photocatalysis for the conversion of biomass into formic acids

ABSTRACT: Formic acid (FA) holds strong promise as both a prospective hydrogen reservoir and a valuable substrate for industrial domains such as textiles and pharmaceuticals. The present worldwide FA demand, quantified at 1.137 million metric tons per annum, mandates the innovation of sustainable methodologies to anticipate forthcoming requisites. In response, we propose a solar-energy-mediated strategy for the generation of formic acid directly from biomass. This intricate process harnesses atmospheric oxygen's potential as an oxidizing agent to transform biomass like sugars, cellulose, and hemicellulose into formic acid. Our catalytic framework realizes the successful conversion of cellulose-abundant ubiquitous materials such as discarded paper and oak cork stoppers of wine bottles into formic acid through a sequence of controlled flow experiments. To comprehensively unravel the reaction's mechanism, we have conducted meticulous mechanistic inquiries, including density functional theory (DFT) calculations, aimed at gaining insights into the reaction pathways.

Photocatalytic transformation of biomass to FA

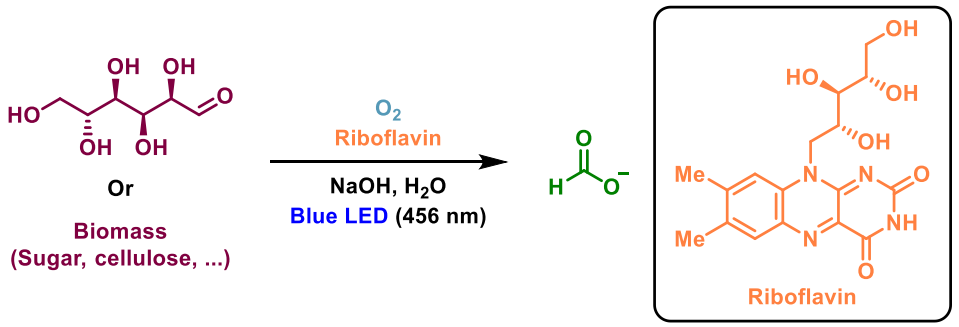

5.1 Introduction

5.1.1. Importance of renewable energies

Current scientific pursuits are significantly directed towards the exploration of renewable energy sources, including solar irradiation, wind power, hydropower, and non-consumable organic resources.[1-2] Within those sources, hydrogen emerges as a preeminent energy carrier, distinguished for its environmental purity and adaptable attributes. Its salient feature lies in its potential to operate within fuel cell frameworks, facilitating the generation of electricity, power, and heat while generating only water as a byproduct.[3-4] Contemporary applications of hydrogen predominantly lie within the spheres of petroleum refinement and fertilizer synthesis, whereas the realms of transportation and utilities are undergoing transformative developments as nascent sectors.[5] However, to accelerate the implementation of this ecologically benign energy carriers, additional endeavours are imperative to tackle the difficulties linked with the storage and conveyance of generated hydrogen (**Figure 5.1**).[6]

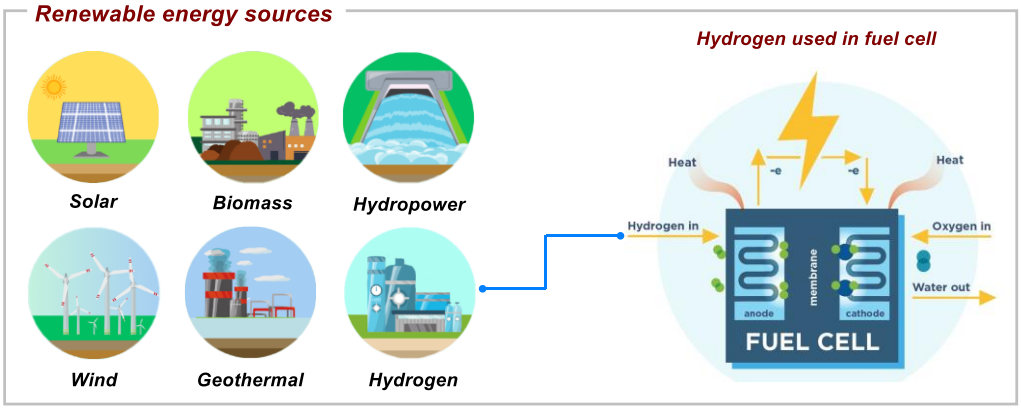

Figure 5.1. Hydrogen as a renewable energy source used in fuel cell.

Currently, there has been extensive discourse concerning diverse strategies for hydrogen storage, approached through physical and chemical perspectives. It is worth noting that the extensively investigated

techniques involve the confinement of hydrogen within high-pressure vessels, achieving pressures of up to 700 bar, or within cryogenic reservoirs, maintained at temperatures as extreme as -253°C.[7] Additionally, alternative methodologies have been proposed, entailing the utilization of low-temperature adsorption and desorption procedures employing materials characterized by considerable internal surface areas, including metal-organic frameworks (MOFs), polymers of intrinsic microporosity (PIMs), zeolites, and carbon nanotubes.[8] Furthermore, organic compounds are acknowledged as prospective candidates for hydrogen storage. Notably, liquid hydrogen carriers (LOHCs), exemplified by carbazole, exhibit intriguing properties, rendering them particularly appealing for storage and conveyance purposes (**Figure 5.2**).[9]

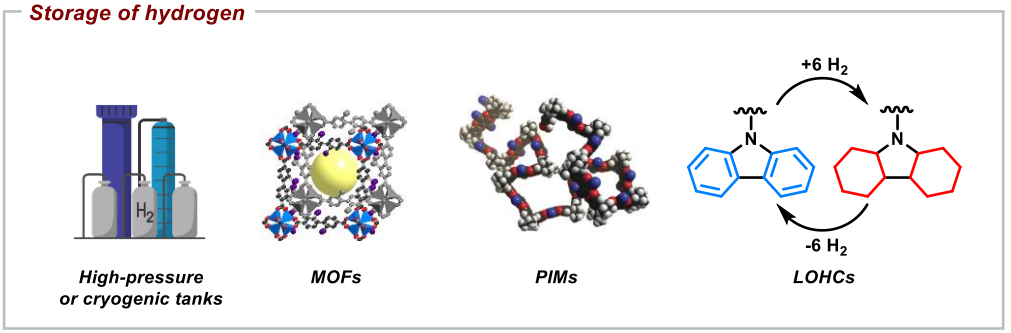

Figure 5.2. Recent methods for the storage of hydrogen.

5.1.2. Advantages of FA as hydrogen carrier

In addition to aforementioned hydrogen carrier, formic acid (FA) as a kinetically stable liquid at room temperature has garnered significant attention in the field of hydrogen storage.[10] Significantly, the utilization of FA demonstrates high atom efficiency due to the complete accessibility of all stored hydrogen for catalytic storage and dehydrogenation (DH) to H_2, and the thermodynamic feasibility of the conversion to CO_2 is evidenced by a negative standard Gibbs free energy change ($\Delta G°$) of -32.9 kJ mol^{-1} at ambient temperature.[10] Moreover, FA as a valuable

chemical finds widespread applications across diverse sectors such as pharmaceuticals, textiles, food, and agriculture. It is worth noting that the present global demand necessitates an annual supply of 1.137 million metric tons of FA. Consequently, there exists a significant imperative to develop sustainable methods to produce FA in order to meet the future energy requirements (**Figure 5.3**).[9-11]

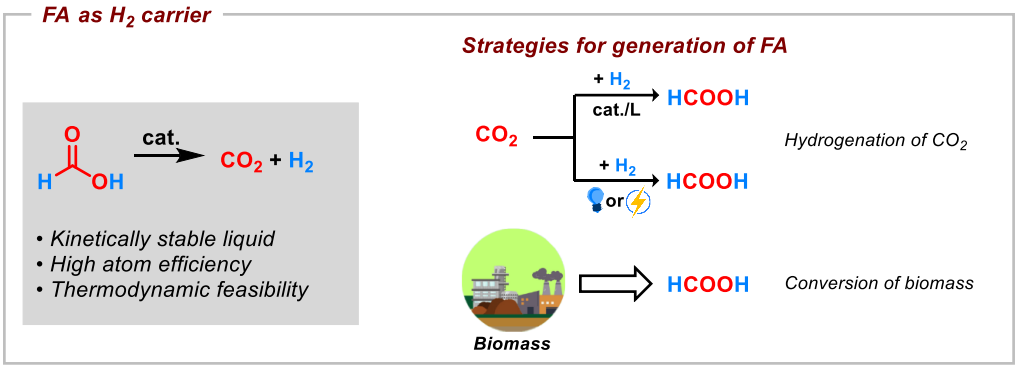

Figure 5.3. Formic acid as a hydrogen carrier and strategies for the formation of formic acid.

5.1.3. Literature for FA generation from CO_2

The hydrogenation of CO_2 into FA represents a prevalent pathway, nevertheless, this process necessitates elevated temperatures, pressures, and costly metal catalysts or their associated ligands.[12] Alternatively, the utilization of photocatalytic or electrocatalytic processes for the conversion of CO_2 to FA has gained attention, yet it remains distant from achieving the ultimate goal.[13]

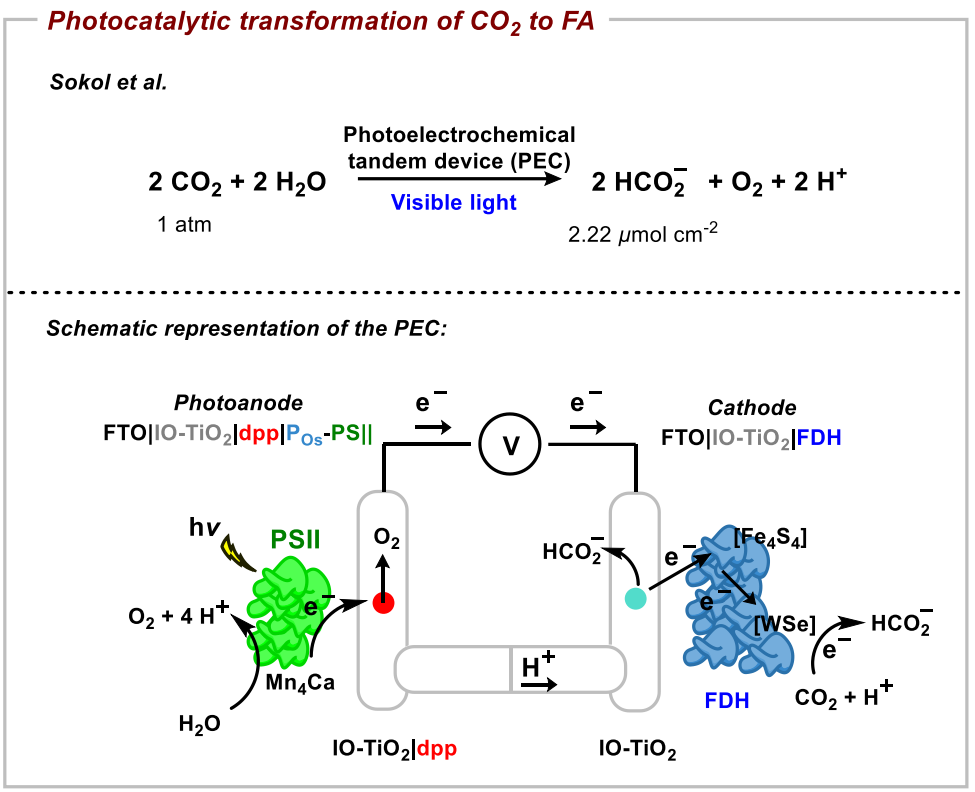

Figure 5.4. The semi-artificial photosynthetic tandem PEC cell for water oxidation and CO_2 reduction to formate.

In 2018, Reisner group has reported a semi-artificial photoelectrochemical (PEC) tandem cell that converted CO_2 to formate in conjunction with enzymes formate dehydrogenase (FDH) and photosystem II (PSII) (**Figure 5.4**).[14a] As elucidated in **Figure 5.4**, water was oxidized by oxygen-evolving complex (Mn_4Ca) in PSII to generate oxygen and protons. Simultaneously, the electrons were transferred to cathode through the exrternal circuit. The migration of electrons from the CB of titanium dioxide (TiO_2) to iron-sulfur clusters, tetranuclear iron-sulfur clusters (Fe_4S_4). These clusters serve as conduits, establishing a connection between the active site of formate dehydrogenase (FDH) and the surface of the material. The transferred electrons arrived at [WSe]-active site at the end, where CO_2 was reduced to formate with 2.22 μmol cm^{-2}.

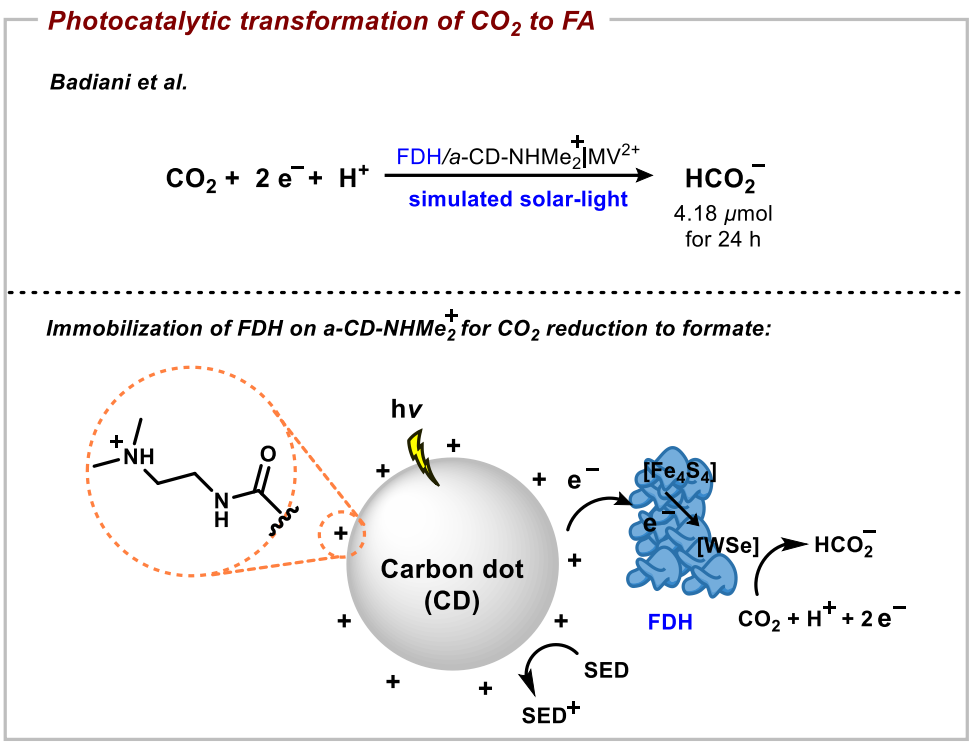

Figure 5.5. Photocatalytic CO_2 reduction to formate mediated by FDH immobilized on *a*-CD-NHMe$_2^+$.

Since FDH serves as the prototypical enzymatic electrocatalyst employed in the process of electrochemical reduction of CO_2 into formate, Reisner group continuously developed a photocatalytic CO_2 reduction system for formate generation (**Figure 5.5**).[14b] The FDH was immobilized on photoluminescent carbon dots (CDs) with NHMe$_2^+$ linker. The photogenerated electrons were transferred to [WSe]-active site for CO_2 reduction to formate. The oxidized CDs were regenerated by the sacrificial electron donor (SED). The generation of formate can reach to 4.18 μmol for 24 hours.

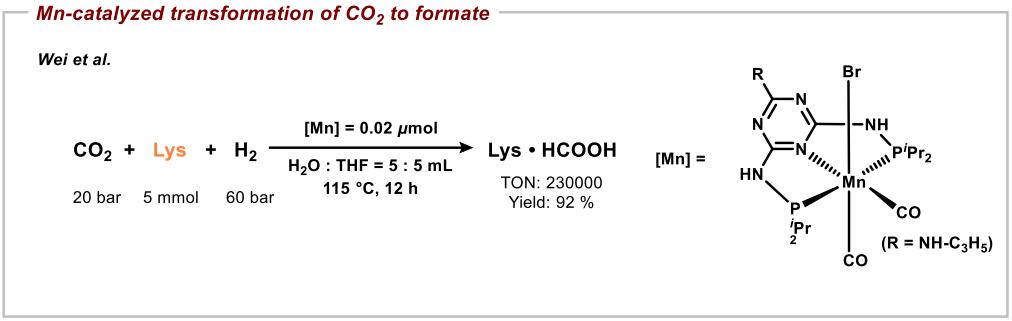

Figure 5.6. Mn-pincer complex-catalyzed hydrogenation of carbon dioxide to FA in the presence of lysine.

In the context of the previously discussed photocatalytic enzyme-mediated systems for CO_2 reduction, it remains a challenge that the production of formate or formic acid (FA) following the acidification process does not yet attain an industrial-scale yield. In 2022, Beller group has developed the lysine-promoted reversible hydrogenation of CO_2 to FA with a Mn-pincer complex (**Figure 5.6**).[12] Utilizing this precisely characterized manganese complex, a highly efficient conversion of CO_2 into FA was achieved (92% yield and 230000 TON). It is imperative to underscore that the identical system exhibits efficiency in facilitating the converse reaction, namely, the generation of H_2 from FA (>99 % yield and 29400 TON).

5.1.4. Literature for FA generation from biomass

In addition to the hydrogenation of CO_2, the utilization of biomass as a prospective source of FA is under consideration owing to its abundant availability and cost-effectiveness.[15] Indeed, the production of FA from biomass through processes like catalytic oxidation and electrocatalysis has been explored. However, these approaches are inadequate in meeting the required quantity of FA and are hindered by challenges like substantial capital investment, substantial energy consumption, elevated operational expenses, or stringent operational requirements (**Figure 5.7**).[16]

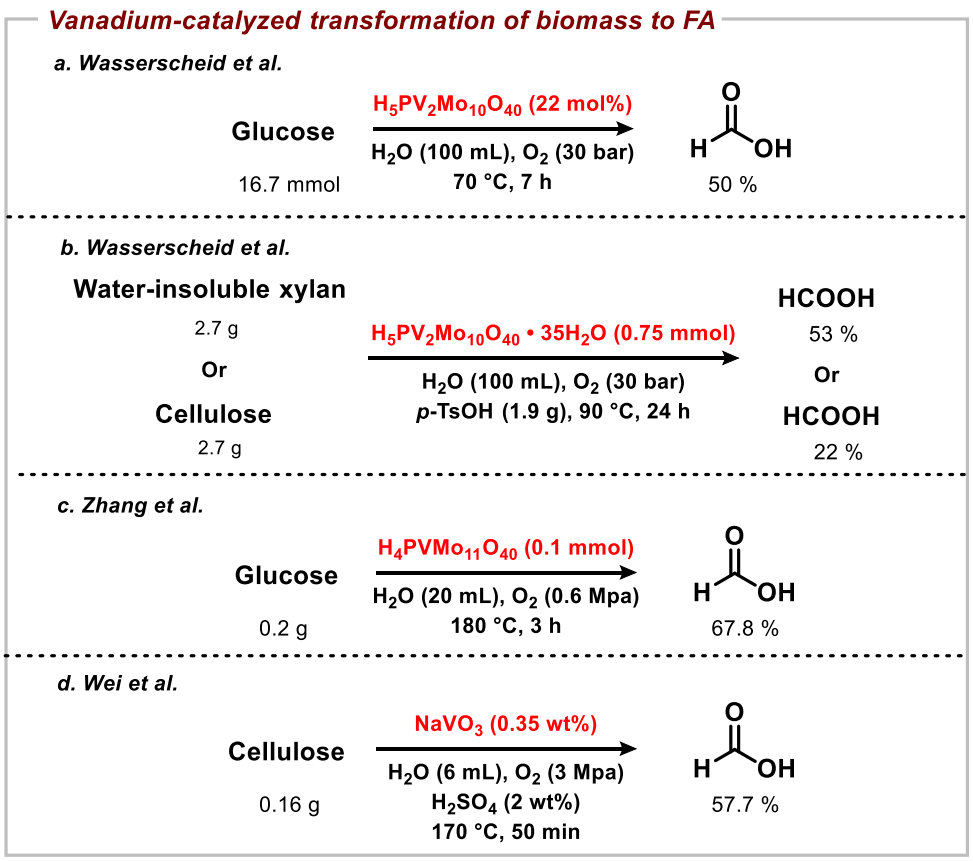

Figure 5.7. Catalytic transformation of biomass to FA mediated by vanadium catalysts.

In 2011, group of Wasserscheid firstly reported that $H_5PV_2Mo_{10}O_{40}$, a Keggin-type heteropoly acid, could effectively convert biobased carbohydrates to FA (**Figure 5.7a**).[16b] Various water soluble mono- and disaccharides were carried out under the conditions to generate FA in 33-50 % yield. The strategy is also named by OxFA process.

In 2012, group of Wasserscheid further optimized the reaction system for the conversion of cellulose feedstock to FA (**Figure 5.7b**).[16d] In this approach, organic acids, such as *p*-toluenesulfonic acid (*p*-TsOH), functioned as efficient solubility promoters and catalysts for the reaction involving biomass that is insoluble in water. For instance, water-

insoluble xylan and cellulose offered FA in 53% and 22% yield under this conditions, respectively.

To further improve the photocatalytic efficency of the conversion of biomass to FA, Zhang *et al.* has analyzed a series of vanadium-substituted phosphomolybdic acids for converting cellulose into FA (**Figure 5.7c**).[17a] After examining those catalysts, $H_4PVMo_{11}O_{40}$ was the best candidate, providing FA in 67.8% yield at 180 °C.

Recently, group of Liang has reported a vanadium-acid catalytic system for biomass conversion to FA (**Figure 5.7d**).[17b] In the presence of 2 wt% sulfuric acid, cellulose was efficiently decomposed and converted to FA with $NaVO_3$ in 57.7 % yield at 170 °C. Importantly, not only the catalytic system was improved, but also the complete mechanism of the cellulose OxFA process has been investigated. In the cleavage-oxidation pathway of each carbon-carbon bond, the aldehyde group and the carboxyl group were the direct precursor of FA and the precursor of the by-product CO_2, respectively. Therefore, this cellulose OxFA mechanism has explained the selectivity of FA and CO_2 in the decomposition of biomass, which also would provide a theoretical framework for further enhancing the efficient conversion of biomass into FA.

5.1.5. Photocatalytic formation of formic acid from biomass

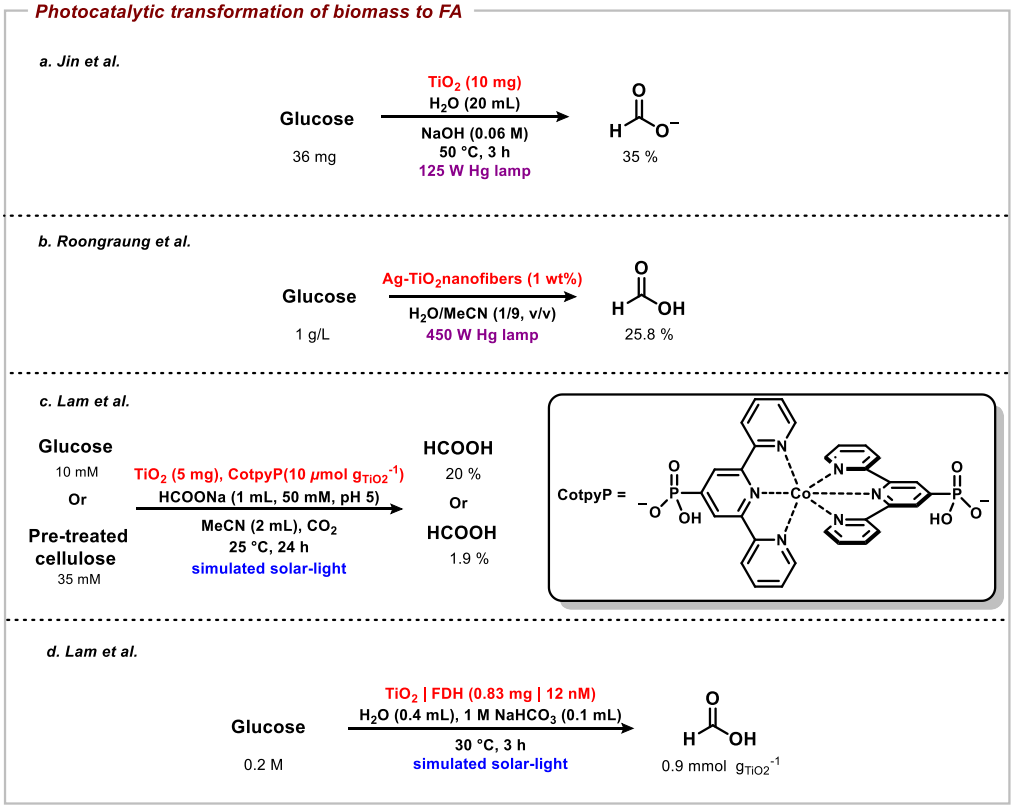

Figure 5.8. Photocatalytic formation of formic acid from biomass.

In 2017, a novel method involving UV-light photocatalysis with nano TiO_2 has been successfully implemented by the group of Jin for the conversion of glucose into formate (**Figure 5.8a**).[18a] Due to the strong oxidation ability of TiO_2, glucose was completely decomposed and converted into formate in 35% yield in the presence of 0.06 M NaOH. Later, Sagawa group also reported silver (Ag)-doped TiO_2 nanofibers for glucose conversion to FA (**Figure 5.8b**).[18b] The nanofibers provided FA in 25.8 % yield and ensure at least four times uses.

As described in the reaction conditions, both systems required high-energy mercury lamps to activated TiO_2, which was energy consuming and costly. To avoid high-energy light sources, Reisner group developed a TiO_2-CotpyP photocatalyst for the transformation of cellulose into

formate (**Figure 5.8c**).[18c] By employing TiO_2-CotpyP photocatalyst, glucose and insoluble cellulose were converted into FA under the irradiation of simulated solar-light. However, the yield of FA generated through this approach, was comparably lower.

Recently, based on the previous work, group of Reisner reported a semi-artificial biohybrid photocatalyst consisting of immobilized FDH on TiO_2 (TiO_2|FDH) for the transformation of cellulose to formate (**Figure 5.8d**).[18d] This sunlight-driven system simultaneously proceeded towards the oxidation of cellulose feedstock and CO_2 reduction with good reactivity and selectivity. Although the yield of formate cannot meet the industrial requirement so far, this approach has paved the direction for the decomposition of cellulose to valuable chemicals by using biohybrid photocatalysts.

5.2 Objective

As elucidated within reported literatures, the transformation of biomass necessitated substantial power output from expensive light source, costly catalyst, or excessive quantity of alkali.[19-20] Therefore, it is imperative to develop a visible-light-mediated method to efficiently convert carbohydrate-based biomass into FA, while minimizing energy consumption. Hence, by leveraging the fundamental process of photosynthesis, the proficient conversion of biomass into FA holds great potential to significantly contribute to the enhancement of sustainable approach around the globe.[21-22] Herein, we aim to develop a visible light-mediated transformation of biomass to FA with a metal-free photocatalyst under ambient temperature and pressure (**Figure 5.9**).

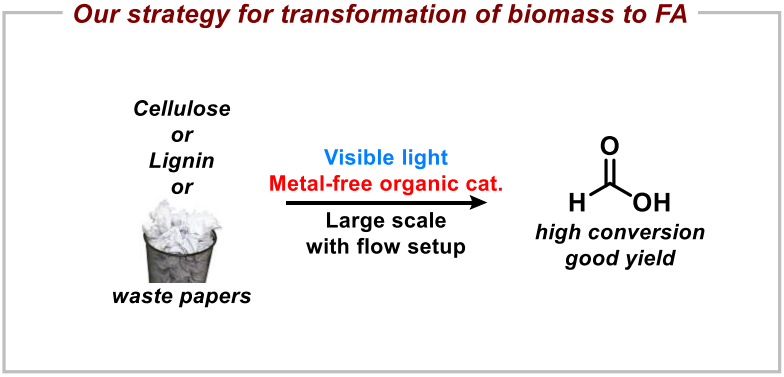

Figure 5.9. Visible light-mediated transformation of biomass to FA with a metal-free photocatalyst.

5.3 Results and discussion

5.3.1. Optimization of reaction conditions

Table 5.1. Initial optimization of reaction conditions for photocatalytic production of FA.

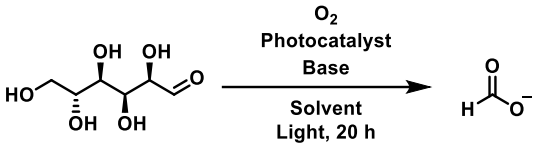

Entry	Catalyst	Solvent (mL)	Base (M)	Light[a] (W)	Yield[b] (%)
1	Riboflavin	*n*-Butanol (0.5)	NaOH (2.5)	12	40
2	-	*n*-Butanol (0.5)	NaOH (2.5)	12	8
3	Riboflavin	*n*-Butanol (0.5)	-	12	n.ob.
[d]4	Riboflavin	*n*-Butanol (0.5)	NaOH (2.5)	12	n.ob.
[e]5	Riboflavin	*n*-Butanol (0.5)	NaOH (2.5)	12	4

Reaction conditions: substrate (36 mg), Photocatalyst (5 mol%), 20 h. [a]Home-made blue LED (456 nm). [b]Formate was acidified to FA with 2 M HCl and yields were determined by ^{1}H NMR with trimesic acid as internal standard. [c]Kessil Lamp (456 nm). [d]Under N_2. [e]No glucose.

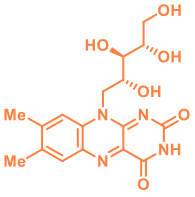

Riboflavin

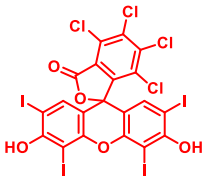

Rose Bengal

Glucose was chosen as the model substrate to optimize the reaction conditions (**Table 5.1**). To investigate the concept of transformation of glucose into formic acid (FA) under the irradiation of visible light, riboflavin was at first utilized as photocatalyst in a solution of glucose and *n*-butanol in the presence of base under O_2 atmosphere. To our delight, FA was obtained in 40% yield in 20 h under the irradiation of 12

W household blue LED (**Entry 1**). To verify the essentiality of each component, a series of control experiments were conducted, revealing the pivotal involvement of the catalyst, base, and oxygen in the functioning of this photocatalytic system (**Entry 2–4**). Interestingly, trace amount of FA was also observed in the absence of starting material, namely glucose (**Entry 5**). The occurrence of unforeseen FA was ascribed to the alcohol oxidation process, subsequently leading to C–C bond cleavage, resulting in FA formation.

Table 5.2. Optimization of light sources.

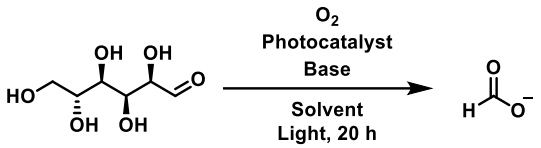

Entry	Catalyst	Solvent (mL)	Base (M)	Light[a] (W)	Yield[b] (%)
1	Riboflavin	H_2O (1)	NaOH (2.5)	12	45
2	Riboflavin	H_2O (1)	NaOH (2.5)	24	43
3	Riboflavin	H_2O (1)	NaOH (2.5)	40[c]	43
4	Riboflavin	H_2O (1)	NaOH (2.5)	20[c]	26
5	Riboflavin	H_2O (1)	NaOH (2.5)	10[c]	29

Reaction conditions: substrate (36 mg), Photocatalyst (5 mol%), 20 h. [a]Home-made blue LED (456 nm). [b]Formate was acidified to FA with 2 M HCl and yields were determined by ^{1}H NMR with trimesic acid as internal standard. [c]Kessil Lamp (456 nm). [d]Under N_2. [e]No glucose.

In order to mitigate excessive FA generation from alcohol, pure water as a solvent was employed, yielding an enhanced FA production of up to 45% (**Table 5.2**, **Entry 1**). The photocatalyst riboflavin can be activated under the irradiation of blue light. Therefore, the household blue LED was utilized as the light source. Additionally, more powerful light

sources were also investigated to increase the yield, however, no improvement was obtained by adjusting the lights (**Entry 2–5**).

Table 5.3. Optimization of the concentration of base.

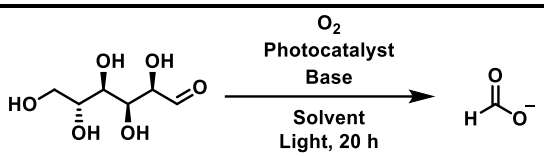

Entry	Catalyst	Solvent (mL)	Base (M)	Light[a] (W)	Yield[b] (%)
1	Riboflavin	H_2O (1)	NaOH (2)	12	43
2	Riboflavin	H_2O (1)	NaOH (1.5)	12	40
3	Riboflavin	H_2O (1)	NaOH (1)	12	35
4	Riboflavin	H_2O (1)	NaOH (3)	12	33
5	Riboflavin	H_2O (1)	NaOH (5)	12	17
6	Rose Bengal	H_2O (1)	NaOH (2)	12	25

Reaction conditions: substrate (36 mg), Photocatalyst (5 mol%), 20 h. [a]Home-made blue LED (456 nm). [b]Formate was acidified to FA with 2 M HCl and yields were determined by ^{1}H NMR with trimesic acid as internal standard. [c]Kessil Lamp (456 nm). [d]Under N_2. [e]No glucose.

In response to the growing demand for environmentally sustainable reaction conditions, reducing the usage of a base is consistently considered a favourable objective, provided that the reaction system remains unaffected. In pursuit of this goal, investigations were conducted by using lower concentrations of sodium hydroxide. The results revealed a clear trend: as the concentration of the base decreased, the yield of FA was also decreased (**Table 5.3**, **Entry 1–3**). Moreover, we expected higher yield of FA based on this trend, however, less FA was generated which was attributed to the limited solubility of sodium hydroxide in a small quantity of water (**Entry 4–5**). According to these optimizations, we determined **Entry 1** in **Table 5.3** as the model reaction

condition. In addition, we explored the use of rose bengal as a homogeneous photocatalyst under the optimized conditions. However, it exhibited inferior photocatalytic performances in the generation of FA. (**Entry 6**).

5.3.2. Investigation of various saccharides

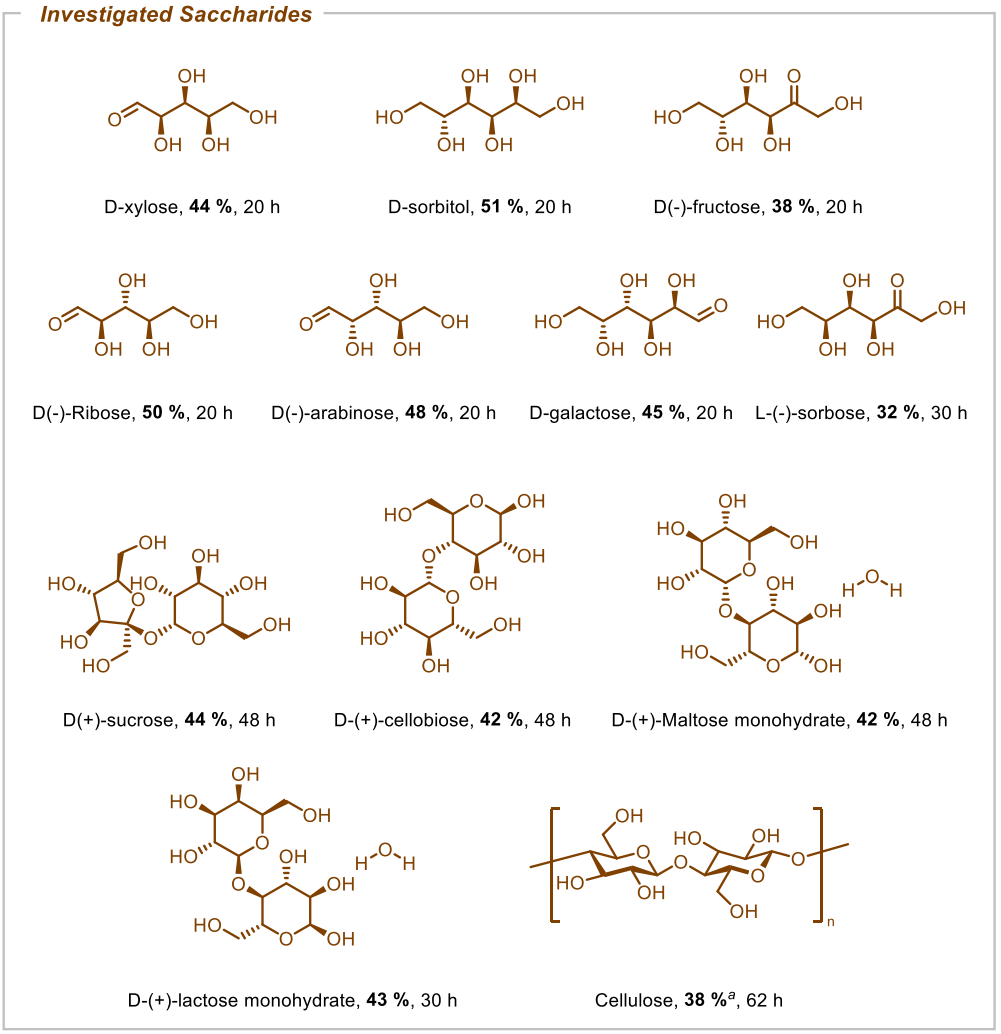

Figure 5.10. Photocatalytic production of FA from biomass. Formate was acidified to FA with 2 M HCl and yields were determined by ^{1}H NMR with trimesic acid as internal standard. [a]Cellulose was pretreated and dissolved in water by using freezing-thawing method.

With the best reaction conditions in hand, we revisited our initial focus which pertained to the photocatalytic conversion of saccharides into FA (**Figure 5.10**). Initially, the substrate scope was expanded by systematically evaluating numerous monosaccharides, including D-xylose, D(-)-fructose, D(-)-Ribose, D(-)-arabinose, D-galactose and L-(-)-sorbose, most of which can be obtained from natural products and biomass. The sugars underwent successful transformation into FA with moderate to good yields through the implementation of optimized photocatalytic reactions. Furthermore, various disaccharides were also employed as substrates, each demonstrating favourable yields. In contrast to monosaccharides, the conversion of disaccharides necessitated longer reaction times. As a polysaccharide, cellulose was subjected to evaluation, revealing that even with an extended reaction time, the yield of FA obtained was comparatively lower. The diminished photocatalytic performance was attributed to cellulose's limited solubility in water, which served as a crucial limiting factor. Nevertheless, a significant improvement in cellulose solubility was achieved through a pre-treatment by employing the freezing-thawing method, resulting in a notable FA yield of 38%.

5.3.3. Upscaling reaction with flow setup

In the realm of photocatalysis, the challenges of extended reaction time and scaling up processes pose notable obstacles. Inspired by our previous work, to enhance the efficiency of the developed photosystems, it was plausible to explore the implementation of reactions conducted within a flow system.[23] Following a systematic examination of the oxygen and sample rates within the flow setup, the optimized conditions for flow reactions were ultimately determined (See details of optimizations in **Table 5.7**). Polysaccharides, namely cellulose and xylan, were capable of generating FA with the production rates of 0.60 and 0.61 mmol/h, respectively (**Table 5.4**, **Entries 1–2**). Lignin, a group of intricate organic polymers, could also provide FA under our conditions with the

production rates of 0.37 mmol/h (**Table 5.4**, **Entry 3**). Remarkably, the valorisation of daily waste materials such as wastepaper and oak plugs demonstrated the capability to produce valuable FA at promising production rates through a well-designed flow system (**Table 5.4**, **Entries 4–5**).[24]

Table 5.4. Evaluation of various biomass-materials from daily life.

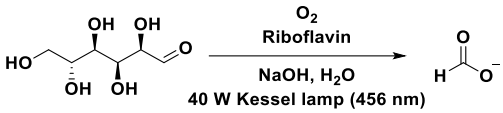

Entry	Substrate	O_2 flow rate	Sample rate	Production rate
1	Cellulose	1 mL/h	0.3 mL/h	0.60 mmol/h
2	Xylan	1 mL/h	0.3 mL/h	0.61 mmol/h
3	Lignin	1 mL/h	0.3 mL/h	0.37 mmol/h
4	Pre-treated waste paper	1 mL/h	0.3 mL/h	0.18 mmol/h
5	Pre-treated oak plug	1 mL/h	0.3 mL/h	0.24 mmol/h

Reaction conditions: substrate (135 mg), riboflavin (5 mol%), NaOH (2 M), H_2O (15 mL), 2x lamp kessil (40 W, 427 nm). The volumn of tube under the irradiation is 4 mL. Formate was acidified to FA with 2 M HCl and yields were determined by ^1H NMR with trimesic acid as internal standard.

5.4 Mechanistic studies

5.4.1. Quenching experiments

To elucidate the mechanistic pathway, a series of quenching experiments were conducted (**Table 5.5**). Specifically, radical scavengers, namely BHT (Butylated hydroxytoluene) and TEMPO ((2,2,6,6-Tetramethylpiperidin-1-yl)oxyl), were introduced into the reaction system. While BHT exhibited negligible impact on the yield, the addition of TEMPO significantly reduced the formation of FA. Similarly, 9,10—diphenylanthracene and copper(II) chloride ($CuCl_2$) were incorporated as scavengers for singlet oxygen and single electron transfer (SET) process, respectively. The results demonstrated that singlet oxygen adversely affected the production of FA, as evidenced by an obviously lower yield when $CuCl_2$ was present in the system. Moreover, tris(hydroxymethyl)aminomethane and benzoquinone were used as quenchers for hydroxyl radical and superoxide radical, respectively, leading to a reduced yield of FA.

Table 5.5. Quenching experiments.

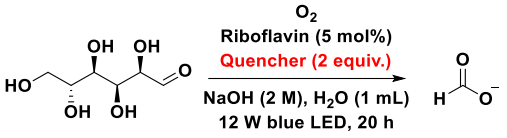

Entry	Quencher	Be quenched	[a]Yield (%)
1	BHT	Radical	44
2	TEMPO	Radical	25
3	9,10—Diphenylanthracene	$^1O_2$	49
4	$CuCl_2$	SET	15
5	Tris(hydroxymethyl)aminomethane	OH radical	8
6	Benzoquinone	$O_2^{\bullet-}$	22

Reaction conditions: substrate (36 mg), riboflavin (5 mol%), NaOH (2 M), H_2O (1 mL), 12 W blue LED. [a]Formate was acidified to FA with 2 M HCl and yields were determined by ^1H NMR with trimesic acid as internal standard.

5.4.2. Investigation of potential intermediates

To investigate potential intermediates formed during the conversion of glucose to FA, diverse substrates were subjected to our experimental conditions (**Table 5.6**). The results in **Table 5.6** demonstrated that glycol, glycolaldehyde, and DL-glyceraldehyde exhibited comparatively satisfactory yields of FA, albeit glycol exhibited low conversion. Conversely, other substrates, including glycolic acid, glyoxylic acid, and glyoxal, achieved 100% conversion, albeit with lower production yields of FA. Based on these findings, we hypothesize that glycol, glycolaldehyde, and DL-glyceraldehyde were the most plausible candidates for the intermediates in this transformation process.

Table 5.6. Identification of possible intermediates.

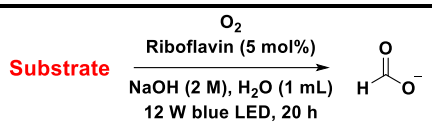

Entry	Substrate	[a]Conversion (%)	[b]Yield (%)
1	Glycol	42	29.68
2	Glycolaldehyde	100	33.46
3	Glycolic acid	Cannot determine	13.57
4	Glyoxylic acid	100	19.05
5	Glyoxal	100	4.28
6	DL-Glyceraldehyde	100	31.28
7	1,3-Dihydroxyacetone	Cannot determine	22.26

Reaction conditions: substrate (0.2 mmol), riboflavin (5 mol%), 20 h, NaOH (2 mM), H_2O (1 mL), 12 W Home-made blue LED (456 nm). [a]Conversions of substrates were

determined by ^{1}H NMR with trimesic acid as internal standard. [b]Formate was acidified to FA with 2 M HCl and yields were determined by ^{1}H NMR with trimesic acid as internal standard.

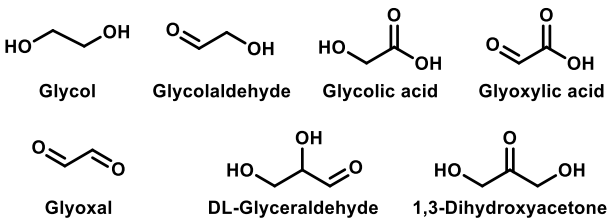

5.4.3. Theoretical calculations

According to the quenching experiments and investigation of possible intermediates, we proposed the possible reactions step by step. To validate our assumption, the theoretical calculations further substantiated the exothermic nature of the free Gibbs free energies involved in the formation of glycol, glycolaldehyde, and DL-glyceraldehyde, as well as the subsequent generation of FA. The energies of each step were also included in the proposed mechanism in **Figure 5.11**.

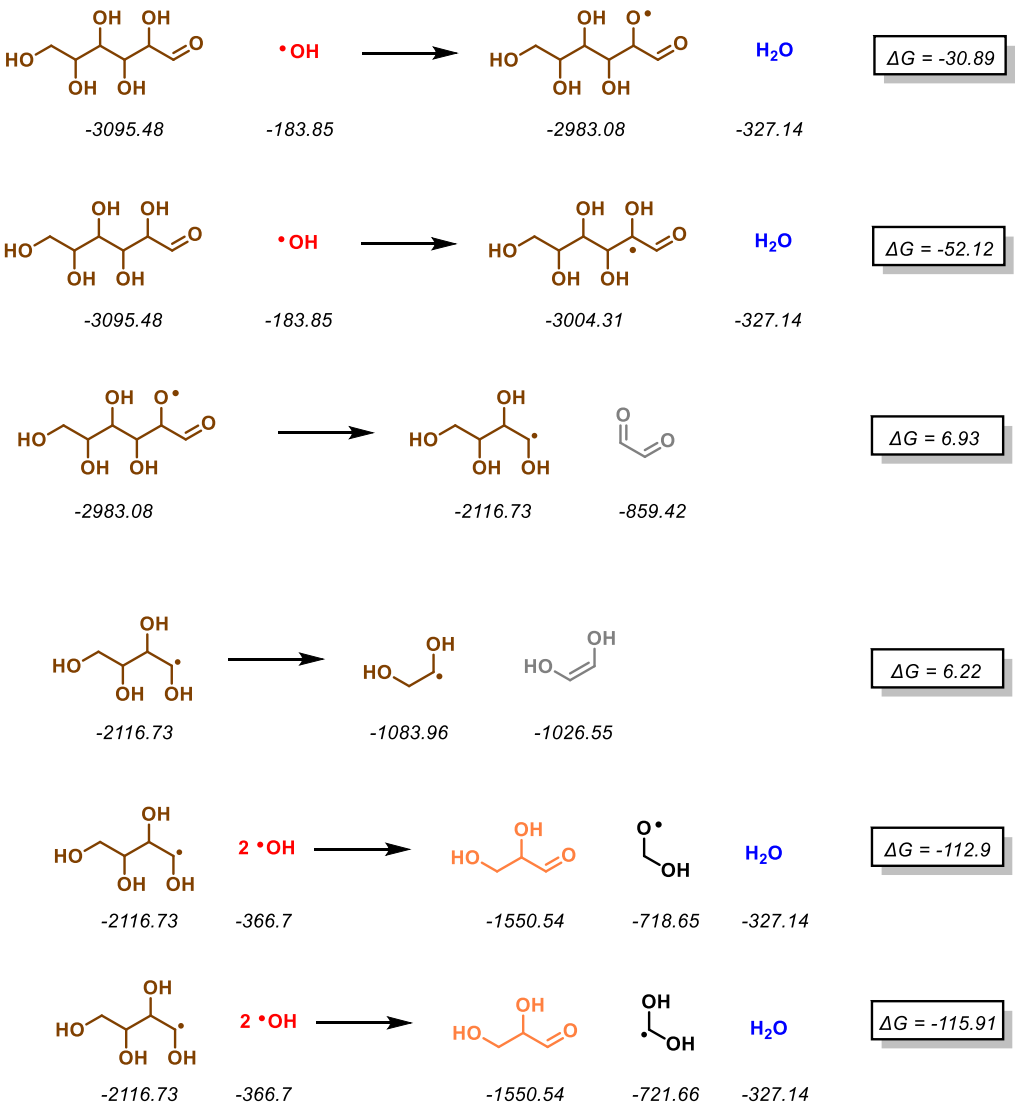

The energies are in kilocalories per mole and indicate the relative free energies

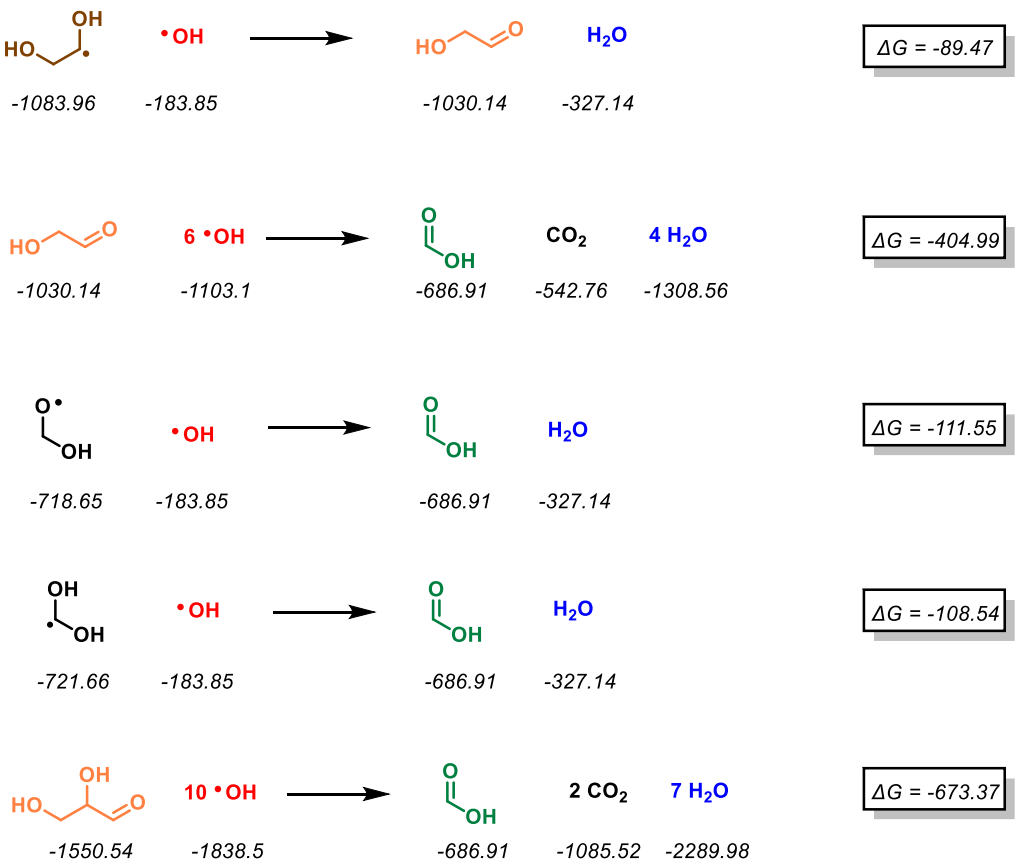

The energies are in kilocalories per mole and indicate the relative free energies

5.5 Proposed mechanism

In summary, we have presented the hypothetical sequence of reaction steps for the conversion of glucose, elucidating its potential transformation pathways (**Figure 5.11**). The hydrogen atom of glucose **A** was extracted by the hydroxyl radical (•OH), which was produced through the reductive quenching of the photocatalytic cycle, leading to the formation of the oxygen-centered radical **B**. Subsequently, a C–C bond cleavage occurred, resulting in the formation of the carbon-centered radical **C** and glyoxal. It is worth noting that the carbon-centered radical **B1** is more thermodynamically favourable based on the gibbs free energy change (ΔG). However, compared to radical **B**, the pathway from radical **B1** to radical **C** was difficult to be rationalized. The possible pathway is *via* 1,2-hydrogen atom (H) shift, which is not favourable since the bond dissociation energy of O–H is higher than the C–H. Therefore, we proposed that radical **B** was directly formed from **A** *via* a HAT process, followed by the generation of radical **C**. Following the formation of **C**, three distinct pathways have been elucidated through mechanistic investigations: Path I involved the subsequent cleavage of radical **C**, resulting in the formation of radical **D**, which subsequently reacted with •OH, leading to the production of one of the possible intermediates glycolaldehyde (**H**). In the alternative pathways, radical **C** directly reacted with •OH, leading to the formation of DL-glyceraldehyde (**F**) along with either the oxygen-centered radical **E** or the carbon-centered radical **G**, which can undergo further reaction with •OH resulting in the generation of FA. Based on the analysis of the intermediate species (**Table 5.4**), it was postulated that compounds **D**, **H**, and **F** underwent subsequent reactions with •OH, ultimately yielding the desired FA, along with the by-products CO_2 and H_2O.

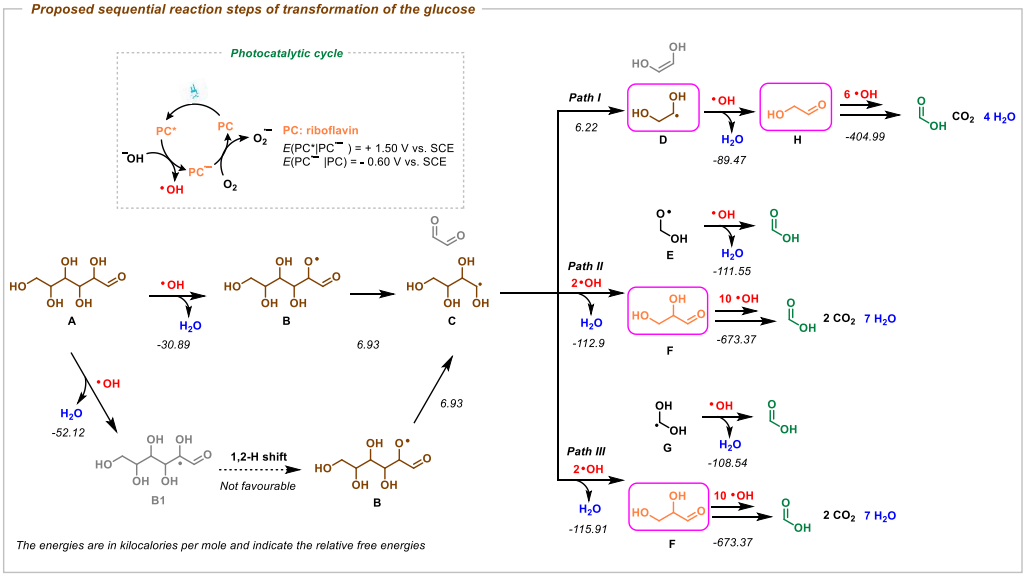

Figure 5.11. Proposed mechanism for sequential reaction steps of transformation of the glucose.

5.6 Conclusion

In summary, we have developed a visible light-mediated photocatalytic system for the transformation of biomass to valuable product formic acid. Notably, our approach operates under mild reaction conditions, effectively circumventing the need for high temperature and high pressure conditions that are commonly associated with such transformations. Furthermore, the implementation of a metal-free photocatalyst, as opposed to noble metal catalysts such as palladium-based catalysts, is employed for the reduction of the capital investment. Significantly, it is worth noting that everyday waste materials, like waste paper and oak plugs, can be effectively valorised to yield high-valued products, aligning with the principles of green chemistry. We believe that our strategy will contribute to the transformation of biomass-materials through visible -light-mediated photocatalysis and promote the advancement of supplementary methodologies in this field.

5.7 Supporting Information

5.7.1 Materials

NaOH, BHT (butylated hydroxytoluene), TEMPO (2,2,6,6-Tetramethylpiperidine-1-oxyl), 9,10-diphenylanthracene, $CuCl_2$, Tert-butanol and Benzoquinone were purchased from Sigma Aldrich; DABCO (1,4-diazabicyclo [2.2.2] octane), Et_3N (N, N-Diethylethanamine), Na_2CO_3, K_3PO_4 were purchased from TCI. Riboflavin was purchased from Alfa Aesar.

5.7.2 Freeze-thaw method

Lignocellulose is Earth's most abundant form of biomass, which is mainly comprised of cellulose (>40 % in wood stems), surrounded by the less crystalline polymers hemicellulose and lignin. Among them, cellulose is a polymer that is widely found in nature and constitutes the main component of plant cell walls.[25] Due to its complex and highly bound structure, dissolving cellulose is not as easy as the normal dissolution process. Although, there are a number of methods that can be used to dissolve cellulose so that it forms a solution under specific conditions, such as dissolution of cellulose with ionic liquids[26] and gasification, pyrolysis and pre-treatment hydrolysis/fragmentation steps,[27] it either needs very expensive ionic liquids as solvents or needs high temperature and high pressure, the most effective method is freeze-thaw treatment.[28-29]

Cellulose and stirring bar were put inside the 2M NaOH solution, then the suspensions were kept in a freezer at -20 °C for 4 h. Then, the formed frozen solids were thawed at room temperature with strong stirring. In the end, a clear and transparent cellulose solution was collected.

Figure 5.4. Comparison of the dissolution effects of cellulose using ordinary stirring and freezing-thawing methods.

Other compounds of Lignocellulose, such as hemicellulose, also can be extracted by using freeze-thaw assisted alkali treatment.[30]

5.7.3 Photocatalytic experiments

5.7.3.1 Experimental procedure in batch reactor

In a 28 mL schlenk tube containing glucose (36 mg), Photocatalyst Riboflavin (5 mol%) and stirring bar capped with rubber septum followed by vacuum (3 minutes) and O_2 flow provided by O_2 balloon (30 seconds) to make pure O_2 atmosphere inside the tube. This process is repeated for three times. After that the O_2 balloon was kept in this schlenk tube where needle is above on the solution, then1 mL 2 M NaOH solution was added into the schlenk tube. At the end, the solution was irradiated at Home-made blue LED (24 W, 456 nm) with vigorous stirring at 30 ^oC temperature for 20 hr. The liquid product formate was first acidified to FA with 2 M HCl and then the yields were determined by ^1H NMR with trimesic acid as internal standard.

5.7.3.2 Experimental procedure in in flow photoreactor

In order to verify the industrial production potential of this method, we conducted large-scale experiment using flow setup.

In a 28 mL schlenk tube containing photocatalyst Riboflavin (5 mol%) and stirring bar capped with rubber septum followed by vacuum (3 minutes) and O_2 flow provided by O_2 balloon (30 seconds) to make pure O_2 atmosphere inside the tube. This process is repeated for three times. After that the O_2 balloon was kept in this schlenk tube where needle is above on the solution, then cellulose solution (9 mg/mL, 15 mL) that prepared by using Freeze-thaw method was added into the schlenk tube.

First of all, in order to make pure O_2 atmosphere inside the flow setup system, the O_2 cylinder should be opened for around 20 minutes to flush the whole tubes by using a high O_2 flow rate. After that, further investigations were conducted out in the flow photoreactor on a fixed O_2 gas flow rate and sample flow rate respectively. At the light irradiation side, the solution was irradiated at 2 lamp kessil (40W, 427 nm). For light set up contains two lights where two lamps were placed up and down and on either side of the reaction tube.

At the end, the liquid product formate was first acidified to formic acid with 2 M HCl and then the yields were determined by ^1H NMR with trimesic acid as internal standard.

5.7.4 Equipment Installation Diagram

5.7.4.1 Schematic representation of flow photoreactor system

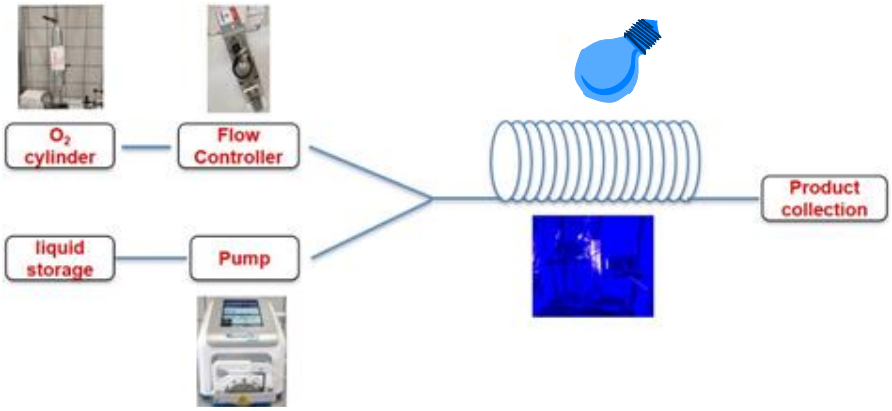

Figure 5.5. Schematic of flow reactor system.

5.7.4.2 Picture of flow photoreactor system

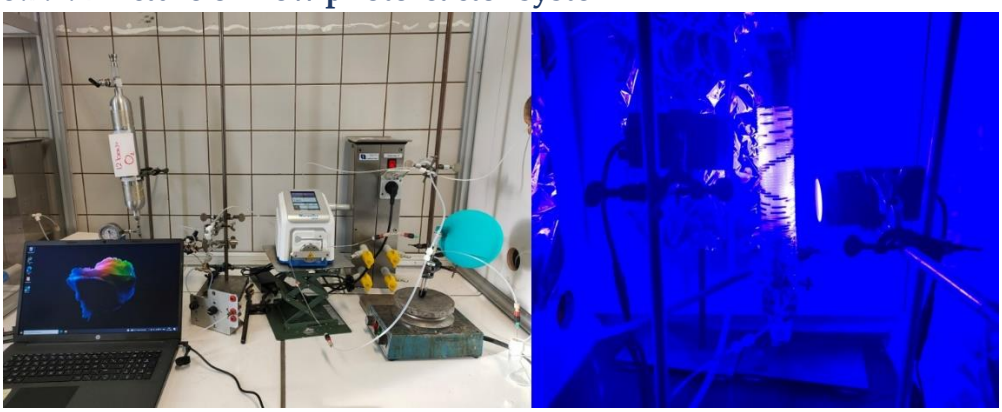

Figure 5.6. Pictures of flow reactor system.

Specific parameters:

[1] Total volume of reaction tube under the irradiation is 4 mL

[2] The distance between lamp and reactor is 3 cm.

5.7.5 Optimization of reaction conditions in flow reactor system

Table 5.7. Flow experiment optimization for cellulose oxidation to FA.

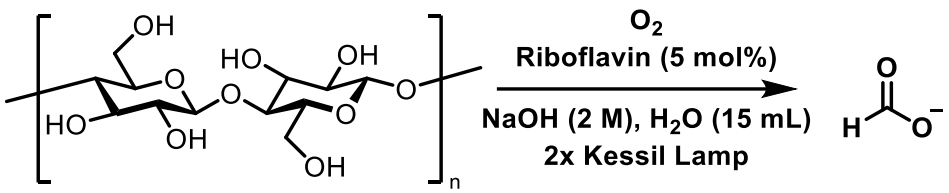

Entry	Amount of Substrate	O_2 flow Rate	Sample flow rate	Yield %
1	18 mg/mL	5 mL/h	3 mL/h	13
2	18 mg/mL	2 mL/h	1 mL/h	29.30
3	18 mg/mL	1 mL/h	0.5 mL/h	32.38
4	9 mg/mL	0.7 mL/h	0.5 mL/h	34.05
4	9 mg/mL	1 mL/h	0.5 mL/h	43.33
5	9 mg/mL	1 mL/h	0.5 mL/h	31.43
6	9 mg/mL	1 mL/h	0.3 mL/h	50
7	9 mg/mL	1.25 mL/h	0.25 mL/h	39.52
8	9 mg/mL	1 mL/h	0.25 mL/h	45.24
9	9 mg/mL	0.75 mL/h	0.25 mL/h	41.90

Following a systematic examination of the oxygen and sample rates within the flow setup, the optimized conditions for flow reactions were ultimately determined as entry 6 in **Table 5.5**. Reaction conditions: substrate, riboflavin (5 mol%), NaOH (2.0 M), H_2O (15 mL), 2 lamp kessil (40 W, 427 nm), 1 mL/h O_2 flow rate and 0.3 mL/h sample flow rate.

5.7.6 Fluorescence Quenching Studies

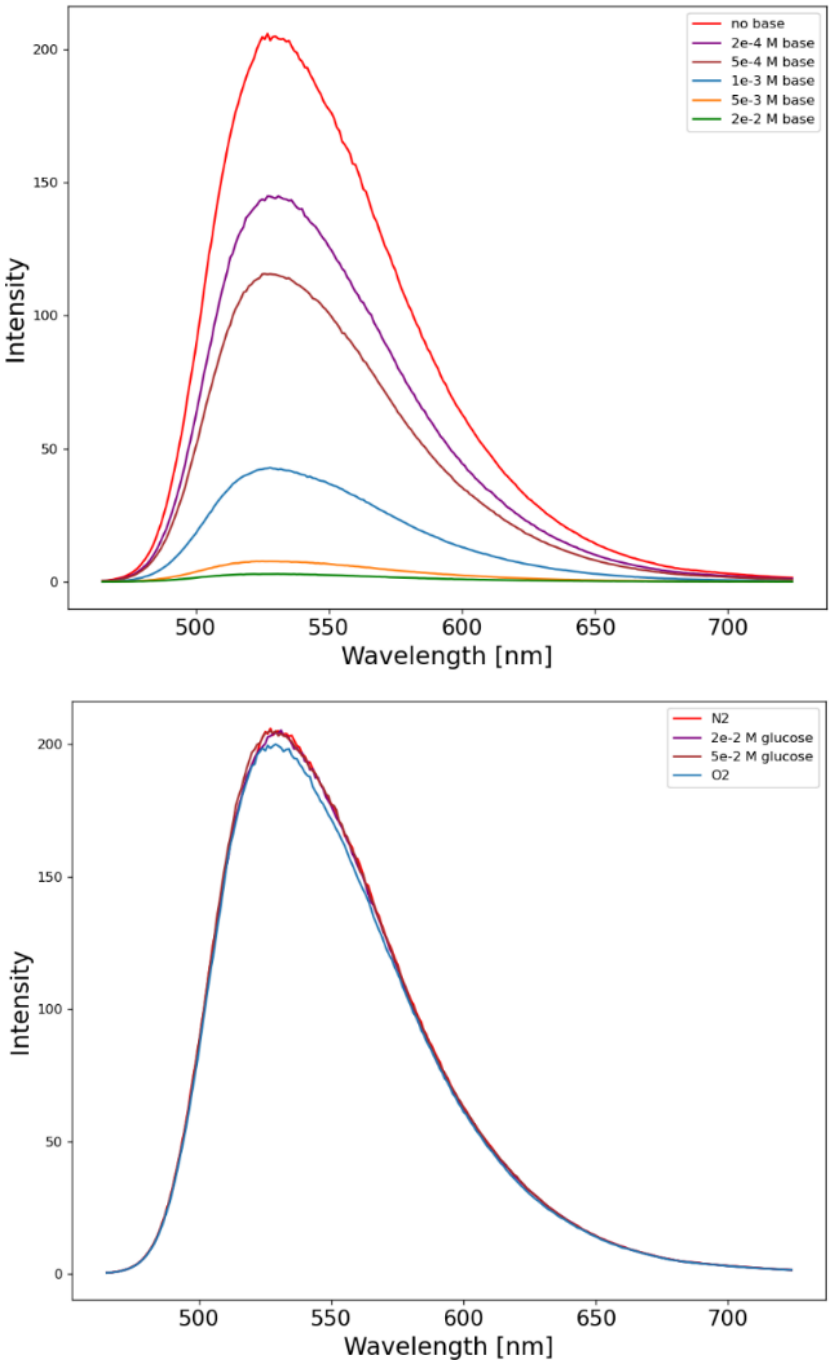

Figure 5.7. Stern-Volmer plot for riboflavin with base, O_2 and glucose as potential quenchers.

In the fluorescence quenching studies, there is no decrease in the emission intensity with O_2 or glucose, but the emission intensity decreases with the increase of the alkali concentration. It is proved that the hydroxide anion (OH^-) rather than O_2 or glucose is the quencher for the excited state of riboflavin.

5.7.7 Evaluation of various bases

Table 5.8. Evaluation of diverse bases with optimized conditions.

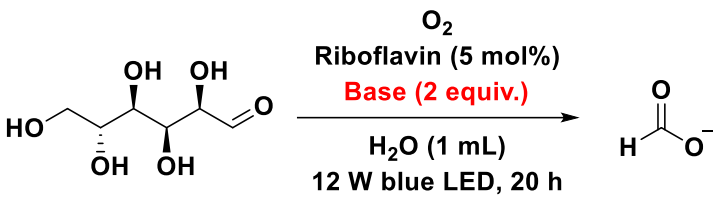

Entry	Substrate	Base (2M)	Time	Yield %
1	Glucose	K_3PO_4	20h	31
2	Glucose	Na_2CO_3	20h	5
3	Glucose	Et_3N	20h	21
4	Glucose	DABCO	20h	4
5	Glucose	NaOH	20h	43
6	Formic acid	NaOH	20h	100

We can clarified from entries 1–5, the externally added hydroxide ions play a key role in biomass degradation and the resulting formate remains stable in this reaction system and is not futher converted (**Entry 6**).

5.7.8 Theoretical calculation

All calculations were performed with the AMS2022 suite.[31-33] The PBE functional[34] was chosen, combined with the TZ2P basis set[35-36] (small frozen core). All geometries were optimized, and frequency calculations[37-38] were performed to characterize the nature of the

stationary point (no imaginary frequencies for minima, 1 imaginary frequency for transistion states). The thermochemical data were calculated at T=298K, and P=1 atm. For radicals, unrestricted DFT calculations were performed, while for the closed-shell species restricted calculations were performed.

5.8 References

1. Potočnik, J. Renewable Energy Sources and the Realities of Setting an Energy Agenda. *Science*. **2007**, *315*, 810–811.
2. MacDowell, N.; Ren, J.; Liu, Y.; Huang, Y.; Petit, T.; Zhang, B. Engineering oxygen-containing and amino groups into two-dimensional atomically-thin porous polymeric carbon nitrogen for enhanced photocatalytic hydrogen production. *Energy Environ. Sci.* **2018**, *11*, 1062.
3. Peighambardoust, S. J. Review of the proton exchange membranes for fuel cell applications. *Int. J. Hydrog. Energy* **2010**, *35*, 9349.
4. Zheng, J.; Du, J.; Wang, B.; Klemeš, J. J.; Liao, Q.; Liang, Y. A hybrid framework for forecasting power generation of multiple renewable energy sources. *Renew. Sust. Energ. Rev.* **2023**, *172*, 113046.
5. Bicelli, L. P. Hydrogen: a clean energy source. *Int. J. Hydrog. Energy*, **1986**, *11*, 555.
6. Tarhan, C.; Çil, M. A. A study on hydrogen, the clean energy of the future: Hydrogen storage methods. *J. Energy Storage*, **2021**, *40*, 102676.
7. Kraytsberg, A.; Ein-Eli, Review of advanced materials for proton exchange membrane fuel cells. Y. *Energy Fuels*, **2014**, *28*, 7303.
8. Felderhoff, M.; von Helmolt, R.; Eberle, U. Hydrogen storage: the remaining scientific and technological challenges. *Phys. Chem. Chem. Phys.* **2007**, *9*, 2643.
9. Preuster, P.; Papp, C.; Wasserscheid, P. Liquid organic hydrogen carriers (LOHCs): toward a hydrogen-free hydrogen economy. *Acc. Chem. Res.* **2017**, *50*, 74.
10. Müller, K.; Brooks, K.; Autrey, T. Hydrogen storage in formic acid: a comparison of process options. *Energy Fuels*, **2017**, *31*, 12603.
11. Moore, J. Thermal hydrogen: an emissions free hydrocarbon economy. *Int. J. Hydrogen Energy* **2017**, *42*, 12047.

12. Wei, D.; Sang, R.; Sponholz, P.; Junge, H.; Beller. M. Reversible hydrogenation of carbon dioxide to formic acid using a Mn-pincer complex in the presence of lysine. *Nat. Energy* **2022**, *7*, 438–447.
13. Bauer, F.; Coenen, L.; Hansen, T.; Palgan, Y. V. Technological innovation systems for biorefineries: a review of the literature. *Biofuels, Bioprod, Bioref* **2017**, *11*, 534.
14. a) Sokol, K. P.; Robinson, W. E.; Oliveira, A. R.; Warnan, J.; Nowaczyk, M. M.; Ruff, A.; Pereira, I. A. C.; Reisner, E. Photoreduction of CO2 with a Formate Dehydrogenase Driven by Photosystem II Using a Semi-artificial Z-Scheme Architecture. *J. Am. Chem. Soc.* **2018,** *140*, 16418–16422; b) Badiani, V. M.; Casadevall, C.; Miller, M.; Cobb, S. J.; Manuel, R. R.; Pereira, I. A. C.; Reisner, E. Engineering Electro- and Photocatalytic Carbon Materials for CO2 Reduction by Formate Dehydrogenase. *J. Am. Chem. Soc.* **2022,** *144*, 14207–14216.
15. a) Saxena, R. C.; Adhikari, D. K.; Goyal, H. B. Biomass-based energy fuel through biochemical routes: A review. *Renew. Sustain. Energy Rev.* **2009**, *13*, 167; b) Li, G.; Liu, W.; Ye, C.; Li, X.; Si, C.-L. Chemocatalytic conversion of cellulose into key platform chemicals. *Int. J. Polym. Sci.* **2018**, *2018*, 4723573; c) Parviainen, A.; King, A. W.; Mutikainen, I.; Hummel, M.; Selg, C.; Hauru, L. K.; Sixta, H.; Kilpelainen, I. Predicting cellulose solvating capabilities of acid–base conjugate ionic liquids. *ChemSusChem* **2013**, *6*, 2161–2169; d) Hou, Y.; Lin, Z.; Niu, M.; Ren, S.; Wu, W. Conversion of Cellulose into Formic Acid by Iron(III)-Catalyzed Oxidation with O2 in Acidic Aqueous Solutions. *ACS Omega* **2018**, *3*, 14910–14917.
16. a) Wang, W.; Niu, M.; Hou, Y.; Wu, W.; Liu, Z.; Liu, Q.; Ren, S.; Marsh, K. N. Catalytic conversion of biomass-derived carbohydrates to formic acid using molecular oxygen. *Green Chem.***, 2014**, *16*, 2614; b) Wölfel, R.; Taccardi, N.; Bösmann, A.; Wasserscheid, P. Selective catalytic conversion of biobased carbohydrates to formic acid using molecular oxygen. *Green Chem.***, 2011**, *13*, 2759; c) Reichert, J.; Brunner,

B.; Jess, A.; Wasserscheid, P.; Albert, J. Biomass oxidation to formic acid in aqueous media using polyoxometalate catalysts–boosting FA selectivity by in-situ extraction. *Energy Environ. Sci.*, **2015**, *8*, 2985-2990; d) Albert, J.; Wörfel, R.; Bösmann, A.; Wasserscheid, P. Selective oxidation of complex, water-insoluble biomass to formic acid using additives as reaction accelerators. *Energy Environ. Sci.*, **2012**, *5*, 7956; e) Albert, J.; Jess, A.; Kern, C.; Pöhlmann, F.; Glowienka, K.; Wasserscheid, P. formic acid-based fischer–tropsch synthesis for green fuel production from wet waste biomass and renewable excess energy. *ACS Sustainable Chem. Eng.* **2016**, *4*, 5078; f) Sarma, B. B.; Neumann, R. Polyoxometalate-mediated electron transfer–oxygen transfer oxidation of cellulose and hemicellulose to synthesis gas. *Nat. Commun.* **2014**, *5*, 4621; g) Li, J.; Ding, D.-J.; Deng, L.; Guo, Q.-X.; Fu, Y. Catalytic Air Oxidation of Biomass-Derived Carbohydrates to Formic Acid. *ChemSusChem* **2012**, *5*, 1313–1318.

17. a) Zhang, J.; Sun, M.; Liu, X.; Han, Y. Catalytic oxidative conversion of cellulosic biomass to formic acid and acetic acid with exceptionally high yields. *Catal. Today* **2014**, *233*, 77–823; b) Wei, G.-H.; Lu, T.; Liu, H.-Y.; Bai, J.-X.; Wang, Q.; Li, G.-Y.; Liang, Y.-H. Exploring the continuous cleavage-oxidation mechanism of the catalytic oxidation of cellulose to formic acid: A combined experimental and theoretical study. *Fuel* **2023**, *341*, 127667.
18. a) Jin, B.; Yao, G.; Wang, X.; Ding, K.; Jin, F. Photocatalytic Oxidation of Glucose into Formate on Nano TiO2 Catalyst. *ACS Sustainable Chem. Eng.* **2017**, *5*, 6377; b) Roongraung, K.; Chuangchote, S.; Laosiripojana, N.; Sagawa, T. Electrospun Ag-TiO2 Nanofibers for Photocatalytic Glucose Conversion to High-Value Chemicals. *ACS Omega* **2020**, *5*, 5862–5872; c) Lam, E.; Reisner, E. A TiO2 -Co(terpyridine)2 Photocatalyst for the Selective Oxidation of Cellulose to Formate Coupled to the Reduction of CO2 to Syngas. *Angew. Chem. Int. Ed.* **2021,** *60*, 23306–23312; d) Lam, E.; Miller, M.; Linley, S.; Manuel, R. R.; Pereira, I. A. C.; Reisner, E. Comproportionation of CO2 and

Cellulose to Formate Using a Floating Semiconductor-Enzyme Photoreforming Catalyst. *Angew. Chem. Int. Ed.* **2023,** *62*, e202215894.

19. a) Colmenares, J. C.; Luque, R. Heterogeneous photocatalytic nanomaterials: prospects and challenges in selective transformations of biomass-derived compounds. *Chem. Soc. Rev.* **2014**, *43*, 765; b) Guo, Y.-J.; Li, S.-J.; Sun, Y.-L.; Wang, L.; Zhang, W.-M.; Zhang, P.; Lan, Y.; Li, Y. Practical DMSO-promoted selective hydrolysis–oxidation of lignocellulosic biomass to formic acid attributed to hydrogen bonds. *Green Chem*. **2021**, *23*, 7041−7052; c) Shen, F.; Smith Jr, R. L.; Li, J.; Guo, H.; Zhang, X.; Qi, X. Critical assessment of reaction pathways for conversion of agricultural waste biomass into formic acid. *Green Chem.* **2021**, *23*, 1536−1561.
20. a) Devi, L. G.; Kavitha, R. A review on non metal ion doped titania for the photocatalytic degradation of organic pollutants under UV/solar light: Role of photogenerated charge carrier dynamics in enhancing the activity. *Appl. Catal. B: Environ.* **2013**, *140*, 559−587; c) Liu, X.; Duan, X.; Wei, W.; Wang, S.; Ni, B.-J. Photocatalytic conversion of lignocellulosic biomass to valuable products. *Green Chem.* **2019**, *21*, 4266−4289; d) Suriyachai, N.; Chuangchote, S.; Laosiripojana, N.; Champreda, V.; Sagawa, T. Synergistic effects of Co-doping on photocatalytic activity of titanium dioxide on glucose conversion to value-added chemicals. *ACS Omega* **2020**, *5*, 20373−20381.
21. a) Schultz, D. M.; Yoon, T. P. Solar synthesis: prospects in visible light photocatalysis. *Science* **2014**, *343*, 1239176; b) de Assis, G. C.; Silva, I. M. A.; dos Santos, T. G.; dos Santos, T. V.; Meneghetti, M. R.; Meneghetti, S. M. P. Photocatalytic processes for biomass conversion. *Catal. Sci. Technol.* **2021**, *11*, 2354−2360; c) Nguyen, V.-C.; Nimbalkar, D. B.; Nam, L. D.; Lee, Y.-L.; Teng, H. Photocatalytic Cellulose Reforming for H2 and Formate Production by Using Graphene Oxide-Dot Catalysts. *ACS Catal.* **2021**, *11*, 4955−4967; d) Zhang, Q.; Yang, C.; Zhang, B.; Deng, K. Cobalt Porphyrazine Supported on

SnO2 with Oxygen Vacancies for Boosting Photocatalytic Aerobic Oxidation of Glucose to Organic Acids in an Aqueous Medium. *ACS Sustainable Chem. Eng.* **2021**, *9*, 2057−2066.

22. a) Detz, R. J.; Reek, J. N. H.; van der Zwaan, B. C. C. The future of solar fuels: when could they become competitive? *Energy Environ. Sci.* **2018**, *11*, 1653; b) Xu, L.; Liu, Y.; Li, L.; Hu, Z.; Yu, J. C. Fabrication of a Photocatalyst with Biomass Waste for H2O2 Synthesis. *ACS Catal.* **2021**, 14480−14488.
23. Gopakumar, A.; Zhang, T.; Das, S. Micro-Batch flow reactor for the photoproduction of H2O2 from water/real seawater. *J. Flow Chem.* **2023**, *13*, 185−192.
24. Qin, Y.; Zhang, T.; Ching, H. V.; Raman, G. S.; Das, S. Integrated strategy for the synthesis of aromatic building blocks via upcycling of real-life plastic wastes. *Chem* **2022**, *8*, 2472−2484.
25. Wakerley, D. W.; Kuehnel, M. F.; Orchard, K. L.; Ly, K. H.; Rosser, T. E.; Reisner, E. Solar-driven reforming of lignocellulose to H2 with a CdS/CdOx photocatalyst. *Nat. Energy* **2017**, *2*, 17021.
26. Zhu, S.; Wu, Y.; Chen, Q.; Yu, Z.; Wang, C.; Jin, S.; Ding, Y.; Wu, G. Dissolution of cellulose with ionic liquids and its application: a mini-review. *Green Chem.* **2006**, *8*, 325−327.
27. Colmenares, J. C.; Luque, R. Heterogeneous photocatalytic nanomaterials: prospects and challenges in selective transformations of biomass-derived compounds. *Chem. Soc. Rev.* **2014**, *43*, 765−78.
28. Isobe, N.; Noguchi, K.; Nishiyama, Y.; Kimura, S.; Wada, M.; Kuga, S. Role of urea in alkaline dissolution of cellulose. *Cellulose* **2013**, *20*, 97−103.
29. Qi, H.; Yang, Q.; Zhang, L.; Liebert, T.; Heinze, T. The dissolution of cellulose in NaOH-based aqueous system by two-step process. *Cellulose* **2010**, *18*, 237−245.
30. Li, J.; Liu, Z.; Feng, C.; Liu, X.; Qin, F.; Liang, C.; Bian, H.; Qin, C.; Yao, S. Green, efficient extraction of bamboo hemicellulose using freeze-thaw assisted alkali treatment. *Bioresour. Technol.* **2021**, *333*, 125107.

31. E.J. Baerends, *ADF2022.01, SCM, Theoretical Chemistry, Vrije Universiteit, Amsterdam, The Netherlands,* http://www.scm.com, 2022.
32. C. Fonseca Guerra, J.G. Snijders, G. te Velde, E.J. Baerends, Towards an order-N DFT method. *Theor. Chem. Acc.* **1998,** *99*, 391−403.
33. G. te Velde, F.M. Bickelhaupt, E.J. Baerends, C. Fonseca Guerra, S.J.A. van Gisbergen, J.G. Snijders, T. Ziegler, Chemistry with ADF. *J. Comput. Chem.* **2001,** *22*, 931−967.
34. J.P. Perdew, K. Burke, M. Ernzerhof, Generalized Gradient Approximation Made Simple, *Phys. Rev. Lett.* **1996**, *77*, 3865−3868.
35. E. van Lenthe, E.J. Baerends, Optimized Slter-type basis sets for the elements 1-118, *J. Comput. Chem.* **2003**, *24*, 1142−1156.
36. D.P. Chong, E. van Lenthe, S.J.A. van Gisbergen, E.J. Baerends, Even-tempered slter-type orbitals revisited: From hydrogen to krypton, *J. Comput. Chem.* **2004**, *25*, 1030−1036.
37. S.K. Wolff, Analytical second derivatives in the Amsterdam density functional package, *Int. J. Quantum Chem.* **2005**, *104*, 645−659.
38. L. Fan, T, Ziegler, Application of density functional theory to infrared absorption intensity calculations on transition-metal carbonyls, *J. Phys. Chem.* **1992**, *96*, 6937−6941.

Summary and Outlook

Broadly, this thesis is primarily focused on the reactions mediated by visible light, which could show the advantage and utility of photochemistry. In **Chapter 1**, the brief history, importance, and advantages of photoredox/catalytic reactions have been discussed. Low energy consumption, sustainability and facile application as the merits inspire us to explore more methodologies based on photochemistry. In the realm of reaction system design, it is of paramount significance to apprehend the redox processes between catalysts and substrates. This comprehension provides the potentials to not only optimize reaction conditions but also predict and expand the scope of substrate applicability. Therefore, three redox pathways of homogeneous photocatalysis have been described with the corresponding examples.

Simultaneously, the stability and facile separability proficiency of heterogeneous catalysts have drawn immensely attention in photocatalysis. In this thesis, metal oxides and metal-free semiconductors including covalent organic framework (COF) and polymeric carbon nitrides (PCN) have been discussed. As 'no one is perfect', each material or catalyst has its shortcoming. To overcome the obstacle, various modifications of catalysts, particularly for PCN, are required and introduced along with selected examples in **Chapter 1**.

Furthermore, photochemistry driven by noncovalent interactions (NCIs) has shown its importance in biological and organic synthetic domains. NCIs including hydrogen bonding, π-interactions, van der Waals, and Coulombic interactions maintain a fundamental role as the driving force within numerous processes. In organic synthesis, π-interactions have garnered extensive utilization, serving not only to facilitate chemical reactions but also to systematically engineer catalysts

through a rational approach. Consequently, diverse categories of π-interactions have been thoroughly discussed, along with their respective examples.

In the last part of **Chapter 1**, red light-mediated photocatalysis has been separately elucidated due to its relatively infrequent utilization within the domain of photocatalysis when contrasted with other wavelengths of visible light.
In contrast to the blue light system, the catalytic efficiency observed in the upscaling reactions under red light irradiation is notably enhanced. This enhancement can be attributed to the increased catalytic proficiency stemming from the superior light penetration characteristics of red light within the reaction medium. The explication of scalability pertaining to the red light-mediated reaction is exemplified through the case study of Stephenson's trifluoromethylation process.

In **Chapter 2–5**, projects based on photochemistry including hydrogen peroxide (H_2O_2) generation with modified PCN (**Chapter 2**), functionalized amines formation via π-π interactions (**Chapter 3**), red light-mediated sulfonyltrifluoromethylation of olefins (**Chapter 4**) and the photocatalytic transformation of biomass to formic acid (**Chapter 5**) have been prepared and explained in detail. All these projects have showcased the efficacy and practicality of employing photochemistry, elucidating its advantages and potential applications. Our scientific contributions in each chapter/project are summarized as follows:

In **Chapter 2**, we have modified PCN by introducing aryl amino moieties to facilitate the photocatalytic H_2O_2 generation by adjusting the electronic structure of PCN. The pivotal progress of this study resides in the fabrication of an efficient photocatalyst for the generation of H_2O_2, along with its detailed elucidation at the atomic level through a conjoined approach of solid-state MAS NMR spectroscopy employing nuclei such as ^{19}F, ^{13}C, ^{1}H, and ^{15}N. Moreover, facilitated by computational

investigations, we elucidated a potential reaction model at the atomic level. This revelation extends novel insights into the optimization of photocatalysts for the advancement of photocatalytic H_2O_2 production.

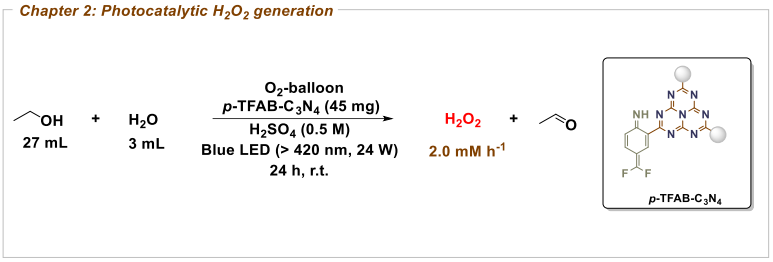

In **Chapter 3**, we have made an innovative approach that utilizes visible-light irradiation to facilitate the reductive production of α-amino radicals, which hold significant synthetic relevance. This procedure uses a π-π stacked ionic complex as a pivotal mediator. Notably, the multiple π interactions serve to stabilize the transient reactive intermediate. The fascinating aspect of this methodology is that it eliminates the need for external photocatalysts or initiators within the Giese-type three-component coupling system. The substrate scope encompasses a broad scope, as a diverse array of amines, aldehydes, and olefins demonstrate pronounced reactivity. We firmly believe that this protocol has the potential to open new possibilities for synthesizing lesser-explored amines, benefiting both the academic and industrial aspects of organic synthesis.

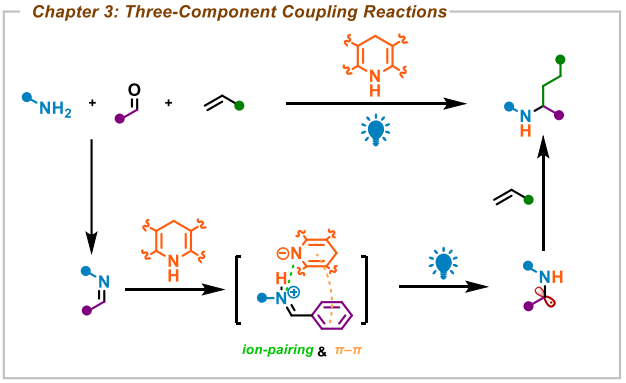

In **Chapter 4**, our efforts have culminated in the development of a pioneering protocol that focuses on red light-mediated photocatalysis to achieve sulfonyltrifluoromethylation on olefin substrates. The well-constructed reaction framework has adeptly surmounted challenges inherent to radical regioselectivity. The impressive range of adaptable substrates and outstanding performance on intricate molecular structures underscore the significant efficiency and exceptional tolerance towards diverse functional groups demonstrated by these transformations. Further investigation through post-functionalization inquiries notably emphasizes the substantial industrial viability of the sulfonyltrifluoromethylated product, thereby affirming the profound significance of our strategy. We believe that our innovative approach will drive forward the realm of regioselective functionalization through the utilization of red light-mediated photocatalysis, thereby catalyzing the development of additional methods in this field.

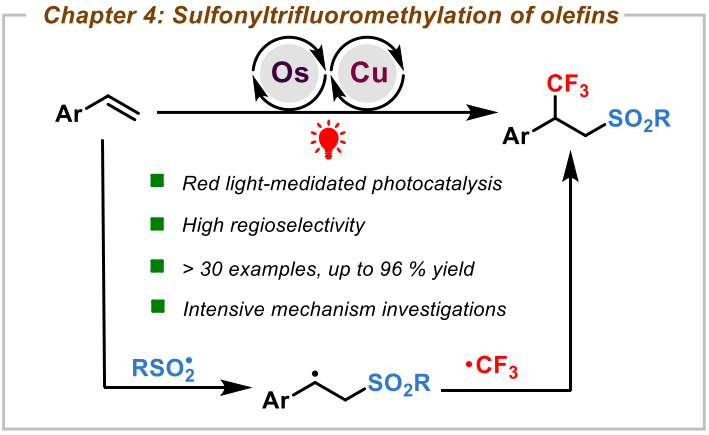

In **Chapter 5**, we have developed a photocatalytic system for the transformation of biomass to formic acid under the irradiation of visible light. Remarkably, our methodology operates within mild reaction parameters, eliminating the need for the elevated temperature and pressure typically associated with such conversions. Furthermore, we have adopted a metal-free photocatalyst, deviating from noble metal counterparts like palladium-based catalysts. Notably, it merits highlighting that everyday waste materials, including discarded paper and oak remnants, can be efficiently upcycled to yield valuable products, aligning harmoniously with the principles of green chemistry. We firmly believe that our innovative approach will significantly contribute to the transformation of biomass-derived materials through visible light-mediated photocatalysis and promote the advancement of supplementary methodologies in this field.

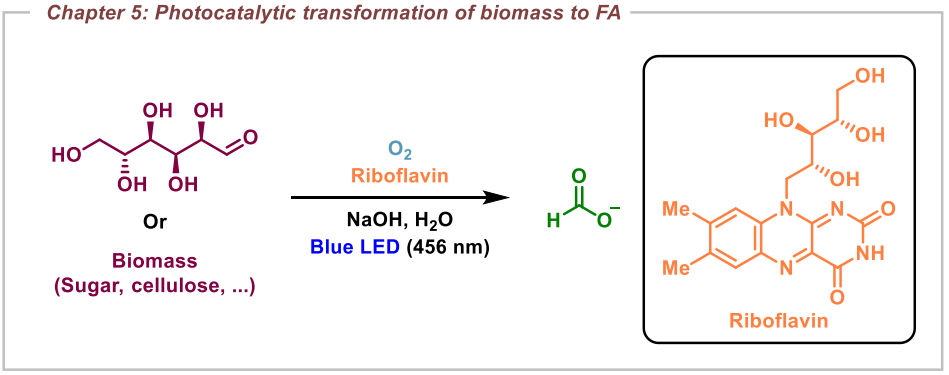

List of Publications and Presentations

Publications:

1. **Zhang**, **T.;** Vanderghinste, J.; Guidetti, A.; Van Doorslaer, S.; Barcaro, G.; Monti, S.; Das, S. Pi-Pi Stacking Complex Induces Three-Component Coupling Reactions to Synthesize Functionalized Amines, *Angew. Chem. Int. Ed*. **2022**, *61*, e202212083. (doi.org/10.1002/anie.202212083)
2. **Zhang**, **T.;** Schilling, W.; Khan, S. U.; Ching, H. Y. V.; Lu, C.; Chen, J.; Jaworski, A.; Barcaro, G.; Monti, S.; De Wael, K.; Slabon, A.; Das, S. Atomic Level Understanding for the Enhanced Generation of Hydrogen Peroxide by Aryl Amino Polymeric Carbon Nitrides, *ACS Catal.* **2021**, *11*, 14087. (doi.org/10.1021/acscatal.1c03733)
3. **Zhang**, **T.;** Zhang, Y.; Das, S. Photoredox Catalysis for the Cycloaddition Reactions, *ChemCatChem*, **2020**, *12*, 6173. (doi.org/10.1002/cctc.202001195)
4. Zhang, Y.$^{+}$; **Zhang**, **T.**$^{+}$**;** Das, S. Selective Functionalization of Benzylic C(sp^3)-H Bonds to Synthesize Complex Molecules, *Chem* **2022**, *8(12)*, 3175. (doi.org/10.1016/j.chempr.2022.10.005)
5. Gopakumar, A.; **Zhang**, **T.;** Das, S. Micro-Batch flow reactor for the photoproduction of H2O2 from water/real seawater, *J. Flow Chem.* **2023**, *13*, 185. (doi.org/10.1007/s41981-023-00257-1)
6. Sahoo, P. K.; **Zhang**, **T.;** Das, S. Oxidative transformation of biomass into formic acid, *Eur. J. Org. Chem.* **2021**, *2021*, 1331. (doi.org/10.1002/ejoc.202001514)
7. Zhang, Y.; **Zhang T.;** Das, S. Catalytic transformation of CO2 into C1 chemicals using hydrosilanes as a reducing agent, *Green Chem.* **2020**, *22*, 1800. (doi.org/10.1039/C9GC04342J)

Presentations:

1. Oral presentation:
   Tong Zhang, "Pi-Pi Stacking Complex Induces Three-Component Coupling Reactions to Synthesize Functionalized Amines" in the Merck Organic Chemistry Symposium, Blankenberge, Belgium (December, 2022).
2. Poster presentation:
   Tong Zhang, "Carboxylic Acids Promote Photoredox Catalysis in the Cancer Cell" in the 17th Belgian Organic Synthesis Symposium (BOSS 2022), Namur, Belgium (July, 2022).
3. Online poster presentation:
   Tong Zhang, "Atomic Level Understanding for the Enhanced Generation of Hydrogen Peroxide by Aryl Amino Polymeric Carbon Nitrides" in the Merck Organic Chemistry Symposium, online (December, 2021).
4. Poster presentation:
   Tong Zhang, "A simple ketone as an efficient metal-free Photocatalyst for visible-light-mediated Diels–Alder and aza-Diels–Alder reactions" in the Merck Organic Chemistry Symposium, Blankenberge, Belgium (December, 2019).